CORROSION AND PROTECTION OF MAGNESIUM ALLOYS

EDITED BY: Liang Wu, Xiao-Bo Chen and Yingwei Song
PUBLISHED IN: Frontiers in Materials

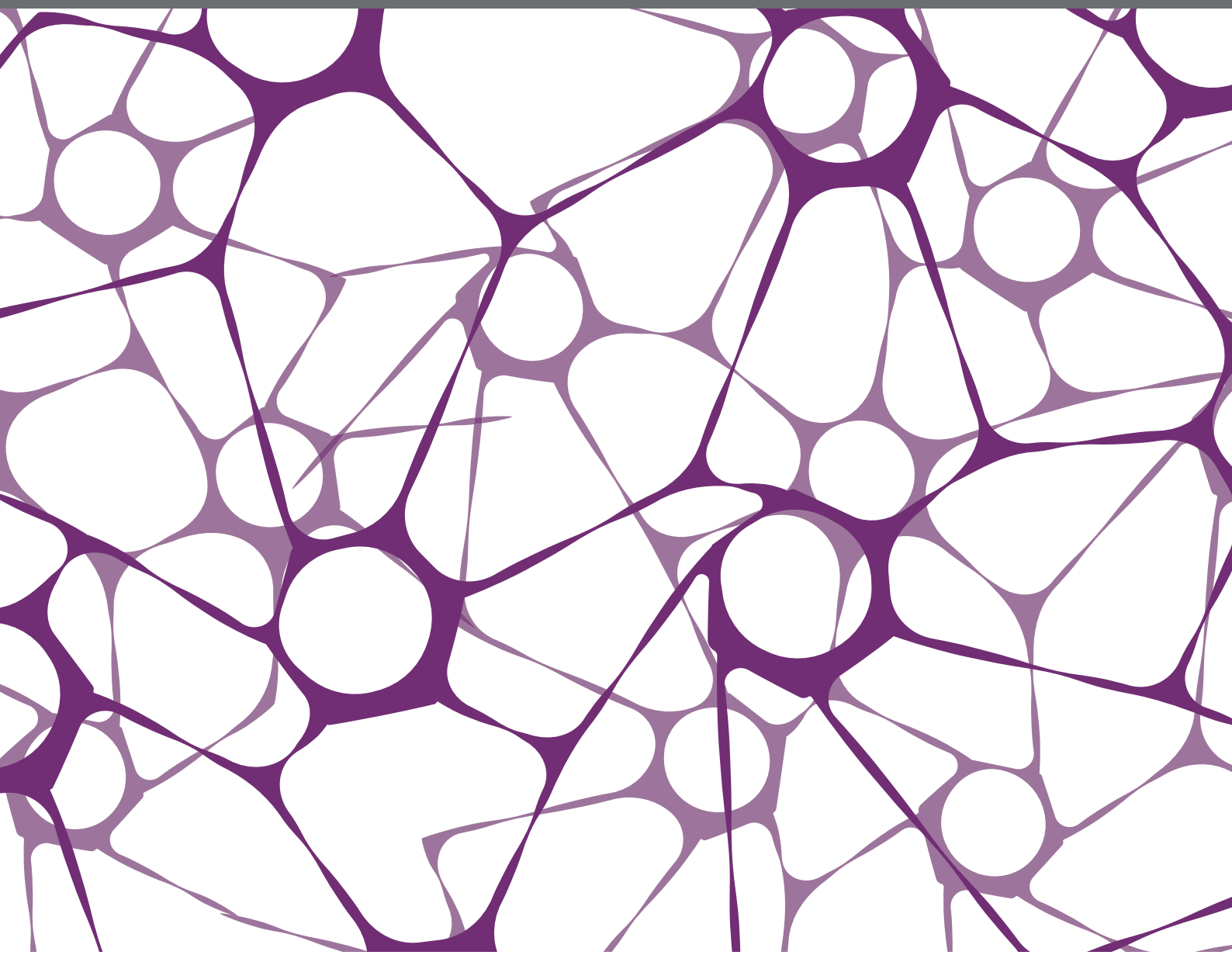

frontiers Research Topics

frontiers

ISSN 1664-8714
ISBN 978-2-83251-561-7
DOI 10.3389/978-2-83251-561-7

About Frontiers

Frontiers is more than just an open-access publisher of scholarly articles: it is a pioneering approach to the world of academia, radically improving the way scholarly research is managed. The grand vision of Frontiers is a world where all people have an equal opportunity to seek, share and generate knowledge. Frontiers provides immediate and permanent online open access to all its publications, but this alone is not enough to realize our grand goals.

Frontiers Journal Series

The Frontiers Journal Series is a multi-tier and interdisciplinary set of open-access, online journals, promising a paradigm shift from the current review, selection and dissemination processes in academic publishing. All Frontiers journals are driven by researchers for researchers; therefore, they constitute a service to the scholarly community. At the same time, the Frontiers Journal Series operates on a revolutionary invention, the tiered publishing system, initially addressing specific communities of scholars, and gradually climbing up to broader public understanding, thus serving the interests of the lay society, too.

Dedication to Quality

Each Frontiers article is a landmark of the highest quality, thanks to genuinely collaborative interactions between authors and review editors, who include some of the world's best academicians. Research must be certified by peers before entering a stream of knowledge that may eventually reach the public - and shape society; therefore, Frontiers only applies the most rigorous and unbiased reviews.
Frontiers revolutionizes research publishing by freely delivering the most outstanding research, evaluated with no bias from both the academic and social point of view. By applying the most advanced information technologies, Frontiers is catapulting scholarly publishing into a new generation.

What are Frontiers Research Topics?

Frontiers Research Topics are very popular trademarks of the Frontiers Journals Series: they are collections of at least ten articles, all centered on a particular subject. With their unique mix of varied contributions from Original Research to Review Articles, Frontiers Research Topics unify the most influential researchers, the latest key findings and historical advances in a hot research area! Find out more on how to host your own Frontiers Research Topic or contribute to one as an author by contacting the Frontiers Editorial Office: frontiersin.org/about/contact

CORROSION AND PROTECTION OF MAGNESIUM ALLOYS

Topic Editors:
Liang Wu, Chongqing University, China
Xiao-Bo Chen, RMIT University, Australia
Yingwei Song, Institute of Metal Research, Chinese Academy of Sciences (CAS), China

Citation: Wu, L., Chen, X.-B., Song, Y., eds. (2023). Corrosion and Protection of Magnesium Alloys. Lausanne: Frontiers Media SA.
doi: 10.3389/978-2-83251-561-7

Table of Contents

frontiers | Frontiers in Materials

TYPE Editorial
PUBLISHED 15 September 2022
DOI 10.3389/fmats.2022.1006444

OPEN ACCESS

EDITED AND REVIEWED BY
John L. Provis,
The University of Sheffield,
United Kingdom

*CORRESPONDENCE
Liang Wu,
wuliang@cqu.edu.cn

SPECIALTY SECTION
This article was submitted to Structural Materials,
a section of the journal
Frontiers in Materials

RECEIVED 29 July 2022
ACCEPTED 22 August 2022
PUBLISHED 15 September 2022

CITATION
Wu L, Chen X-B and Song Y-W (2022), Editorial: Corrosion and protection of magnesium alloys.
Front. Mater. 9:1006444.
doi: 10.3389/fmats.2022.1006444

Editorial: Corrosion and protection of magnesium alloys

Liang Wu[1,2]*, Xiao-Bo Chen[3] and Ying-Wei Song[4]

[1]College of Materials Science and Engineering, Chongqing University, Chongqing, China, [2]National Engineering Research Center for Magnesium Alloys, Chongqing University, Chongqing, China, [3]School of Engineering, STEM College, RMIT University, Melbourne, VIC, Australia, [4]Key Laboratory of Nuclear Materials and Safety Assessment, Institute of Metal Research, Chinese Academy of Sciences, Shenyang, China

KEYWORDS

magnesium alloys, corrosion, protection coatings, inhibitors, alloys elements

Editorial on the Research Topic
Corrosion and protection of magnesium alloys

As green metal engineering materials in the 21st century, magnesium (Mg) and its alloys are abundant in nature and exhibit high commercial value and diverse application prospects in structural engineering, such as automotives, electronic communications, aerospace and defense industry. However, Mg alloys are highly active in terms of chemistry and prone to corrosion, which is one of the key bottlenecks in terms of large scale engineering services. This Research Topic was compiled aiming to highlight the state-of-the art research in relation to corrosion and protection of Mg alloys and provide guidance to the future development of Mg alloys towards robust and sustained corrosion resistance through nine articles combining critical reviews, scientific explorations, and perspectives.

Thermal control over oxidation is a common and conductive approach for tackling corrosion challenges of Mg-based materials for aerospace services. Jiang et al. calculated the Pilling-Bedworth ratio of oxides preferentially formed from the precipitated phases in Mg alloys. Results show that enrichment in Y_2O_3 in the composite oxidation film leads to improved corrosion resistance of Mg-Y samples. Wen et al. explored corrosion behavior of Mg alloy LA103Z with a thermally controlled oxide film in 3.5% NaCl solution. It is evident that corrosion of the Mg-Li alloy with a chemical oxidation film is initiated in pitting format, expands in depth in the early stage, forms corrosion holes, and then gradually develops into river-like morphology. In the last stage, the increasing corrosion products progressively cover the entire sample surface, which reduces the corrosion rate of the Mg alloy.

Combinations with corrosion inhibiting chemicals (*e.g.*, graphene oxide) have been applied to Mg alloy surfaces. Zhang et al. reported a (3-aminopropyl)-triethoxysilane-modified graphene oxide (GO) composite film upon Mg alloy AZ31 substrates. Due to the high barrier properties of layered GO, the silane-GO coatings provide effective protection to Mg alloy substrate and reduce surface defects in the GO film that occur during silane modification. In addition, corrosion products between the outer silane-GO film and Mg

alloy substrate improve the corrosion resistance of Mg alloys. Gao et al. proposed a graphene-modified oil-based epoxy resin coating (G/OEP) on Mg alloy AZ31 with epoxy resin (polyurethane) and corresponding curing agent as primary ingredients. Graphene fills up the physical defects in the hydrophobic coating and improves the shielding ability against attack from corrosive media. A critical concentration (0.6 wt%) of graphene is determined with optimal corrosion resistance.

Rare Earth salts containing chemical conversion coatings is a promising solution to the corrosion challenges of Mg alloys. Li et al. employed micro-arc oxidation to prepare zirconium-containing films with varying concentrations on the surface of Mg alloy AZ91. It was stated that the $ZrSiO_4$ particles in the electrolyte enter the MAO film and reduce film defects. Hong et al. doped yttrium (Y) into Mg-Al layered double hydroxide films (MgAlY-LDHs) upon surface-anodized Mg-2Zn-4Y alloy by means of a hydrothermal approach. Y ions are doped into the MgAl-LDHs film in an isomorphic substitution manner and exhibit high corrosion resistance. The ternary LDHs film grown *in situ* on the Mg-2Zn-4Y alloy provides an alternative option for controlling corrosion of Mg alloys. Han et al. prepared anticorrosion films with superhydrophobic properties. *In-situ* layered double hydroxides (LDHs) were deposited on etched Mg alloy AZ31, and then they were modified into films with micro/nano hierarchical surface morphology. The super-hydrophobic LDH films provide high corrosion resistance owing to the double-protection derived from the LDHs and super-hydrophobicity.

In a Na_2SiO_3-Na_3PO_4 system, Silvina Román et al. investigated corrosion susceptibility of two Al-Mg dilution alloys (Al-0.5wt.%Mg and Al-2wt.%Mg) obtained by directional solidification (columnar, equiaxed and columnar-to-equiaxed transition, CET) at room temperature with different grain characteristics. The columnar grain zone presents higher corrosion resistance than the equiaxed grain zone, and the transversal section presents higher corrosion resistance than the longitudinal section. In addition, the decreasing polarization resistance as a function of distance from the base increases grain size, secondary dendritic arm spacings and hardness. When the polarization resistance increases, the critical temperature gradient decreases. Calado et al. reviewed the latest progress of WE series Mg alloys (such as mechanical properties, corrosion properties) in terms of correlations between those properties and microstructure, the individual role of specific alloying elements in the WE series, and sound protective strategies to manage their corrosion behavior.

The present contributions in the compiled articles are broad in nature, emphasizing the science and technology in relation to corrosion and protection of Mg alloys. This is also the purpose of this Research Topic, in which various methods of protecting magnesium alloys from corrosion are widely depicted. Cross-fertilization of new ideas are likely to emanate by compiling such complementary but not necessarily overlapping articles.

Author contributions

LW drafted the manuscript. X-BC and Y-WS edited and proof-read the manuscript.

Conflict of interest

The authors declare that the research was conducted in the absence of any commercial or financial relationships that could be construed as a potential conflict of interest.

Publisher's note

frontiers in Materials

ORIGINAL RESEARCH
published: 18 August 2021
doi: 10.3389/fmats.2021.739334

The Corrosion Resistance of Graphene-Modified Oily Epoxy Coating on AZ31 Magnesium Alloys

*Zhengyuan Gao, Chengjin Sun, Lianteng Du, Dong Yang, Xiang Zhang and Zhiguo An**

School of Mechatronics and Vehicle Engineering, Chongqing Jiaotong University, Chongqing, China

In order to enhance the corrosion resistance of AZ31 magnesium alloy, graphene-modified oily epoxy resin coating (G/OEP) were prepared on the surface of magnesium alloy. SEM observations show that graphene has fewer surface defects, and can significantly improve the surface quality of the coating and reduce defects. FI-TR testing shows that coating are mainly composed of epoxy resin (polyurethane) and its corresponding curing agent. Electrochemical testing shows that the coating can provide good corrosion protection for magnesium alloy. Compared with the corrosion current density of magnesium alloy of 6.20×10^{-7} A/cm^2, the G/OEP can significantly reduce the corrosion current density to 6.96×10^{-12} A/cm^2. Analysis of the morphology of the coating after electrochemical corrosion found that graphene can improve the shielding ability of the coating to corrosive media, and reduce the damage of corrosion to the coating structure, and enhance the corrosion resistance of the coating. The content of graphene for excellent corrosion resistance of coating during this experiment is 0.6 wt%. The graphene can fill the defects generally in the coating during the curing process to prevent substrate from penetration of corrosive media caused by the density and hydrophobicity of coating are increased.

Keywords: AZ31 magnesium alloy, graphene, corrosion resistance, oily epoxy resin, coating

OPEN ACCESS

Edited by:
Liang Wu,
Chongqing University, China

Reviewed by:
Bo Song,
Southwest University, China
Jiejun He,
Guizhou Institute of Technology, China

****Correspondence:***
Zhiguo An
anzhiguo@cqjtu.edu.cn

Specialty section:
This article was submitted to Environmental Degradation of Materials, a section of the journal Frontiers in Materials

Received: *10 July 2021*
Accepted: *31 July 2021*
Published: *18 August 2021*

Citation:
Gao Z, Sun C, Du L, Yang D, Zhang X and An Z (2021) The Corrosion Resistance of Graphene-Modified Oily Epoxy Coating on AZ31 Magnesium Alloys. Front. Mater. 8:739334. doi: 10.3389/fmats.2021.739334

INTRODUCTION

In recent decades, due to the increasingly serious environmental problems, magnesium alloy materials are extremely suitable for material substitution standards for energy-saving and light-weight design. Therefore, they have been widely used in many fields such as automobiles and aerospace (Tekumalla et al., 2014; Dziubińska et al., 2016; Zeng et al., 2018; Ramalingam et al., 2019; Song et al., 2020). However, magnesium is extremely reactive. The standard electrode potential of magnesium is 2.37 V, which is very easy to corrode. The naturally formed $MgO/Mg(OH)_2$ has a loose and porous structure, resulting in a weak corrosion resistance of the magnesium alloy itself (Song and Atrens, 2003; Song, 2005; Chu et al., 2019; Chen et al., 2019).

In response to this problem, epoxy resin organic coating is the most economical and effective method from an industrial point of view (Shi et al., 2012; He et al., 2014; Guo et al., 2020). It's easy to operate, low cost, and has natural advantages in industrial applications (Jin et al., 2015; Ou et al., 2020). At present, oily coatings have good film-forming properties, strong water resistance and excellent corrosion resistance. Although epoxy resin has shown excellent anti-corrosion protection for magnesium alloy matrix, it is affected by the cross-linking density of epoxy bonds, and the coating will be affected in the later curing and cross-linking process.

Defects such as holes and cracks are generated, thereby reducing the corrosion protection ability of the substrate. Therefore, in recent years, researchers have done a lot of research in this direction,

the main method is to add corrosion inhibitor fillers to the coating materials (Dong et al., 2013; Deyab et al., 2016; Xie et al., 2019; Rahman et al., 2019). Graphene has excellent corrosion inhibition performance among many corrosion inhibitor fillers (Zhang et al., 2015; Hao et al., 2018; Xia et al., 2018; Ziat et al., 2020). Graphene is a carbon material with a two-dimensional structure, and has excellent physical properties and stable chemical properties. The special structure can have extremely high resistance to oxygen and water permeability (Zhao et al., 2013; Wu et al., 2018; Zhou et al., 2018; Cui et al., 2019; Ding et al., 2019). Compared with other methods, the oily epoxy resin coating modified by the graphene is stable in the corroded state for the substrate. Moreover, the inhibition effect can be improved by the dispersion in oily epoxy resin and the hydrophobicity is better than waterborne epoxy resin. As soon as these advantages were discovered, they received extremely high attention from research scholars. Chen et al. modified graphene carbonitride nanosheets (g-C3N4) and graphene through π-π bond interactions to increase the dispersion performance of graphene in epoxy resin coatings, and significantly improve the corrosion resistance of the coating (Chen et al., 2020).

At present, there are few studies on using graphene modified oily epoxy resin coatings to improve the corrosion resistance of magnesium alloys. Therefore, this article explores the effect of the coating on the corrosion resistance of AZ31 magnesium alloy by modifying oily epoxy resin coatings with different contents of graphene.

MATERIALS AND METHODS

Materials

This experiment used a deformed AZ31B magnesium alloy sheet as the substate material, and its composition is shown in **Table 1**.

The sample preparation process is as follows: the magnesium alloy sheet was cut into many samples of 20 mm × 20 mm × 10 mm with a wire cutting machine, and then the cutting fluid on the sample surface was removed with acetone solution in the ultrasonic cleaner, and then the surface was polished step by step using 500, 800, 1200, 2000 and 3,000 mesh alumina abrasive sandpapers, respectively. After there are no obvious scratches on the surface of the samples, clean them with alcohol, dry them with hot air, and put them in a drying dish for use.

The graphene used in this experiment was purchased from Changzhou Sixth Element Material Technology Co., Ltd. Oily bisphenol A epoxy resin paint and phenolic amine oily epoxy resin curing agent were purchased from Guangzhou Tuan Anti-corrosion Technology Co., Ltd.

TABLE 1 | Main components of AZ31B magnesium alloy/wt%.

Element	Al	Zn	Mn	Cu	Ni	Fe	Mg
Content	3.007	1.054	0.488	0.001	0.002	0.004	Bal

Coating Preparation

The oil-based epoxy resin coating was modified with four different contents of graphene, and the weight ratio of graphene to the epoxy resin coating was 0 wt%, 0.1 wt%, 0.3 wt%, and 0.6 wt%, respectively. The specific operation method of coating preparation is as follows: according to the corresponding ratio, the graphene of different weights and 50 g oily epoxy resin paint were stirred with a mechanical stirrer at a high speed for 30 min. After stirring until the mixture is uniform, mix the mixed paint and the curing agent according to the ratio of 3:1. Then continued to mechanically stir the mixed paint until the mixing was uniform, and finally used a wool brush to coat the mixed paint on the surface of the AZ31 magnesium alloy, and cured at room temperature for 14 days to obtain a coating with a dry film thickness of 600 ± 20 μm. For the convenience of analysis, the graphene modified oily epoxy resin coating is marked as G/OEP-0 wt%, G/OEP-0.1 wt%, G/OEP-0.3 wt%, G/OEP-0.6 wt%.

Test Method

JSM-6610 scanning electron microscope was used to observe the surface morphology of graphene and coating. FTIR analysis was used to characterize the structure and composition of graphene and the coating, the specific working parameters were the detection range of 4,000 cm^{-1}– 400 cm^{-1} and the resolution of 4 cm^{-1}. The CHI660E series electrochemical workstation was used to test the anti-corrosion performance, and the classic three-electrode test system was used; the magnesium alloy substrate and the coating sample were used as the working electrode, and the working area was 1 cm^2, the counter electrode was a platinum electrode, the reference electrode was a saturated glycerin mercury electrode, the test solution was 3.5 wt% NaCl solution, e tests were performed at room temperature. All samples were tested for open circuit potential (OCP) multiple times until the potential stabilized, and then the potentiodynamic polarization curve was tested. The specific test parameters were: voltage sweep interval of −3 to 1 V and sweep speed of 1 mV/s.

RESULTS AND DISCUSSION

Characterization of Graphene and Coatings

Figure 1 is a picture of the microscopic morphology of graphene. From **Figure 1A**, it can be seen that graphene has small flakes that exist in a single-layer structure, and there are also large flakes that agglomerate into a multilayer structure. These agglomerations are caused by the interaction of π-π bonds between graphene, which will also have a certain impact on the dispersion properties of graphene in coatings. It can also be seen from the figure that the size of single-layer and multi-layer graphene generally does not exceed 20 μm, and the size of single-layer graphene can reach 10 μm or less. In addition, as shown in **Figure 1B**, the sheet-like structure of graphene can be further clearly seen, and the surface is slightly wrinkled, indicating that the surface structure of graphene has low defects.

Figure 2 shows the test results of graphene Fourier infrared spectroscopy. It can be seen from the figure that graphene mainly

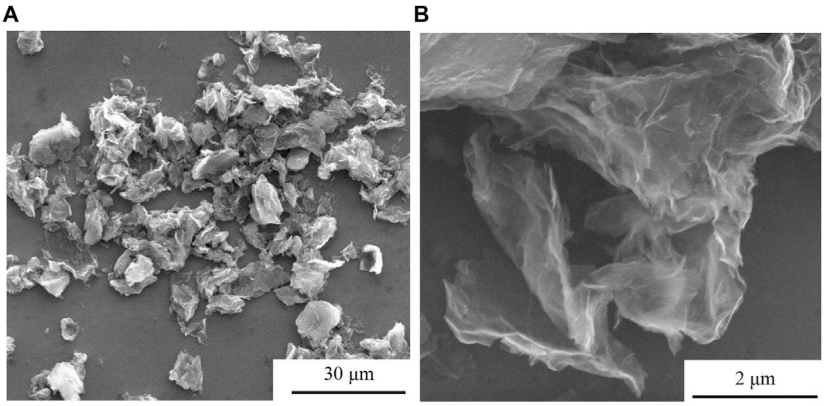

FIGURE 1 | Graphene micro-topography under different magnifications: **(A)** 2,400 times, **(B)** 40,000 times.

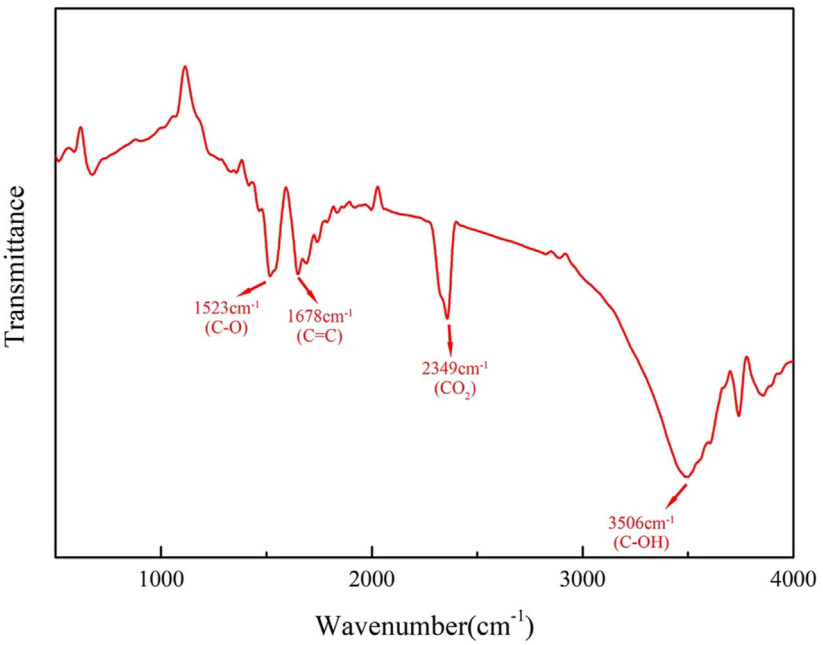

FIGURE 2 | Graphene FI-TR test spectrum.

contains four peaks in the spectrum, of which the peak at 1,523 cm^{-1} corresponds to the tensile vibration of the C-O bond in the epoxy group. The peak corresponding to 1678 cm^{-1} is related to the vibration of the C=C bond of the benzene ring. The peak at 2349 cm^{-1} is due to the symmetrical vibration of CO2 in the air inside the Fourier test space. The absorption peak at 3,506 cm^{-1} is caused by the C-OH bond (Ye et al., 2020).

The FTIR spectrum of the oily epoxy resin coating is shown in **Figure 3**. Among them, the absorption peaks of methyl and methylene on the molecular chain of epoxy resin appear near 2,900 cm^{-1} and 2,800 cm^{-1}, respectively. The absorption peak near 1,250 cm^{-1} corresponds to the vibration of the C=C bond in the benzene ring. The absorption peaks at 1,510 cm^{-1} and 1,480 cm^{-1} correspond to the vibration of the N-H and C-N bonds in the phenalkamine curing agent, respectively. The absorption peak at 1,010 cm^{-1} is derived from the epoxy group in epoxy resin. The absorption peak at 1,640 cm^{-1} is the carbonyl group (Siva et al., 2014; Wang et al., 2018).

Figure 4 is a picture of the micro morphology of modified oily epoxy resin coatings with different contents of graphene. It can be seen from **Figure 4A** that when the graphene corrosion inhibitor filler is not added, the microstructure shows that the coating surface has more defects and larger roughness, which may be caused by the rupture of bubbles generated during the curing process. **Figure 4B** shows that when 0.1 wt% graphene is added,

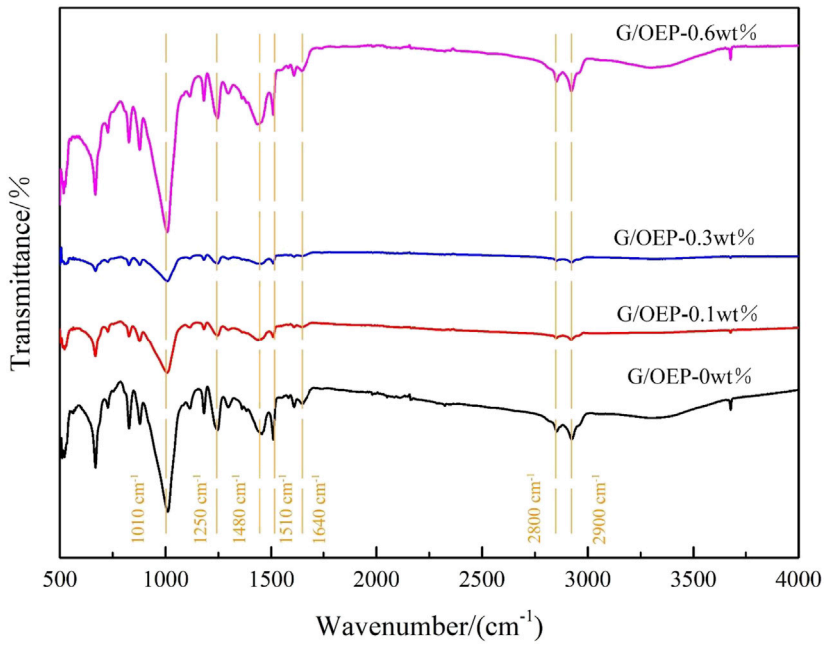

FIGURE 3 | Graphene FI-TR test spectrum.

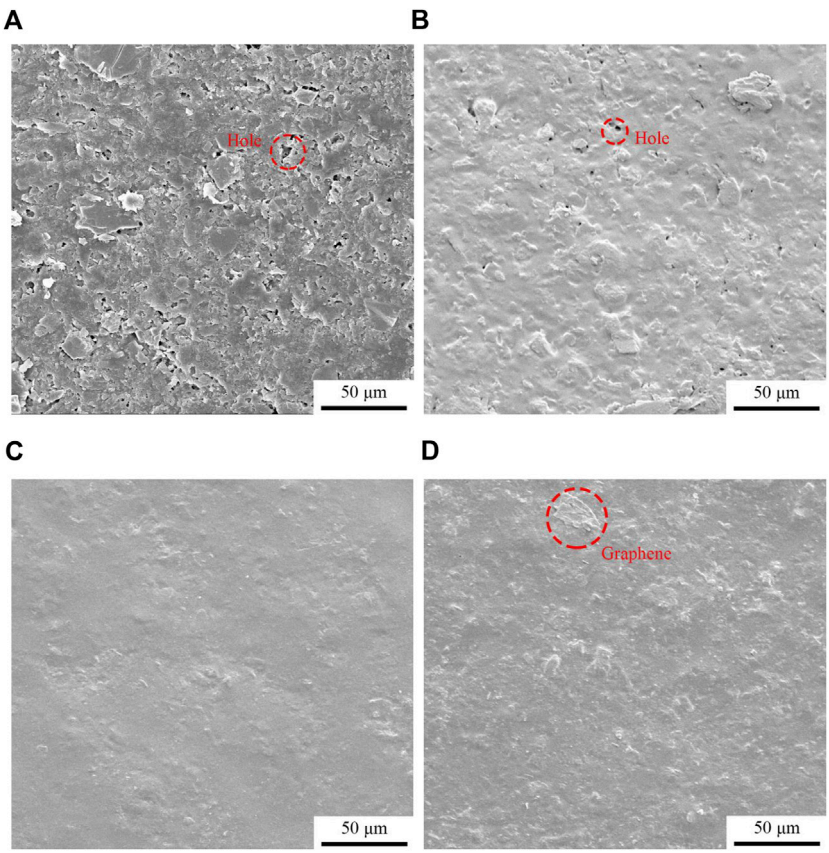

FIGURE 4 | Micro morphology of graphene modified oily epoxy resin coating: **(A)** G/OEP-0 wt%, **(B)** G/OEP-0.1 wt%, **(C)** G/OEP-0.3 wt%, **(D)** G/OEP-0.6 wt%.

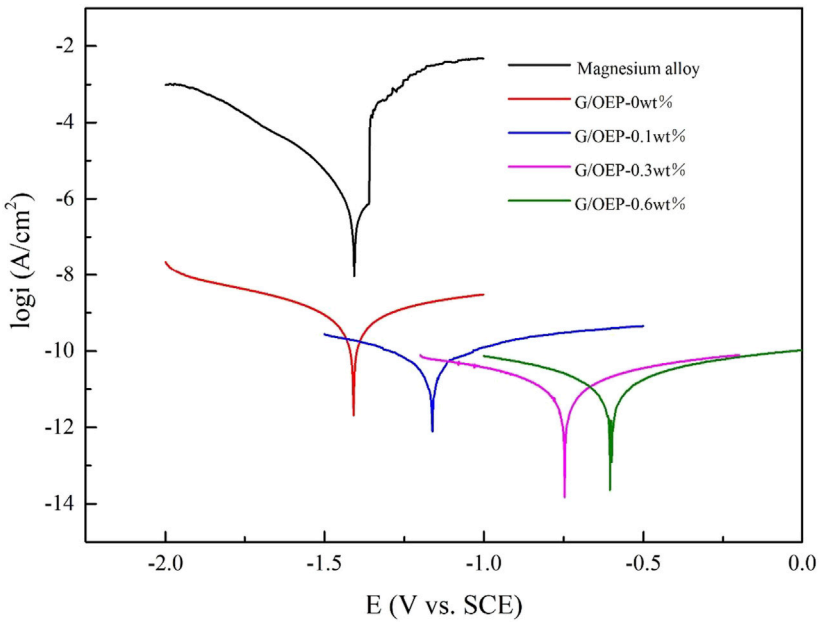

FIGURE 5 | Potential polarization curve of magnesium alloy and coating.

TABLE 2 | Related parameters of potentiodynamic polarity curve.

Sample	Corrosion current density (A/cm^2)	Corrosion potential(V)
Magnesium alloy	6.20×10^{-7}	−1.47
G/OEP-0 wt%	3.98×10^{-10}	−1.49
G/OEP-0.1 wt%	6.47×10^{-11}	−1.16
G/OEP-0.3 wt%	7.22×10^{-12}	−0.75
G/OEP-0.6 wt%	6.96×10^{-12}	−0.60

the surface defects and roughness of the coating are significantly reduced, and the holes and pits are also significantly reduced. This is because with the addition of graphene, the two-dimensional flaky structure can well fill the holes and pits caused by the bubble burst during the coating curing, which greatly improves the surface defects of the coating. As the graphene content continues to increase, when it reaches 0.3 wt%, **Figure 4C** shows that the coating surface is relatively smooth, with almost no obvious holes visible, and the coating has a higher surface quality, which is because as the graphene content continues to increase, the graphene filler has reached a better dispersion state inside the coating. Using its own structural characteristics, it almost covers the entire coating surface, which can well fill the coating surface defects. However, **Figure 4D** shows that when the content of graphene filler reaches 0.6 wt%, the surface quality of the coating decreases, but no obvious defects appear. Analysis believes that this is due to the fact that as the content of graphene increases, the mutual attraction between π-π bonds leads to a decrease in the dispersion quality of graphene inside the coating, and agglomeration begins to occur during the curing process of the coating. The agglomerated graphene has been exposed on the surface of the coating, which will prevent the graphene from being well dispersed on the entire coating surface to fill the defects, and the agglomerated graphene will increase the surface roughness of the coating.

Coating Electrochemical Performance

Figure 5 shows the potentiodynamic polarization curves of magnesium alloys and coatings. **Table 2** lists the electrochemical parameters, including specific values of corrosion current density and corrosion potential. Since the corrosion potential is greatly affected by environmental factors, the corrosion current density is generally used to judge the corrosion resistance of the test sample. The smaller the corrosion current density, the better the corrosion resistance. It can be seen from **Table 2** that the corrosion current density of the magnesium alloy matrix is 6.20×10^{-7} A/cm^2, and the corrosion current density of the oily epoxy resin coating is lower than that of the magnesium alloy. It shows that the coating can significantly improve the corrosion resistance of magnesium alloys. The corrosion current density of G/OEP-0.6 wt% is the lowest, reaching 6.96×10^{-12} A/cm^2, which is 5 orders of magnitude lower than that of the magnesium alloy matrix.

In order to facilitate the analysis of the influence of different contents of graphene on the corrosion resistance of the coating. **Figure 6** shows the changing trend of the corrosion current density of the oily epoxy resin coating with different graphene content. It can be seen from the figure that with the addition of graphene, the corrosion resistance of the coating has been significantly improved. The corrosion current density of the coating is reduced by

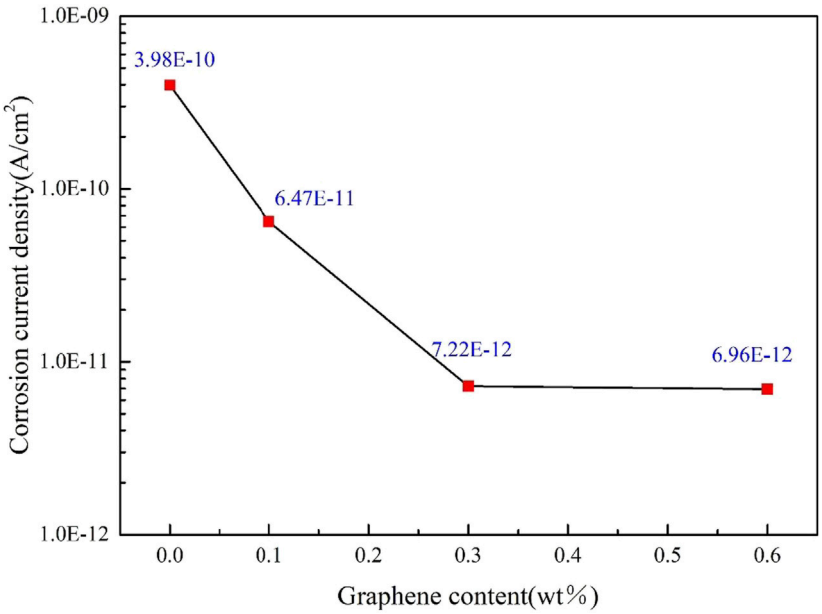

FIGURE 6 | Variation trend of corrosion current density of oily epoxy resin coating with different graphene content.

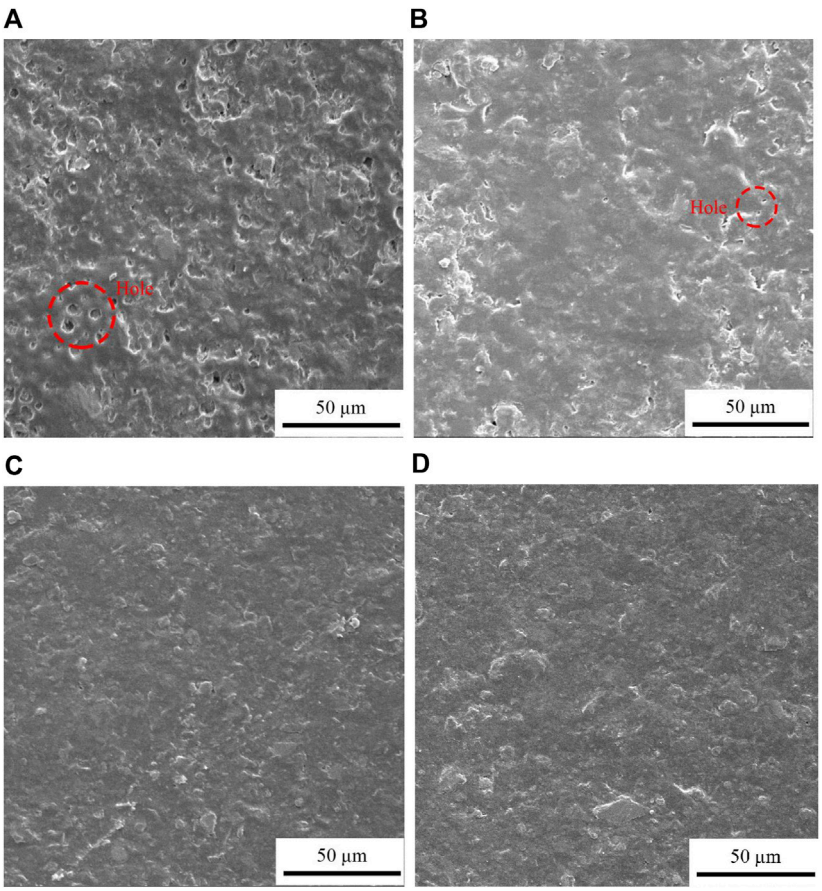

FIGURE 7 | Corrosion morphology of modified oily epoxy resin coating with different graphene content: **(A)** G/OEP-0 wt%, **(B)** G/OEP-0.1 wt%, **(C)** G/OEP-0.3 wt %, **(D)** G/OEP-0.6 wt%.

two orders of magnitude, from 3.98×10^{-10} A/cm^2 to 6.96×10^{-12} A/cm^2. Based on the analysis of **Figure 4**, it is believed that the addition of graphene reduces the pores of the coating, increases the diffusion resistance of the corrosive medium to the surface of the substrate, and improves the corrosion resistance of the coating. In addition, graphene will preferentially agglomerate inside the coating as the content increases. Although it still plays a shielding role for corrosive media, it reduces the corrosion inhibition effect. Therefore, the decline trend of the corrosion current density of G/OEP-0.6 wt% tends to be gentle.

Analysis of Coating Corrosion Mechanism

Figure 7 shows the morphology of modified oily epoxy resin coatings with different graphene content after corrosion. As shown in **Figure 7A**, before graphene is added, the corrosion of the coating is more serious and there are more holes. With the addition of graphene, it can be seen from **Figure 7B** that 0.1 wt% of graphene has improved the corrosion resistance of the coating, and the holes caused by corrosion are significantly reduced. When the graphene content in the coating reaches 0.3 wt% and 0.6 wt%, **Figures 7C,D** show that after a period of electrochemical corrosion, there are almost no related holes caused by corrosion on the surface of the coating. And the coating surface is smoother, showing excellent anti-corrosion performance. This is also mutually corroborating the results of the potential polarization curve of the coating, indicating that the epoxy resin coating modified by graphene can provide good corrosion resistance for the substrate and avoid damage to the coating surface by corrosive media. And after adding the graphene content to 0.6 wt%, the coating is least affected by corrosion and has good corrosion resistance.

Based on the analysis of relevant literature reports (Liao et al., 2017; Lu et al., 2018; Wu et al., 2018). If graphene is not added, the coating has relatively porous holes, which cannot well shield the penetration of corrosive media to the coating, so that the coating is greatly affected by corrosion. When a small amount of graphene is added for modification, the graphene is dispersed and arranged inside the coating, increasing the length of the corrosive medium penetration path. However, the coating and the substrate are affected by corrosion caused by H_2O and O_2 molecules and Cl^- ions will still penetrate the coating during diffusion. When the content of graphene increases to 0.3%–0.6% wt, because the number of pores on the surface of the coating is reduced, not only the density of the graphene coating can be increased, but also the hydrophobicity of the coating will be enhanced, which make it difficult for the corrosive media to penetrate the interface between the coating and the substate, so that the corrosion resistance of the coating can be greatly improved.

CONCLUSION

The G/OEP coating was prepared on the surface of AZ31 magnesium alloy by brush coating technology. Graphene has fewer surface defects and is successfully doped into the coating. The G/OEP coating significantly improves the corrosion resistance of magnesium alloys. With the graphene content increases, the corrosion resistance of the coating is gradually improved. The corrosion current density of the G/OEP coating is reduced by two orders of magnitude, from 3.98×10^{-10} A/cm^2 to 6.96×10^{-12} A/cm^2. The graphene can fill the defects generally in the coating during the curing process to prevent substrate from penetration of corrosive medium caused by the density and hydrophobicity of coating are increased.

DATA AVAILABILITY STATEMENT

The original contributions presented in the study are included in the article/Supplementary Material, further inquiries can be directed to the corresponding author.

AUTHOR CONTRIBUTIONS

Conceptualization, ZG; methodology, CS; validation, DY and XZ; formal analysis, ZG, CS, and ZA; data curation, DY and XZ; writing—original draft preparation, ZG, CS, and XZ; writing—review and editing, ZG, CS, and ZA; supervision, ZG and ZA; funding acquisition, ZG. All authors have read and agreed to the published version of the manuscript.

FUNDING

The present work is supported by the Scientific and Technological Research Program of Chongqing Science and Technology Bureau (Grant No. cstc2019jcyj-msxmX0761), the Scientific and Technological Research Program of Chongqing Municipal Education Commission (Grant No. KJQN201800731), the Scientific and Technological Research Program of Chongqing Jiaotong University (Grant No. 16JDKJC-A005).

REFERENCES

Chen, C., He, Y., Xiao, G., Zhong, F., Xia, Y., and Wu, Y. (2020). Graphic C3N4-Assisted Dispersion of Graphene to Improve the Corrosion Resistance of Waterborne Epoxy Coating. *Prog. Org. Coat.* 139, 105448. doi:10.1016/j.porgcoat.2019.105448

Chen, Y., Li, J., Yang, W., Gao, S., and Cao, R. (2019). Enhanced Corrosion Protective Performance of Graphene Oxide-Based Composite Films on AZ31 Magnesium Alloys in 3.5 wt% NaCl Solution. *Appl. Surf. Sci.* 493, 1224–1235. doi:10.1016/j.apsusc.2019.07.101

Chu, J. H., Tong, L. B., Wen, M., Jiang, Z. H., Wang, K. S., and Zhang, H. J. (2019). Graphene Oxide Film as a Protective Barrier for Mg alloy: Worse or Better Is Dependent on a Chemical Reduction Process. *Carbon* 145, 389–400. doi:10.1016/j.carbon.2019.01.037

Cui, G., Bi, Z., Zhang, R., Liu, J., Yu, X., and Li, Z. (2019). A Comprehensive Review on Graphene-Based Anti-Corrosive Coatings. *Chem. Eng. J.* 373, 104–121. doi:10.1016/j.cej.2019.05.034

Deyab, M. A., De Riccardis, A., and Mele, G. (2016). Novel Epoxy/metal Phthalocyanines Nanocomposite Coatings for Corrosion protection of Carbon Steel. *J. Mol. Liquids* 220, 513–517. doi:10.1016/j.molliq.2016.04.115

Ding, R., Chen, S., Lv, J., Gui, T.-J., Wang, X., Zhao, X.-D., et al. (2019). Review of Theoretical and Applied Research of Graphene in Anti-Corrosion Film and Organic Anti-Corrosion Coatings. *Acta Chim. Sinica* 77, 1140–1155. doi:10.6023/a19050174

Dong, Y., Ma, L., and Zhou, Q. (2013). Effect of the Incorporation of Montmorillonite-Layered Double Hydroxide Nanoclays on the Corrosion protection of Epoxy Coatings. *J. Coat. Technol. Res.* 10, 909–921. doi:10.1007/s11998-013-9519-x

Dziubińska, A., Gontarz, A., Dziubiński, M., and Barszcz, M. (2016). The Forming of Magnesium alloy Forgings for Aircraft and Automo-Tive Applications. *Adv. Sci. Technol. Res. J.* 10, 158–168. doi:10.12913/22998624/64003

Guo, L., Gu, C., Feng, J., Guo, Y., Jin, Y., and Tu, J. (2020). Hydrophobic Epoxy Resin Coating with Ionic Liquid Conversion Pretreatment on Magnesium alloy for Promoting Corrosion Resistance. *J. Mater. Sci. Technol.* 37, 9–18. doi:10.1016/j.jmst.2019.06.024

Hao, S. S., Sun, X. F., Song, W., Li, Z. M., and Qiu, J. (2018). Preparation and Properties of Graphene Modified Epoxy Resin Coating. *China Surf. Eng.* 31, 108–115. doi:10.11933/j.issn.1007-9289.20180120003

He, X.-L., Wei, Y.-H., Hou, L.-F., Yan, Z.-F., Guo, C.-L., and Han, P.-J. (2014). Corrosion Fatigue Behavior of Epoxy-Coated Mg-3Al-1Zn alloy in NaCl Solution. *Rare Met.* 33, 276–286. doi:10.1007/s12598-014-0278-3

Jin, F.-L., Li, X., and Park, S.-J. (2015). Synthesis and Application of Epoxy Resins: A Review. *J. Ind. Eng. Chem.* 29, 1–11. doi:10.1016/j.jiec.2015.03.026

Liao, Z., Zhang, T., Qiao, S., and Zhang, L. (2017). Preparation and Electrochemical Properties of Graphene/epoxy Resin Composite Coating. *IOP Conf. Series: Earth Environ.* 94, 012072. doi:10.1088/1755-1315/94/1/012072

Lu, C., Feng, C., Zhu, L., Jiang, L., Gao, G., Han, L., et al. (2018). "Graphene Modified Epoxy Coating Tubing Applied in the Water Injection wells," in *Advances in Materials Processing*, Beijing: Springer, 1075–1082. doi:10.1007/978-981-13-0107-0_102

Ou, B., Wang, Y., and Lu, Y. (2020). A Review on Fundamentals and Strategy of Epoxy-Resin-Based Anticorrosive Coating Materials. *Polym-Plast. Tech. Mat.* 60, 1–25. doi:10.1080/25740881.2020.1819317

Rahman, M. M., Islam, M. M., Khan, M. M. R., Ong, H. R., Uddin, M. T., and Islam, M. A. (2019). IBA-Modified Gypsum-Containing Epoxy Resin Coating for Rebar: Corrosion Performance and Bonding Characteristics. *Int. J. Plast. Technol.* 23, 20–28. doi:10.1007/s12588-019-09238-3

Ramalingam, V. V., Ramasamy, P., Kovukkal, M. D., and Myilsamy, G. (2019). Research and Development in Magnesium Alloys for Industrial and Biomedical Applications: A Review. *Met. Mater. Int.* 26, 409–430. doi:10.1007/s12540-019-00346-8

Shi, H. W., Liu, F. C., and Han, E.-H. (2012). Improving Corrosion Resistance of Epoxy Coatings Modified with Silane Monomers on AZ31D Magnesium Alloy. *Can. Metallurgical Q.* 51, 485–490. doi:10.1179/1879139512y.0000000017

Siva, T., Kamaraj, K., and Sathiyanarayanan, S. (2014). Epoxy Curing by Polyaniline (PANI) - Characterization and Self-Healing Evaluation. *Prog. Org. Coat.* 77, 1095–1103. doi:10.1016/j.porgcoat.2014.03.019

Song, G., and Atrens, A. (2003). Understanding Magnesium Corrosion-A Framework for Improved Alloy Performance. *Adv. Eng. Mater.* 5, 837–858. doi:10.1002/adem.200310405

Song, G. (2005). Recent Progress in Corrosion and Protection of Magnesium Alloys. *Adv. Eng. Mater.* 7, 563–586. doi:10.1002/adem.200500013

Song, J., She, J., Chen, D., and Pan, F. (2020). Latest Research Advances on Magnesium and Magnesium Alloys Worldwide. *J. Magnesium Alloys* 8, 1–41. doi:10.1016/j.jma.2020.02.003

Tekumalla, S., Seetharaman, S., Almajid, A., and Gupta, M. (2014). Mechanical Properties of Magnesium-Rare Earth Alloy Systems: A Review. *Metals* 5, 1–39. doi:10.3390/met5010001

Wang, M.-H., Li, Q., Li, X., Liu, Y., and Fan, L.-Z. (2018). Effect of Oxygen-Containing Functional Groups in Epoxy/reduced Graphene Oxide Composite Coatings on Corrosion protection and Antimicrobial Properties. *Appl. Surf. Sci.* 448, 351–361. doi:10.1016/j.apsusc.2018.04.141

Wu, W., Liu, J., Li, X., Hua, T., Cong, X., Chen, Z., et al. (2018). Incorporation Graphene into Sprayed Epoxy-Polyamide Coating on Carbon Steel: Corrosion Resistance Properties. *Corrosion Eng. Sci. Technol.* 53, 625–632. doi:10.1080/1478422x.2018.1521590

Xia, W., Wang, T., Song, L., Gong, H., Guo, H., Fan, X. L., et al. (2018). Graphene/Epoxy Composite Coating Damage Under Gamma-Ray Irradiation and Corrosion protection. *J. Inorg. Mater.* 33, 35–41. doi:10.15541/jim20170143

Xie, Y. K., Liu, W. Q., Liang, L. Y., Liu, C. H., He, S., Zhang, F. Y., et al. (2019). Enhancement of Anticorrosion Property and Hydrophobicity of Modified Epoxy Coatings with Fluorinated Polyacrylate. *Colloid Surf. A-Physicochem. Eng. Asp.* 579, 10. doi:10.1016/j.colsurfa.2019.123659

Ye, Y., Yang, D., Zhang, D., Chen, H., Zhao, H., Li, X., et al. (2020). POSS-Tetraaniline Modified Graphene for Active Corrosion Protection of Epoxy-Based Organic Coating. *Chem. Eng. J.* 383, 123160. doi:10.1016/j.cej.2019.123160

Zeng, Z., Stanford, N., Davies, C. H. J., Nie, J.-F., and Birbilis, N. (2018). Magnesium Extrusion Alloys: A Review of Developments and Prospects. *Int. Mater. Rev.* 64, 27–62. doi:10.1080/09506608.2017.1421439

Zhang, Z., Zhang, W., Li, D., Sun, Y., Wang, Z., Hou, C., et al. (2015). Mechanical and Anticorrosive Properties of Graphene/Epoxy Resin Composites Coating Prepared by Iin-Ssitu Method. *Int. J. Mol. Sci.* 16, 2239–2251. doi:10.3390/ijms16012239

Zhao, Y., Xie, Y., Hui, Y. Y., Tang, L., Jie, W., Jiang, Y., et al. (2013). Highly Impermeable and Transparent Graphene as an Ultra-Thin Protection Barrier for Ag Thin Films. *J. Mater. Chem. C* 1, 4956. doi:10.1039/c3tc30743c

Zhou, S., Wu, Y., Zhao, W., Yu, J., Jiang, F., and Ma, L. (2018). Comparative Corrosion Resistance of Graphene Sheets with Different Structures in Waterborne Epoxy Coatings. *Colloids Surf. A: Physicochemical Eng. Aspects* 556, 273–283. doi:10.1016/j.colsurfa.2018.08.045

Ziat, Y., Hammi, M., Zarhri, Z., and Laghlimi, C. (2020). Epoxy Coating Modified with Graphene: A Promising Composite against Corrosion Behavior of Copper Surface in Marine Media. *J. Alloy. Compd.* 820, 6. doi:10.1016/j.jallcom.2019.153380

Conflict of Interest: The authors declare that the research was conducted in the absence of any commercial or financial relationships that could be construed as a potential conflict of interest.

Publisher's Note: All claims expressed in this article are solely those of the authors and do not necessarily represent those of their affiliated organizations, or those of the publisher, the editors and the reviewers. Any product that may be evaluated in this article, or claim that may be made by its manufacturer, is not guaranteed or endorsed by the publisher.

frontiers in Materials

ORIGINAL RESEARCH
published: 23 September 2021
doi: 10.3389/fmats.2021.737792

Silane-Modified Graphene Oxide Composite as a Promising Corrosion-Inhibiting Film for Magnesium Alloy AZ31

You Zhang[1]*, *Juping Wang*[1], *Zheng Zhang*[1], *Kai Wei*[1], *Zhe Zhang*[1], *Xuelong Hao*[2,3]* and *Fei Chen*[1]

[1]College of New Materials and Chemical Engineering, Beijing Institute of Petrochemical Technology, Beijing, China, [2]General Research Institute for Nonferrous Metals, Beijing, China, [3]China United Testing and Certification Co., Ltd., Beijing, China

In this study, (3-aminopropyl)-triethoxysilane–modified graphene oxide (GO) composite thin films were synthesized on magnesium alloy AZ31 substrate. The structure, composition, and morphology of silane-GO films were analyzed. Electrochemical measurements and immersion tests showed that silane-GO coatings provide effective protection for magnesium alloy substrates, owing to the good barrier property of the layered GO, and decrease the defects on the GO film surface due to the silane modification. In addition, the corrosion product between the outer silane-GO film and Mg alloy substrate also improved the corrosion resistance of the Mg alloy. Thus, silane-GO composite thin films provide an effective approach for protecting the lightweight metal substrate.

Keywords: graphene oxide, silane, film, corrosion resistance, Mg alloy

OPEN ACCESS

Edited by:
Liang Wu,
Chongqing University, China

Reviewed by:
Yaming Wang,
Harbin Institute of Technology, China
Zhihui Xie,
China West Normal University, China

***Correspondence:**
You Zhang
youzhang@bipt.edu.cn
Xuelong Hao
xlhaogrinm@126.com

Specialty section:
This article was submitted to Structural Materials, a section of the journal Frontiers in Materials

Received: *07 July 2021*
Accepted: *13 August 2021*
Published: *23 September 2021*

Citation:
Zhang Y, Wang J, Zhang Z, Wei K, Zhang Z, Hao X and Chen F (2021) Silane-Modified Graphene Oxide Composite as a Promising Corrosion-Inhibiting Film for Magnesium Alloy AZ31. Front. Mater. 8:737792. doi: 10.3389/fmats.2021.737792

INTRODUCTION

In recent years, magnesium alloys have gained considerable attention due to their remarkable mechanical and biodegradable properties (Wu et al., 2013; Zainal Abidin et al., 2013; Hernández-Barrios et al., 2020; Daavari et al., 2021). With numerous magnesium alloy applications, the problem of corrosion resistance has been obstructing their further use in many specific situations (Gnedenkov et al., 2016; Pan et al., 2016; Zhou et al., 2020). Therefore, some experiments have been carried out to improve the corrosion resistance of magnesium alloys.

Graphene, as a 2D layer of sp2-hybridized carbon atoms, has gained significant attention for metal protection (Prasai et al., 2012; Hsieh et al., 2014; Kyhl et al., 2015) due to its unique properties, such as excellent mechanical property, thermal and chemical stability, gas impermeability, higher aspect ratio, lower density, and good barrier property (Aneja et al., 2017; Jo et al., 2017). However, owing to the high electrical conductivity of graphene, the galvanic corrosion of the metal can be greatly promoted when corrosion occurs in the defects (such as cracks or wrinkles) of graphene layers, severely bring down the corrosion resistance in the long term (Lei et al., 2017; Sanjid et al., 2019).

Graphene oxide (GO), possessing plenty of oxygen functional groups on its basal planes and edges, has gathered equal attention because of its useful metal protection properties. Generally, GO and modified GO sheets can be used as nano-additives to enhance the anticorrosive properties of organic coatings. Some researchers (Chang et al., 2012; Yu et al., 2014) prepared GO-reinforced composite coatings, which exhibited strong resistance to oxidation and corrosion, using the chemical modification method. However, many researchers have found that simple doping of GO

cannot decrease their surface energy, which is the reason they tend to agglomerate. Several recent studies (Wan et al., 2014; Sun et al., 2015; Ma et al., 2016; Ramezanzadeh et al., 2016) have shown that GO can be covalently functionalized with silane and then embedded into an organic coating to improve the barrier property of the coating by suppressing the penetration of an aggressive medium. Meanwhile, the covalent bond (Si-O-Me) can be formed by the reaction of silane with the hydroxyl groups on the metal surface (Me-OH) (Liu et al., 2015a; Yu et al., 2015; Matinlinna et al., 2018; Fernández-Hernán et al., 2021).

Therefore, in order to inhibit the agglomeration of GO in coatings, the GO can be modified using silane coupling agents to reduce their surface energy. In addition, the silane can be linked with a metal substrate with covalent bonding, ensuring a high adhesion strength between the coating and the substrate.

In this study, a (3-aminopropyl)-triethoxysilane (APS)–modified GO film was prepared on the surface of magnesium alloy to investigate the effect of silane-grafted GO on corrosion resistance of the as-obtained coating. It is expected that by applying the APS agent as a "bridge" to covalently link GO to the magnesium alloy substrate, the silane-GO film with good adhesion strength and corrosion resistance property would be realized.

EXPERIMENTAL SECTION

Materials

Magnesium alloy AZ31 sheets of size 30 mm × 30 mm × 5 mm (approximate minority components, wt.%: Al 3.19, Zn 0.81, Mn 0.33, and balance Mg) were used as substrate materials in this study. Before coating, the samples were ground with SiC paper to 2000 grit. All specimens were rinsed in distilled water, then cleaned ultrasonically in alcohol for 10 min, and eventually dried in warm air. Graphene oxide (10 ml/L, 5 wt.%, with few layers) was purchased from Beijing Carbon Century Technology Co., Ltd., China. 3-Aminopropyl-triethoxysilane (analytical grade) was purchased from Beijing J&K, China. Alcohol and glacial acetic acid (analytical grade) were purchased from Beijing Chemical Works, China.

Silanization of GO and Preparation of Silane-GO Film on Magnesium Alloy

0.1 g GO powders were ultrasonically dispersed into 50 ml deionized water for 8 h. Then, 150 ml of alcohol was added to the mixture under vigorous stirring to obtain a GO suspension (~0.5 mg/ ml). After that, 2 ml APS was added into the suspension gradually. Such low APS concentration was used to obtain a graphene-based film rather than a silane-based film. Then, the pH of the suspension was adjusted to 5 using glacial acetic acid. In this way, the hydrolysis reaction of APS was promoted, and the condensation reaction was restrained. The mixture was sealed and continuously stirred for 12 h at 50 °C, forming a silane-GO suspension. In addition, APS solution with 1 vol. % was prepared by combining APS, glacial acetic acid, deionized water, and alcohol, and then stirred for 12 h at 50 °C as a comparison.

The preparation of films was carried out using a dip coater (PTLMM01, China) at room temperature. The pretreated Mg alloy samples were immersed into the silane-GO suspension for 5 min, then taken out at the speed of 200 mm/min, and subsequently cured at room temperature for 15 min. The above process was performed twice. Finally, the samples were cured at 60 °C for 60 min. All samples were kept in a drying chamber for more than 24 h before use. The synthesis and silanization of GO and the preparation of silane-GO (GO-APS) films on Mg alloy are depicted schematically in **Figure 1**.

Characterization

The zeta potentials of GO, APS, and GO-APS in suspension were measured using a nanoparticle analyzer (Malvern Zetasizer Nano, UK) to evaluate the stability of the solution. The electrical conductivity of GO and GO-APS powder was measured using a resistivity tester (SZT-D, China) to evaluate the effect of GO and GO-APS on the corrosion process. Atomic force microscopy (AFM; SPM9500-J3) of GO and GO-APS sheets was carried out through drop-casting deposition on a silicon wafer. The surface morphology of films was examined using a field-emission scanning electron microscope (SEM; JEOL JSM-7800) at the voltage of 20 kV. The structure of films was characterized by Raman spectra (Model Laboratory RAM HR800, HORIBA Jobin Yvon) through a 50× objective (NA = 0.5) with a 514.5-nm Ar–Kr laser. To avoid laser-induced thermal damage, the power of the laser was kept at 0.4 mW on the sample. Adhesion testing was carried out by the pull-off test as per the EN-ISO 4624 standard by using a CMT5504 machine at a crosshead speed of 2 mm/min. Glow discharge optical emission spectroscopy (GDOES; HORIBA GD-Profiler 2) depth profile analysis of the coated samples was measured at a pressure of 650 Pa and power of 30 W with an anode 4 mm in diameter.

Electrochemical Measurements

Electrochemical impedance spectra (EIS) measurements were carried out on an electrochemical workstation (CS360) by using a three-electrode system in 0.05 M NaCl aqueous solution. A low concentration of the NaCl solution was used to decrease the rate of the corrosion processes and allow a more correct estimation of the processes at the early stages (Yu et al., 2015). A saturated calomel electrode (SCE) was used as the reference electrode, a platinum plate as the counter electrode, and film-coated samples as the working electrode. After immersion in 0.05 M NaCl aqueous solution for 1 h, the open-circuit potential (OCP) of the films was monitored continuously. The frequency range of EIS measurements was from 100 kHz to 10 mHz with an AC excitation amplitude of 10 mV.

RESULTS AND DISCUSSION

Figure 2 shows the Zeta potential of APS, GO, and GO-APS stable and homogeneous sols. The Zeta potential of the GO

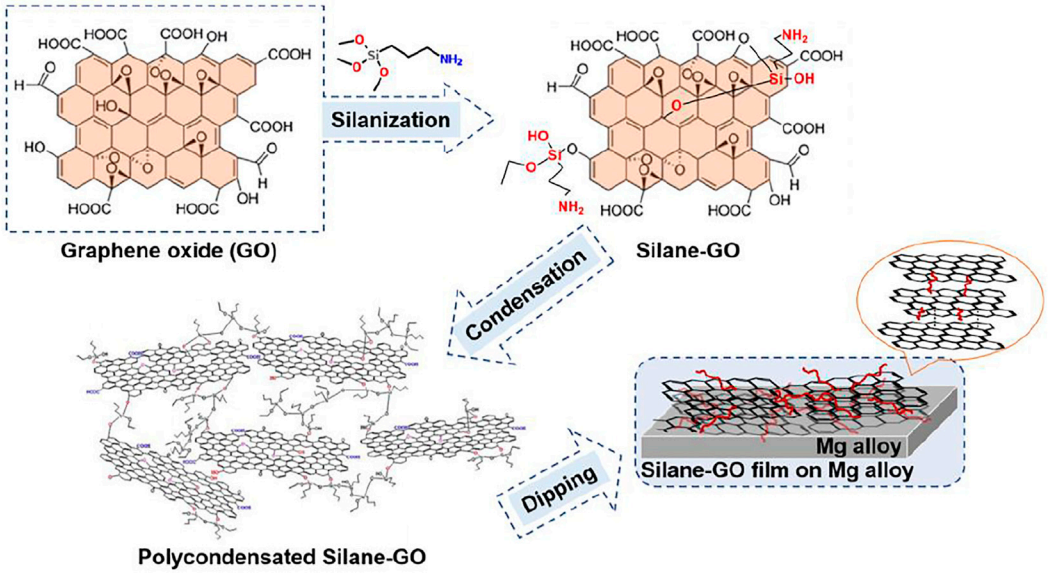

FIGURE 1 | Schematic representation of the synthesis and silanization of GO and the preparation of silane-GO films on the Mg alloy.

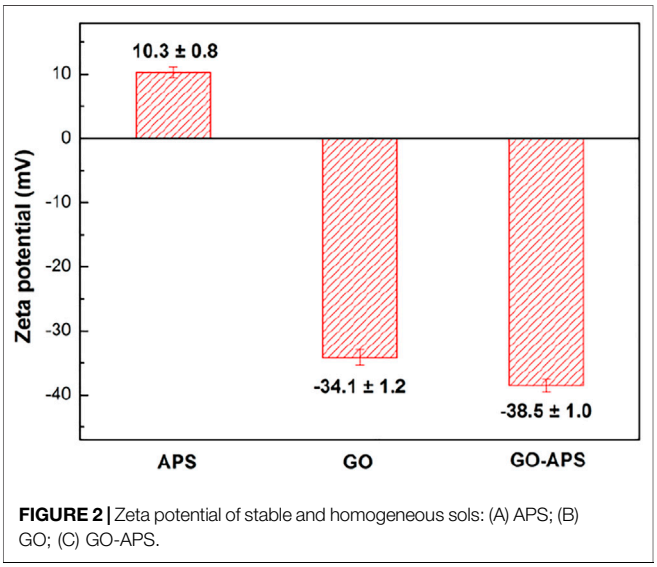

FIGURE 2 | Zeta potential of stable and homogeneous sols: (A) APS; (B) GO; (C) GO-APS.

suspension after silane modification is close to that of the GO suspension, which is more negative than that of APS sol, indicating that the main component of the GO suspension after silane modification is GO instead of cross-linked APS sol particles. Comparing the conductivity of the GO with silane-modified GO effect on the corrosion process with the GO with the APS-modified GO powder using the conductivity test, the results showed that the conductivity of the silane-modified GO becomes lower, mainly because of a nonconductive organic silane group grafted to the surface of the GO (Yu et al., 2015).

AFM observation of GO and GO-APS deposited on a silicon wafer through drop-casting was carried out. Representative AFM images of GO and GO-APS are shown in **Figure 3**. There is no apparent decrease in thickness of GO-APS by the presence of silane chains grafted on the GO surface, but with the GO layers of local fragmentation.

The FE-SEM images of GO, APS, and GO-APS film–coated Mg alloy samples are displayed in **Figure 4**. Under the action of the film-forming liquid, a layer of sheet structure vertical to the surface of the substrate was formed between the film and the substrate due to the rapid dissolution of the magnesium surface. On the surface of the GO film sample, the sheet GO coating on the surface is not continuously dense. The defects can be significantly seen from the partial enlargement of **Figure 4A$_2$**. The APS film surface has a magnesium alloy corrosion product layer, while no corrosion products of the magnesium alloy surface layer were found on the silane-modified GO layer. The surface layer has continuous density, and the GO of the lamella is evenly distributed in the layer, showing that APS plays an important role in improving the uniformity of the GO film. Moreover, the GO film is partially accumulated after modification by APS as shown in **Figure 4C$_2$**.

Figure 5 presents the Raman spectra of GO, APS, and GO-APS films deposited on Mg alloys. The APS-silane film shows almost no obvious peak near 1,500 cm^{-1}. Two obvious peaks are detected in GO and GO-APS films, which are ascribed to the structural defects of the GO membrane of carbon (Ferrari et al., 2006; Ma et al., 2019). The spectrum of the GO film displays the G peak and the D peak at 1,352 cm^{-1} and 1,589 cm^{-1}, respectively, which are consistent with the results of other researchers (Yu et al., 2015; Zhang et al., 2018). The D peak is caused by the disorder of C-C key vibration, characterization of the sp^3 hybridization structure of carbon atoms; the G peak is caused by the stretching vibration of C-C bonds and represents the carbon atoms of the sp^2 hybridized structure (Stankovich et al., 2007). After the modification of APS, the positions of D peak and

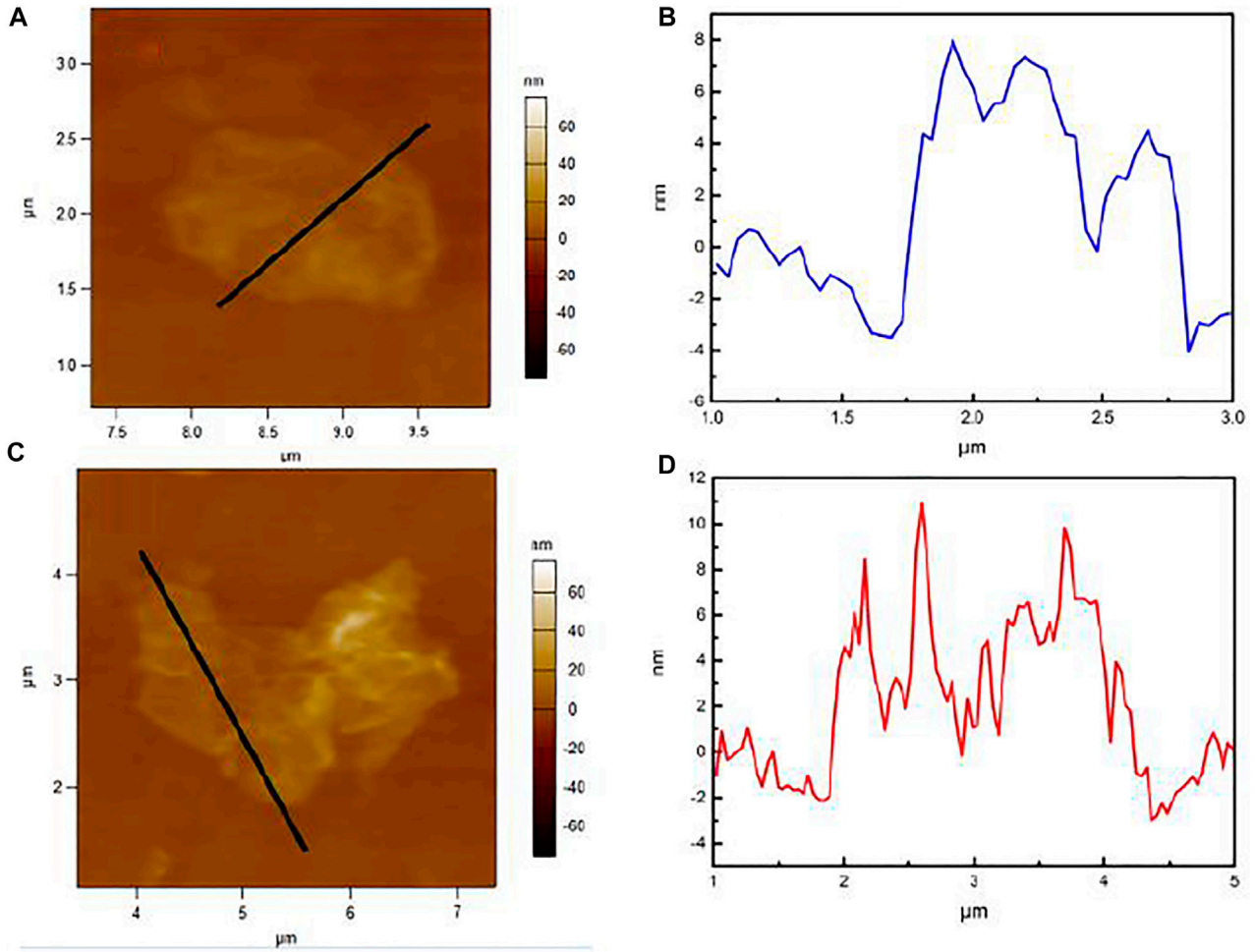

FIGURE 3 | AFM images of films deposited on a silicon wafer through drop-casting: **(A, B)** GO; **(C, D)** GO-APS.

G peak remained unchanged, indicating that the modification process connects the APS molecules and the GO surface by chemical bonds without significantly changing the structure of GO. The increase of the D/G intensity ratio (ID/IG) in the Raman spectrum of GO-APS films mean the size of the sp^2 hybrid structure of the carbon zone (graphite crystallite) decreases and disorder increases (Gómez-Navarro et al., 2007). The GO fragmentation is due to the chemical reduction of the silane coupling agent (Singh et al., 2013; Tang et al., 2013; Liu et al., 2015b), consistent with the AFM results.

The adhesion strength of the GO, APS, and GO-APS films was measured by the pull-off tests, as shown in **Figure 6**. There is a significant difference in the adhesion strength of the three films. The GO film demonstrates low adhesion strength (~9.2 MPa) compared with the adhesion strength of the GO-APS films (~20.4 MPa). The adhesion strength of the APS film is 22.5 MPa, suggesting good adhesion of the film. The high adhesion strength of the APS film implies that the increase in adhesion strength of the GO-APS films must be related to the amount of APS.

Figure 7 displays the depth profiles of elemental analysis across the GO and GO-APS films by the GDOES method. In **Figure 7A**, the GO covered sample comprises three layers, including the GO outer layer, the magnesium alloy corrosion product layer, and the oxide transition inner layer. Clear C and O signals were detected on the surface of the GO sample, corresponding to the GO layer (~0.17 μm). It is essential that the Mg signal be observed across the GO film, demonstrating that the Mg on the surface of the substrate participates in the GO film–forming reaction. Then both O and Mg signals reach a plateau attributed to the corrosion product layer (~0.4 μm) sputtering. After that, the decrease in the O signal and the increase in the Mg signal confirm the transition from layer to Mg alloy during sputtering. Finally, the Mg concentration reached a platform, and the Al signal disappears due to the alloy's sputtering. In **Figure 7B**, there is an evident increase in thickness of the GO-APS films (GO layer ~0.17 μm, GO-APS layer ~0.57 μm) due to the presence of silane chains grafted on the GO surface (the Si signal can be detected). Meanwhile, the decrease in thickness of the corrosion product layer indicates

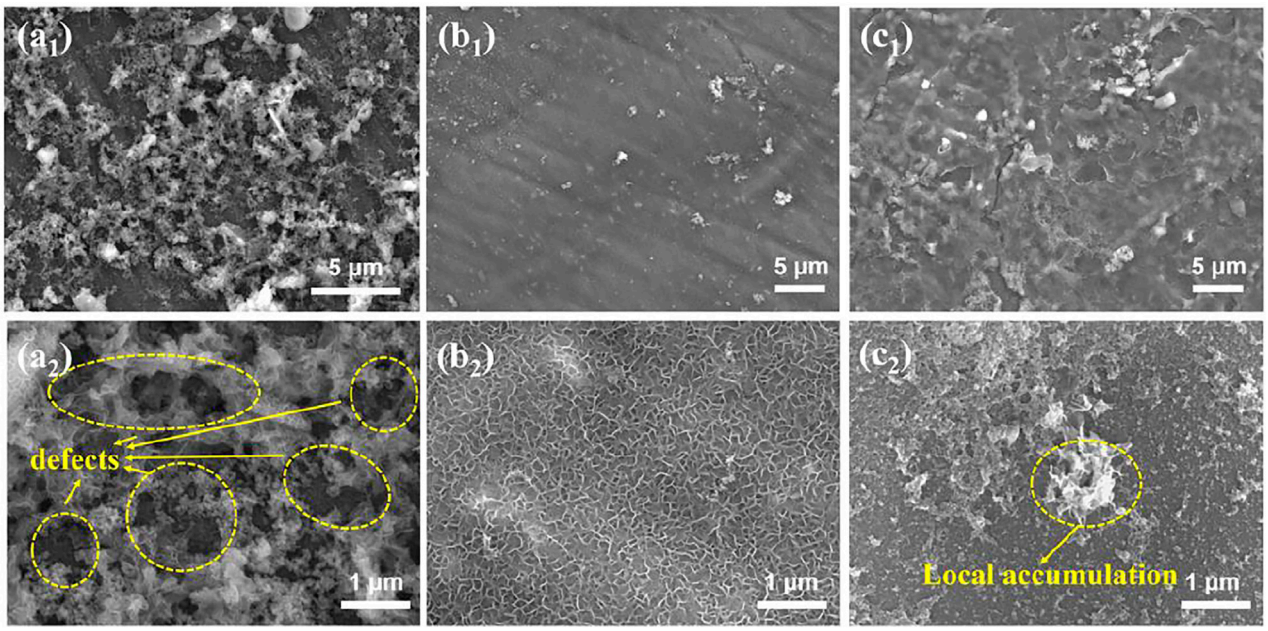

FIGURE 4 | FE-SEM images of film-coated Mg alloy samples: **(A_1,A_2)** GO film; **(B_1,B_2)** APS film; **(C_1,C_2)** GO-APS films.

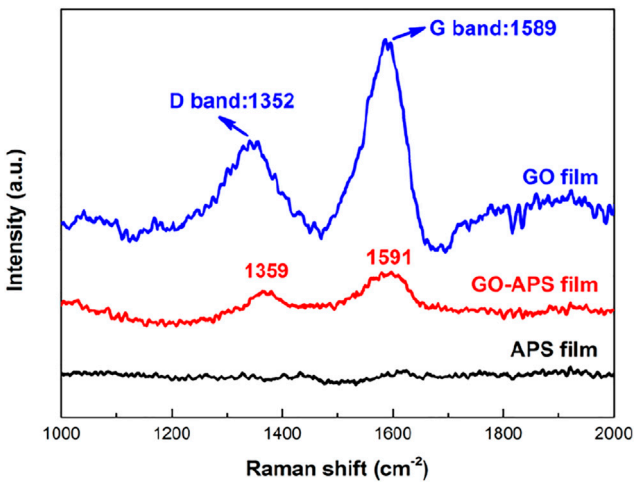

FIGURE 5 | Raman spectra of film-coated Mg alloy samples: **(A)** GO film; **(B)** APS film; **(C)** GO-APS film.

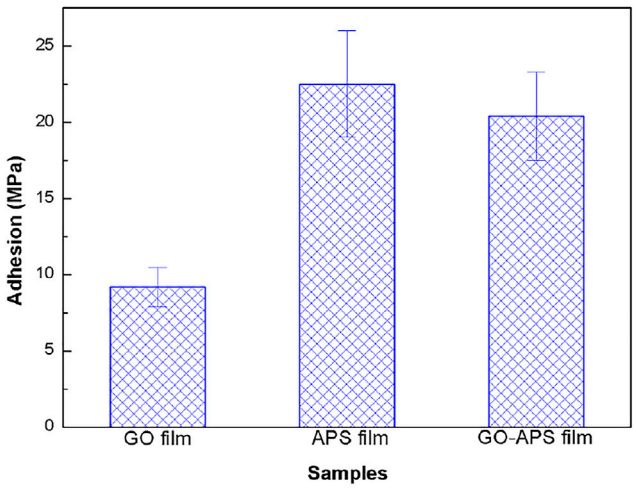

FIGURE 6 | Adhesion results of the pull-off tests of GO, APS, and GO-APS films.

that the GO-APS layers can be considered as good physical barrier layers that can provide sufficient protection.

Figure 8 shows the EIS results of bare Mg alloy and GO, APS, and GO-APS film–coated Mg alloy samples immersed for 24 h. In the Bode plots of phase angle, two well-defined time constants can be found in the spectra of different samples. The one appearing at high frequency is contributed by the porous layer, while the other appears at medium frequency due to the barrier layer. It is well known that coatings with a higher *Z* modulus (|*Z*|) at lower frequencies exhibit better corrosion resistance on metal substrates (Yu et al., 2015; Ma et al., 2016). There is an increase in |Z|0.01Hz value the GO-APS films due to the presence of silane chains grafted on the GO surface compared with that of the GO film. The results showed that the APS-modified film significantly improved the corrosion resistance of Mg alloy. Correspondingly, two capacitor rings of different samples can also be seen in the Nyquist plots, representing the porous layer and the barrier layer, respectively. The size of the capacitor ring represents the degree of corrosion resistance. In **Figure 8A**, the GO-APS film presents the largest diameter, indicating that the film has the best corrosion resistance.

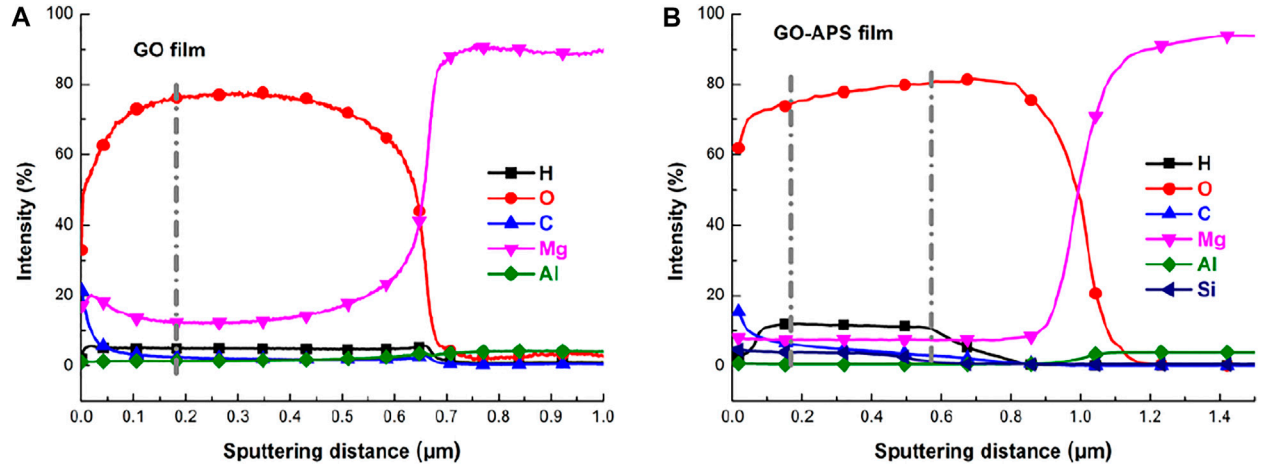

FIGURE 7 | GDOES depth profile of GO and GO-APS film–coated Mg alloy samples: **(A)** GO film; **(B)** GO-APS films.

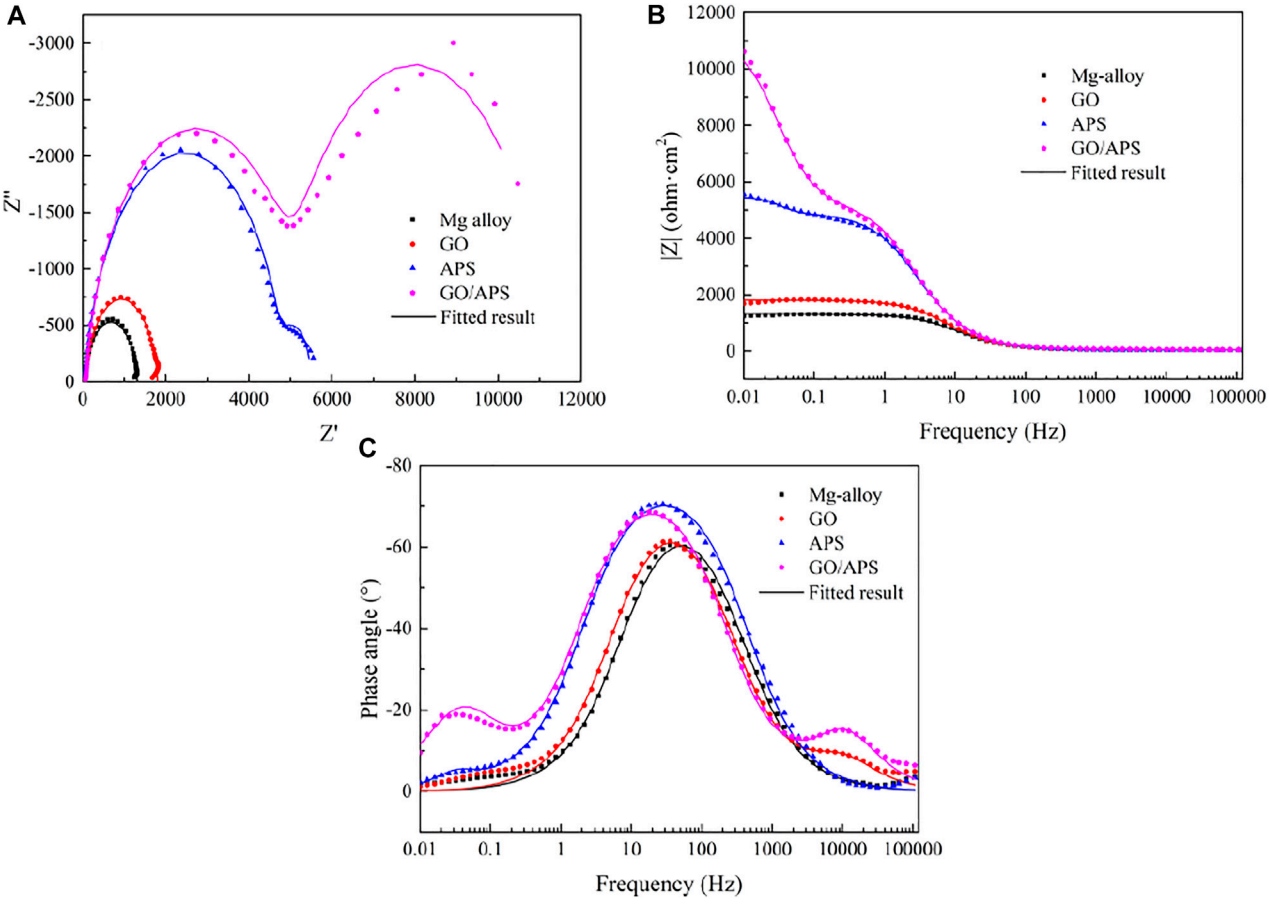

FIGURE 8 | EIS curves and fitted results of bare Mg alloy and GO, APS, and GO-APS film–coated Mg alloy samples after 24 h of immersion in 0.05 M NaCl solution: **(A)** Nyquist plot; **(B)** Bode impedance modulus plot; **(C)** Bode impedance phase angle plot.

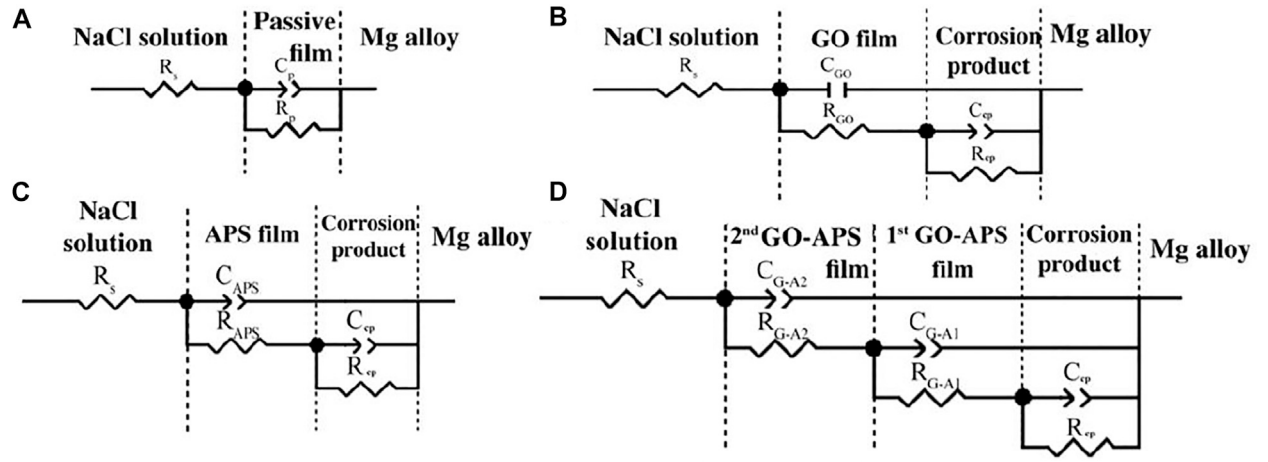

FIGURE 9 | Equivalent circuits of EIS results: **(A)** bare Mg alloy; **(B)** GO film–coated Mg alloy; **(C)** APS film–coated Mg alloy; **(D)** GO-APS film–coated Mg alloy.

TABLE 1 | Parameter values for ECs of various samples.

Sample	Bare Mg alloy	GO film–coated Mg alloy	APS film–coated Mg alloy	GO-APS film–coated Mg alloy
R_s/(Ω cm^2)	41.4	42.25	39.4	42.97
C_p/(F)	2.6631E-5	—	—	—
R_p/(Ω cm^2)	1274	—	—	—
C_{GO}/(F)	—	1.2443E-6	—	—
R_{GO}/(Ω cm^2)	—	16.05	—	—
C_{APS}/(F)	—	—	2.2014E-5	—
R_{APS}/(Ω cm^2)	—	—	4828	—
$C_{G\text{-}A2}$/(F)	—	—	—	6.5417E-7
$R_{G\text{-}A2}$/(Ω cm^2)	—	—	—	30.39
$C_{G\text{-}A1}$/(F)	—	—	—	2.1302E-5
$R_{G\text{-}A1}$/(Ω cm^2)	—	—	—	5242
C_{cp}/(F)	—	2.4594E-5	8.3614E-3	9.0208E-4
R_{cp}/(Ω cm^2)	—	1744	610.1	5879

Figure 8 presents the results obtained from the EIS data of bare Mg alloy and GO, APS, and GO-APS film–coated Mg alloy. The equivalent circuits (ECs) obtained from the fitted results are revealed in **Figure 9**. For all samples, R_s in the ECs represent the resistance in NaCl solution. According to the simulated ECs, the following can be determined: C_p and R_p correspond to the passive film formed on the surface of the Mg alloy; C_{cp} and R_{cp} correspond to the corrosion product layer between the outer film and the Mg alloy substrate; the GO film coated on the Mg alloy can be expressed by C_{GO} and R_{GO}; C_{APS} and R_{APS} represent the APS film; and the double layer films can be deduced for the GO-APS film–coated Mg alloy, which is signified by $C_{G\text{-}A1}$ and $C_{G\text{-}A2}$.

Each value of the elements in ECs is exhibited in **Table 1**. Regarding the GO film on Mg alloy, R_{GO} and R_{cp} demonstrate the rise in corrosion resistance due to the GO film. The high value of R_{cp} indicates the corrosion product between the GO film and Mg alloy substrate dominated in the protection from corrosion. The low value of R_{GO} could be caused by the cracks on the GO film (Prasai et al., 2012; Yu et al., 2015). Also, the higher R_{cp} value of the GO film–coated Mg alloy than the R_p value of the bare Mg alloy proved the adequate protection of the GO film from corrosion. As for the APS film–coated Mg alloy, in the same way, the high R_{APS} and R_{cp} values also explained the protective effect of the APS film from corrosive NaCl solution. In the case of the silane-modified GO film, the corrosion resistances of first GO-APS layers and the corrosion product layer between

TABLE 2 | Comparison of corrosion resistance of GO-based films/coatings on Mg alloys.

Substrate	Films/coatings	R_{ct}/R_{cp}(Ω cm^2)	Ref
AZ31	HQ/GO/MgO	243.6	Soliman et al. (2020)
AZ31	GO	992	Ikhe et al. (2016)
PPFS/GO		3598	
AZ31	HA/GO	329.4	Peng et al. (2020)
Mg-Zn-Ca	rGO-PVA	1804	Chu et al. (2019)
GO-PVA		285.3	
AZ31	EPD-GO	873.5	Maqsood et al. (2020)
AZ31	GO-APS	5879	This article

the GO-APS films and Mg alloy substrate are much higher than those of the GO film–coated Mg alloy, indicating that silane modification greatly improved the resistance of the GO film from corrosion. Besides, the higher $R_{G\text{-}A1}$ and R_{cp} values than the $R_{G\text{-}A2}$ value demonstrate that the corrosion resistance of GO-APS films is dominated by the first layer of the GO-APS films and the corrosion product formed in the process of immersion in GO-APS sol. Therefore, the GO-APS film exhibits good corrosion protection and is superior to most of the GO-based anticorrosive coatings on magnesium alloys, as shown in **Table 2**.

The possible protective mechanism of silane-modified GO films is as follows:

1) The surface modification of silane reduces the conductivity of GO and inhibits the promotion of GO to metal corrosion at film defects (Yu et al., 2015).
2) The impermeability of GO improves the physical barrier property of the film and prevents the infiltration and erosion of the corrosive medium (Chu et al., 2019; Maqsood et al., 2020).
3) The corrosion product layer was formed at the interface between the GO-silane layer and the magnesium alloy substrate, which formed the synergistic protective effect.

CONCLUSION

The surface modification of GO was carried out by using APS. The results showed that APS successfully modified the surface of GO, and the prepared film significantly improved the corrosion resistance of the magnesium alloy. Results indicated that GO films could not be applied on magnesium alloy AZ31 because of the formed corrosion product layer and unavoidable defects. In contrast, APS plays an important role in improving the uniformity and adhesion of the GO film and decreasing the thickness of the corrosion product layer. The GO-APS films can be formed as a good physical barrier layer that can provide effective corrosion protection. This method provides a new idea for the application of graphene-based thin films on the magnesium alloy surface.

DATA AVAILABILITY STATEMENT

The original contributions presented in the study are included in the article/supplementary material; further inquiries can be directed to the corresponding authors.

AUTHOR CONTRIBUTIONS

All authors listed have made a substantial, direct, and intellectual contribution to the work and approved it for publication.

FUNDING

This work was supported by the Natural Science Foundation of Beijing (Grant Nos. 2182017 and 2202017), Science and Technology Project of Beijing Education Commission (KM201910017004), and URT program of Beijing Institute of Petrochemical Technology (2021J00135 and 2021J00134).

REFERENCES

Aneja, K. S., Böhm, H. L. M., Khanna, A. S., and Böhm, S. (2017). Functionalised Graphene as a Barrier against Corrosion. *FlatChem.* 1, 11–19. doi:10.1016/j.flatc.2016.08.003

Chang, C.-H., Huang, T.-C., Peng, C.-W., Yeh, T.-C., Lu, H.-I., Hung, W.-I., et al. (2012). Novel Anticorrosion Coatings Prepared from Polyaniline/graphene Composites. *Carbon* 50, 5044–5051. doi:10.1016/j.carbon.2012.06.043

Chu, J. H., Tong, L. B., Wen, M., Jiang, Z. H., Wang, K. S., and Zhang, H. J. (2019). Graphene Oxide Film as a Protective Barrier for Mg alloy: Worse or Better Is Dependent on a Chemical Reduction Process. *Carbon* 145, 389–400. doi:10.1016/j.carbon.2019.01.037

Daavari, M., Atapour, M., Mohedano, M., Arrabal, R., Matykina, E., and Taherizadeh, A. (2021). Biotribology and Biocorrosion of MWCNTs-Reinforced PEO Coating on AZ31B Mg alloy. *Surf. Inter.* 22, 100850. doi:10.1016/j.surfin.2020.100850

Fernández-Hernán, J. P., López, A. J., Torres, B., and Rams, J. (2021). Influence of Roughness and Grinding Direction on the Thickness and Adhesion of Sol-Gel Coatings Deposited by Dip-Coating on AZ31 Magnesium Substrates. A Landau-Levich Equation Revision. *Surf. Coat. Tech.* 408, 126798. doi:10.1016/j.surfcoat.2020.126798

Ferrari, A. C., Meyer, J. C., Scardaci, V., Casiraghi, C., Lazzeri, M., Mauri, F., et al. (2006). Raman Spectrum of Graphene and Graphene Layers. *Phys. Rev. Lett.* 97, 187401. doi:10.1103/physrevlett.97.187401

Gnedenkov, A. S., Sinebryukhov, S. L., Mashtalyar, D. V., and Gnedenkov, S. V. (2016). Protective Properties of Inhibitor-Containing Composite Coatings on a Mg alloy. *Corrosion Sci.* 102, 348–354. doi:10.1016/j.corsci.2015.10.026

Gómez-Navarro, C., Weitz, R. T., Bittner, A. M., Scolari, M., Mews, A., Burghard, M., et al. (2007). Electronic Transport Properties of Individual Chemically Reduced Graphene Oxide Sheets. *Nano Lett.* 7, 3499–3503. doi:10.1021/nl072090c

Hernández-Barrios, C. A., Saavedra, J. A., Higuera, S. L., Coy, A. E., and Viejo, F. (2020). Effect of Cerium on the Physicochemical and Anticorrosive Features of TEOS-GPTMS Sol-Gel Coatings Deposited on the AZ31 Magnesium alloy. *Surf. Inter.* 21, 100671. doi:10.1016/j.surfin.2020.100671

Hsieh, Y.-P., Hofmann, M., Chang, K.-W., Jhu, J. G., Li, Y.-Y., Chen, K. Y., et al. (2014). Complete Corrosion Inhibition through Graphene Defect Passivation. *ACS Nano* 8, 443–448. doi:10.1021/nn404756q

Ikhe, A. B., Kale, A. B., Jeong, J., Reece, M. J., Choi, S.-H., and Pyo, M. (2016). Perfluorinated Polysiloxane Hybridized with Graphene Oxide for Corrosion Inhibition of AZ31 Magnesium alloy. *Corrosion Sci.* 109, 238–245. doi:10.1016/j.corsci.2016.04.010

Jo, M., Lee, H. C., Lee, S. G., and Cho, K. (2017). Graphene as a Metal Passivation Layer: Corrosion-Accelerator and Inhibitor. *Carbon* 116, 232–239. doi:10.1016/j.carbon.2017.02.008

Kyhl, L., Nielsen, S. F., Čabo, A. G., Cassidy, A., Miwa, J. A., and Hornekær, L. (2015). Graphene as an Anti-corrosion Coating Layer. *Faraday Discuss.* 180, 495–509. doi:10.1039/c4fd00259h

Lei, J., Hu, Y., Liu, Z., Cheng, G. J., and Zhao, K. (2017). Defects Mediated Corrosion in Graphene Coating Layer. *ACS Appl. Mater. Inter.* 9, 11902–11908. doi:10.1021/acsami.7b01539

Liu, J., Hua, L., Li, S., and Yu, M. (2015). Graphene Dip Coatings: An Effective Anticorrosion Barrier on Aluminum. *Appl. Surf. Sci.* 327, 241–245. doi:10.1016/j.apsusc.2014.11.187

Liu, J., Zhang, Y., Yu, M., Li, S., Xue, B., and Yin, X. (2015). Influence of Embedded ZnAlCe-No3− Layered Double Hydroxides on the Anticorrosion Properties of

Sol-Gel Coatings for Aluminum alloy. *Prog. Org. Coat.* 81, 93–100. doi:10.1016/j.porgcoat.2014.12.015

Ma, B., Rodriguez, R. D., Ruban, A., Pavlov, S., and Sheremet, E. (2019). The Correlation between Electrical Conductivity and Second-Order Raman Modes of Laser-Reduced Graphene Oxide. *Phys. Chem. Chem. Phys.* 21, 10125–10134. doi:10.1039/c9cp00093c

Ma, Y., Di, H., Yu, Z., Liang, L., Lv, L., Pan, Y., et al. (2016). Fabrication of Silica-Decorated Graphene Oxide Nanohybrids and the Properties of Composite Epoxy Coatings Research. *Appl. Surf. Sci.* 360, 936–945. doi:10.1016/j.apsusc.2015.11.088

Maqsood, M. F., Raza, M. A., Ghauri, F. A., Rehman, Z. U., and Ilyas, M. T. (2020). Corrosion Study of Graphene Oxide Coatings on AZ31B Magnesium alloy. *J. Coat. Technol. Res.* 17, 1321–1329. doi:10.1007/s11998-020-00350-3

Matinlinna, J. P., Lung, C. Y. K., and Tsoi, J. K. H. (2018). Silane Adhesion Mechanism in Dental Applications and Surface Treatments: A Review. *Dental Mater.* 34, 13–28. doi:10.1016/j.dental.2017.09.002

Pan, F., Yang, M., and Chen, X. (2016). A Review on Casting Magnesium Alloys: Modification of Commercial Alloys and Development of New Alloys. *J. Mater. Sci. Tech.* 32, 1211–1221. doi:10.1016/j.jmst.2016.07.001

Peng, F., Zhang, D., Wang, D., Liu, L., and Liu, X. (2020). Enhanced Corrosion Resistance and Biocompatibility of Magnesium alloy by Hydroxyapatite/graphene Oxide Bilayer Coating. *Mater. Lett.* 264, 127–322. doi:10.1016/j.matlet.2020.127322

Prasai, D., Tuberquia, J. C., Harl, R. R., Jennings, G. K., and Bolotin, K. I. (2012). Graphene: Corrosion-Inhibiting Coating. *ACS Nano* 6, 1102–1108. doi:10.1021/nn203507y

Ramezanzadeh, B., Ahmadi, A., and Mahdavian, M. (2016). Enhancement of the Corrosion protection Performance and Cathodic Delamination Resistance of Epoxy Coating through Treatment of Steel Substrate by a Novel Nanometric Sol-Gel Based Silane Composite Film Filled with Functionalized Graphene Oxide Nanosheets. *Corrosion Sci.* 109, 182–205. doi:10.1016/j.corsci.2016.04.004

Sanjid, A., Banerjee, P. C., and Raman, R. K. S. (2019). Multi-layer Graphene Coating for Corrosion Resistance of Monel 400 alloy in Chloride Environment. *Surf. Coat. Tech.* 370, 227–234. doi:10.1016/j.surfcoat.2019.04.077

Singh, B. P., Nayak, S., Nanda, K. K., Jena, B. K., Bhattacharjee, S., and Besra, L. (2013). The Production of a Corrosion Resistant Graphene Reinforced Composite Coating on Copper by Electrophoretic Deposition. *Carbon* 61, 47–56. doi:10.1016/j.carbon.2013.04.063

Soliman, H., Qian, J., Tang, S., Xian, P., and Wan, G. (2020). Hydroxyquinoline/nano-graphene Oxide Composite Coating of Self-Healing Functionality on Treated Mg Alloys AZ31. *Surf. Coat. Tech.* 385, 125–395. doi:10.1016/j.surfcoat.2020.125395

Stankovich, S., Dikin, D. A., Piner, R. D., Kohlhaas, K. A., Kleinhammes, A., Jia, Y., et al. (2007). Synthesis of Graphene-Based Nanosheets via Chemical Reduction of Exfoliated Graphite Oxide. *Carbon* 45, 1558–1565. doi:10.1016/j.carbon.2007.02.034

Sun, W., Wang, L., Wu, T., Wang, M., Yang, Z., Pan, Y., et al. (2015). Inhibiting the Corrosion-Promotion Activity of Graphene. *Chem. Mater.* 27, 2367–2373. doi:10.1021/cm5043099

Tang, L.-C., Wan, Y.-J., Yan, D., Pei, Y.-B., Zhao, L., Li, Y.-B., et al. (2013). The Effect of Graphene Dispersion on the Mechanical Properties of Graphene/epoxy Composites. *Carbon* 60, 16–27. doi:10.1016/j.carbon.2013.03.050

Wan, Y.-J., Gong, L.-X., Tang, L.-C., Wu, L.-B., and Jiang, J.-X. (2014). Mechanical Properties of Epoxy Composites Filled with Silane-Functionalized Graphene Oxide. *Composites A: Appl. Sci. Manufacturing* 64, 79–89. doi:10.1016/j.compositesa.2014.04.023

Wu, G., Ibrahim, J. M., and Chu, P. K. (2013). Surface Design of Biodegradable Magnesium Alloys - A Review. *Surf. Coat. Tech.* 233, 2–12. doi:10.1016/j.surfcoat.2012.10.009

Yu, M., Xue, B., Liu, J., Li, S., and Zhang, Y. (2015). Electrophoretic Deposition of Hybrid Coatings on Aluminum alloy by Combining 3-aminopropyltrimethoxysilan to Silicon-Zirconium Sol Solutions for Corrosion protection. *Thin Solid Films* 590, 33–39. doi:10.1016/j.tsf.2015.07.055

Yu, Y.-H., Lin, Y.-Y., Lin, C.-H., Chan, C.-C., and Huang, Y.-C. (2014). High-performance Polystyrene/graphene-Based Nanocomposites with Excellent Anti-corrosion Properties. *Polym. Chem.* 5, 535–550. doi:10.1039/c3py00825h

Zainal Abidin, N. I., Rolfe, B., Owen, H., Malisano, J., Martin, D., Hofstetter, J., et al. (2013). The *In Vivo* and *In Vitro* Corrosion of High-Purity Magnesium and Magnesium Alloys WZ21 and AZ91. *Corrosion Sci.* 75, 354–366. doi:10.1016/j.corsci.2013.06.019

Zhang, Y., Yu, P., Wang, J., Li, Y., Chen, F., Wei, K., et al. (2018). LDHs/Graphene Film on Aluminum Alloys for Active protection. *Appl. Surf. Sci.* 433, 927–933. doi:10.1016/j.apsusc.2017.10.126

Zhou, Z., Zheng, B., Lang, H., Qin, A., and Ou, J. (2020). Corrosion Resistance and Biocompatibility of Polydopamine/hyaluronic Acid Composite Coating on AZ31 Magnesium alloy. *Surf. Inter.* 20, 100560. doi:10.1016/j.surfin.2020.100560

Conflict of Interest: Author XH was employed by China United Testing & Certification Co., Ltd.

The remaining authors declare that the research was conducted in the absence of any commercial or financial relationships that could be construed as a potential conflict of interest.

The handling editor declared a past co-authorship with one of the authors YZ.

Publisher's Note: All claims expressed in this article are solely those of the authors and do not necessarily represent those of their affiliated organizations, or those of the publisher, the editors, and the reviewers. Any product that may be evaluated in this article, or claim that may be made by its manufacturer, is not guaranteed or endorsed by the publisher.

frontiers in Materials

ORIGINAL RESEARCH
published: 16 November 2021
doi: 10.3389/fmats.2021.761052

The Pilling-Bedworth Ratio of Oxides Formed From the Precipitated Phases in Magnesium Alloys

Quantong Jiang[1,2,3]*, *Dongzhu Lu*[1,2,3], *Chang Liu*[1,2,3], *Nazhen Liu*[1,2,3]* and *Baorong Hou*[1,2,3]

[1]CAS Key Laboratory of Marine Environmental Corrosion and Bio-Fouling, Institute of Oceanology, Chinese Academy of Sciences, Qingdao, China, [2]Open Studio for Marine Corrosion and Protection, Pilot National Laboratory for Marine Science and Technology (Qingdao), Qingdao, China, [3]School of Materials Science and Engineering, Qilu University of Technology, Jinan, China

The Pilling-Bedworth ratio of oxides preferentially formed from the precipitated phases in magnesium alloys were calculated. The results showed that the PBR value of Nd_2O_3 preferentially formed from $Mg_{12}Nd$ was 1.0584, and the PBR value of Y_2O_3 preferentially formed from $Mg_{24}Y_5$ was 1.1923. Both the Nd_2O_3 and Y_2O_3 would provide a good protection to the Mg matrix. The Gd_2O_3 preferentially formed from Mg_3Gd, whereas the MgO preferentially formed from $MgNi_2$. The PBR value of these two oxides were both larger than 2. The corresponding oxides formed from the common precipitated phases $Mg_{17}Al_{12}$, $MgZn_2$, $MgCu_2$, Mg_2Ca, $Mg_{12}Ce$, and MgAg were all less than 1. The oxide films formed on surfaces of pure Mg and Mg-xY (x = 3, 5, 7 wt.%) alloys at high temperatures were analyzed. The results showed that the oxide films were composed of a Y_2O_3/MgO outer layer and an inner layer rich with Y_2O_3. The formation of Y_2O_3 was mainly caused by the oxidation of $Mg_{24}Y_5$. The more Y_2O_3 existed in the composite oxidation film, the better corrosion resistance of the Mg-Y samples.

Keywords: oxide, PBR value, magnesium alloys, precipitated phases, Mg-Y

OPEN ACCESS

Edited by:
Yingwei Song,
Institute of Metals Research (CAS), China

Reviewed by:
Jun Chen,
Xihua University, China
Fuyong Cao,
Xiamen University, China

***Correspondence:**
Quantong Jiang
jiangquantong@qdio.ac.cn
Nazhen Liu
liunazhen@qdio.ac.cn

Specialty section:
This article was submitted to Structural Materials, a section of the journal Frontiers in Materials

Received: *19 August 2021*
Accepted: *08 October 2021*
Published: *16 November 2021*

Citation:
Jiang Q, Lu D, Liu C, Liu N and Hou B (2021) The Pilling-Bedworth Ratio of Oxides Formed From the Precipitated Phases in Magnesium Alloys. Front. Mater. 8:761052. doi: 10.3389/fmats.2021.761052

INTRODUCTION

The PBR (Pilling-Bedworth Ratio) value of oxide film is an important parameter to evaluate the film protection performance to the base metal (Xu and Gao, 2000). When the PBR value is less than 1, the protection performance of the oxide film is poor, due to the existing tensile stress and the resultant incomplete coverage of the oxide film to the metal. Similarly, when the PBR value is larger than 3, the oxide film also shows a weak protection, due to the compressive stress in the film. When the PBR value is between 1 and 2, the oxide film is protective (Bradford 1993; Tan et al., 2016; Song et al., 2021).

Magnesium is active, so the α-Mg matrix and precipitated phases in magnesium alloys are prone to be oxidized in the atmospheric environment (Czerwinski 2002; Liu et al., 2009; Medved et al., 2009), leading to the formation of different kinds of oxidation films on the magnesium alloy surface (Czerwinski, 2012; Czerwinski, 2015). The PBR value of oxidation film formed on pure magnesium is about 0.8, which is not protective (You et al., 2000; Mebarki et al., 2005; Cheng et al., 2009; López et al., 2010).

There are many precipitated phases existing in magnesium alloys, including $Mg_{17}Al_{12}$, $MgZn_2$, Mg_2Ca, Mg_5Gd, $Mg_{12}Nd$ and $Mg_{24}Y_5$, etc., (Nie 2012; Zhu and Chen, 2019; Kaya, 2020; Shi et al., 2020). The crystallography of the precipitated phases determines the microstructure and property of magnesium alloys. According to the literatures, the film formed by oxidation of precipitated phases during the heat treatment process, has good corrosion resistance (Sudholz et al., 2011; Chang et al.,

TABLE 1 | Absolute atomic mass of different alloying elements.

Atomic species	C^{12}	Mg	Al	Zn	Cu	Ca
Relative mass	12.017	24.305	26.982	65.409	63.546	40.078
Absolute mass/10^{-26}Kg	1.9927	4.0303	4.4742	10.846	10.537	6.6450
Atomic species	**Gd**	**Nd**	**Ce**	**Ag**	**Ni**	**Y**
Relative mass	157.25	144.242	140.116	107.868	58.693	88.905
Absolute mass/10^{-26}Kg	26.0757	23.9187	23.2345	17.887	9.733	14.7425

2015; Yu et al., 2015). Due to the different activity of alloying elements, the property of oxide film formed from the precipitated phases in the atmospheric environment is different (Van Orman and Crispin, 2010). PBR is the ratio of oxide volume consisting metal and oxygen on the metal surface, to the volume of base metal atoms, which reflects the stress condition in the oxide film. The corrosion tendency of magnesium alloy is closely related to the conditions of the oxide layer (Wang et al., 2007; Fan et al., 2011).

In this work, the PBR values of oxides formed from the precipitated phases in magnesium alloys were calculated. In order to verify the PBR calculation results of oxides formed from the precipitated phases in magnesium alloys, the morphologies of oxidation films formed on the surfaces of pure Mg and Mg-xY alloys (x = 3, 5, 7 wt.%) at high temperature were characterized. The effect of the oxidation films on corrosion resistance were also studied. This work is expected to give a scientific and reasonable method to improve intrinsic corrosion resistance of magnesium alloys by regulating the types of precipitates.

CALCULATION OF THE PILLING-BEDWORTH RATIO VALUE

Calculation of Absolute Atomic Mass

The relative atomic mass values of the alloying elements, including Al,Zn, Cu, Ca, Gd, Nd, Ce, Ag, Ni, Y and C^{12} were obtained from the periodic table of elements. The absolute atomic mass values of the alloying elements were calculated via the following formula:

$$Absolute\ tomic\ mass = \frac{Relative\ atomic\ mass\ of\ \ alloying\ elements}{Relative\ atomic\ mass\ of\ C12} \times 1.9927 \times 10^{-26} Kg \quad (1)$$

The results were shown in **Table 1**.

Molar Volume of Precipitated Phases Mg_AX_B in Magnesium Alloys

The crystal structure and parameters of the common precipitated phases in the magnesium alloys, including $Mg_{17}Al_{12}$, $MgZn_2$, $MgCu_2$, Mg_2Ca, Mg_3 Gd, $Mg_{12}Nd$, $Mg_{12}Ce$, MgAg, $MgNi_2$ and $Mg_{24}Y_5$ were obtained by the phase diagram.

The atom number in a single unit cell of the precipitated phases Mg_AX_B was calculated via the crystal structure. For example, the crystal structure of $Mg_{24}Y_5$ is body-centered cubic (BCC), so there are two $Mg_{24}Y_5$ intermetallics in each unit cell. The total atom number in a single $Mg_{24}Y_5$ unit cell is 2 × (24Mg+5Y) = 48Mg + 10Y. The absolute mass of a single $Mg_{24}Y_5$ unit cell (the sum of 48Mg atoms and 10 Y atoms) was obtained as following: 48 × 4.0303×10^{-23} g + 10 × 14.7425×10^{-23} g = 340.8794×10^{-23} g. The absolute mass of other single precipitated phases Mg_AX_B was calculated via the same method with results shown in **Table 2**.

The volume of a single unit cell was calculated according to the crystal structure and parameters obtained from the XRD card. The density of a single unit cell was calculated via the following formula:

$$Density\ of\ a\ \ single\ unit\ cell = \frac{Absolute\ mass\ of\ a\ single\ unit\ cell}{Volume\ of\ a\ single\ unit\ cell} \quad (2)$$

The $Mg_{24}Y_5$ unit cell is body-centered cubic (BCC) structure, and the lattice parameters is a = 1.1257×10^{-7} cm. So the Volume of a single unit cell is a^3 = $(1.1257 \times 10^{-7}\ cm)^3$ = $1.4265 \times 10^{-21}\ cm^3$, the density of a single $Mg_{24}Y_5$ unit cell is $\frac{340.8794\times10^{-23}g}{1.4265\times10^{-21}cm^3}$ = 2.3896/cm^3, according to **Eq. 2**. The densities of single unit cells of the other precipitated phases were obtained via the same method. The density of a single $Mg_{24}Y_5$ unit cell is the density of the $Mg_{24}Y_5$ intermetallics.

The molar volume of precipitated phases Mg_AX_B in magnesium alloys was calculated via the formula as follow:

$$Molar\ volume\ of\ \ precipituated\ phases = \frac{Molar mass of precipitated phases}{Density of a single MgAXB unit cell} \quad (3)$$

For example, the molar volume of $Mg_{24}X_5 \frac{1027.845}{2.3896}$ = 430.132 cm^3. All the calculated results are shown in **Table 2**.

Pilling-Bedworth Ratio Calculation of Oxidation Formed From Precipitated Phases

According to the formation Gibbs energies of the metal's oxides (James 2005), the preferential metal atom of the precipitated

TABLE 2 | Molar volume of precipitated phases Mg_AX_B in magnesium alloys.

Precipitated phases	Crystal structure	A single unit cell of precipitated phases MgAXB					Molar mass	Molar volume
		Number of atoms	Mass/ 10^{-23}g	Lattice parameters	Volume $10^{-21}cm^3$	Density g/cm^3		
$Mg_{24}Y_5$	BCC	48+10	340.8794	a = 1.1257	1.4265	2.3896	1,027.845	430.132
Mg_3Gd	FCC	12+4	152.6664	a = 0.7326	0.3932	3.8828	230.165	59.2781
$Mg_{12}Ce$	BCC	24+2	143.1962	a = 1.033 c = 0.5964	0.6364	2.2501	431.776	191.892
$Mg_{12}Nd$	BCC	4+2	144.5646	a = 1.031 c = 0.593	0.6303	2.297	435.902	189.770
$Mg_{17}Al_{12}$	BCC	34+24	244.411	a = 1.056	1.1776	2.078	736.969	354.653
$MgZn_2$	HCP	2+4	51.4458	a = 0.5222 c = 0.8568	0.6075	4.960	155.123	31.275
$MgCu_2$	FCC	4+8	100.4204	a = 0.7048	0.3415	5.745	151.397	25.880
Mg_2Ca	HCP	4+2	29.4130	a = 0.623 c = 1.012	1.0212	1.732	88.688	51.206
MgAg	SC	1+1	21.9173	a = 0.3314	0.0364	6.030	132.173	21.919
$MgNi_2$	HCP	2+4	46.9914	a = 0.4824 c = 1.5826	0.9575	5.902	107.303	18.181

phases Mg_AX_B in magnesium alloys during oxidation reaction in the atmospheric environment were:

1) $\Delta_fG^\circ Al_2O_3 = -38.5$ kJ/mol > $\Delta_fG^\circ MgO = -135.27$ kJ/mol; $Mg_{17}Al_{12} \rightarrow Mg \rightarrow MgO$
2) $\Delta_fG^\circ ZnO = -76.08$ kJ/mol > $\Delta_fG^\circ MgO = -135.27$ kJ/mol; $MgZn_2 \rightarrow Mg \rightarrow MgO$
3) $\Delta_fG^\circ CuO = -31.0$ kJ/mol > $\Delta_fG^\circ MgO = -135.27$ kJ/mol; $MgCu_2 \rightarrow Mg \rightarrow MgO$
4) $\Delta_fG^\circ CaO = -144.25$ kJ/mol < $\Delta_fG^\circ MgO = -135.27$ kJ/mol; $Mg_2Ca \rightarrow Ca \rightarrow CaO$
5) $\Delta_fG^\circ Gd_2O_3 = -434.9$ kJ/mol < $\Delta_fG^\circ MgO = -135.27$ kJ/mol; $Mg_3Gd \rightarrow Gd \rightarrow Gd_2O_3$
6) $\Delta_fG^\circ Nd_2O_3 = -411.3$ kJ/mol < $\Delta_fG^\circ MgO = -135.27$ kJ/mol; $Mg_{12}Nd \rightarrow Nd \rightarrow Nd_2O_3$
7) $\Delta_fG^\circ Ce_2O_3 = -407.80$ kJ/mol < $\Delta_fG^\circ MgO = -135.27$ kJ/mol; $Mg_{12}Ce \rightarrow Ce \rightarrow Ce_2O_3$
8) $\Delta_fG^\circ Ag_2O = -2.68$ kJ/mol > $\Delta_fG^\circ MgO = -135.27$ kJ/mol; $MgAg \rightarrow Mg \rightarrow MgO$
9) $\Delta_fG^\circ NiO = -50.6$ kJ/mol > $\Delta_fG^\circ MgO = -135.27$ kJ/mol; $MgNi_2 \rightarrow Mg \rightarrow MgO$
10) $\Delta_fG^\circ Y_2O_3 = -434.19$ kJ/mol < $\Delta_fG^\circ MgO = -135.27$ kJ/mol; $Mg_{24}Y_5 \rightarrow Y \rightarrow Y_2O_3$

If there is one type of precipitated phase A_UB_V in magnesium alloy, the preferentially oxidized element is B-content in the A_UB_V single unit cell. Because the preferentially oxidized B-content is derived from A_UB_V, which is a solid solution structure. Therefore, the volume of B-content can be obtained from the volume of A_UB_V single unit cell subtracted the volume of unoxidized A-content (Xu and Gao, 2000), as shown by the following formula,

$$Volume\,of\,x_B = Volume\,of\left[(\mathbf{X/V})_{\mathbf{AuBv}}\right] - Volume\,of\left[(ux/v)_A\right] \quad (4)$$

For example, the molar volume of Y atom in $Mg_{24}Y_5$ unit cell was calculated via: $1/5[V_{Mg_{24}Y_5} - 24V_{Mg}] = 1/5 \times [430.132 - 24 \times 13.9845]cm^3 = 18.9008\,cm^3$. In consideration of x in **Eq. 6** (2 for Y_2O_3), the volume of 2 mol of Y in alloy is calculated by $2 \times 18.9008\,cm^3 = 37.8016\,cm^3$.

Then, the density and molar mass of oxide product can be obtained via periodic table of elements. Thus, the molar volume of oxidized product can be calculated via the formula:

$$Molar\,volume\,of\,oxide = \frac{Molar\,mass\,of\,oxide\,product}{Density\,of\,oxide\,product} \quad (5)$$

For example, the molar volume of oxide product Y_2O_3 from the oxidation of precipitated phases $Mg_{24}Y_5$ was calculated as follow: $\frac{M_{Y_2O_3}}{D_{Y_2O_3}} = \frac{225.81\ g/mol}{5.01\ g/cm^3} = 45.0719$.

The PBR value of oxidation films formed from the precipitated phases in magnesium alloys was calculated via the formula:

$$PBR_{\text{precipitated phases}}\,\frac{Volume\,of\,one\,mole\,of\,B_xO_y}{Volume\,of\,x\,moles\,of\,B\,in\,\,alloy} \quad (6)$$

All the results were shown in **Table 3**.

Characteristic of Oxide Films on the Mg-xY (x = 3, 5, 7 wt.%) Alloys Surfaces

Commercially pure Mg (99.9 wt. %), Mg- 3Y wt.%, Mg- 5Y wt.% and Mg- 7Y wt.% were used to characterize the oxide film on the surface of magnesium alloys. The samples with dimensions of 1 cm × 1 cm×1 cm were heated in the dry air at 400°C for 36 h. These samples were used to analyze the microstructure of oxide films, including the morphologies, thicknesses and compositions by scanning electron microscopy (SEM) and energy dispersive spectroscopy (EDS). The samples with dimensions of 2 cm × 2 cm × 0.5 cm were also heated in dry air at 400°C for 36 h, which were used to test the open circuit potential (OCP) using the electrochemical workstation. Three parallel samples were used to ensure the accuracy of the test results. All the samples were polished with 1,000, 3,000 and 5,000# SiC papers and then cleaned with absolute ethanol.

Due to the affinity of oxygen to magnesium alloys, samples are oxidized rapidly at a high temperature in dry air. The rate of oxidation increases first linearly, then exponentially with the

TABLE 3 | PBR value of the oxide film formed from the precipitated phases of magnesium alloys.

Precipitated phases Mg_AX_B in magnesium alloys	Mg_AX_B Volume/cm^3	The lower metal activity element in Mg_AX_B		The molar volume of the preferentially oxidized metal/cm^3	Preferentially oxidized product			PBR value of oxidation films formed from Mg_AX_B
		Density (g/cm3)	Volume/ cm^3		Molar mass	Density g/cm^3	Volume/ cm^3	
$Mg_{24}Y_5$	430.132	Mg = 1.738	13.9845	Y = 37.8016	Y2O3 = 225.81	5.01	45.0719	1.1923
Mg_3Gd	59.2781	Mg = 1.738	13.9845	Gd = 17.3246	Gd2O3 = 362.49	7.41	48.9201	2.8237
$Mg_{12}Ce$	191.892	Mg = 1.738	13.9845	Ce = 48.156	Ce2O3 = 328.24	7.13	46.0365	0.9560
$Mg_{12}Nd$	189.770	Mg = 1.738	13.9845	Nd = 43.912	Nd2O3 = 336.47	7.24	46.4738	1.0584
$Mg_{17}Al_{12}$	354.653	Al = 2.70	9.9933	Mg = 13.8078	MgO = 40.304	3.65	11.042	0.7997
$MgZn_2$	31.275	Zn = 7.14	9.1609	Mg = 12.9532	MgO = 40.304	3.65	11.042	0.8525
$MgCu_2$	25.880	Cu = 8.96	7.0922	Mg = 11.6956	MgO = 40.304	3.65	11.042	0.9441
Mg_2Ca	51.206	Mg = 1.738	13.9845	Ca = 23.237	CaO = 56.077	3.25	17.254	0.7425
MgAg	21.919	Ag = 10.49	10.2829	Mg = 11.429	MgO = 40.304	3.65	11.042	0.9661
$MgNi_2$	18.181	Ni = 8.908	6.5888	Mg = 5.0034	MgO = 40.304	3.65	11.042	2.2069

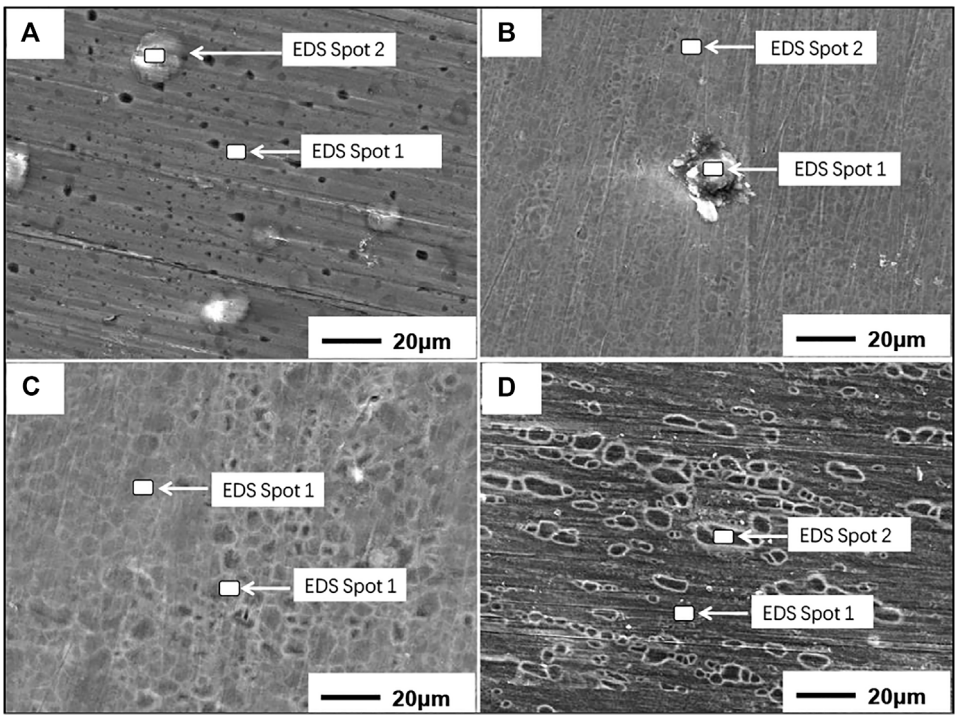

FIGURE 1 | The oxides morphologies of different samples: **(A)** pure Mg; **(B)** Mg-3Y; **(C)** Mg-5Y; **(D)** Mg-7Y.

extension of oxidation time (Zhou et al., 2013; Yu et al., 2016). Below 400–450°C, the magnesium alloys have certain oxidation resistance, with a parabolic oxidation kinetics and intact oxide film (Yu et al., 2018). Once the temperature exceedes 400°C, the oxidation reaction kinetics will change from parabolic to linear. The acceleration of oxidation reaction leads to the formation of film cracks on the surface. Therefore, in order to study the microstructure of the dense oxide films on Mg-Y alloys, the oxidation temperature of 400°C was chosen. The thermo gravimetric analysis (TGA) was used to measure the weight increment of different samples. The heating rate was 10°C/min in the air environment from room temperature to 500°C.

As shown in **Figure 1**, the morphologies of oxide films formed on Mg-xY (x = 0, 3, 5, 7 wt.%) samples are quite different. Many MgO particles and pores existed on the surface of pure Mg, indicating a poor corrosion resistance of the oxide film. With the addition of 3 wt.% Y, the surface tended to be smooth and compact, and the pores were also disappeared. However, there

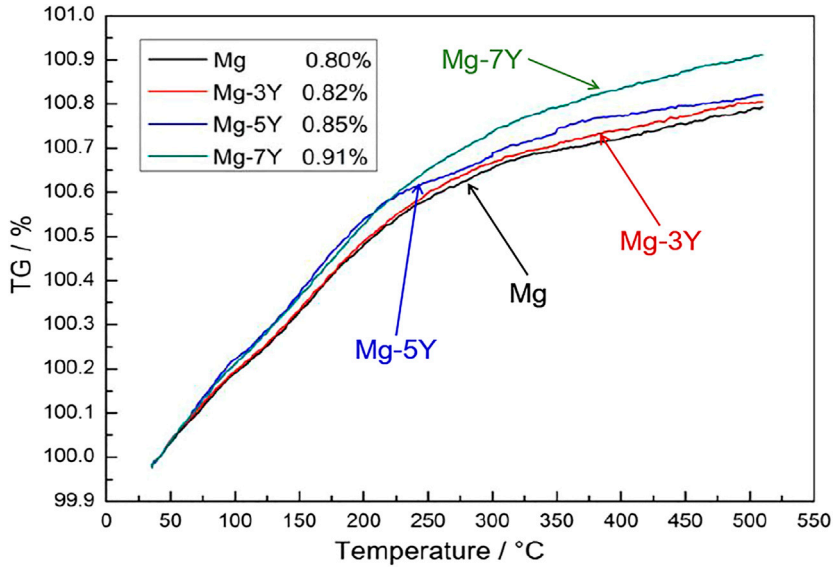

FIGURE 2 | The thermo gravimetric analysis results of different samples.

TABLE 4 | The EDS results of oxides of different materials.

Materials	Locations	Weight %		
		Element Mg *K*	Element O *K*	Element Y *K*
Mg	Spot 1	98.4	1.6	—
	Spot 2	95.6	4.4	—
Mg-3Y	Spot 1	71.5	15.6	12.8
	Spot 2	60.2	21.7	18.1
Mg-5Y	Spot 1	64.0	17.2	18.7
	Spot 2	53.0	22.5	24.5
Mg-7Y	Spot 1	57.0	21.4	21.6
	Spot 2	55.6	23.2	21.2

TABLE 5 | The EDS mapping analysis of different samples.

Materials	Locations	Weight %		
		Element Mg *K*	Element O *K*	Element Y *K*
Mg	mapping	97.5	2.5	—
Mg-3Y	mapping	65.1	13.8	21.1
Mg-5Y	mapping	62.1	14.1	23.8
Mg-7Y	mapping	57.0	16.1	26.9

were still a small amount of MgO particles on the sample surface. With the increasing of Y-content, MgO particles disappeared completely, whereas the squama-like oxides formed on the surface of Mg-5Y alloys. As the Y content increased to 7 wt.%, the size of the squama-like oxides becomes larger, and the boundary of oxides turned clearly.

The EDS results of oxides on the surface of Mg-xY (x = 0, 3, 5, 7 wt.%) samples are shown in **Table 4**. The Y-contents in the oxides are more than the matrix. Both the O-content and Y-content increased with the addition of Y element, whereas the Mg-content decreased. This phenomenon because that the activity of Y element is higher than Mg element. With the extension of oxidation time, the thickness of oxides increased. The oxidation rate of all the samples was reduced by the oxides barrier, which inhibited the inward diffusion of O_2 and the outward diffusion of Mg^{2+}. According to the calculation in **Table 3**, the PBR of Y_2O_3 formed from the $Mg_{24}Y_5$ unit cell was 1.1923, which indicated that the Y_2O_3 oxidation film was compact. Moreover, the chemical property of Y_2O_3 was relatively stable. Therefore, when Mg-Y alloys were exposed in the high temperature environment, the dense MgO/Y_2O_3 composite oxide layers were formed on the sample surfaces. The composite oxide layer acted as a physical barrier to hinder the oxidation reaction, thus the oxidation of magnesium alloys was slowed down (Wang et al., 2008).

The TGA result was shown in **Figure 2**. From the trends of the curves in the figure, all samples had a fast oxidation rate at the initial stage. The oxidation reaction rate decreased with the prolong of oxidation reaction time and the rising of temperature. The Mg-5Y alloys had the faster oxide reaction rate than the pure Mg, Mg-3Y and Mg-7Y samples at the initial stage of oxidation. Then, the thin, smooth and dense oxide films were formed on the surface of samples, the oxidation rates were all reduced. At the maximum temperature, the weight improvement ratio of pure Mg, Mg-3Y, Mg-5Y and Mg-7Y was 0.80, 0.82, 0.85 and 0.91%, respectively. This phenomenon indicated that Y element had the higher activity to bind with oxygen than Mg.

According to the mapping results in **Figure 3**, the difference of Y-content in Mg-xY (x = 3, 5, 7 wt.%) alloys led to the different elementary composition in the oxidation products.

As shown in **Table 5**, mapping analysis on the surface of pure magnesium showed that the O content was only 2.5%. This

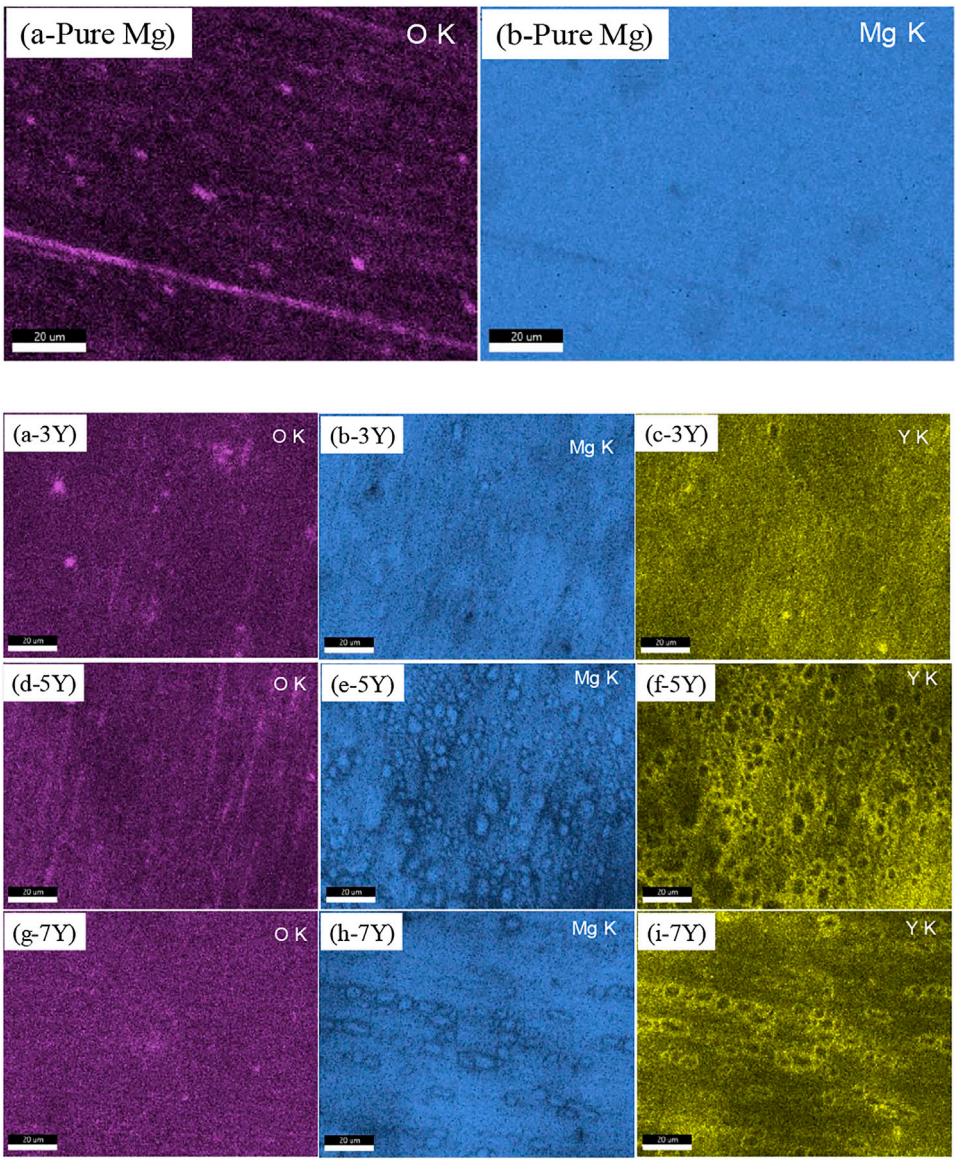

FIGURE 3 | The mapping results of elementary composition in the oxidation products on different samples surfaces: (a-pure Mg) and (b-pure Mg): pure Mg; (a-3Y) and (b-3Y) and (c-3Y): Mg-3Y; (d-5Y) and (e--5Y) and (f-5Y): Mg-5Y; (g-7Y) and (h-7Y) and (i-7Y): Mg-7Y.

phenomenon proved that the oxide film on the surface was very thin, so that the electron beam can penetrate the oxide film and reach the Mg matrix. The oxidation films of Mg-3Y samples were composed of MgO as the major constituent and minor Y_2O_3. When Y-content was 3 wt.%, the average content of oxygen element in the surface mapping analysis was about 13.8 wt.%, and the Y element was about 21.1 wt.%, which indicated that a large number of Y_2O_3 were formed in the oxide film. The content of Y element was larger than that of in the alloy matrix without oxidation. With the increase of Y-content to 7 wt.%, the O element on the surface film increased to 16.1 wt.%, while the Y content increased to 26.9 wt.%.

The average thicknesses of oxidation films for different samples were measured by backscattered electrons scanning spectroscopy, as shown in **Figure 3**. And the elemental composition at different cross-section locations was also analyzed by EDS, with results summarized in **Table 6**. In **Figure 4** the average thickness of oxidation films on the surface of pure Mg was about 0.4 μm. With the addition of Y-content, the oxidation film thickness increased from 0.5 μm (Mg-3Y) to more than 1.5 μm (Mg-7Y). This phenomenon was attributed to the high activity of Y element, which preferentially combines with oxygen to form oxide films (Wang et al., 2009).

As shown in **Table 6**, all the oxidation films were consisted of Y_2O_3 and MgO. For both pure Mg and Mg-xY (x = 3, 5, 7 wt.%) alloys, the major content of the oxidation film is MgO. However, the closer to the top surface of the oxide film, the larger amount of Y_2O_3-content. In general, the protection

TABLE 6 | The elemental composition of different cross-section locations.

Materials	Locations	Weight %		
		Element Mg *K*	Element O *K*	Element Y *K*
Mg	Spot 1	92.8	7.2	—
	Spot 2	95.2	4.8	—
	Spot 3	99.3	0.7	—
Mg-3Y	Spot 1	41.9	28.7	29.4
	Spot 2	44.8	25.7	29.5
	Spot 3	74.6	16.5	8.8
Mg-5Y	Spot 1	35.1	32.3	32.6
	Spot 2	33.6	31.4	35.0
	Spot 3	83.4	14.0	2.7
Mg-7Y	Spot 1	39.3	32.1	28.7
	Spot 2	42.2	31.4	26.3
	Spot 3	75.6	17.8	6.6

performance of oxidation products to α-Mg matrix was related the PBR of films covered on the samples, which determine the diffusion rate of metal atoms from metal/oxide interface to oxide/air interface, and the diffusion rate of oxygen atoms from oxide/air interface to metal/oxide interface (Zhao et al., 2018). The inward diffusion of oxygen atoms and the outward diffusion of Mg atoms through the oxide films was suppressed due to the compact microstructure of Y_2O_3-content.

Figure 5 shows the open circuit potential of pure Mg and Mg-xY alloys covered with oxidation films in 3.5% NaCl solution. As time increased, all the ocp values decreased, due to the desquamation of oxidation films covered on the surface of samples (Jiang, et al., 2021). The OCP value of Mg-7Y alloy was the most positive, indicating the most alleviated local corrosion of Mg-7Y alloy among the samples. In addition, with the extension of immersion time, the OCP of Mg-Y alloys tended to be stable, indicating a stabilized surface state. The electrochemical activity of the samples decreased in the order of Mg-7Y > Mg-5Y > Mg-3Y > pure Mg. The corrosion tendency of Mg-7Y was the lowest in the exposure of 3.5% NaCl for 1200s, due to the protection of the thick and compact oxidation film.

The Tafel slopes of pure Mg and Mg-xY alloys covered with oxidation films measured in 3.5% NaCl solution was shown in **Figure 6**. The corrosion reactions were identical according to the similarity of all the Tafel curves. As shown in **Figure 6**, the characteristic anode branches were generally sharp formation, which represented the dissolution of α-Mg. The cathodic hydrogen evolution was the main reaction, which determined the reaction rate of the electrochemical corrosion. When the potential was more negative than the pitting potential, the cathodic branch showed up linear Tafel characteristics. Therefore, the corrosion current density of pure Mg and Mg-xY alloys was calculated by the tangent of linear cathode branch. The results of corrosion current density were shown in the table of **Figure 6**. Due to the different resistance of oxides films to the

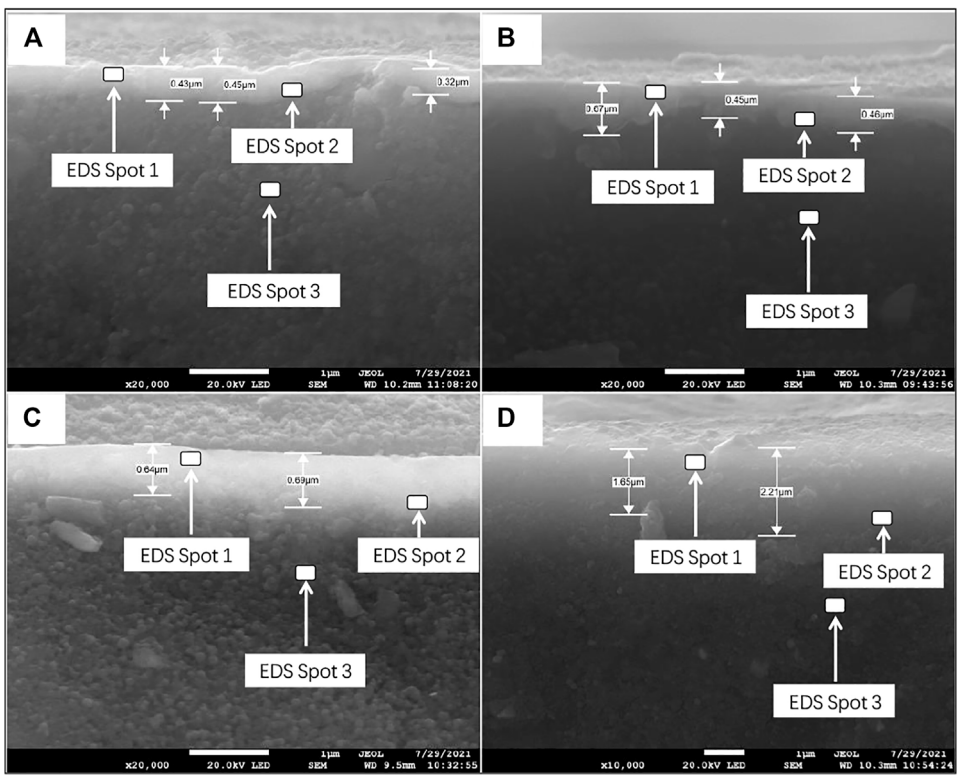

FIGURE 4 | The thicknesses of oxidation films on different samples measured by backscattered electrons: **(A)** pure Mg; **(B)** Mg-3Y; **(C)** Mg-5Y; **(D)** Mg-7Y.

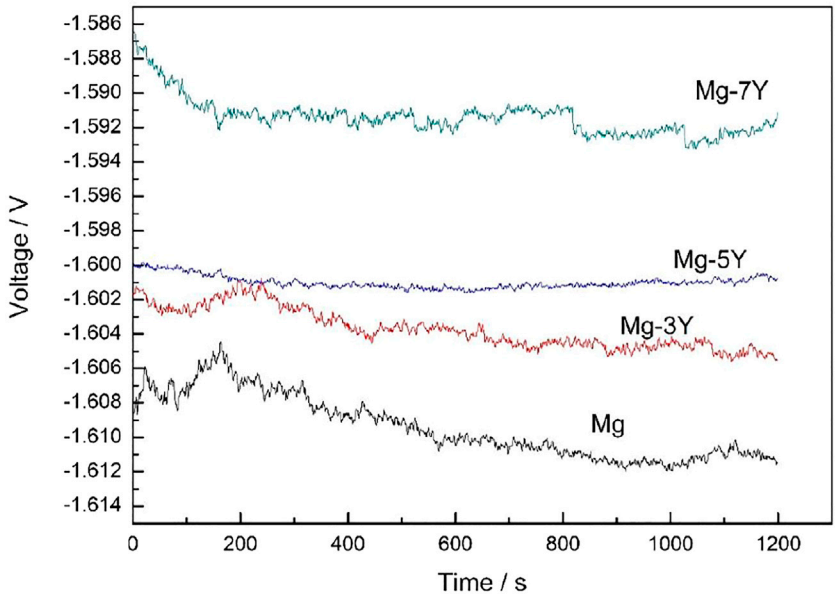

FIGURE 5 | The electrochemical open circuit potential of samples covered with oxidation films in the surface measured in 3.5% NaCl solution.

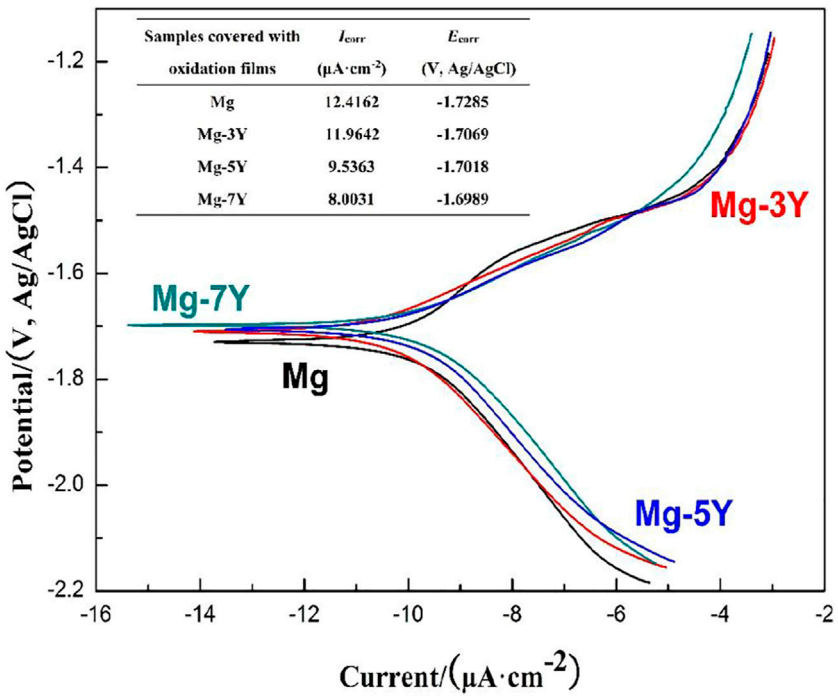

FIGURE 6 | The electrochemical Tafel slopes of samples covered with oxidation films in the surface measured in 3.5% NaCl solution.

corrosion reaction, the pure Mg showed a largest I_{corr}, whereas the Mg-7Y alloy showed the smallest. The results depended on thickness and density of oxides films, which indicated that the oxides films formed in the surface of Mg-7Y alloy showed a best corrosion barrier effect.

The electrochemical impedance spectra curves of pure Mg and Mg-xY alloys covered with oxidation films measured in 3.5% NaCl solution was shown in **Figure 7**. The largest electrochemical impedance spectra of Mg-7Y alloy samples indicated that hydrogen evolution of the α-Mg matrix reaction had the

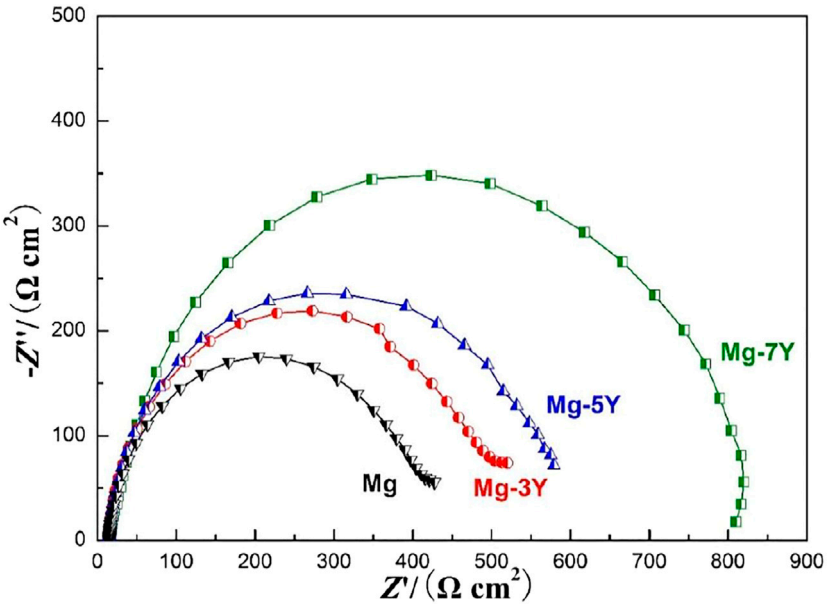

FIGURE 7 | The electrochemical impedance spectra curves of samples covered with oxidation films in the surface measured in 3.5% NaCl solution.

largest energy barrier. According to the results in **Figure 6**, the corrosion resistance can be ranked as follows: pure Mg < Mg-3Y < Mg-5Y < Mg-7Y, which demonstrated that the tendency was consistent with the preceding data in this study. The electrochemical impedance spectra curves of different samples were different, which represented distinctive dynamic corrosion process. The larger of the PBR of oxides films, the stronger of the barrier effect on the ion diffusion of corrosion reaction. Therefore, the alloy with the most Y-content showed the best corrosion resistance.

PBR is the ratio of oxide volume generated from the combination of metal and oxygen on the metal surface to the volume of consumed metal atoms, which reflects the stress condition in the oxide film. The corrosion tendency of magnesium alloy is closely related to the conditions of oxide layer during oxidation. The PBR of Y_2O_3 films generated from $Mg_{24}Y_5$ was about 1.1923, which indicated the Y_2O_3 films were continuous and compact (Okamoto, 1992). Therefore, the content of Y-content increased, the corrosion tendency of Mg-Y alloys decreased. When PBR is less than 1 or more than 2, tensile stress or excessive compressive stress exists in the oxide film, and the film is prone to rupture. The PBR value of MgO/Mg was 0.81, which indicated that the MgO layer had a large internal tensile stress, and the film structure was loose (Lin, et al., 2010; Qin, et al., 2016; Lee, et al., 2017). As a result, the pure Mg had the largest corrosion tendency than Mg-Y alloys.

As shown in **Figure 8**, the oxidation mechanism of pure Mg and Mg-Y alloys in this study. With the increasing of Y-content, the amount and volume fraction of precipitated phases on grain boundary of Mg-Y binary alloys became larger before heat treatment. After the heat treatment, pure Mg reacted with O atom to form a loose porous oxide film in **Figure 7A**. For Mg-Y binary alloys, the Y atom bonded to the O atom preferentially, and then the Mg atom bonded to the O atom at the high temperatures. The Y_2O_3 and MgO products formed in the surface of different Mg-Y binary alloys. With the increasing of Y-content, the ratio of Y_2O_3 formed in the oxides became larger. Moreover, the volume and dimensions of Y_2O_3 also showed a large improvement. As the oxidation reaction processed, the equilibrium state of the interface between the alloy and the oxidation environment changed (You, et al., 2014). At the initial stage of oxidation, the equilibrium state of the alloy interface was alloy-oxidation environment. With the formation of oxidation films, the equilibrium state of the interface changed to alloy/oxidation products/oxidation environment. During the oxidation reaction, the PBR value of MgO products was only about 0.8, which could not protect the α-Mg matrix from the further corrosion reaction effectively. However, the PBR value of Y_2O_3 was larger than 1, which improved the overall density of mixed oxide in the surface to a certain extent. Therefore, the protective effect of mixed oxide on the matrix was improved. This phenomenon indicated that the more of Y-content, the stronger the protective effect of oxide film on the α-Mg matrix.

On the other hand, precipitated phases in the magnesium alloys often act as the cathode of microelectrochemical coupling reaction, accelerating the corrosion of α-Mg matrix. With the alloying element increased gradually, more and more Y-content reacted with α-Mg matrix, the number of precipitated phases also increased tremendously. However, In the heating process, the precipitated phases containing rare earths were easier to oxidize than the magnesium matrix. And then the Y_2O_3 formed have a better protection effect on the α-Mg matrix. The more precipitated phases contained rare earth were, the more Y_2O_3 is oxidized, which resulted a improvement to the corrosion resistance of α-Mg matrix.

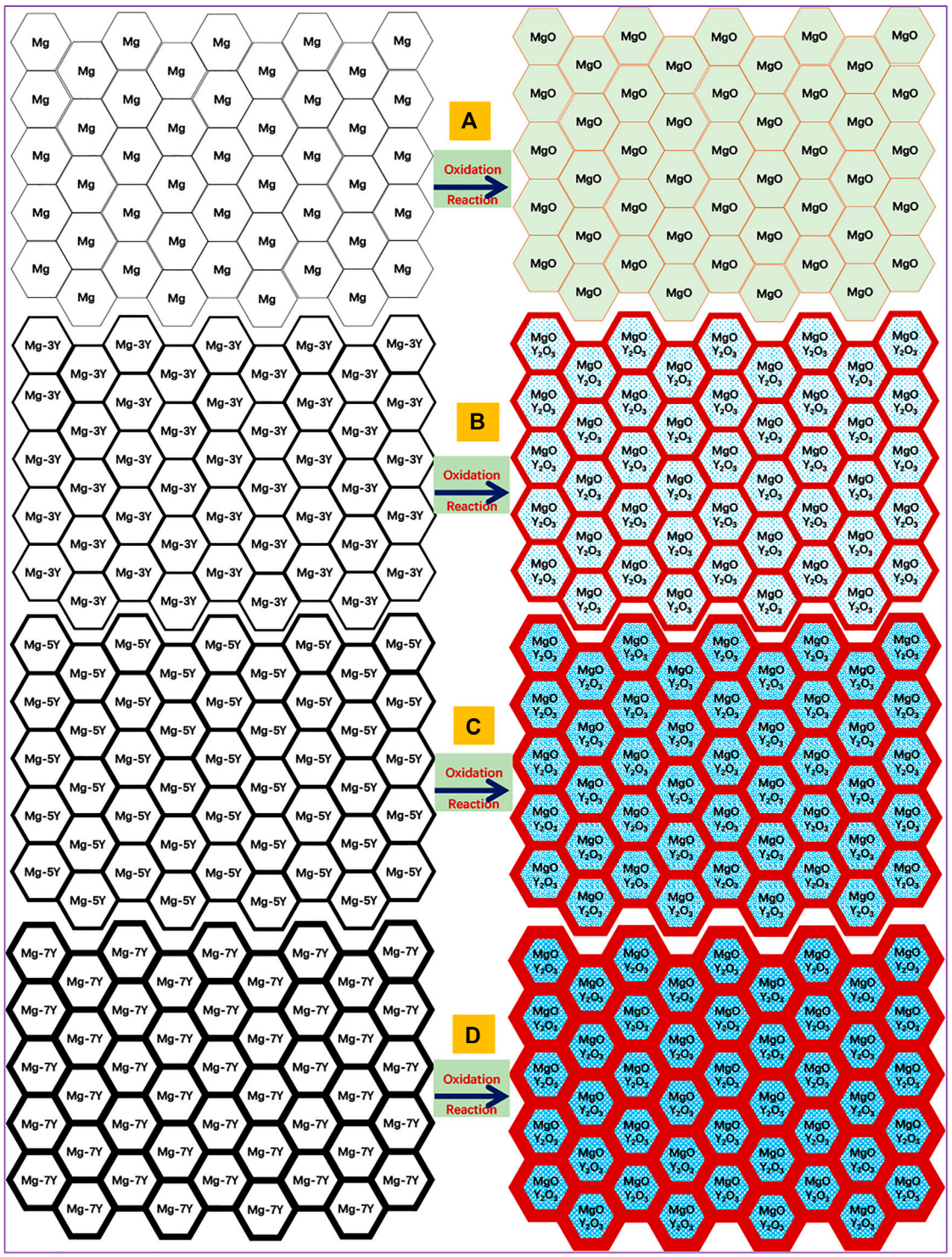

FIGURE 8 | The oxidation mechanism of pure Mg and Mg-Y alloys in this study.

In fact, different types of precipitated phases may exist in the same magnesium alloy. Moreover, one alloying element also may form different kinds of precipitated phases in the magnesium alloys with the changes of the alloying element content. In this work, the PBR values of the oxide film formed from the common precipitated phases in magnesium alloys were calculated. In the actual oxidation process of magnesium alloys, it is possible that multiple oxidation reactions occur simultaneously. This research

is expected to provide guidance in the development of heat-resistant magnesium alloys by adjusting the types of alloying elements and film formation from the precipitated phases.

CONCLUSION

1) The PBR values of preferentially oxides formed from $Mg_{12}Nd$ and $Mg_{24}Y_5$ were 1.0584 and 1.1923, respectively, which indicated a good protection for the Mg matrix. The PBR values of preferentially oxides formed from Mg_3Gd and $MgNi_2$ were larger than 2, which existed a compressive stress. The PBR values of preferentially oxides formed from $Mg_{17}Al_{12}$, $MgZn_2$, $MgCu_2$, Mg_2Ca, $Mg_{12}Ce$, and MgAg were less than 1, which existed a tensile stress. Both compressive stress and tensile stress would lead the fracture of oxides. These PBR values of oxides indicated a poor protection of Mg matrix.
2) The oxide films formed on the surfaces of Mg-xY (x = 3, 5, 7 wt.%) samples were consisted of Y_2O_3 and MgO. The formation of Y_2O_3 was caused by the oxidation of $Mg_{24}Y_5$. The PBR values of preferentially oxides formed from $Mg_{24}Y_5$ was 1.1923, and then increased the PBR of MgO formed from Mg matrix to a certain extent. The electrochemical experiments proved that the corrosion resistance of Mg-Y alloys improved with the increasing of Y-content.
3) In the actual oxidation process, multiple oxidation reactions will occur simultaneously. The composition of oxide films on the surface of magnesium alloys are complex. This work is expected to give a scientific and reasonable method to improve intrinsic corrosion resistance of magnesium alloys by regulating the types of precipitates.

DATA AVAILABILITY STATEMENT

The original contributions presented in the study are included in the article/Supplementary Material, further inquiries can be directed to the corresponding author.

AUTHOR CONTRIBUTIONS

QJ and DL conceived and designed the study and experiment plan. CL performed the experiments. NL analyzed the energy dispersive spectrum datas. BH verified the experimental results. QJ wrote the paper. DL, CL, NL, and BH reviewed and edited the manuscript. All authors read and approved the manuscript.

FUNDING

The present work was supported by National Natural Science Foundation of China for Exploring Key Scientific Instrument (No.41827805) and the Open Funds of the State Key Laboratory of Rare Earth Resource Utilization (No. RERU2021017) for providing support.

ACKNOWLEDGMENTS

The authors gratefully acknowledge professor Kui Zhang of State Key Laboratory for Fabrication and Processing of Nonferrous Metals.

REFERENCES

Bradford, S. A. (1993). *Oxidation: Metal-Gas Reactions, Corrosion Control*. Boston, MA, US: Springer, 289–312. doi:10.1007/978-1-4684-8845-6_14

Chang, C. L., Lu, S., Fu, Y. Y., and Zhang, H. P. (2015). Flammability and the Oxidation Kinetics of the Magnesium Alloys AZ31, WE43, and ZE10. *Corrosion Sci.* 100, 177–185. doi:10.1016/j.corsci.2015.07.020

Cheng, S. L., Yang, G. C., Fan, J. F., Li, Y. J., and Zhou, Y. H. (2009). Effect of Ca and Y Additions on Oxidation Behavior of AZ91 alloy at Elevated Temperatures. *Trans. Nonferrous Met. Soc. China* 19, 299–304. doi:10.1016/S1003-6326(08)60268-X

Czerwinski, F. (2002). The Oxidation Behaviour of an AZ91D Magnesium alloy at High Temperatures. *Acta Mater.* 50, 2639–2654. doi:10.1016/S1359-6454(02)00094-0

Czerwinski, F. (2012). Oxidation Characteristics of Magnesium Alloys. *JOM* 64 (12), 1477–1483. doi:10.1007/s11837-012-0477-z

Czerwinski, F. (2015). The Reactive Element Effect on High-Temperature Oxidation of Magnesium. *Int. Mater. Rev.* 60 (5), 264–296. doi:10.1179/1743280415Y.0000000001

Fan, J. F., Yang, C. L., Han, G., Fang, S., Yang, W. D., and Xu, B. S. (2011). Oxidation Behavior of Ignition-Proof Magnesium Alloys with Rare Earth Addition. *J. Alloys Comp.* 509 (5), 2137–2142. doi:10.1016/j.jallcom.2010.10.168

James, G. S. (2005). *Lange's Handbook of Chemistry*. New York, NY MCGRAW-HILL, 1.238–1.279.

Jiang, Q. T., Lu, D. Z., Wang, N., Wang, X. T., Zhang, J., Duan, J. Z., et al. (2021). The Corrosion Behavior of Mg-Nd Binary Alloys in the Harsh marine Environment. *J. Magnesium Alloys* 9 (1), 292–304. doi:10.1016/j.jma.2019.12.010

Kaya, A. A. (2020). Review on Developments in Magnesium Alloys. *Front. Mater.* 7, 198. doi:10.3389/fmats.2020.00198

Lee, D. B., Abro, M. A., and You, B. S. (2017). High-temperature Oxidation of AZ91-0.3%Ca-0.1%Y alloy in Air. *Met. Mater. Int.* 23 (4), 720–725. doi:10.1007/s12540-017-6745-2

Lin, P. Y., Zhou, H., Sun, N., Li, W. P., Wang, C. T., Wang, M. X., et al. (2010). Influence of Cerium Addition on the Resistance to Oxidation of AM50 alloy Prepared by Rapid Solidification. *Corrosion Sci.* 52, 416–421. doi:10.1016/j.corsci.2009.09.029

Liu, J., Li, Y., and Wang, F. (2009). The High Temperature Oxidation Behavior of Mg-Gd-Y-Zr alloy. *Oxid Met.* 71, 319–334. doi:10.1007/s11085-009-9145-2

López, M. D., Múnez, C. J., Carboneras, M., Rodrigo, P., Escalera, M. D., and Otero, E. (2010). Influence of Temperature on Oxidation Behaviour of ZE41 Magnesium alloy. *J. Alloys Comp.* 491 (1/2), 131–136. doi:10.1016/j.jallcom.2009.10.163

Mebarki, N., Ravi Kumar, N. V., Blandin, J. J., Suery, M., Pelloux, F., and Khelifati, G. (2005). Correlation between Ignition and Oxidation Behaviours of AZ91 Magnesium alloy. *Mater. Sci. Technol.* 21, 1145–1151. doi:10.1179/174328405X58904

Medved, J., Mrvar, P., and Vončina, M. (2009). Oxidation Resistance of Cast Magnesium Alloys. *Oxid Met.* 71 (5/6), 257–270. doi:10.1007/s11085-009-9141-6

Nie, J. F. (2012). Precipitation and Hardening in Magnesium Alloys. *Metall. Mater. Trans. A* 43, 3891–3939. doi:10.1007/s11661-012-1217-2

Okamoto, H. (1992). Mg-Y (Magnesium-Yttrium). *J. Phase Equilib.* 13 (1), 105–106. doi:10.1007/BF02645395

Qin, L., Ding, J., Zhao, W. M., and Fang, Z. (2016). Oxidation Behavior and Surface Tension of Mg-1.2Ca alloy with Ce Addition. *Rare Metal Mater. Eng.* 45 (1), 23–27. doi:10.1016/S1875-5372(16)30039-X

Shi, Z. Z., Chen, H. T., Zhang, K., Dai, F. Z., and Liu, X. F. (2020). Crystallography of Precipitates in Mg Alloys. *J. Magnesium Alloys* 9 (2), 416–431. doi:10.1016/j.jma.2020.06.013

Song, X., Wang, Z. W., and Zeng, R. C. (2021). Magnesium Alloys: Composition, Microstructure and Ignition Resistance. *Chin. J. Nonferrous Met.* 31 (3), 598–622. doi:10.11817/j.ysxb.1004.0609.2021-40013

Sudholz, A. D., Gusieva, K., Chen, X. B., Muddle, B. C., Gibson, M. A., and Birbilis, N. (2011). Electrochemical Behaviour and Corrosion of Mg-Y Alloys. *Corrosion Sci.* 53 (6), 2277–2282. doi:10.1016/j.corsci.2011.03.010

Tan, Q., Atrens, A., Mo, N., and Zhang, M.-X. (2016). Oxidation of Magnesium Alloys at Elevated Temperatures in Air: A Review. *Corrosion Sci.* 112, 734–759. doi:10.1016/j.corsci.2016.06.018

Van Orman, J. A., and Crispin, K. L. (2010). Diffusion in Oxides. *Rev. Mineralogy Geochem.* 72 (1), 757–825. doi:10.2138/rmg.2010.72.17

Wang, X. M., Zeng, X. Q., Wu, G. S., Yao, S. S., and Li, L. B. (2007). Surface Oxidation Behavior of MgNd Alloys. *Appl. Surf. Sci.* 253 (22), 9017–9023. doi:10.1016/j.apsusc.2007.05.023

Wang, X. M., Zeng, X. Q., Zhou, Y., Wu, G. S., Yao, S. S., and Lai, Y. J. (2008). Early Oxidation Behaviors of Mg-Y Alloys at High Temperatures. *J. Alloys Comp.* 460 (1), 368–374. doi:10.1016/j.jallcom.2007.06.065

Wang, X. M., Wu, W. D., Tang, Y. J., Zeng, X. Q., and Yao, S. S. (2009). Early High Temperature Oxidation Behaviors of Mg-10Gd-3Y Alloys. *J. Alloys Comp.* 474 (1/2), 499–504. doi:10.1016/j.jallcom.2008.06.122

Xu, C., and Gao, W. (2000). Pilling-Bedworth Ratio for Oxidation of Alloys. *Mater. Res. Innov.* 3, 231, 235. doi:10.1007/s100190050008

You, B.-S., Park, W.-W., and Chung, I.-S. (2000). The Effect of Calcium Additions on the Oxidation Behavior in Magnesium Alloys. *Scripta Mater.* 42, 1089, 1094. doi:10.1016/S1359-6462(00)00344-4

You, B. S., Kim, Y. M., Yim, C. D., and Ha, S. K. (2014). "Oxidation and Corrosion Behavior of Non-flammable Magnesium Alloys Containing , Ca and Y," in *Magnesium Technology*. Editors M. Alderman, M. V. Manuel, N. Hort, and N. R. Neelameggham (New York, US: John-wiley), 325–329. doi:10.1002/9781118888179.ch62

Yu, X. W., Jiang, B., Yang, H., Yang, Q. S., Xia, X. S., and Pan, F. S. (2015). High Temperature Oxidation Behavior of Mg-Y-Sn, Mg-Y, Mg-Sn Alloys and its Effect on Corrosion Property. *Appl. Surf. Sci.* 353, 1013–1022. doi:10.1016/j.apsusc.2015.07.011

Yu, X., Shen, S., Jiang, B., Jiang, Z. T., Yang, H., and Pan, F. S. (2016). The Effect of the Existing State of Y on High Temperature Oxidation Properties of Magnesium Alloys. *Appl. Surf. Sci.* 370, 357–363. doi:10.1016/j.apsusc.2016.02.156

Yu, X. W., Jiang, B., He, J. J., Liu, B., and Pan, F. S. (2018). Oxidation Resistance of Mg-Y Alloys at Elevated Temperatures and the protection Performance of the Oxide Films. *J. Alloys Comp.* 749, 1054–1062. doi:10.1016/j.jallcom.2018.03.342

Zhao, X. Y., Ning, Z. L., Li, Z. Q., Zou, W. B., Li, B. H., He, K., et al. (2018). In-mold Oxidation Behavior of Mg-4.32Y-2.83Nd-0.41Zr alloy. *J. Mater. Sci.* 53 (15), 11091–11103. doi:10.1007/s10853-018-2271-y

Zhou, N., Zhang, Z. Y., Dong, J., Jin, L., and Ding, W. J. (2013). Selective Oxidation Behavior of an Ignition-Proof Mg-Y-Ca-Ce alloy. *J. Rare Earths* 31 (10), 1003–1008. doi:10.1016/S1002-0721(13)60021-6

Zhu, C. Y., and Chen, B. (2019). Atomic Scale Investigation on Precipitates and Defects of Mg-RE Alloys: a Review. *Adv. Eng. Mater.* 21 (3), 1800734. doi:10.1002/adem.201800734

Conflict of Interest: The authors declare that the research was conducted in the absence of any commercial or financial relationships that could be construed as a potential conflict of interest.

Publisher's Note: All claims expressed in this article are solely those of the authors and do not necessarily represent those of their affiliated organizations, or those of the publisher, the editors and the reviewers. Any product that may be evaluated in this article, or claim that may be made by its manufacturer, is not guaranteed or endorsed by the publisher.

frontiers in Materials

ORIGINAL RESEARCH
published: 18 November 2021
doi: 10.3389/fmats.2021.717663

Corrosion Initiation Behavior of Thermal Control Oxidation Film of LA103Z Alloy

Chen Wen, Jingying Bai, Kuo Zhao, Qingxin Cui, Baocheng Jiao, Xuguang Wang and Ligong Zhang*

Beijing Spacecrafts, China Academy of Space Technology, Beijing, China

The magnesium lithium thermal control oxidation is a commonly used conductive anti-corrosion treatment method for aerospace. The corrosion behaviors of thermal control oxidation films for LA103Z alloys were studied in 3.5% NaCl solution. The corrosion characteristics with different immersion time were characterized by using scanning electron microscopy, energy spectroscopy, and electrochemical methods. The results showed that the corrosion of Mg-Li alloy with chemical oxidation film starts from pitting corrosion, gradually expands in depth in the early stage, forms corrosion holes, and then gradually develops into river-like morphology. In the last stage, the increasing corrosion products slow down the corrosion rate and gradually covers the entire sample surface. The corrosion product mainly consists of MgO, LiF, and $MgCl_2$. Combined with the electrochemical characteristics, the corrosion mechanism was investigated.

Keywords: corrosion, LA103Z, thermal control coating, electrochemical, electrochemical., initiation

OPEN ACCESS

Edited by:
Liang Wu,
Chongqing University, China

Reviewed by:
You Zhang,
Beijing Institute of Petrochemical Technology, China
Zhihui Xie,
China West Normal University, China

****Correspondence:***
Jingying Bai
baijy1213@163.com

Specialty section:
This article was submitted to Structural Materials, a section of the journal Frontiers in Materials

Received: *31 May 2021*
Accepted: *27 August 2021*
Published: *18 November 2021*

Citation:
Wen C, Bai J, Zhao K, Cui Q, Jiao B, Wang X and Zhang L (2021) Corrosion Initiation Behavior of Thermal Control Oxidation Film of LA103Z Alloy. Front. Mater. 8:717663. doi: 10.3389/fmats.2021.717663

INTRODUCTION

As the lightest metallic structural materials (1.30–1.65 g/cm^3), Mg-Li alloys have been widely used in space fields (Wu et al., 2020a; Wu et al., 2020b). In order to satisfy the functional requirements and adapt to the space environment, it needs to take out surface treatment such as plating, oxidation, and coatings for Mg-Li alloys (Xia et al., 2019; Zhang et al., 2019; Liu et al., 2021). However, due to the electrochemical activity of Mg and Li, the alloys have great corrosion risks in the service environment (Prando et al., 2019; Sun et al., 2020). Although there are few corrosive factors in space, the coastal launch site can bring severe corrosion for the products. Oxidation methods can form thermal control coatings, anti-corrosion coatings, coating suitable for bonding, etc., which are suitable for the structure applications of satellites (Shi et al., 2015; Guo et al., 2017; Yang et al., 2018; Qiu et al., 2020).

In order to improve cementing property, it is needed to reduce thickness of the coating; however, the thin coating is useless for preventing corrosion. Many researchers have made efforts to form thin coating with good corrosion resistance (Wang et al., 2007; Chen et al., 2011; Formosa et al., 2012; Fernández et al., 2019). Fernandez et al. (Fernández et al., 2019) found that reduced graphene oxide onto magnesium discs by electrochemical and chemical methods can decrease the corrosion rate. The results obtained by Chen et al. (Chen et al., 2011) indicated that all the conversion coating formed in different solutions exhibits amorphous structure. The formation of Mo on the surface of Mg alloys after chemical oxidation can significantly improve the corrosion resistance (Shao et al., 2017). Xu et al. (Xu et al., 2008) produced oxide film of 2–3 μm by the environment friendly chemical oxidation method. The corrosion resistance rate of the film in 3% NaCl solution was only 1/15 of Mg alloy substrates. Wang et al. (Liu et al., 2016) used black chemical oxidation to form a film, which had uniform blackness and dense film.

TABLE 1 | Chemical composition of LA103Z magnesium-lithium alloy (wt%).

Element	Li	Al	Zn	Si	Fe	Mg
Content/%	10.0	3.2	2.8	0.05	0.05	Bal

In this paper, the thin film of magnesium lithium LA103Z was fabricated by chemical oxidation, and the corrosion behavior was studied by immersion test in 3.5wt% NaCl solution. The morphologies and corrosion products were characterized, combined with the electrochemical analysis of sample with different corrosion time, and the corrosion evolution mechanism was also studied.

EXPERIMENTAL SECTION

Experimental Sample and Procedure

The specimen used for the test is LA103Z magnesium lithium alloy, and the chemical composition is given in **Table 1**. The material was cut into 40 mm × 40 mm×2 mm for experiment. Moreover, the specimens were polished by sandpaper from 400#, 800#, to 1,000#.

Before oxidation, the specimens of LA103Z magnesium lithium alloy were degreased with absolute ethanol and then cleaned by deionized water → activation treatment by fluoride salt with concentration of 2.5 g/L → cleaned by deionized water → dried by compressed air. The chemical oxidation was carried out to obtain a thermal control film.

After oxidation, the specimens were sealed and protected by chloroprene rubber, except for an area of 40 mm × 40 mm for the immersion test. The specimens were soaked in 3.5% NaCl solution at the temperature 45°C with different times (1, 3, 6, 12, 18, 24 h). After immersion with the assumed time, the specimens were cleaned by deionized water and dried by compressed air. Specimens with different immersion time were cut off by cross-section and observed by SEM.

Characterization

After immersion test, the morphologies of the specimens were characterized by metallurgical microscope (MO, Canon E60) and scanning electron microscope (SEM, SUPRA55VPX,Germany). The composition of corrosion products was characterized by x-ray diffraction (XRD, Bruker AXS D8, Cu target, scan rate of 5°/min, scan range of 10°–90°).

The electrochemical evaluation with different immersion time was performed by using IM6 electrochemical equipment in 3.5wt % NaCl solution at room temperature. The experiment employed a three-electrode system, a saturated calomel (SCE) electrode as reference electrode, a Pt electrode as counter electrode, the magnesium lithium alloy chemical oxidation sample as working electrode, and the sample exposure area was 1 cm^2. The open circle potential (OCP) was tested for 600 s. The electrochemical impedance spectroscopy (EIS) was tested with sinusoidal signal disturbance voltage amplitude of 10 mV. The frequency range is 100 kHz–10 mHz. The polarization curve test range is -0.5 V ~ +0.5 V (*vs* OCP), scan rate is 5 mV/s, the range of cyclic voltammetry test voltage is -0.25 V ~ +0.25 V (*vs* OCP), and the scan rate is 5 mV/s.

RESULTS AND DISCUSSION

Corrosion Morphologies

The morphology of the film and its element content are shown in **Figure 1**. The surface of the film contains many micro cracks and holes. The main elements are Mg, O, and Cr.

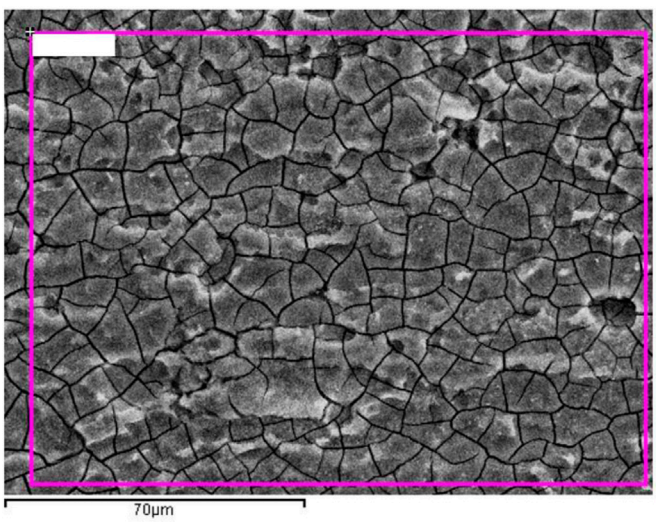

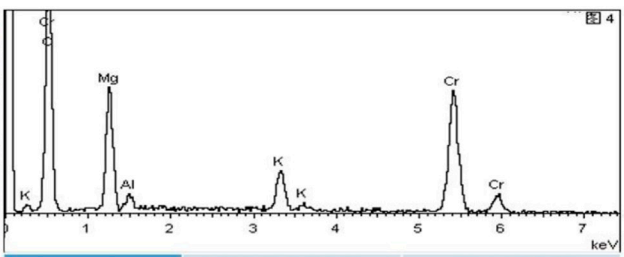

Element	Wight (%)	Atom(%)
O	46.55	67.02
Mg	15.50	14.69
Al	1.88	1.61
K	4.85	2.86
Cr	31.22	13.83

FIGURE 1 | The morphology and element content of the film.

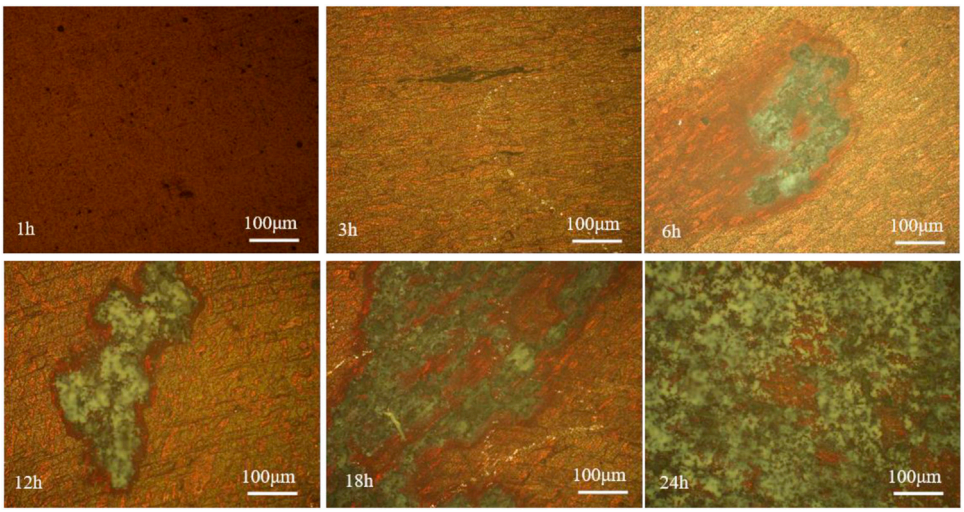

FIGURE 2 | Surface morphologies of the specimens in 3.5% NaCl solution.

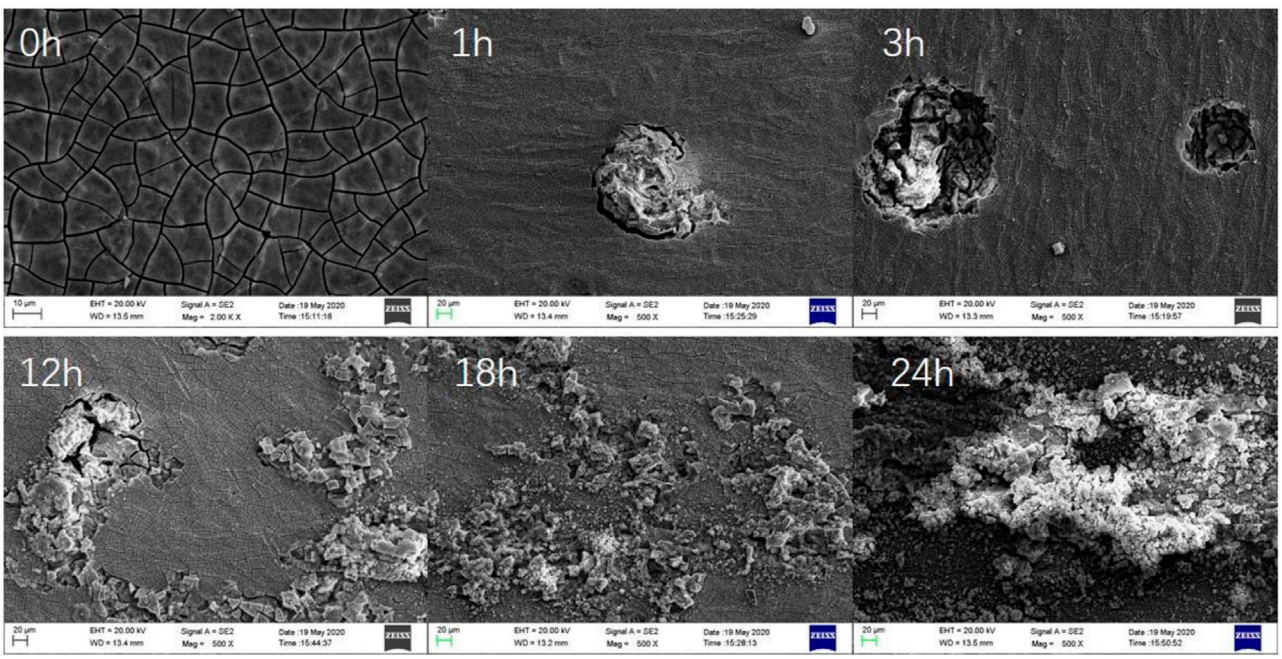

FIGURE 3 | SEM morphologies of the specimens in 3.5% NaCl solution.

The morphologies of the specimens after different immersion time are shown in **Figure 2**. It can be seen that when the specimens are immersed in NaCl solution, the surface forms black pits, which demonstrated that the pitting corrosion happens on the surface for 1 h. As the immersion time increases to 3 h, the surface is impregnated and the pits become dense, some of which develop to line. As the reaction continues, a big gray-green corrosion hole forms and gradually evolves into severe corrosion (6–12 h). The corrosion expands from the corrosion holes, which accelerates the corrosion, until the corrosion products almost cover the whole specimen surface (24 h).

In order to further study the evolution of the corrosion in NaCl solution, the micro morphologies after immersion for different time were characterized by SEM, which are shown in

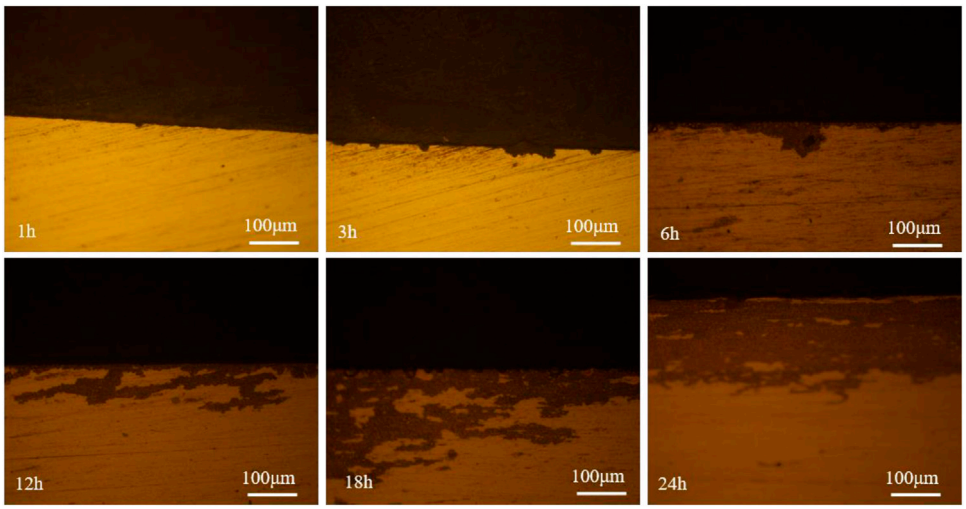

FIGURE 4 | Cross-section morphologies of the specimens in 3.5% NaCl solution.

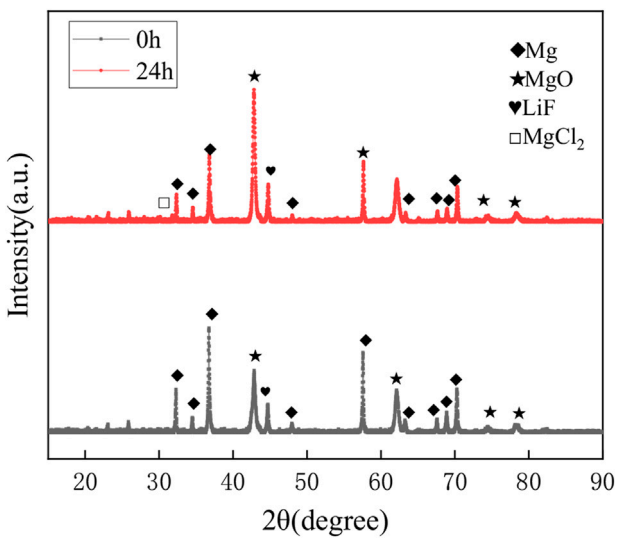

FIGURE 5 | XRD results of the specimens in 3.5% NaCl solution.

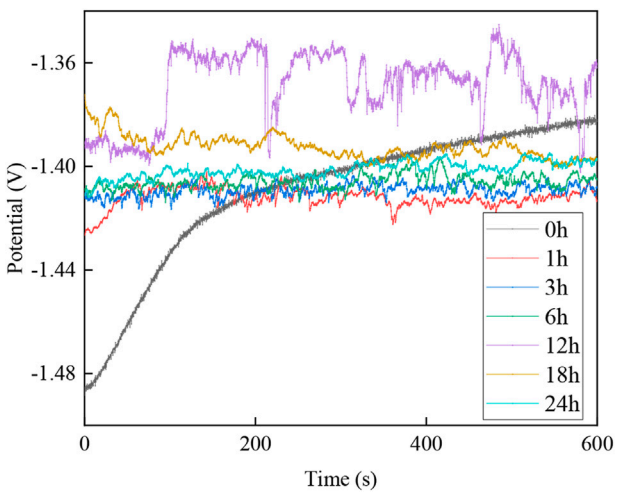

FIGURE 6 | Open circuit potential (OCP) plots of specimens with different immersion time.

Figure 3. After oxidation, the surface film is flat and locally covered with micro cracks. When immersed in the NaCl solution for 1 h, the electro active surface of the sample is dissolved and the corrosion products fall off, which promotes to the formation of pits. As the corrosion develops, the corrosion pit expands along the grain boundary (12 h) and the corrosion products present river-like morphology (12–18 h). As the corrosion exacerbates, fluffy corrosion products cover the surface of the sample.

The cross-section morphologies were characterized and shown in **Figure 4**. It can be seen that in the early stage of immersion (1 h), the corrosion is slight, and sporadic corrosion pits exist on the surface. Once the pit forms, the pits develop rapidly, which connect to form notch

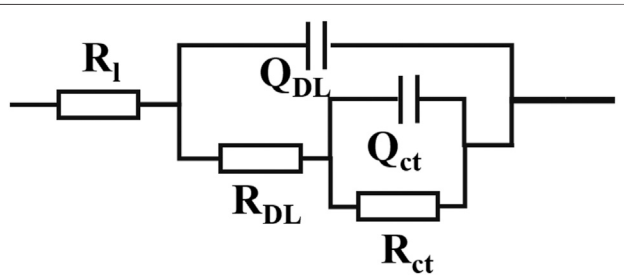

FIGURE 7 | Electrical equivalent circuit model for the EIS results, R (Q (R (QR))) (R_I stands for solution resistance, Q_{DL} and R_{DL} are electric double layer capacitance and resistance respectively, Q_{ct} and R_{ct} are reaction capacitance and resistance respectively; Q is a constant phase angle element).

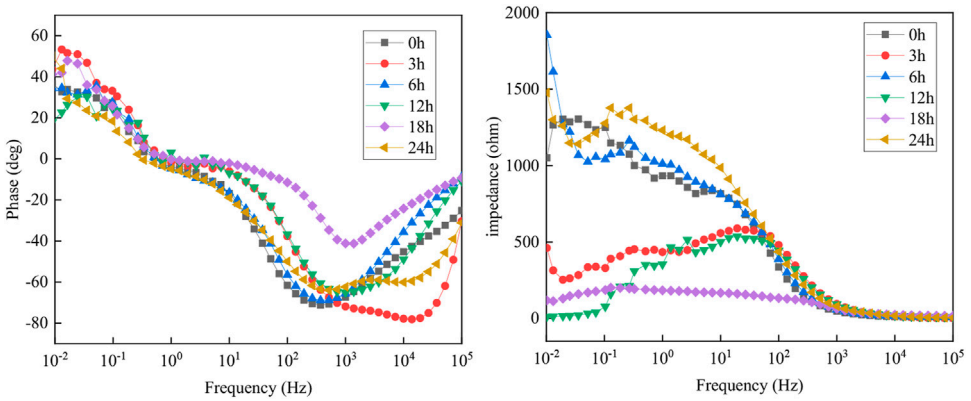

FIGURE 8 | EIS results of specimens after different immersion time.

TABLE 2 | Fitted data by Zsimpwin of EIS results.

Time (h)	R_l (ohm)	Q_{DL}		R_{DL}	Q_{ct}		R_{ct} (ohm)
		Y_{DL} (Ω^{-1} cm^{-2} s^{-n})	n		Y_{DL} (Ω^{-1} cm^{-2} s^{-n})	n	
0	13.02	4.129×10^{-6}	0.8907	947.8	7.660×10^{-6}	0.9453	1,050.5
3	10.72	6.858×10^{-6}	0.9324	664.1	4.393×10^{-6}	1	497.2
6	8.95	8.897×10^{-6}	0.9645	411.1	9.972×10^{-7}	1	475.7
12	15.91	2.608×10^{-6}	0.7756	334.1	7.106×10^{-7}	1	65.8
18	17.85	1.783×10^{-6}	0.7403	186.5	5.322×10^{-7}	1	103.6
24	22.37	1.282×10^{-6}	0.7193	122.6	2.628×10^{-7}	1	1,301.4

morphology. And the corrosion expands to depth direction, promoting the formation of corrosion holes. Based on the corrosion pits, the horizontal expansion of corrosion is obviously better than the vertical expansion, and finally a piece of corrosion morphology is formed, which gradually covers the entire sample surface.

The corrosion products were analyzed by XRD and the results are shown in **Figure 5**. It can be found that the oxidation film is consisted with MgO, LiF, and $MgCl_2$. As the corrosion happens, the diffraction peak intensity of MgO is much higher than that of Mg, which shows the opposite characters for 0 h, and the corrosion products contains $MgCl_2$, which indicates that Chloride ions participate in the reaction and promote the formation of corrosion products.

Electrochemical Results

The OCP results of the specimens after different immersion time are shown in **Figure 6**. After immersion, the potential of the sample quickly becomes positive and gradually stabilizes. With the immersion time increase, the open circuit potential becomes positive until 12 h and then gradually negative. It indicated that at the early stage (before 12 h), the corrosion product attaches to the surface and prevents the corrosion from developing, but as the immersion time goes on, the corrosion products become loose and blade off from the surface.

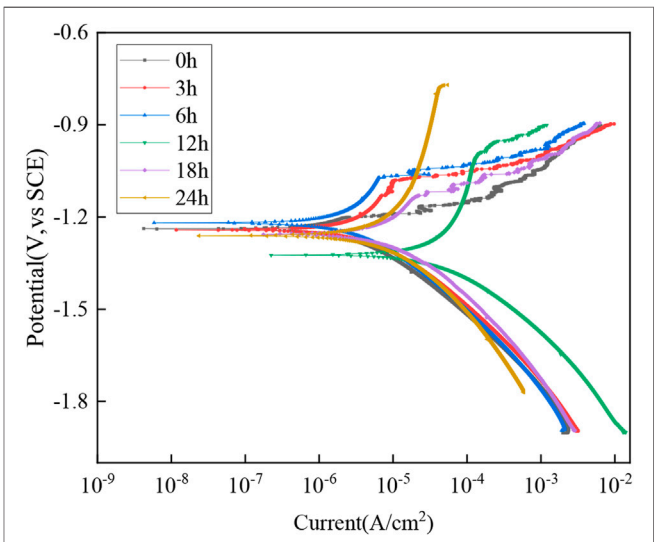

FIGURE 9 | The polarization curves of the specimens with different immersion time.

The structure of the electrochemical model of the specimens was characterized by EIS, and the fitting results for different immersion time of all specimens according to the electrical

TABLE 3 | The fitting calculation results for linear polarization zone of polarization curves.

Time (h)	E_{corr} (V)	I_{corr} (A/cm^2)	b_a (mV dec^{-1})	b_c (mV dec^{-1})
0	−1.255	2.435×10^{-6}	168.9	−132.1
3	−1.250	8.747×10^{-6}	67.5	−125.7
6	−1.232	9.238×10^{-6}	67.2	−124.5
12	−1.318	5.861×10^{-4}	38.6	−113.2
18	−1.247	1.103×10^{-5}	69.2	−111.7
24	−1.286	1.165×10^{-5}	75.3	−110.3

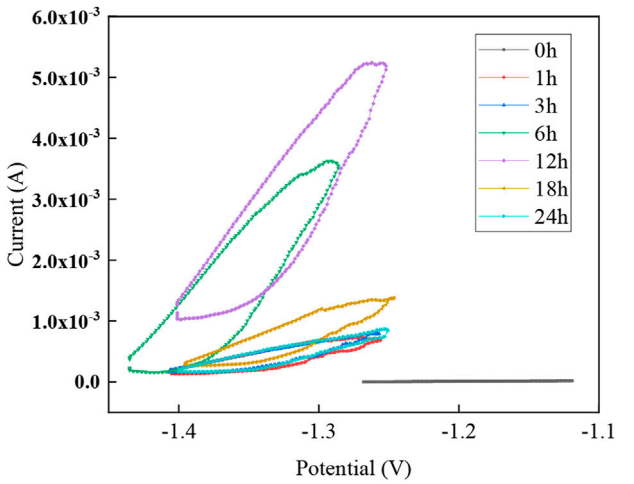

FIGURE 10 | The cyclic voltammetry curves after different immersion time.

equivalent circuit model in **Figure 7** are shown in **Figure 8** and **Table 2**, respectively. From the Q_{ct} results can be seen that the capacitance value decreases from $7.660 \times 10^{-6}\ \Omega^{-1}\ cm^{-2}\ s^{-n}$ to $7.660 \times 10^{-6}\ \Omega^{-1}\ cm^{-2}\ s^{-n}$ as the immersion time increases from 0 to 24 h, which demonstrated that the resistance of corrosion product layer is reduced. However, although the reaction resistance is lower than that without immersion, as the immersion time increases from 1 h to 12 h, the reaction resistance decreases from 1,050.5 Ω to 65.8 Ω, indicating that the corrosion resistance of the sample decreases. From 12 to 24 h, the reaction resistance increases from 65.8 to 1,301.4 Ω. Combined with the morphologies, the corrosion happens when the specimens immersing in the NaCl solution and mainly forms pits and holes before 12 h, and then the corrosion products formed on the surface for 12–24 h, which has a certain blocking effect in the film layer, and the corrosion rate decreases.

The polarization plots after different immersion time are shown in **Figure 9**. The self-corrosion potential and self-corrosion current obtained by the linear fitting for polarization zone are given in **Table 3**. Compared with the non-immersed sample, the immersed sample has a smaller corrosion current and higher corrosion resistance, which indicates that the immersion reduced the corrosion resistance of the film. The self-corrosion potential shows the same trend with the open circuit potential. From the self-corrosion, current data show that the current increases from 2.435×10^{-6} A/cm^2 to 5.861×10^{-4}A/cm^2 before 12 h, which indicates that the corrosion reaction is exacerbated, consistent with the reaction resistance. However, as the corrosion products cover the reaction area (anodic zone), which prevents the corrosion, the anodic resistance (b_a) of the specimen increases after 12 h. However, the cathode area is still exposed to the solution and the continuous reaction leads to a decrease in cathode reaction resistance (b_c) from 132.1 mV dec^{-1} to 110.3 mV dec^{-1} with the increasing time from 0 to 24 h.

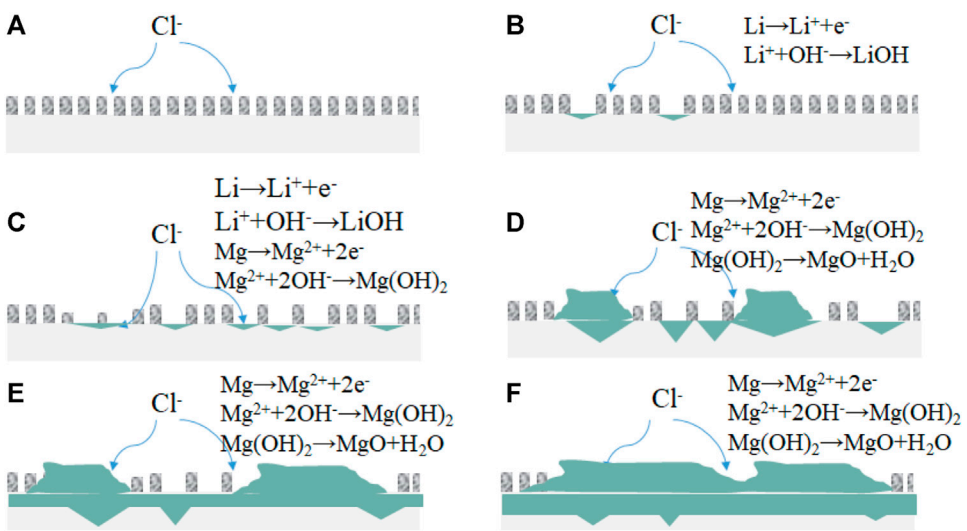

FIGURE 11 | The reaction model of the corrosion initiation and expansion for different immersion time **(A)**: 0 h, **(B)**: 1–3 h; **(C)**: 3–6 h; **(D)**: 6–12 h; **(E)**: 12–18 h; **(F)**: 18–24 h).

The cyclic voltammetry curves after different immersion time are shown in **Figure 10**. It can be seen that the current response to voltage change of the specimens without immersion is the smallest and basically presents a reversible process, which indicates that the sample has good corrosion resistance. The corrosion processes are shown in **Figure 11**. As the reaction time increases from 0 to 12 h, the current response is more obvious and the degree of reversibility gets lower and lower, which demonstrates that the electrochemical reaction is more and more violent. But the irreversible process of the reaction weakens from 12 to 24 h, which is caused by the corrosion products.

Discussion

From the corrosion morphologies, composition of the corrosion products, and the electrochemical results, the process of corrosion initiation and development is given as **Figure 10**. The corrosion process can be concluded into the following processes.

The initial stage of corrosion initiation (a-b) is mainly the formation of pits due to the electrochemical solution of Li, as it is the most electrochemically active element. When the immersion continues, the element Mg happens in corrosion, and Li reacts further and dissolves off, which leads to the pits expanding to corrosion holes (b-c), and corrosion rate increasing as the corrosion products accumulate on the surface of the specimen (c-d), the micro-electro-battery and dissolution effect are more obvious, and the corrosion is further intensified, and corrosion develops mainly towards horizontal (d-e). However, after the corrosion products cover most of the surface, the micro-battery effect reduces, and the horizontal reaction slows down. And the corrosion products on the surface changes from $Mg(OH)_2$ to MgO, which is more loose than $Mg(OH)_2$, leading to depth corrosion acceleration. The wedge effect of corrosion products leads to thickening of corrosion products.

CONCLUSION

1) The corrosion of Mg-Li alloy with chemical oxidation film starts from pitting corrosion, gradually expands in depth in the early stage, forms corrosion holes, and then gradually develops into river-like morphology. In the last stage, the increasing corrosion products slow down the corrosion rate and gradually cover the entire sample surface.
2) The corrosion product is mainly consisted with MgO, LiF, and $MgCl_2$.
3) The initial stage of corrosion initiation is mainly the formation of pits due to the electrochemical solution of Li. When the immersion continues, the element Mg happens as corrosion, and Li reacts further and dissolves off, leading to the pits expanding to corrosion holes. As the corrosion products accumulate on the surface of the specimen, the micro-electro-battery and dissolution effect are more obvious, and the corrosion is further intensified, and corrosion develops mainly towards horizontal.

DATA AVAILABILITY STATEMENT

The raw data supporting the conclusions of this article will be made available by the authors, without undue reservation.

AUTHOR CONTRIBUTIONS

All authors listed have made a substantial, direct, and intellectual contribution to the work and approved it for publication.

REFERENCES

Chen, D. C., Wu, J. F., Liang, Y. Q., Ye, S. L., and Li, W. F. (2011). Preparation and Elements Analysis of Porous Fluorescent Glasses. *Trans. Nonferrous Met. Soc. China.* 21, 1905–1910. doi:10.1016/s1003-6326(11)60948-5

Fernández, J., El Ouardi, Y., Bonastre, J., Molina, J. M., and Cases, F. (2019). Modification of the Magnesium Corrosion Rate in Physiological saline 0.9 Wt % NaCl via Chemical and Electrochemical Coating of Reduced Graphene Oxide. *Corros. Sci.* 152, 75–81. doi:10.1016/j.corsci.2019.01.025

Formosa, J., Chimenos, J. M., Lacasta, A. M., and Niubo, M. (2012). Interaction between Low-Grade Magnesium Oxide and Boric Acid in Chemically Bonded Phosphate Ceramics Formulation. *Ceram. Int.* 38, 2483–2493. doi:10.1016/j.ceramint.2011.11.017

Guo, L., Zhang, F., Song, L., Zeng, R.-C., Li, S.-Q., and Han, E.-H. (2017). Corrosion Resistance of Ceria/polymethyltrimethoxysilane Modified Magnesium Hydroxide Coating on AZ31 Magnesium alloy. *Surf. Coat. Tech.* 328, 121–133. doi:10.1016/j.surfcoat.2017.08.039

Liu, R., Liu, Z. H., Wang, F., Jia, Y. F., Ding, Y. D., Ban, G. D., et al. (2016). Development of Corrosion Surface Modification Technology for Magnesium Alloys. *Mater. Protect.* 45 (4), 124–133. doi:10.16490/j.cnki.issn.1001-3660.2016.04.021

Liu, S., Qi, Y., Peng, Z., and Liang, J. (2021). A Chemical-free Sealing Method for Micro-arc Oxidation Coatings on AZ31 Mg alloy. *Surf. Coat. Tech.* 406, 126655–126665. doi:10.1016/j.surfcoat.2020.126655

Prando, D., Nicolis, D., Bolzoni, F., Pedeferri, M., and Ormellese, M. (2019). Chemical Oxidation as Repairing Technique to Restore Corrosion Resistance on Damaged Anodized Titanium. *Surf. Coat. Tech.* 364, 225–230. doi:10.1016/j.surfcoat.2019.03.005

Qiu, Z.-m., Zeng, R.-c., Zhang, F., Song, L., and Li, S.-q. (2020). Corrosion Resistance of Mg–Al LDH/Mg(OH)2/silane–Ce Hybrid Coating on Magnesium alloy AZ31. *Trans. Nonferrous Met. Soc. China* 30, 2967–2979. doi:10.1016/s1003-6326(20)65435-8

Shao, Z., Zhang, F., and Zhang, Q. (2017). Preparation of Grayish Black Film on Am50 Magnesium Alloy by Chemical Conversion–Micro-Arc Oxidation. *Surf. Rev. Lett.* 24 (1), 1750012–1750019. doi:10.1142/s0218625x17500123

Shi, P., Niu, B., and Li, Q. (2015). Preparation and Characterization of PLA Coating and PLA/MAO Composite Coatings on AZ31 Magnesium alloy for Improvement of Corrosion Resistance. *Surf. Coat. Tech.* 262, 26–32. doi:10.1016/j.surfcoat.2014.11.069

Sun, Y., Wang, R., Peng, C., and Cai, Z. (2020). Microstructure and Corrosion Behavior of As-Extruded Mg-xLi-3Al-2Zn-0.2Zr Alloys (X = 5, 8, 11 wt.%). *Corrosion Sci.* 167, 108487–108501. doi:10.1016/j.corsci.2020.108487

Wang, W., Qiao, X. L., Chen, J. G., and Li, H. J. (2007). Facile Synthesis of Magnesium Oxide Nanoplates via Chemical Precipitation. *Mater. Lett.* 61, 3218–3220. doi:10.1016/j.matlet.2006.11.071

Wu, G., Zhao, D., Lin, X., Liu, J., and Ji, X. (2020). Investigation of an Environmentally Friendly Coloring Coating for Magnesium-Lithium alloy Micro-arc Oxidation. *Surf. Inter.* 20, 100513–100518. doi:10.1016/j.surfin.2020.100513

Wu, G., Zhao, D., and Sun, L. (2020). Microstructure and Mechanical Properties of Wire-Filled Tungsten Argon Arc Welded Joints for LA141 Magnesium-Lithium-Aluminum alloy. *Mater. Today Commun.* 23, 100881–100886. doi:10.1016/j.mtcomm.2019.100881

Xia, Q., Zhang, D., Li, D., Jiang, Z., and Yao, Z. (2019). Preparation of the Plasma Electrolytic Oxidation Coating on Mg Li alloy and its thermal Control Performance. *Surf. Coat. Tech.* 369, 252–256. doi:10.1016/j.surfcoat.2019.04.073

Xu, H., Wang, Q., and Zhang, Z. (2008). *Mater. Prot.* 41 (9), 20–23.

Yang, W., Xu, D., Wang, J., Yao, X., and Chen, J. (2018). Microstructure and Corrosion Resistance of Micro Arc Oxidation Plus Electrostatic Powder Spraying Composite Coating on Magnesium alloy. *Corrosion Sci.* 136, 174–179. doi:10.1016/j.corsci.2018.03.004

Zhang, Y., Chen, F., Zhang, Y., Liu, Z., Wang, X., and Du, C. (2019). Influence of Graphene Oxide on the Antiwear and Antifriction Performance of MAO Coating Fabricated on Mg Li alloy. *Surf. Coat. Tech.* 364, 144–156. doi:10.1016/j.surfcoat.2019.01.103

Conflict of Interest: The authors declare that the research was conducted in the absence of any commercial or financial relationships that could be construed as a potential conflict of interest.

frontiers in Materials

ORIGINAL RESEARCH
published: 23 December 2021
doi: 10.3389/fmats.2021.743112

Facile Fabrication and Properties of Super-hydrophobic MgAl-LDH Films With Excellent Corrosion Resistance on AZ31 Magnesium Alloy

Xing Han[1], Jia Hu[1,2], Yong-Qin Wang[1], Tian-Bing Xiao[3]*, Wei Xia[3]*, Yan-Ning Chen[1] and Liang Wu[1,2]*

[1]College of Materials Science and Engineering, Chongqing University, Chongqing, China, [2]National Engineering Research Center for Magnesium Alloys, Chongqing University, Chongqing, China, [3]People's Hospital of FengJie, Chongqing, China

OPEN ACCESS

Edited by:
Yong A. Zhang,
University of Science and Technology Beijing, China

Reviewed by:
Sheng Lu,
Jiangsu University of Science and Technology, China
Pavlo Maruschak,
Ternopil Ivan Pului National Technical University, Ukraine
Songqin Xia,
North China Electric Power University, China

***Correspondence:**
Jia Hu
hujia827@cqu.edu.cn
Tian-Bing Xiao
70441840@qq.com
Wei Xia
690065056@qq.com

Specialty section:
This article was submitted to Structural Materials, a section of the journal Frontiers in Materials

Received: 17 July 2021
Accepted: 22 November 2021
Published: 23 December 2021

Citation:
Han X, Hu J, Wang Y-Q, Xiao T-B, Xia W, Chen Y-N and Wu L (2021) Facile Fabrication and Properties of Super-hydrophobic MgAl-LDH Films With Excellent Corrosion Resistance on AZ31 Magnesium Alloy. Front. Mater. 8:743112. doi: 10.3389/fmats.2021.743112

A super-hydrophobic anti-corrosion film was facilely prepared *via in situ* growth of layered double hydroxides (LDHs) on the etched AZ31 magnesium alloy and then modification by 1H, 1H, 2H, 2H-perfluorooctyltrimethoxysilane (PFOTMS) in this work. The morphology, structure, composition, surface roughness and water contact angles (WCA), and the anti-corrosion performance of the samples were investigated. The results revealed that the micro/nano hierarchical surface morphology of the films was composed of island structures obtained after chemical etching and MgAl-LDH nanowalls grown *in situ*. The best hydrophobicity (CA = 163°) was obtained on the MgAl-LDHs with the maximum surface roughness. Additionally, the potentiodynamic polarization, electrochemical impedance spectroscopy, and immersion test indicated that the super-hydrophobic LDH films provided better corrosion resistance to AZ31 magnesium alloy due to the double-protection derived from the LDHs and super-hydrophobic properties. Furthermore, the contact angle could be kept at above 140° after dipped in 3.5 wt% NaCl solution for 6 days.

Keywords: LDH films, super-hydrophobic, corrosion protection, magnesium alloys, properties

1 INTRODUCTION

Magnesium alloys have been applied in automotive, aerospace fields, and military equipment on a large scale because of low density, high thermal conductivity, good electromagnetic shielding, and easy recyclability (Xie et al., 2018; Yao et al., 2020; Yang et al., 2021). However, magnesium alloys are vulnerable to aggressive media due to their high chemical activity (Song et al., 2021), which severely restricts the potential application of magnesium alloys. So, a variety of surface-modification methods to enhance their corrosion resistance have been proposed in recent decades, such as micro-arc oxidation (Xu et al., 2021), friction stir processing, laser surface modification, physical vapor deposition, (Zhang et al., 2020), and so on. However, it has been reported that these above methods not only needed to use expensive equipment, but also the formed coatings showed a porous structure. Moreover, this coatings prepared *via* the above methods only can provide a passive physical barrier function (Bocchetta et al., 2021), which cannot significantly improve the corrosion resistance. Currently, an active anticorrosion layered double hydroxides (LDHs) films, which can store corrosion inhibitor, have attracted extensive attention due to that corrosion inhibitors can spread to the metal surface around the defect and react with the

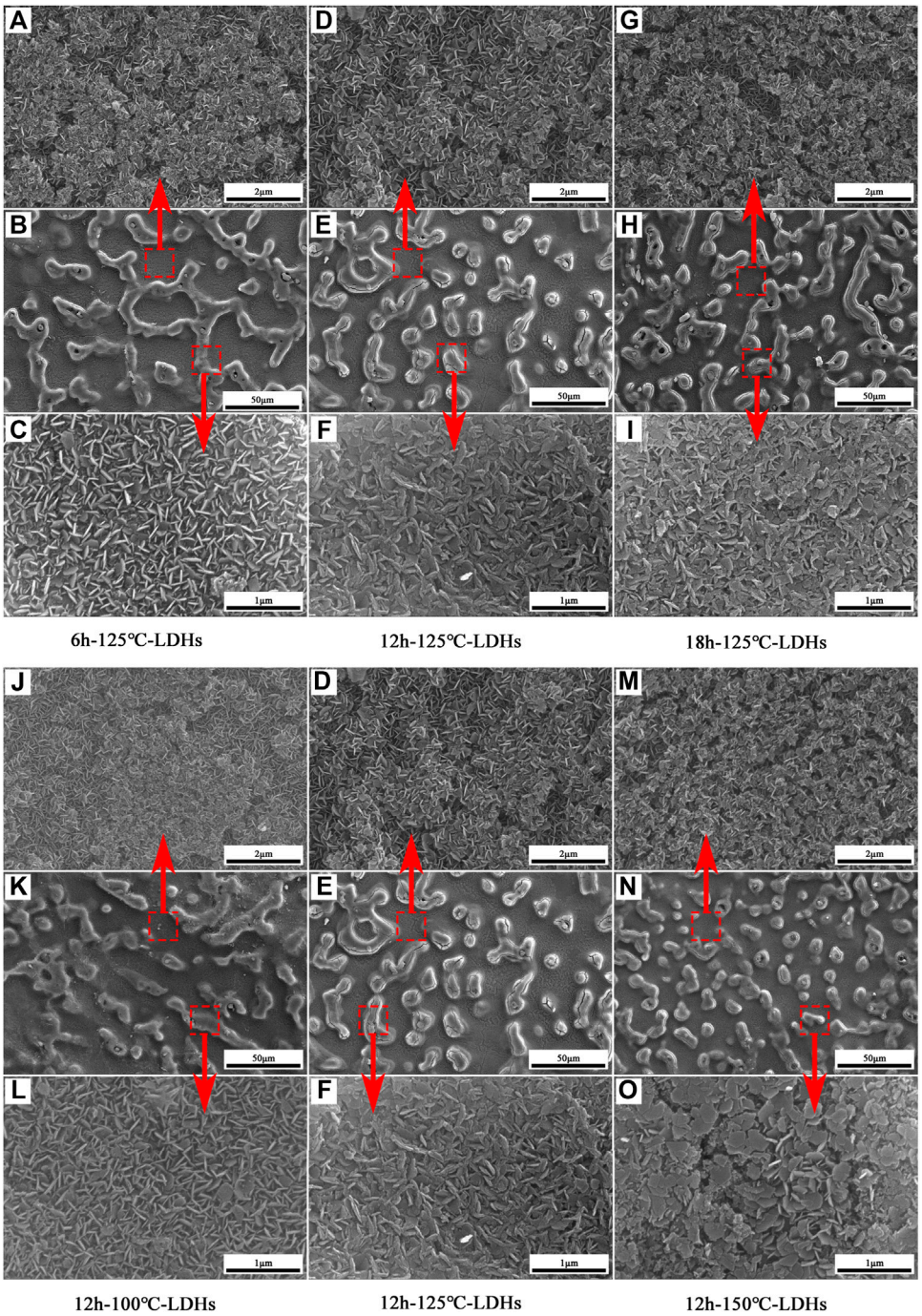

FIGURE 1 | SEM images of different specimens: **(A,B,C)** 6h-125°C-LDHs, **(D,E,F)** 12h-125°C-LDHs, **(G,H,I)** 18h-125°C-LDHs, **(J,K,L)** 12h-100°C-LDHs, and **(M,N,O)**12 h-150°C-LDHs.

substrate to form the stable precipitations on the defect, aiming to heal films in time (Zhang et al., 2018). LDH film loaded with corrosion inhibitors can provide both passive physical barrier function and active corrosion resistance to the magnesium alloy, because the film itself acts as a strong physical barrier and LDHs possess the anion-exchange capacity.

LDHs, known as hydrotalcite-like compounds, is a class of nanocarrier loaded with corrosion inhibitor. The unique hierarchical structure of LDHs endows it with anion-exchange capability (Chen J. et al., 2021; Wu et al., 2021). Hence, an active protective LDH film grown *in situ* on the surface of the metal substrate can present significant advantages. The LDH films require neither the complicated molecular design nor the

sophisticated preparation process. Furthermore, the LDH films can capture aggressive anions and release corrosion inhibitors based on the ion exchange performance (Chen et al., 2020), and the continuous LDH films itself also can provide a firm physical barrier for magnesium alloys, effectively preventing the corrosive medium from invading into the substrate (Cao et al., 2018). However, anionic inhibitors loaded in LDHs will rapidly release when exposing to external high concentration solution environment or immersing corrosion solution for a long time, directly leading to a severe decline in corrosion resistance of the LDH films. Generally speaking, the LDH films grown on metal substrate display non-closed structure. Furthermore, the LDH structure can provide not only the accommodation for corrosion mediums but also the channel for corrosion mediums passing through to the substrate (Chen et al., 2013). Thereby, the corrosion protection of single LDH film for metal substrate is limited. Inspired by outstanding water-repellency and self-cleaning ability of these natural super-hydrophobic surface (Xie et al., 2018), researchers have successfully designed and fabricated artificial super-hydrophobic surface on metallic substrate. The non-wetting performance of super-hydrophobic surface can effectively prevent the attachment of corrosion solution. So, it is anticipated that the design of super-hydrophobic surface on LDHs can impede the attack of corrosive liquid, furthermore improving the corrosion resistance of LDH film. Unfortunately, the researches on the super-hydrophobic LDH films are limited in this field. Moreover, the preparing process of the super-hydrophobic LDH films reported in previous literatures was relatively complex and the stability of super-hydrophobicity was not deeply discussed. Wang and co-workers (Wang et al., 2020) obtained the load-inhibitors MgAl-LDH films on the porous anodized Mg alloys *via in situ* growth method and then post-sealing it by a super-hydrophobic coating, showing active corrosion protection property. Wu et al. (Wu et al., 2019) used different kinds of low surface energy substances to modify LDHs *in situ* grown on anodized AZ31 Mg alloy. The result suggested that LDHs modified by fluoroalkylsilane can offer a better corrosion protection for AZ31 Mg alloy than the fatty acid with long carbon chains. Chen et al. (Chen et al., 2006) reported that the LDH crystallite orientation prepared on a PAO/Al substrate can be tailored by controlling the hydrothermal crystallization temperature and time, further providing the appropriate micro and nanostructures to obtain the super-hydrophobic LDH films. Similarly, the orientation of the LDH microsheet layer produced on Al-enriched Mg alloys was tailored by adjusting the hydrothermal temperature, time, and pH to produce a water-repellent surface after modification with fluorinated silane (Zhang et al., 2015). Therefore, in our work, a facile method was used to fabricate directly super-hydrophobic anti-corrosion LDH films on AZ31 Mg alloy. To be specific, LDH nanosheets was formed on etched AZ31 surface by *in situ* hydrothermal crystallization method, which provided a micro/nanostructure for the preparation of super-hydrophobic surface. Then, the LDH films were modified by 1H, 1H, 2H, 2H-perfluorooctyltrimethoxysilane (PFOTMS) to lower the surface energy. The influences of the hydrothermal treatment time and temperature on the surface morphology and corrosion resistance of the super-hydrophobic LDH films were investigated, and the stability of super-hydrophobicity was analyzed. The results demonstrated that the super-hydrophobic LDH films improved significantly the corrosion resistance of Mg alloy and displayed excellent stability of super-hydrophobicity in corrosive liquid.

2 EXPERIMENTAL SECTION

2.1 Materials

Commercial cast magnesium alloy AZ31 ingot was cut into 16 mm × 16 mm × 5 mm cubes by wire-cutting. $Al(NO_3)_3{\cdot}9H_2O$, $NaNO_3$, NaOH, and ethanol were purchased from Chongqing Huanghui Chemical Dangerous Goods Sales Co., Ltd, and 1H, 1H, 2H, 2H-perfluorooctyltrimethoxysilane was ordered from Aladdin Industrial Corporation. All reagents were used as received without further purification. All solutions were prepared with deionized water.

2.2 Pretreatment of AZ31 Mg Alloy Cubes

The AZ31 specimens were sequentially polished with emery sand paper of grades 400, 800, and 1,200 to obtain bright mirror plane, ultrasonically cleaned in absolute ethyl alcohol for 10 min, and then dried in warm stream. The dried substrates were etched in 6.5 wt. % HNO_3 for 20 s at room temperature, aiming to mainly remove oxide and build the micro-nano rough structure on AZ31 Mg alloy surface.

2.3 Preparation of MgAl-LDHs

The MgAl-LDH films were prepared by *in situ* hydrothermal crystallization treatment on chemical etched AZ31 magnesium alloy substrate. $Al(NO_3)_3{\cdot}9H_2O$ (0.01 mol) and $NaNO_3$ (0.005 mol) were sequentially dissolved in deionized water with continuous magnetic stirring to form a clear solution with a total volume of 100 ml. Then, the pH of the solution was adjusted to 10.7 by adding 4.0 M NaOH solution dropwise further to get turbid liquids. The etched specimens were vertically placed in Teflon-lined stainless steel autoclaves containing mixture solution, and then the hydrothermal treatment was carried out at 125°C for different times (6, 12, 18 h) or at different temperatures (100°C, 125°C, 150°C) for 12 h. Finally, the as-prepared specimens were removed with tweezers, rinsed with running deionized water and ethanol, and dried with a warm air flow. The obtained samples were denoted as 6h-125°C-LDHs, 12h-125°C-LDHs, and 18h-125°C-LDHs at the same temperature 125°C, 12h-100°C-LDHs, 12h-125°C-LDHs, and 12h-150°C-LDHs at the same time 12 h, respectively.

2.4 Fabrication of the Super-hydrophobic Surface

The super-hydrophobicity of MgAl-LDH film surface was obtained by immersing in the mixed solution containing 2 ml PFOTMS and 100 ml ethanol at 60°C for 1 h in the oven. After

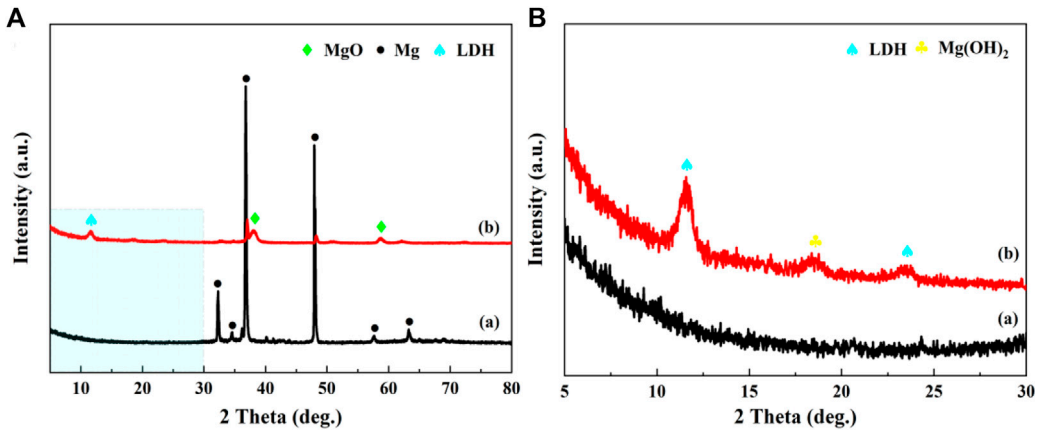

FIGURE 2 | (A) Wide-angle XRD pattern of AZ31 sample (curve a: Mg substrate) and small-angle XRD pattern of MgAl-LDHs (curve b: MgAl-LDHs); **(B)** the magnification of Figure 2A from 5° to 30°.

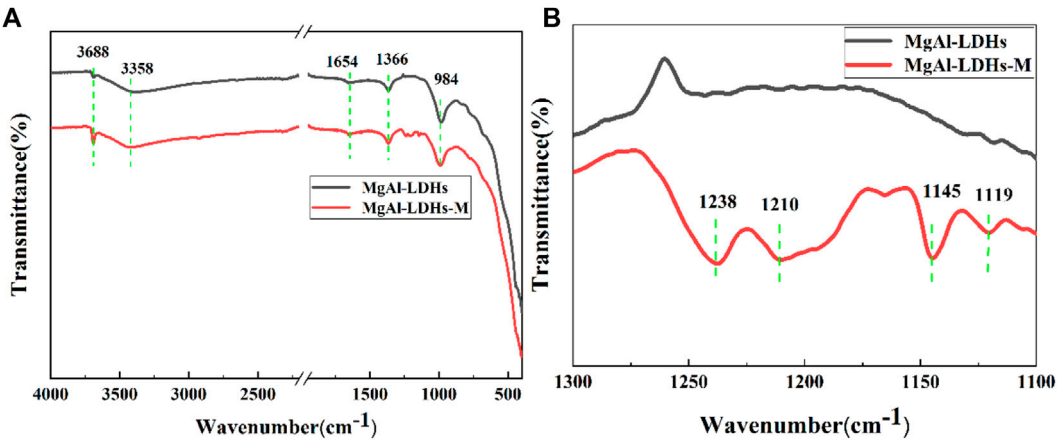

FIGURE 3 | (A,B) FT-IR spectra of different samples; please note that Figure 3B is the magnification of Figure 3A from 1300 cm^{-1} to 1100 cm^{-1}.

immersion, the as-prepared samples were continually dried at 60°C for 1 h in the oven. The final products were labelled as 6h-125°C-LDH-M, 12h-125°C-LDH-M, 18h-125°C-LDH-M, 12h-100°C-LDH-M, and 12h-150°C-LDH-M, respectively.

2.5 Surface Characterization

The surface morphology of different samples was obtained by scanning electronic microscopy with an EDX attachment (SEM, Thermo Scientific Quattro S) under electron accelerating voltage of 20 kV. The SEM specimens were sputtered with gold to avoid discharge problems before performing the SEM observation. A three dimensional laser scanning confocal microscope system (OLS40-SU, Olympus, Japan) was used for surface roughness measurements of different samples. The crystal structure of the samples was characterized by the X-ray diffraction (XRD, Rigaku D/Max 2,500X) with Cu Kα radiation (λ = 1.5406 Å) at 40 kV and 30 mA, within the range of 2θ = 5–80°. The wide-angle XRD and small-angle XRD spectra was performed at a scanning rate of 10°/min and 1°/min, respectively. Fourier transform infrared spectroscopy (FTIR, Nicolet IS5 Thermo Scientific, United States) spectra were obtained in the range of 4,000–400 cm^{-1} at a resolution of 4 cm^{-1} using 16 scans. Static water contact angles (CA) were measured by a sessile drop with 10 μl liquid droplet using a contact angle meter (SDC-100, SINDIN, China) at an ambient temperature. The CA values reported in the form of mean values were calculated from measurements made on at least three different locations of each sample.

2.6 Electrochemical Test

To evaluate corrosion resistance of different specimens, polarization curves and electrochemical impedance spectra (EIS) were performed successively on electrochemical workstation (PARSTAT4000A, Princeton, America) with a three-electrode corrosion cell at room temperature. The cell was placed in a Faraday cage to avoid external electromagnetic

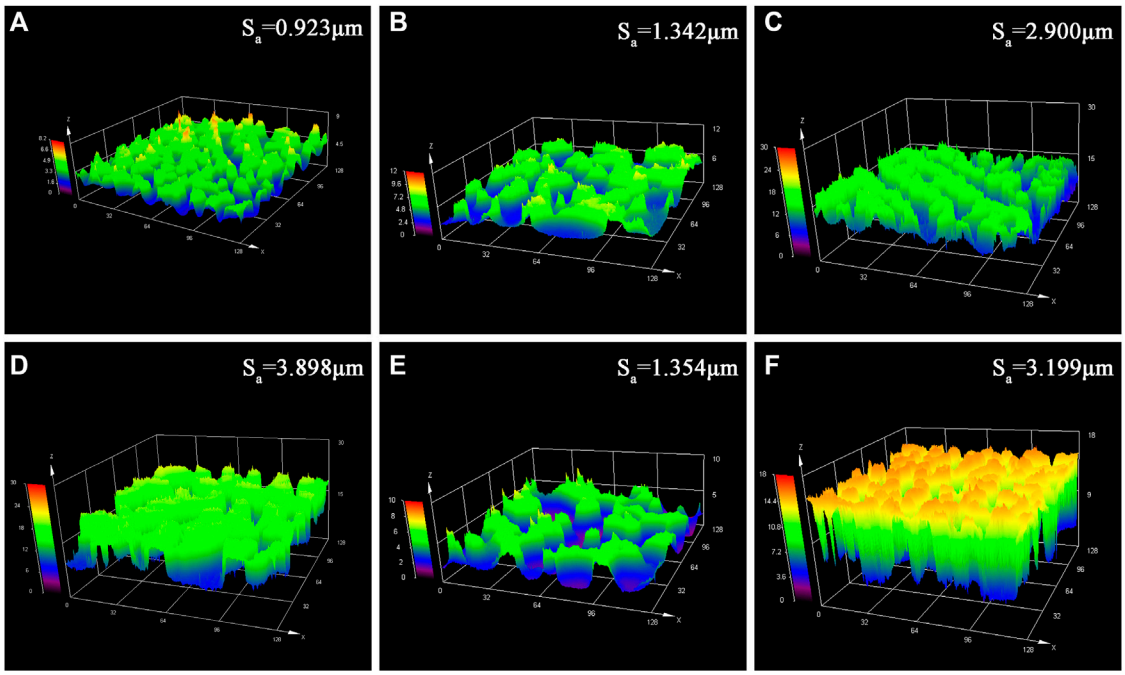

FIGURE 4 | Laser microscopy images of different samples: **(A)** etched Mg-substrate, **(B)** 6 h-125°C-LDHs, **(C)** 18 h-125°C-LDHs, **(D)** 12 h-125°C-LDHs, **(E)** 12 h-100°C-LDHs, and **(F)** 12 h-150°C-LDHs.

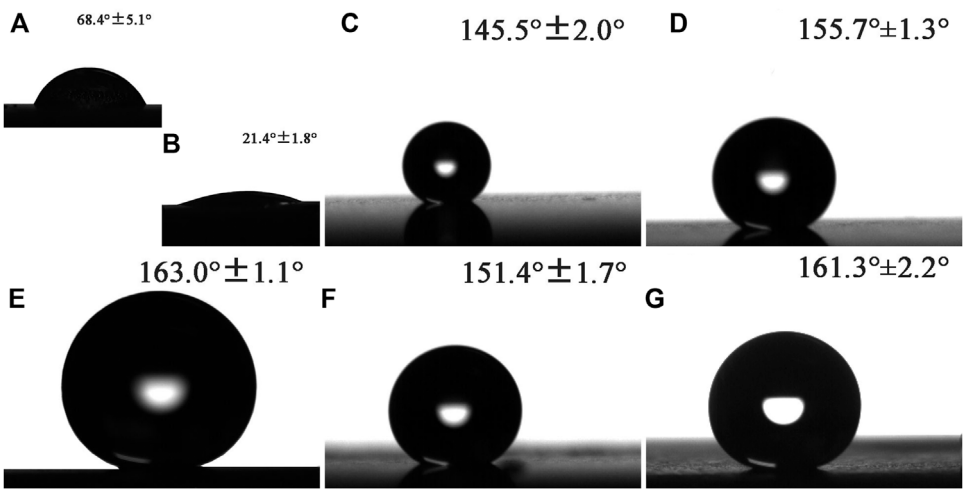

FIGURE 5 | Shapes of water droplets on the surface of different samples and the corresponding water CA: **(A)** etched Mg substrate, **(B)** MgAl-LDHs, **(C)** 6 h-125°C-LDHs-M, **(D)** 18 h-125°C-LDHs-M, **(E)** 12 h-125°C-LDHs-M, **(F)** 12 h-100°C-LDHs-M, and **(G)** 12 h-150°C-LDHs-M.

interference in the environment. The working electrode was as-prepared sample with exposure area of 1 cm^2, and the Ag/AgCl sat. KCl electrode with a Luggin capillary and platinum sheet were used as the reference electrode and the counter electrode, respectively. The samples were immersed in 3.5 wt% NaCl solution for 30 min to reach a steady state before they were tested. Open circuit potential was measured firstly, and then EIS measurement was performed in the frequency range from 100 kHz to 10 mHz using a sine signal with an amplitude of 10 mV. EIS data were fitted by using different equivalent circuits with ZSimpWin software, and the quality of the EIS fitting results was evaluated by the value of χ^2 (Chen L.-Y. et al., 2021). The polarization curves were measured from −0.5 to +0.5 versus OCP at a scanning rate 1 mV/s. Each of the electrochemical test was repeated at least three times to guarantee the reproducibility.

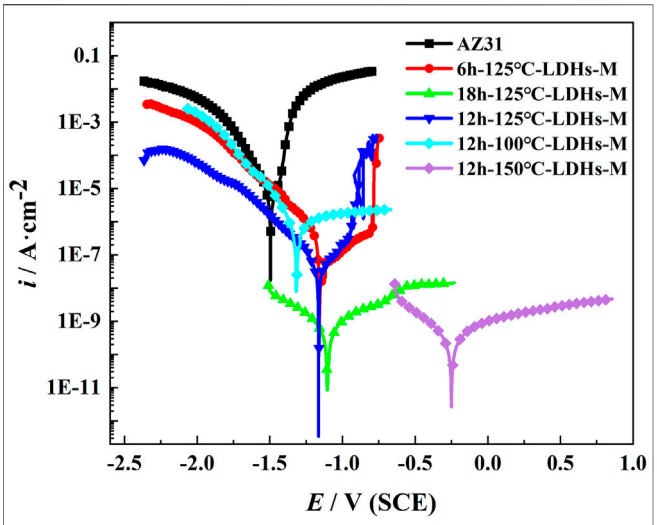

FIGURE 6 | Polarization curves of different samples in 3.5 wt% NaCl solution.

2.7 The Stability of Super-hydrophobicity

The chemical stability of the prepared super-hydrophobic LDH films was studied by immersing the samples in 3.5 wt% NaCl solution for 6 days, and the static CA of water was measured every day. Besides, the surface morphology of samples was observed by SEM during the immersing process.

3 RESULTS AND DISCUSSION

3.1 Surface Characterization

Figure 1 depicts the SEM images of different samples. It can be seen clearly from **Figure 1** that different specimens possessed hump island structures under a low resolution because of the etched AZ31 Mg alloy. The hexagonal plate-like LDH nanosheets grown on the surface of AZ31 Mg alloy were observed in SEM images of the high resolution. The platelets of LDH crystallites were perpendicular to the substrate and covered the entire metal surface. As can be seen from the high-resolution SEM diagrams, morphology on the islands showed significantly different structures as the hydrothermal time extended. According to **Figure 1C**, the island structure of 6 h–125°C-LDHs sample was composed of laminate interlocked LDH nanoplates vertical to substrate. As the growth time increased, the dense and flat LDH nanosheets on the island were shown in **Figure 1F, I**. According to **Figure 1L, F, O**, the similar changes in the morphology of the LDH nanoplates can be found as the hydrothermal temperature ascended. From **Figure 1**, the morphology of 12 h–150°C-LDH film obviously consisted of flat-lying hexagonal LDH nanosheets. The SEM images revealed that the micro/nanoscale coarse structure of metal surface was composed of the small island obtained after chemical etching and the LDH nanosheets *in situ* grown. A cross-sectional view of the MgAl-LDH films (**Supplementary Figure S1A**) clearly demonstrated that a layer of the LDH crystals with a thickness of about 20.2 μm was assembled on the etched magnesium alloy substrate. This observation could be confirmed by energy dispersive X-ray (EDX) analysis, presented in **Supplementary Figure S1B**. Along EDX line scans over the LDH layer and a part of the metal substrate, the Mg Kα profile of the EDX increased with the depths. However, the O Kα profile of the EDX rapidly decreased to almost zero at the interface of the LDH films and the metal matrix, indicating the absence of O species inside the substrate.

TABLE 1 | Electrochemical parameters estimated from the polarization data in **Figure 6**.

Samples	E_{corr}/V (SCE)	i_{corr}/μA cm^{-2}
AZ31	−1.494	6.19
6 h-125°C-LDHs-M	−1.129	6.39×10^{-2}
18 h-125°C-LDHs-M	−1.105	8.55×10^{-4}
12 h-125°C-LDHs-M	−1.062	6.20×10^{-3}
12 h-100°C-LDHs-M	−1.311	7.85×10^{-1}
12 h-150°C-LDHs-M	−0.241	2.74×10^{-4}

3.2 Structure and Composition of LDH Films

The XRD patterns of treated hydrothermally sample and AZ31 Mg alloy substrate sample were shown in **Figure 2A, B**, respectively. As can be seen from **Figure 2A**, the peaks around 32°, 37°, and 48° were contributed to the reflection peaks from AZ31 Mg alloy substrate. In addition, the peaks around 38° and 58° of samples belonged to the reflection peaks of MgO. The peaks belonged to LDH films cannot be clearly observed in that the intensity of the peaks from AZ31 substrate was extremely high. Therefore, the more delicate pattern of **Figure 2A** from 5° to 30° was shown in **Figure 2B**. According to **Figure 2B**, new peaks from the treated hydrothermal samples were found, suggesting the change of the crystal structure on metal surface. As can be seen from **Figure 2B**, the characteristic peak at around 18° was assigned to the reflection peak of $Mg(OH)_2$. In addition, the peaks at about 11.6° and 23.5° corresponded to the (003) and (006) planes of MgAl-LDHs, indicating a typical layered structure of LDHs (Tang et al., 2019). The d-spacing of 0.863 nm corresponding to the (003) plane of LDH film was obtained based on the Bragg's law ($2d \cdot \sin\theta = n \cdot \lambda$). The height of the interlayered corridor was almost consistent with the reported literatures (Cao et al., 2018). Through the above analysis, it was concluded that the MgAl-LDHs was successfully prepared on the surface of the AZ31 substrate.

Figure 3A presents the FT-IR spectra of MgAl-LDHs and MgAl-LDHs-M (MgAl-LDHs modified by PFOTMS) on AZ31 metal surface within the 400–4,000 cm^{-1} region, respectively. It can be seen from **Figure 3A** that the sharp absorption peak at approximately 3,688 cm^{-1} and the broad peak at about 3,358 cm^{-1} were ascribed to water molecules absorbed physically in LDHs and metal hydroxyl groups on the LDHs surface, respectively (Zhang et al., 2018). The peak at around 1,654 cm^{-1} can be attributed to the bending vibration of crystal water between the LDH layers. In addition, the band

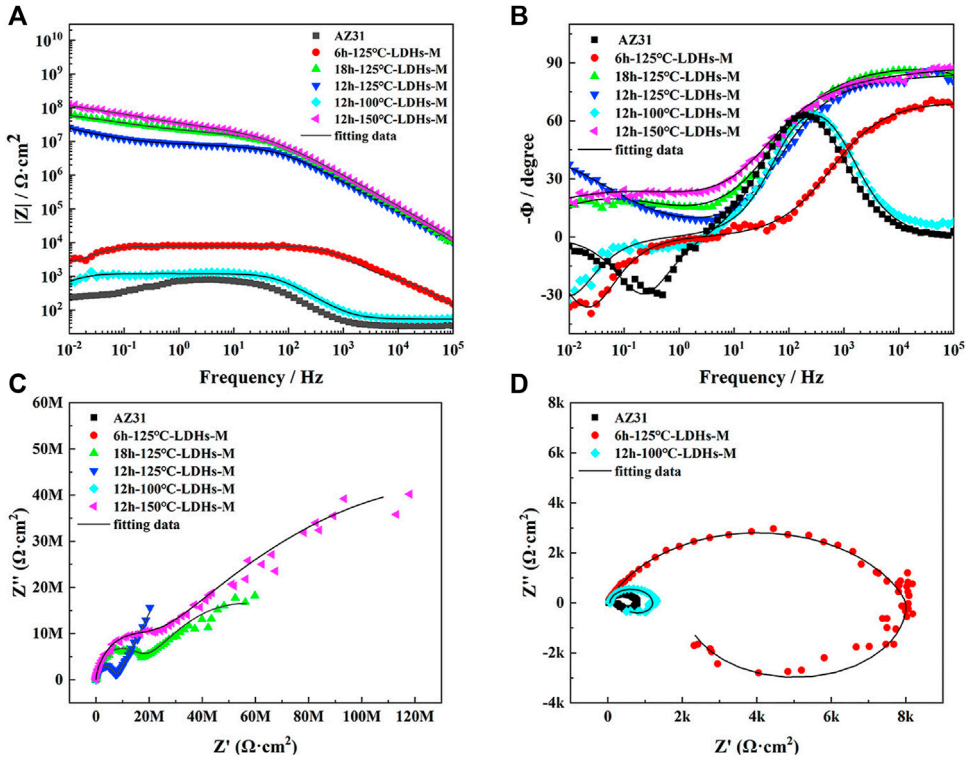

FIGURE 7 | (A) Impedance-frequency Bode plots, **(B)** phase-frequency Bode plots, **(C)** Nyquist plots of different samples in 3.5 wt% NaCl solution after immersion for 30 min, and **(D)** the magnifying graph of **(C)**.

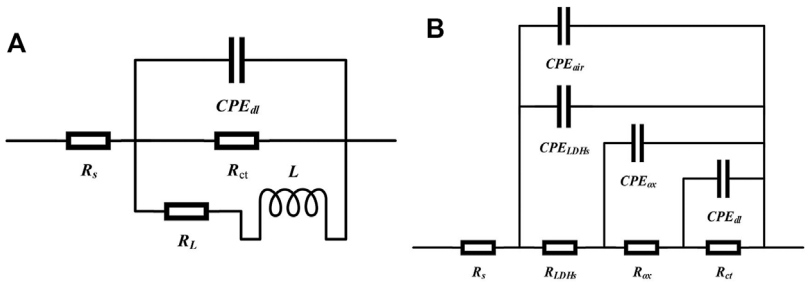

FIGURE 8 | The equivalent circuits used to simulate EIS data of **(A)** AZ31 substrate, 6h-125°C-LDHs-M, and 12h-100°C-LDHs-M; **(B)** 12 h-125°C-LDHs-M, 18 h-125°C-LDHs-M, and 12 h-150°C-LDHs-M after immersion in 3.5 wt% NaCl solution for 30 min.

observed at 1,366 cm^{-1} can be assigned to the stretching vibration of the interlayer NO_3^- in MgAl-LDHs. The intensity of the peaks observed in the range 1,100–1300 cm^{-1} was weak, thus enlarging this range to obtain more refined data in **Figure 3B**. The emerging new absorption peaks that belonged to MgAl-LDHs-M were observed in **Figure 3B**. It was reported in the previous literatures that the absorption bands in 1,100–1,300 cm^{-1} corresponded to the presence of C-F groups (Zhang et al., 2015), and the emerging absorption peaks at around 1,273, 1,191, 1,134, and 1111cm^{-1} were assigned to the vibration of C-F_2 groups (Pazokifard et al., 2012). Thus, **Figure 3B** presents that the two bimodal absorption bands that belonged to MgAl-LDHs-M (1,238, 1,210 cm^{-1} and 1,145, 1119 cm^{-1}) were attributed to the stretching vibration of C-F_2 groups. The above results demonstrated that LDH films were prepared successfully on metal surface, which were in good agreement with the XRD results. It also could be concluded that LDH films were modified successfully by PFOTMS.

TABLE 2 | Fitted parameters of the EIS spectra of the bare AZ31 and coated samples using the same equivalent circuits shown in **Figure 8A**.

Parameters	AZ31	6h-125°C-LDHs-M	12h-100°C-LDHs-M
R_s (Ω·cm^2)	3.33E+01	3.53E+01	2.96E+01
R_{ct} (Ω·cm^2)	7.47E+02	8.91E+03	1.27E+03
CPE_{dl} Y_{dl} (F·cm^{-2})	8.19E-06	2.84E-07	3.24E-06
n_{dl}	9.44E-01	8.61E-01	9.26E-01
R_L (Ω·cm^2)	3.32E+02	2.82E+03	4.17E+02
L (H·cm^2)	4.44E+02	4.14E+04	1.33E+04
χ^2	3.03E-03	3.32E-03	3.51E-03

3.3 Roughness and Wetting Properties of Films

Supplementary Figure S2 showed clearly that different specimens possessed almost the same surface morphologies at the very low resolution, which were composed of a great number of small hump islands. The small island structures offered micro-scale roughness to the super-hydrophobic films. Similarly, LDH nanosheets grown *in situ* on the etched Mg substrate played an important role on the effect of surface roughness. So the 3D roughness profiles of different samples obtained by a laser microscope were shown in **Figure 4**. The etched AZ31 substrate showed a surface roughness of 0.923 μm. As can be seen clearly from **Figure 4**, the surface roughness of these samples treated hydrothermally showed a remarkable increase. The surface roughness of 6h-125°C-LDHs, 12h-125°C-LDHs, and 18h-125°C-LDHs corresponded to Sa = 1.342μm, Sa = 3.898 μm, and Sa = 2.900 μm, respectively. It can be found that the roughness rises first and then decreases with the extension of hydrothermal treatment time. Meanwhile, the surface roughness has a similar change with increasing temperature. The surface roughness of samples treated hydrothermally was significantly increased compared to the etched magnesium alloy, which was attributed to the combination of microscale coarse structure resulting from the etching and nanoscale coarse structure resulting from hydrothermal treatment.

The surface wettability of different samples was evaluated by the CA measurements, and the corresponding CA results were shown in **Figure 5**. The CA of etched metal substrate was 68.4° ± 5.1°, indicating the hydrophilic nature. The water CA of MgAl-LDH film decreased remarkably to 21.4° ± 1.8° compared with the etched substrate, which can be attributed to the increased roughness of the surface because of the existence of LDH nanosheets. After the LDH films were modified by PFOTMS, the LDHs sample almost presented super-hydrophobicity with a CA of more than 150°. It was worth noting that the water CA of 12h–125°C-LDHs-M was the largest, upping to 163.0° ± 1.1°, and the corresponding roughness was also the maximum. The roughness results in **Figure 4** strongly supported the wettability results, revealing that the CA value increased with the roughness under certain conditions. The combination of the roughness in **Figure 4** with the CA in **Figure 5** was in perfect agreement with this conclusion. The corresponding theoretical foundation was presented as follows. Wenzel investigated the relationship between surface roughness and water CA and proposed the theoretical Wenzel equation.

$$\boldsymbol{cos\theta w = r \cdot cos\theta o} \quad (1)$$

where θ_w means the Wenzel CA, θ_o represents the water CA on the ideal surface, and r is the so-called surface roughness (the ratio of the actual surface area to the projected surface area). Based on the above equation, it can be concluded that θ_o will decrease with increasing the surface roughness, when $\theta_w < 90°$; θ_o will increase with increasing the surface roughness, when $\theta_w > 90°$. So, the results of **Figure 5** were in good agreement with the results of **Figure 4**.

3.4 Anti-corrosive Performance

3.4.1. Polarization Characterization

Figure 6 shows the polarization curves of AZ31 substrate and LDH films modified by PFOTMS immersed in 3.5 wt% NaCl aqueous solution for 30 min. According to **Figure 6**, AZ31 exhibited the most negative corrosion potential with the highest corrosion current density among all samples. MgAl-LDHs-M samples presented more positive E_{corr} and lower I_{corr}, which were attributed to the blocking of corrosion media by LDH nanosheets and super-hydrophobic surfaces. Generally speaking, the corrosion potential is a thermodynamic parameter, and the more positive the corrosion potential represents better corrosion protection

TABLE 3 | Fitted parameters of the EIS spectra of coated samples using equivalent circuits shown in **Figure 8B**.

Parameters		12 h-125°C-LDHs-M	18 h-125°C-LDHs-M	12 h-150°C-LDHs-M
R_s (Ω·cm^2)		**3.89E+01**	**5.81E+01**	**4.50E+01**
CPE_{air}	Y_{air} (F·cm^{-2})	1.46E-10	1.58E-10	1.09E-10
	n_{air}	9.75E-01	1.00E+00	1.00E+00
R_{LDHs} (Ω·cm^2)		1.21E+04	1.89E+07	1.74E+07
CPE_{LDHs}	Y_{LDHs} (F·cm^{-2})	4.29E-10	2.20E-09	8.14E-10
	n_{LDHs}	9.22E-01	5.12E-01	8.00E-01
R_{ox} (Ω·cm^2)		8.94E+06	6.85E+07	2.69E+08
CPE_{ox}	Y_{ox} (F·cm^{-2})	6.65E-09	5.23E-08	6.68E-08
	n_{ox}	3.14E-01	4.91E-01	4.72E-01
R_{ct} (Ω·cm^2)		—	—	—
CPE_{dl}	Y_{dl} (F·cm^{-2})	—	—	—
	n_{dl}	—	—	—
χ^2		1.28E-03	3.03E-03	2.49E-03

"/" represents that low-frequency data were not well-fitted because the parameter is out of the frequency range.

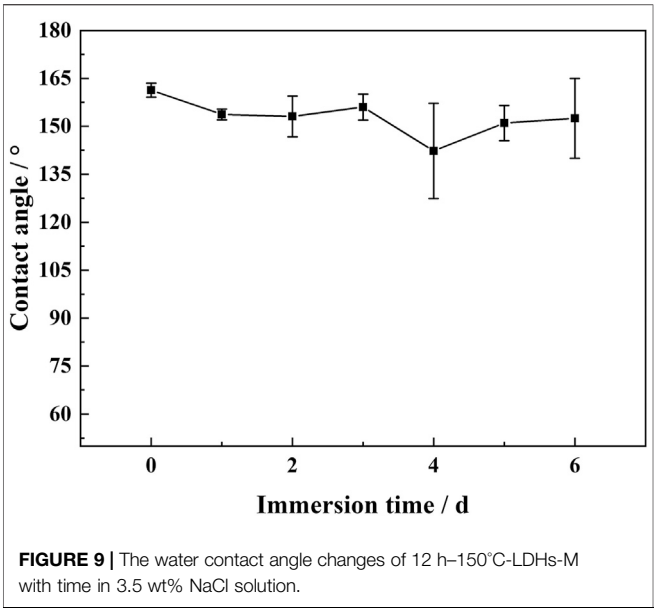

FIGURE 9 | The water contact angle changes of 12 h–150°C-LDHs-M with time in 3.5 wt% NaCl solution.

effect; the corrosion current density is the kinetic parameter, and lower corrosion current densities correspond to lower corrosion rates. The strong polarization area of the polarization curve was selected for obtaining the corrosion potential and the corrosion current density by the Tafel extrapolation method. The values of E_{corr} and I_{corr} of each sample obtained by the fitting procedure were shown in **Table 1**.

From **Table 1**, E_{corr} of super-hydrophobic LDH films were apparently higher than that of AZ31 Mg alloy, indicating that MgAl-LDHs-M can block the attack of corrosive liquids. Particularly, the E_{corr} of 12h–150°C-LDHs-M was nearly one order of magnitude than that of AZ31 substrate, upping to −0.241 V. As can be also seen clearly from **Table 1**, the corrosion current density gradually decreased with the LDHs growth time extending. The corrosion current density of 18h–125°C-LDHs-M in the series of different hydrothermal times was nearly four orders of magnitude lower than that of AZ31 Mg alloy, indicating excellent corrosion protection, because the LDH nanosheets grew more dense and compact on the surface of the magnesium alloy. Similarly, the I_{corr} declined with the LDHs growth temperature improving. It was noteworthy that the I_{corr} of 12h–150°C-LDHs-M in the series of different hydrothermal temperatures was the lowest (I_{corr} = 2.74×10^{-4} μA cm^{-2}), implying the extremely good corrosion protection effect. On the basis of the polarization measurements, the corrosion resistance of the AZ31 substrate was effectively enhanced by double protection from super-hydrophobic LDH films.

3.4.2. Electrochemical Impedance Spectra Characterization

According to **Figure 7C, D**, it can be seen that the Nyquist plots of different samples had apparent difference. Usually, the greater arc radius at the high frequency in the Nyquist plots corresponds to better corrosion protection effect. As shown in the Nyquist plots, the super-hydrophobic LDH films had a better corrosion protection compared with AZ31 substrate. To interpret the obtained EIS results clearly, two kinds of equivalent circuits were shown in **Figure 8**. The equivalent circuit in **Figure 8A** was used to simulate the EIS data of AZ31, 6 h-125°C-LDHs-M, and 12 h-100°C-LDHs-M. In this equivalent circuit, R_s represented the resistance of the solution between the reference electrode and the film surface; the parallel of the constant phase element (CPE_{dl}) and the charge transfer resistance (R_{ct}) was used to describe the electrochemical process of the corrosion process; inductance elements (L) and inductive impedance (R_L) were often used to explain the inductive loop that appeared at low frequency, which originated from adsorbed/desorbed intermediates on the electrode surface (Zhou et al., 2015). In the case of the 12 h-125°C-LDHs-M, 18h-125°C-LDHs-M, and 12 h-150°C-LDHs-M system, their EIS data could be fitted by an equivalent circuit with three time constants. The first time constant at higher frequency was attributed to the effect of super-hydrophobic LDH films, represented by a CEP_{LDHs} in parallel with the resistance of LDH films (R_{LDHs}). Considering that the super-hydrophobic film produced a layer of air film, the CPE_{air} was introduced to characterize the trapped air. The second time constant appearing at intermediate frequency may be related to the oxide film produced on the surface of the substrate, expressed by a CEP_{ox} in parallel with the oxide resistance (R_{ox}). The third time constant occurring at low frequency was associated with the electrochemical corrosion process, denoted as CPE_{dl} and R_{ct}.

Based on the above equivalent circuits shown in **Figure 8A**, the data fitting results are listed in **Table 2**. Usually, the error value of χ^2 represents the quality of fitting results, and the value of $\chi 2$ around 10^{-3} or less indicates good fit (Wang et al., 2020; Qin et al., 2021). As can be shown in **Table 2**, the R_{ct} value of 12h–100°C-LDHs-M was slightly higher than that of AZ31 substrate, indicating the limited protection by super-hydrophobic LDH films prepared at 100°C for the Mg substrate. Notably, the 6h-125°C-LDHs-M sample had the maximum R_{ct} value in the three samples that used the equivalent electron circuit shown in **Figure 8A**, approximately 10 times higher than the AZ31, suggesting that the super-hydrophobic LDH films provided effective protection for the magnesium alloy matrix. The results were consistent with that obtained from Nyquist plots in **Figure 7D**. The low frequency inductance loop shown in **Figure 7D** was associated with the dissolution of the substrate.

Based on a more complex circuit model (**Figure 8B**), the fitted EIS data were shown in **Table 3**. Combining the Nyquist diagram and the fitted data, it was found that the super-hydrophobic LDH film provided corrosion protection to metal substrate that can be effectively improved with the extension of hydrothermal treatment time or the increasing of hydrothermal temperature. As for three samples in **Table 3**, n_{air} was almost one and Y_{air} was extremely small, indicating that the air trapped in the film behaved as the dielectric of the pure parallel plate capacitor, which well suppressed the transfer of the charge between the

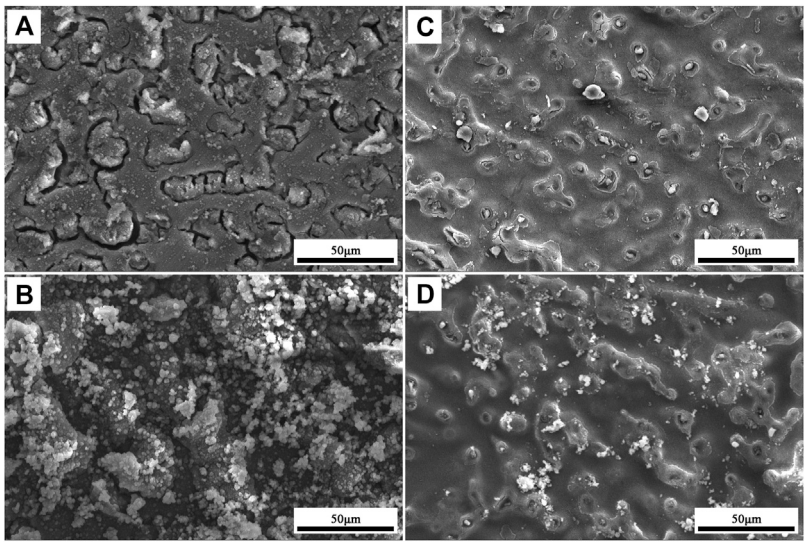

FIGURE 10 | Corrosion morphology of **(A)** AZ31 substrate for immersion 1 h, **(B)** AZ31 substrate for immersion 1 day, **(C)** 12 h-150°C-LDHs-M for immersion 2 days, and **(D)** 12 h-150°C-LDHs-M for immersion 6 days.

electrolyte and the substrate (Wang et al., 2011). Furthermore, the R_{ox} values of all three samples were more than $10^6\ \Omega\ cm^2$, implying that this oxide film provided extremely good protection for the substrate. The oxide film layer between LDHs and the matrix was the last physical barrier preventing corrosive media from invading into the matrix. When the samples do not suffer from corrosion activity, the resistance of the oxide film layer is considered as an important criterion for evaluating the protective performance of the film. It was worth noting that R_{ox} of 12h–150°C-LDHs-M was higher than that of other samples that used the same equivalent circuit shown in **Figure 8B**, which suggested that the oxide layer was much more compact and was protected greatly by the LDH layer and the air film outside. The LDH films played an important role in the whole film, which not only played a physical protection role against the substrate, but also made ion-exchange reactions with the corrosive mediums. The R_{LDHs} values of 18h–125°C-LDHs-M in the series of different hydrothermal times and 12h-150°C-LDHs-M in the series of different hydrothermal temperatures all were approximately three orders of magnitude higher than that of 12h–125°C-LDHs-M, showing the more compact and less porous structure of the LDH films. There was an agreement with results of SEM.

Notably, there were no signs of wetting on the surface of samples shown in **Table 3** after the electrochemical test. It was inferred that only the very slight corrosion has occurred on the surface during the electrochemical test because the surface of the super-hydrophobic samples could not be completely wet during the electrochemical test. Therefore, we cannot obtain accurate the fitting results of R_{ct} and CPE_{dl} since the corrosion process did not completely occurred at this time (Cao et al., 2018). Furthermore, it was also concluded that the corrosion resistance of the three samples shown in **Table 3** was higher than that of the samples presented in **Table 2** from the Nyquist plots and Bode plots shown in **Figure 7**. The above comprehensive analysis demonstrated that the 18h-125°C-LDHs-M in the series of different hydrothermal times and 12h-150°C-LDHs-M in the series of different hydrothermal temperatures had a better corrosion resistance performance than the other samples.

3.5 The Stability of Super-hydrophobicity in Corrosive Liquid

The above results of electrochemical test demonstrated that super-hydrophobic LDH films provided good corrosion protection for AZ31 substrate. Particularly, the 12h-150°C-LDHs-M presented excellent corrosion resistance properties. However, the electrochemical results obtained in a short time can only evaluate corrosion resistance of films in the short term. Therefore, the stability of super-hydrophobic surface was investigated for the evaluation of the long-term corrosion protection of super-hydrophobic films. The 12h-150°C-LDHs-M sample was immersed in the 3.5 wt% NaCl aqueous solution, and the water contact angle and the corrosion morphology were analyzed at 0–6 days to assess the stability of the super-hydrophobicity.

Figure 9 displays the CA changes of 12h–150°C-LDHs-M in 3.5 wt% NaCl solution. It can be apparently observed that the CA of 12h–150°C-LDHs-M still maintained super-hydrophobic property (CA > 150°) within the initial immersion time of 24 h, indicating that the non-wettability of the films remained. Overall, the contact angle of the films can maintain above 140 within 6°days of immersing. From **Figure 10A, B**, it can be inferred that AZ31 immersed in the

3.5°wt % NaCl aqueous solution occurred corrosion after immersion for 1°h; corrosion products precipitated on the surface of AZ31 after immersion for 1°day. As shown in **Figure 10C**, after the 12°h-150°C-LDHs-M immersed in 3.5 wt% NaCl aqueous solution for 48°h, the local area of the film surface began to appear in the corrosion products, and the corresponding water contact angle fluctuated slightly. From **Figure 10D**, the corrosion products increased significantly when immersion time was up to 6°days, and the corresponding water contact angles fluctuated sharply, but the CA values maintained at around 140. On the basis of the above result, it can be concluded that the super-hydrophobic LDH films presented excellent stability in the high concentration corrosion fluid due to the stable micro/nanostructures on metal surface.

4 CONCLUSION

In this work, super-hydrophobic LDH films have been fabricated successfully by a facile method. The conclusions were obtained as follows:

1 The super-hydrophobic LDHs can be prepared on the surface of etched AZ31 substrate *via in situ* growth hydrothermal crystallization, followed by the modification of PFOTMS. The structure of LDH film was composed of small islands and LDH crystal nanosheets, which provided micro/nanoscale roughness structure to manufacture super-hydrophobic surface.
2 The contact angle was influenced evidently by the surface roughness. The surface roughness of LDH films increased gradually with increasing hydrothermal time or temperature. The highest water contact angle of the film was up to about 163.
3 The super-hydrophobic LDH films can effectively improve the corrosion resistance of the AZ31 Mg alloy. The corrosion current density of samples with the best corrosion resistance was approximately four orders of magnitude lower than that of AZ31 substrate. The corrosion resistance of super-hydrophobic LDH film increased with the increased hydrothermal time or temperature.
4 The obtained super-hydrophobic LDH film still can keep above 140° after immersed in 3.5 wt% NaCl solution for 6 days, indicating the good stability of the super-hydrophobic LDH film.

DATA AVAILABILITY STATEMENT

The original contributions presented in the study are included in the article/**Supplementary Material**. Further inquiries can be directed to the corresponding authors.

AUTHOR CONTRIBUTIONS

XH and JH were responsible for the experimental ideas, methodology and paper writing. YW carried out the acquisition of supplementary data. TX and WX guided the trial process and the paper revision. LW and YC participated in part of data analysis work.

FUNDING

This work was supported by the Natural Science Foundation of Chongqing (cstc2018jcyjAX0450, cstc2019jcyj-msxmX0566), Scientific and Technological Research Program of Chongqing Municipal Education Commission (KJKJQN201800102, KJQN201800619), Visiting Scholar Foundation of Key Laboratory of Biorheological Science and Technology (Chongqing University), Ministry of Education of China (No.CQKLBST-2015-003), Chongqing Special Key Project of Technology Innovation and Application Development, China (Grant No. cstc2019jscx-dxwtBX0016), and the grant project of "Preparing process and properties of antibacterial ureteric stent material with degradable and portable" (H20200113).

ACKNOWLEDGMENTS

We thank Analytical and Testing Center of Chongqing University for performing SEM test and National Engineering Research Center for Magnesium Alloys for XRD, FT-IR, and electrochemical experiments.

SUPPLEMENTARY MATERIAL

The Supplementary Material for this article can be found online at: https://www.frontiersin.org/articles/10.3389/fmats.2021.743112/full#supplementary-material

REFERENCES

Bocchetta, P., Chen, L.-Y., Tardelli, J. D. C., Reis, A. C. d., Almeraya-Calderón, F., and Leo, P. (2021). Passive Layers and Corrosion Resistance of Biomedical Ti-6Al-4V and β-Ti Alloys. *Coatings* 11 (5), 487. doi:10.3390/COATINGS11050487

Cao, Y., Zheng, D., Li, X., Lin, J., Wang, C., Dong, S., et al. (2018). Enhanced Corrosion Resistance of Superhydrophobic Layered Double Hydroxide Films with Long-Term Stability on Al Substrate. *ACS Appl. Mater. Inter.* 10 (17), 15150–15162. doi:10.1021/acsami.8b02280

Chen, H., Zhang, F., Fu, S., and Duan, X. (2006). *In Situ* microstructure Control of Oriented Layered Double Hydroxide Monolayer Films with Curved Hexagonal Crystals as Superhydrophobic Materials. *Adv. Mater.* 18 (23), 3089–3093. doi:10.1002/adma.200600615

Chen, J.-l., Fang, L., Wu, F., Zeng, X.-g., Hu, J., Zhang, S.-f., et al. (2020). Comparison of Corrosion Resistance of MgAl-LDH and ZnAl-LDH Films Intercalated with Organic Anions ASP on AZ31 Mg Alloys. *Trans. Nonferrous Met. Soc. China* 30 (9), 2424–2434. doi:10.1016/s1003-6326(20)65389-4

Chen, J., Song, Y., Shan, D., and Han, E.-H. (2013). Modifications of the Hydrotalcite Film on AZ31 Mg alloy by Phytic Acid: The Effects on Morphology, Composition and Corrosion Resistance. *Corrosion Sci.* 74, 130–138. doi:10.1016/j.corsci.2013.04.034

Chen, J., Wu, L., Ding, X., Liu, Q., Dai, X., Song, J., et al. (2021a). Effects of Deformation Processes on Morphology, Microstructure and Corrosion Resistance of LDHs Films on Magnesium alloy AZ31. *J. Mater. Sci. Tech.* 64, 10–20. doi:10.1016/j.jmst.2019.10.007

Chen, L.-Y., Zhang, H.-Y., Zheng, C., Yang, H.-Y., Qin, P., Zhao, C., et al. (2021b). Corrosion Behavior and Characteristics of Passive Films of Laser Powder Bed Fusion Produced Ti-6Al-4V in Dynamic Hank's Solution. *Mater. Des.* 208, 109907. doi:10.1016/j.matdes.2021.109907

Pazokifard, S., Mirabedini, S. M., Esfandeh, M., and Farrokhpay, S. (2012). Fluoroalkylsilane Treatment of TiO2 Nanoparticles in Difference pH Values: Characterization and Mechanism. *Adv. Powder Tech.* 23 (4), 428–436. doi:10.1016/j.apt.2012.02.006

Qin, P., Chen, L. Y., Zhao, C. H., Liu, Y. J., Cao, C. D., Sun, H., et al. (2021). Corrosion Behavior and Mechanism of Selective Laser Melted Ti35Nb alloy Produced Using Pre-alloyed and Mixed Powder in Hank's Solution. *Corrosion Sci.* 189, 109609. doi:10.1016/j.corsci.2021.109609

Song, Y., Tang, Y., Fang, L., Wu, F., Zeng, X., Hu, J., et al. (2021). Enhancement of Corrosion Resistance of AZ31 Mg Alloys by One-step *In Situ* Synthesis of ZnAl-LDH Films Intercalated with Organic Anions (ASP, La). *J. Magnesium Alloys* 9 (2), 658–667. doi:10.1016/j.jma.2020.03.013

Tang, Y., Wu, F., Fang, L., Guan, T., Hu, J., and Zhang, S. (2019). A Comparative Study and Optimization of Corrosion Resistance of ZnAl Layered Double Hydroxides Films Intercalated with Different Anions on AZ31 Mg Alloys. *Surf. Coat. Tech.* 358, 594–603. doi:10.1016/j.surfcoat.2018.11.070

Wang, P., Zhang, D., Qiu, R., and Hou, B. (2011). Super-hydrophobic Film Prepared on Zinc as Corrosion Barrier. *Corrosion Sci.* 53 (6), 2080–2086. doi:10.1016/j.corsci.2011.02.025

Wang, X., Jing, C., Chen, Y., Wang, X., Zhao, G., Zhang, X., et al. (2020). Active Corrosion protection of Super-hydrophobic Corrosion Inhibitor Intercalated Mg-Al Layered Double Hydroxide Coating on AZ31 Magnesium alloy. *J. Magnesium Alloys* 8 (1), 291–300. doi:10.1016/j.jma.2019.11.011

Wu, L., Ding, X., Zheng, Z., Tang, A., Zhang, G., Atrens, A., et al. (2021). Doublely-doped Mg-Al-Ce-V2o74- LDH Composite Film on Magnesium alloy AZ31 for Anticorrosion. *J. Mater. Sci. Tech.* 64, 66–72. doi:10.1016/j.jmst.2019.09.031

Wu, L., Wu, J., Zhang, Z., Zhang, C., Zhang, Y., Tang, A., et al. (2019). Corrosion Resistance of Fatty Acid and Fluoroalkylsilane-Modified Hydrophobic Mg-Al LDH Films on Anodized Magnesium alloy. *Appl. Surf. Sci.* 487, 569–580. doi:10.1016/j.apsusc.2019.05.121

Xie, J., Hu, J., Lin, X., Fang, L., Wu, F., Liao, X., et al. (2018). Robust and Anti-corrosive PDMS/SiO2 Superhydrophobic Coatings Fabricated on Magnesium Alloys with Different-Sized SiO2 Nanoparticles. *Appl. Surf. Sci.* 457, 870–880. doi:10.1016/j.apsusc.2018.06.250

Xu, C., Chen, L.-Y., Zheng, C.-B., Zhang, H.-Y., Zhao, C.-H., Wang, Z.-X., et al. (2021). Improved Wear and Corrosion Resistance of Microarc Oxidation Coatings on Ti-6Al-4V alloy with Ultrasonic Assistance for Potential Biomedical Applications. *Adv. Eng. Mater.* 23 (4), 2001433. doi:10.1002/adem.202001433

Yang, H., Wu, L., Jiang, B., Liu, W., Song, J., Huang, G., et al. (2021). Clarifying the Roles of Grain Boundary and Grain Orientation on the Corrosion and Discharge Processes of α-Mg Based Mg-Li Alloys for Primary Mg-Air Batteries. *J. Mater. Sci. Tech.* 62, 128–138. doi:10.1016/j.jmst.2020.05.067

Yao, W., Liang, W., Huang, G., Jiang, B., Atrens, A., and Pan, F. (2020). Superhydrophobic Coatings for Corrosion protection of Magnesium Alloys. *J. Mater. Sci. Tech.* 52, 100–118. doi:10.1016/j.jmst.2020.02.055

Zhang, G., Wu, L., Tang, A., Ma, Y., Song, G.-L., Zheng, D., et al. (2018). Active Corrosion protection by a Smart Coating Based on a MgAl-Layered Double Hydroxide on a Cerium-Modified Plasma Electrolytic Oxidation Coating on Mg alloy AZ31. *Corrosion Sci.* 139, 370–382. doi:10.1016/j.corsci.2018.05.010

Zhang, L.-C., Chen, L.-Y., and Wang, L. (2020). Surface Modification of Titanium and Titanium Alloys: Technologies, Developments, and Future Interests. *Adv. Eng. Mater.* 22 (5), 1901258. doi:10.1002/adem.201901258

Zhang, X., Wu, G., Peng, X., Li, L., Feng, H., Gao, B., et al. (2015). Mitigation of Corrosion on Magnesium alloy by Predesigned Surface Corrosion. *Sci. Rep.* 5, 17399. doi:10.1038/srep17399

Zhou, M., Pang, X., Wei, L., and Gao, K. (2015). Insitu Grown Superhydrophobic Zn-Al Layered Double Hydroxides Films on Magnesium alloy to Improve Corrosion Properties. *Appl. Surf. Sci.* 337, 172–177. doi:10.1016/j.apsusc.2015.02.086

Conflict of Interest: The authors declare that the research was conducted in the absence of any commercial or financial relationships that could be construed as a potential conflict of interest.

Publisher's Note: All claims expressed in this article are solely those of the authors and do not necessarily represent those of their affiliated organizations, or those of the publisher, the editors and the reviewers. Any product that may be evaluated in this article, or claim that may be made by its manufacturer, is not guaranteed or endorsed by the publisher.

frontiers in Materials

REVIEW
published: 19 January 2022
doi: 10.3389/fmats.2021.804906

Rare Earth Based Magnesium Alloys—A Review on WE Series

Lénia M. Calado[1]*, *Maria J. Carmezim*[1,2] *and M. Fátima Montemor*[1]

[1]Centro de Química Estrutural-CQE, DEQ, Instituto Superior Técnico, Universidade de Lisboa, Lisbon, Portugal, [2]ESTSetúbal, CDP2T, Instituto Politécnico de Setúbal, Setúbal, Portugal

Magnesium and magnesium alloys have attracted growing attention over the last decades as lightweight materials for a wide range of applications. In particular, WE series magnesium alloys have experienced growing interest over the last years due to their favourable mechanical properties at room and elevated temperatures. In addition, it has been reported that these rare earth-containing alloys possess superior corrosion resistance compared to other commonly used magnesium alloys, such as AZ series. This review aims at providing a concise overview of the research efforts made during recent years regarding the properties of WE series magnesium alloys (e.g., mechanical properties, corrosion behaviour), how these properties can be enhanced by controlling the microstructure of these materials, and the role of specific alloying elements that are used for the WE series. The widespread use of these materials has been limited, mainly due to their susceptibility to corrosion. Thus, in the present review, strong emphasis has been given to recent work studying the corrosion behaviour of the WE series alloys, and to protective strategies that can be employed to mitigate their degradation.

Keywords: magnesium alloys, rare earth elements, corrosion, corrosion protection, coatings

OPEN ACCESS

Edited by:
Yingwei Song,
Institute of Metals Research (CAS), China

Reviewed by:
Quantong Jiang,
Institute of Oceanology (CAS), China
Bo Song,
Southwest University, China
Jinhui Liu,
Zhengzhou University, China

***Correspondence:**
Lénia M. Calado
leniacalado@tecnico.ulisboa.pt

Specialty section:
This article was submitted to Structural Materials, a section of the journal Frontiers in Materials

Received: *29 October 2021*
Accepted: *27 December 2021*
Published: *19 January 2022*

Citation:
Calado LM, Carmezim MJ and Montemor MF (2022) Rare Earth Based Magnesium Alloys—A Review on WE Series. Front. Mater. 8:804906. doi: 10.3389/fmats.2021.804906

INTRODUCTION

Magnesium and Magnesium Alloys

Magnesium Alloys as Lightweight Solution

Growing environmental concerns have been leading to the need for reduction of greenhouse gas emissions into the atmosphere. This reduction in emissions has been heavily regulated for several industries. In particular, the automotive and aeronautic sectors are expected to meet specific targets over the next years (European Union, 2009; European Union, 2014). Thus, substantial research efforts regarding possible solutions for mitigation of greenhouse gas emissions, such as improved component design and performance, and fuel efficiency improvement, have been made in these industries. Weight reduction of components has been regarded as the most simple and cost-effective solution to improve fuel efficiency and reduce greenhouse gas emissions (Grote et al., 2014; Kiani et al., 2014; Esmaily et al., 2017). To meet this goal, the use of lightweight magnesium alloys represents an interesting approach for component weight reduction, since magnesium is the lightest structural metal. With densities ranging between 1.74 and 1.81 g/cm^3, magnesium and magnesium alloys are lighter than the most commonly used materials in the automotive and aeronautic industries, such as aluminium (density of 2.7 g/cm^3) and steel (density of 7.86 g/cm^3) (Kulekci, 2008; Prabhu et al., 2017). Furthermore, magnesium alloys possess high strength-to-weight ratio, good castability, and good damping capacity, while being non-toxic and recyclable (Čížek et al., 2004; Kulekci, 2008).

TABLE 1 | Lettering code for main alloying elements in magnesium alloys. Data based on (Moosbrugger, 2017).

A	Aluminium	**J**	Strontium	**R**	Chromium
B	Bismuth	**K**	Zirconium	**S**	Silicon
C	Copper	**L**	Lithium	**T**	Tin
D	Cadmium	**M**	Manganese	**V**	Gadolinium
E	Rare Earths	**N**	Nickel	**W**	Yttrium
F	Iron	**P**	Lead	**Y**	Antimony
H	Thorium	**Q**	Silver	**Z**	Zinc

The Challenges

Despite the advantages of magnesium alloys for overall structural weight reduction, the widespread use of these materials has been limited, mainly due to their high susceptibility to corrosion, and, to some extent, due to inferior mechanical properties compared to other structural metals. Therefore, magnesium alloys are currently used for non-structural applications. In the automotive industry, magnesium alloys are used, for instance, for manual transmission housings, steering wheels, and clutch and brake pedal support brackets, while the aeronautic industry makes use of magnesium alloys for aircraft door panels, gearboxes, and transmission casings, for example (Kulekci, 2008; James et al., 2011; Mirza et al., 2013; Czerwinski, 2014; Moosbrugger, 2017). Other applications for magnesium alloys include frames for eyeglasses, electronic devices, and luggage (Callister and Rethwisch, 2014). Furthermore, in recent years, magnesium alloys have been intensively studied as materials for biodegradable implants (Córdoba et al., 2016) due to their high biocompatibility. However, the high corrosion susceptibility of these materials is a concern for biomedical applications as well. Different strategies have been used to mitigate this issue and, as a consequence, magnesium alloys are gaining interest as bioresorbable materials (Zomorodian et al., 2013; Zomorodian et al., 2015).

Alloying Magnesium

Over the past years, many different magnesium alloy systems have been developed as an effort to improve the mechanical properties and corrosion resistance of these lightweight materials. To date, the coding system developed by the American Society for Testing and Materials (ASTM) has been the most widely used both in industry and in research (Moosbrugger, 2017; Mouritz, 2012). It is an alphanumeric system, in which each alloy designation is composed of four main parts, in the following order: two letters indicating the main alloying elements; two numbers indicating the percentage of each of the main alloying elements (rounded-off); one letter to distinguish different alloys that differ only in type and amount of minor alloying elements; and temper designation (Moosbrugger, 2017). The lettering code for alloying elements in magnesium alloys is shown in **Table 1**. For example, magnesium alloy WE43C-T5 has yttrium (W) and rare earths (E) as main alloying elements, in approximate amounts of 4 wt.% and 3 wt.%, respectively. The letter C indicates that it is the third composition of this alloy that became standard, and T5 designates the temper condition (Moosbrugger, 2017).

The most common magnesium alloys belong to the AZ series. These alloys typically consist of a α-Mg matrix and intermetallic β-$Mg_{17}Al_{12}$ phase, distributed along the α grain boundaries (Song et al., 1999). These intermetallic particles have a strengthening effect, and the presence of aluminium-containing β-phase increases the corrosion resistance of the magnesium alloy (Song and Atrens, 1999; Mouritz, 2012). The presence of zinc is believed to enhance the tolerance of magnesium alloys for impurity elements, such as nickel and iron (Song and Atrens, 1999; Kabirian and Mahmudi, 2009). However, the use of these types of alloys is limited to low-temperature applications due to deterioration of alloy properties at temperatures above 120°C, ascribed to the softening of the β-$Mg_{17}Al_{12}$ phase at high temperatures (Ghali and Revie, 2011; Mokhtarishirazabad et al., 2013). This issue can be overcome by the introduction of other alloying elements, such as calcium or rare earth elements (REEs), thereby creating thermally stable precipitates (Mokhtarishirazabad et al., 2013). Another problem associated with the AZ series is the fact that their toughness and ductility tend to be low (Mouritz, 2012). For this reason, magnesium alloys with a reduced aluminium content were developed, namely AM60 and AM50, which display improved toughness and ductility due to a reduction of $Mg_{17}Al_{12}$ intermetallic particles (Magnesium Alloy Fatigue Data, 1995).

Most magnesium alloys possess inferior mechanical properties than other commonly used structural metals such as aluminium, steel, and titanium (Callister and Rethwisch, 2014; Prabhu et al., 2017). Compared to these widely used materials, magnesium alloys generally possess lower strength, creep resistance, fatigue properties, and high-temperature capability (Toda-Caraballo et al., 2014; Manakari et al., 2017; Kujur et al., 2018). Furthermore, the flammability, and ignition behaviour of magnesium alloys can also constitute a downside to their use for many potential applications (Czerwinski, 2014).

The use of different alloying elements has been an effective way to improve the properties of magnesium alloys. For example, zinc is often used to improve the strength of magnesium-based materials, leading to grain refinement and precipitation strengthening (Gupta and Sharon, 2011; Hu et al., 2018; Juan et al., 2021). Creep resistance and thermal stability of magnesium alloys can be enhanced with the addition of calcium (Li et al., 2016; Kondori and Mahmudi, 2017; Incesu and Gungor, 2020). The use of calcium as alloying element leads to the formation of Al_2Ca secondary phase, replacing the thermally unstable β-$Mg_{17}Al_{12}$ phase. Furthermore, calcium also improves the biocompatibility of the alloys (Esmaily et al., 2017). Besides alloying, the properties of magnesium alloys can also be improved with addition of nanoparticles. Metal oxide nanoparticles such as ZnO (Tun et al., 2012) or CeO_2 (Kujur et al., 2018) have been shown to improve the strength of magnesium alloys, while SiC nanoparticles have been studied as reinforcements to improve the creep resistance (Ganguly and Mondal, 2018). These types of nanoparticles hinder dislocation motions, thereby reinforcing the alloy (Ganguly and Mondal, 2018; Kujur et al., 2018). The improvement of magnesium alloy properties with addition of rare earth elements has been described since the 1930s (Luo, 2004). For example, cerium can improve

deformability at room temperature (Wang et al., 2019a), addition of neodymium has been shown to decrease the corrosion rate (Zhang et al., 2011; Arrabal et al., 2012), and yttrium has been found to improve the ultimate tensile strength and elongation of magnesium alloys (Li et al., 2007).

Corrosion of Magnesium and Magnesium Alloys

Corrosion can be defined as the degradation of a material and its properties due to interaction with its environment (Montemor, 2014). To this regard, magnesium is an extremely reactive material. It is anodic to almost all metals and will, therefore, corrode preferentially when present in any galvanic couple. Corrosion of magnesium in aqueous media involves metal dissolution and water reduction, via the following generally accepted reaction (Makar and Kruger, 1993):

$$Mg + 2H_2O \rightarrow Mg(OH)_2 + H_2 \quad (1)$$

During magnesium corrosion, formation of a magnesium hydroxide film on the surface of the metal occurs, accompanied by local alkalization (Makar and Kruger, 1993). The global corrosion reaction of magnesium (**Eq. 1**) can be divided into an anodic and a cathodic reaction (Feliu and Llorente, 2015):

$$Mg \rightarrow Mg^{2+} + 2e^- \quad (2)$$

$$2H_2O + 2e^- \rightarrow 2OH^- + H_2 \quad (3)$$

Some authors consider that the magnesium oxidation reaction (**Eq. 2**) could be a two-step process, involving the formation and hydrolysis of monovalent magnesium ions (Makar and Kruger, 1993; Natta, 2001; Gomes et al., 2019). However, the increased reactivity of Mg^+ would lead to a significantly short lifetime of this ion in solution, and recent experimental evidence, as well as computational analysis, point to direct conversion from Mg to Mg^{2+} as the most probable mechanism for magnesium dissolution (Cain et al., 2017; Esmaily et al., 2017; Yuwono et al., 2019). Nevertheless, the monovalent Mg theory is, to date, still a controversial and intensively discussed topic.

The nature and composition of the surface film formed on magnesium and magnesium alloys during corrosion depends on the alloy composition and on its external environment. Research work regarding this topic has shown that this surface film can be composed of an inner MgO and outer $Mg(OH)_2$ layer (Santamaria et al., 2007; Liu et al., 2009). In the specific case of magnesium-aluminium alloys, a three-component surface layer has been suggested, with an inner aluminium-enriched layer at the alloy surface, followed by a middle MgO layer and an outer layer composed of $Mg(OH)_2$ (Zhang et al., 2015; Esmaily et al., 2016). Furthermore, it has been shown that atmospheric exposure of magnesium alloys can lead to a mixed surface film, composed of MgO, $Mg(OH)_2$, and $MgCO_3$ (Feliu et al., 2009; Feliu and Llorente, 2015). Alongside the surface film, the exact composition of the corrosion products that are formed is also dependent on the elements present in the magnesium alloy (Ghali and Revie, 2011).

Aluminium, neodymium, yttrium, cerium, and zinc have been shown to improve the corrosion behaviour of magnesium alloys (Zhang et al., 2009; Ghali and Revie, 2011; Zhang et al., 2011; Gusieva et al., 2015). The beneficial effects are, however, greatly dependent on the concentration of the alloying elements. While some detrimental effects on the corrosion rate have been observed with the addition of calcium, for example, magnesium alloy corrosion is heavily accelerated when iron, nickel, copper, and/or cobalt are present (Song and Atrens, 1999). These elements are generally known as impurity elements and their concentration in the alloy is maintained as low as possible (Song and Atrens, 1999). Manganese is often added to Mg-Al alloys as scavenger for impurity elements, decreasing the corrosion rate of the alloy due to the decrease of impurity contents (Song and Atrens, 1999; Gusieva et al., 2015).

One of the most efficient strategies against magnesium and magnesium alloy corrosion has been the application of protective coatings. These coatings act as a physical barrier between the underlying metal and the external environment (Montemor, 2014). Many different types of coatings have been developed and applied to various magnesium alloys. Examples include epoxy-based coatings, sol-gel coatings, and protective films formed via plasma electrolytic oxidation. In addition, the concept of self-healing coatings has been studied in more detail in recent years. These coatings contain corrosion inhibitors that are able to impart active protection to the substrate. Furthermore, these corrosion inhibitors can be stored in appropriate carriers, and release of the inhibitor (or inhibitors) is achieved in response to specific stimuli, such as mechanical stress, the presence of certain ions, or changes in local pH (Montemor, 2014). These types of coatings have been designated as "smart" coatings throughout the literature (Montemor, 2014).

WE SERIES MAGNESIUM ALLOYS

As previously mentioned, WE series magnesium alloys possess yttrium and rare earths as major alloying elements (see *Corrosion of Magnesium and Magnesium Alloys*). Usually, minor alloying elements for this series of alloys include neodymium, zinc, and zirconium.

Development of Mg-Y alloys has been an ongoing process for several decades (Polmear, 1994). Continuous demands for high performance lightweight alloys led to the development of the WE series magnesium alloys (Lyon et al., 1991). Several different alloys are part of this category, but the most common are WE43 and WE54. Other alloys in this class include WE32, WE33, and WE94. However, to date, these alloys have rarely been discussed in literature, and no significant studies can be found regarding these alloys. This is mainly related to the fact that WE43 and WE54 possess the most adequate cost-benefit relation of the alloys included in the WE series. In recent years, the increasing interest in WE43 and WE54 as lightweight solutions for different industry sectors has brought on and increasing number of publications regarding these two alloys, in detriment of other alloys included in the WE series. For this reason, the present

TABLE 2 | Comparison of mechanical properties at room temperature of as-fabricated WE43, WE54, and AZ91.

	WE43	WE54	AZ91	References
Tensile Strength (MPa)	220–300	280	165–230	(Gupta and Sharon, 2011; Penghuai et al., 2014; Chen et al., 2019; Zeng et al., 2019)
Elongation (%)	7–14	4	3	(Gupta and Sharon, 2011; Penghuai et al., 2014; Chen et al., 2019; Zeng et al., 2019)
Ultimate Shear Strength (MPa)	162	150	140	Gupta and Sharon, (2011)

TABLE 3 | Comparison of different physical properties of as-fabricated WE43, WE54, and AZ91.

	WE43	WE54	AZ91	References
Thermal Conductivity ($Wm^{-1}K^{-1}$)	51.3	52	84	Gupta and Sharon, (2011)
Electrical Resistivity (nΩm)	148	173	141	Gupta and Sharon, (2011)
Melting Range (°C)	540–640	545–640	470–595	Gupta and Sharon, (2011)

review focuses primarily on WE43 and WE54. However, with continued research regarding WE series Mg alloys, new and improved alloy formulations are likely to be developed and implemented in industry.

Properties

Magnesium alloys with addition of yttrium and rare earth elements were designed to possess enhanced properties compared to other commonly used alloys, such as AZ31. Room temperature mechanical properties of WE alloys are superior when compared to other magnesium alloys (Szakács et al., 2014). **Table 2** shows the comparison of some room temperature mechanical properties of WE43 and WE54 with the properties of the most used all-purpose magnesium alloy today, AZ91. A summary of additional alloy properties is shown in **Table 3**.

WE43 and WE54 are able to retain their properties at high temperatures (Gupta and Sharon, 2011), which is a clear advantage to the use of magnesium alloys belonging to the AZ, QE, and ZE series (Szakács et al., 2014). Long-time exposure tests at temperatures up to 250 °C showed that WE43 retains its initial tensile properties, exhibiting a superior high-temperature performance than aluminium alloys (Lyon et al., 1991). Furthermore, WE series alloys have been shown to be more creep resistant than other magnesium alloys (Jahedi et al., 2018a), while also displaying superior ductility, strength, and corrosion resistance (Ghorbanpour et al., 2019a). In addition, these alloys are biodegradable (Oshibe et al., 2019), extending even further the advantages of their use for a wide range of applications.

Contrary to alloys belonging to the AM series, for example, WE series alloys are age hardenable (Pan et al., 2016). Typically, depending on the specified conditions, higher hardness is achieved with the lowest ageing temperature, while the highest ageing temperature leads to a decrease in peak ageing time (Kang et al., 2017). Throughout literature, the hardness testing conditions, the ageing temperature and ageing time ranges, as well as the initial state of the alloy before testing vary greatly. Nevertheless, the general consensus lies in the good age hardening response of WE series magnesium alloys below 300°C, as well as the fact that lower ageing temperatures generally lead to increased peak ageing hardness values (Mengucci et al., 2008; Kandalam et al., 2015; Huang, 2017; Kang et al., 2017; Kiełbus et al., 2018). In addition, it has been reported that double-step ageing treatments can bring additional benefits for WE alloy performance (Riontino et al., 2008). The age hardening characteristics of WE series magnesium alloys are closely related to the precipitates that are formed during these treatments (see *Heat Treatments*).

Comparing the age hardening behaviour of WE alloys with other magnesium alloys, WE43 and WE54 usually present enhanced age hardening response. AZ31, for example, exhibits a weak strengthening effect, displaying a nearly constant hardness over ageing time (Xu et al., 2018). Furthermore, artificial ageing processes have also a more positive effect on the mechanical properties of WE series magnesium alloys than on EV31 (Kiełbus et al., 2018).

Microstructure

The microstructures of both WE43 and WE54 have been reported to be rather similar. These alloys consist of the α-Mg matrix, usually with Y and Nd present in solid solution in the matrix, and several types of precipitates distributed along grain boundaries and in the grain interiors (Rzychoń and Kiełbus, 2007; Soltan et al., 2019; Kang et al., 2020). **Figure 1** shows a typical microstructure of as-cast WE43. The most commonly identified precipitate phases in WE series magnesium alloys are based on the ternary Mg-Y-Nd system (Zumdick et al., 2019). Rectangular-shaped precipitates are found in these alloys mostly along grain boundaries (Xiang et al., 2018). These precipitates have been identified as $Mg_{24}Y_5$ (Soltan et al., 2019). In addition, fine particles composed of $Mg_{41}Nd_5$ phase and Zr-rich globular precipitates are also part of the microstructure of these alloys (Barylski et al., 2017; Soltan et al., 2019).

In order to further enhance alloy performance, WE series magnesium alloys are usually subjected to different heat treatments (see *Heat Treatments*). Heat treatment has an important influence on alloy microstructure and, therefore, on the alloy properties.

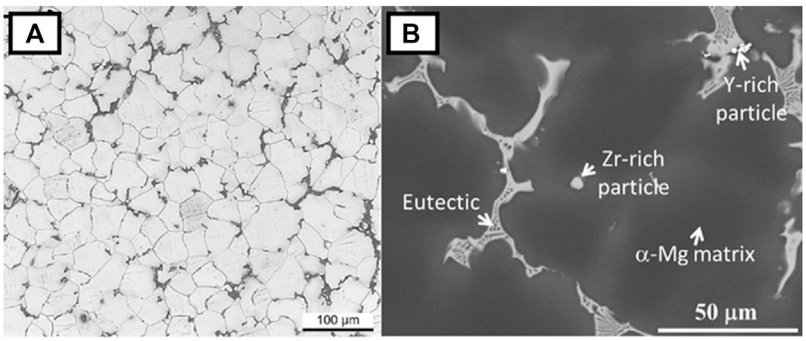

FIGURE 1 | Microstructure of as-cast WE43. **(A)** Optical micrograph evidencing the α-Mg matrix of WE43; **(B)** Scanning Electron Microscopy image of WE43. Images reproduced from (Kang et al., 2020) under the terms of the Creative Commons CC-BY 4.0 License.

Heat Treatments

Tempers designate a series of different natural or artificial ageing procedures. The designation of each temper for magnesium alloys follows the system generally used for aluminium alloys. For WE series magnesium alloys, the most used tempers are the age-hardening processes (Mouritz, 2012) T5 and T6. T5 indicates that the alloy was cooled from fabrication temperature and then artificially aged, while T6 indicates solution-treatment, followed by artificial ageing (Mouritz, 2012). During T6 treatment, the alloy undergoes full recrystallization (Ghorbanpour et al., 2019a; Ghorbanpour et al., 2019b). The precipitates formed during this process tend to be localized at grain-boundaries (Ghorbanpour et al., 2019a). In contrast, the materials' original grain structure is maintained during T5 treatment, and the formed precipitates are more evenly distributed (Ghorbanpour et al., 2019a).

Precipitation during ageing treatments of WE series magnesium alloys and the effect of these precipitates on alloy properties have been heavily studied topics in recent years (Nie and Muddle, 2000; Nie et al., 2001; Antion et al., 2003; Nie, 2012; Jiang et al., 2017). The exact structure and composition of the formed precipitates depend on the processing history of the material (Ghorbanpour et al., 2019b). The most commonly encountered precipitates in WE alloys are designated as β", β′, β_1, and β (Ghorbanpour et al., 2019b). The β" phase is characterized by a Mg_3Nd composition and contributes to an increase in alloy hardness during the initial stages of the ageing process (Liu et al., 2010; Ghorbanpour et al., 2019b). This β" phase is gradually transformed to β′ phase ($Mg_{12}NdY$) at ageing temperatures between 200°C and 250°C (Jiang et al., 2017; Ghorbanpour et al., 2019b). Ageing of the alloy at 250°C leads to the appearance of the β_1 phase, with a $Mg_3(Nd,Y)$ composition (Jiang et al., 2017; Ghorbanpour et al., 2019b). If the ageing process is being conducted at 250°C for a long time, precipitation of the equilibrium β phase ($Mg_{14}Nd_2Y$) occurs (Jiang et al., 2017; Ghorbanpour et al., 2019b). From these precipitation phases, β′ has been identified as the phase mostly responsible for the enhanced strength of WE series magnesium alloys after heat treatment, although it has been found that β" can also contribute to the precipitation strengthening effect (Nie and Muddle, 2000; Liu et al., 2013; Jahedi et al., 2018a). It has been demonstrated that the shape and orientation of β' precipitates can have an important effect on dislocation motions by creating effective barriers to this movement (Nie and Muddle, 2000; Xu et al., 2018).

In general, WE series magnesium alloys exhibit superior mechanical properties after appropriate heat treatment, compared to their properties before these treatments (Yu et al., 2008). Comparing the effects of T5 and T6 treatments to WE43, it has been demonstrated that WE43-T6 usually exhibits limited ductility compared to WE43-T5 due to large grain-boundary precipitates that facilitate intergranular fracture (Jahedi et al., 2018a; Ghorbanpour et al., 2019c). Furthermore, fatigue strength of WE43-T5 tends to be improved in comparison to WE43-T6 due to finer grain size achieved after the T5 treatment (Adams et al., 2016; Wang et al., 2019b; Ghorbanpour et al., 2019c).

Processing Methodologies

To date, magnesium alloys are most commonly produced by casting methods (Luo, 2013), and the WE series is no exception. WE43 and WE54 are often processed by sand casting or permanent mould casting (Jiang et al., 2017; Westengen et al., 2006). In recent years, direct-chill casting has emerged as a favourable alternative to conventional casting methods. Direct-chill casting makes use of a higher cooling rate than other casting techniques (Jahedi et al., 2018b). A higher solidification rate of the cast material leads to high supersaturation and solid solubility of Nd and Y in the α-Mg matrix (Jiang et al., 2017). Therefore, an improvement in strength and hardness of the as-cast material can be achieved (Jiang et al., 2017). In general, however, magnesium alloys are not used in the as-cast condition, as further property improvement is usually needed for most applications (Jahedi et al., 2018b). In this sense, the cast material is subjected to mechanical and/or thermal processing (thermal treatments were discussed in *Heat Treatments*) (Jahedi et al., 2018b).

Mechanical deformation is employed for alloy grain refinement and microstructure homogenization (Jahedi et al., 2018b). Examples of common deformation techniques include hot-rolling (Yu et al., 2008), forging (Salandari-Rabori et al., 2018), and hydrostatic pressing (Pachla et al., 2012), all of which have been employed for grain refinement of WE43 (Lukyanova et al., 2017). Alloy deformation by rolling, for example, leads to

crystallographic reorientation of the grains, which can lead to an increase in dislocation density in the alloy microstructure (Jahedi et al., 2018b). Dislocations represent preferential sites for precipitate formation (Ghorbanpour et al., 2019b). Thus, an increase in dislocation density can lead to increased density of precipitates within the microstructure of the processed alloy, with consequent improvement in alloy strength, elongation in tension, and fatigue resistance (Ghorbanpour et al., 2019b). This has been demonstrated for WE43 (Ghorbanpour et al., 2019b). If both mechanical deformation techniques and heat treatments are employed to the same alloy, the deformation techniques are used before the thermal treatments (Choudhuri et al., 2013).

Continuous improvements in alloy processing technology have led to the development of several new processing techniques to further enhance the properties of magnesium alloys in general, and WE series in particular (Minárik et al., 2018). Many of these techniques are based on severe plastic deformation (SPD) of the material (Minárik et al., 2018). From these, the most commonly studied in combination with WE series magnesium alloys are Equal Channel Angular Pressing (ECAP) and High Pressure Torsion (HPT) (Torkian et al., 2018).

During ECAP, the material (usually in rod or bar form) is forced through a bended channel (Pereira et al., 2017). At the channel bend, shear strain is generated in the material as it passes through (Shaat, 2018). The intensity of the shear deformation can be controlled by varying the internal channel angle and the outer curvature angle of the channel (Shaat, 2018). Furthermore, higher strains can be obtained by repeating the process several times (Wang et al., 2017). These multiple passes can be performed repetitively with no change to the processing conditions, or a rotation can be imposed on the material between different ECAP passes (Wang et al., 2017). Scalability of the ECAP process to industrial standards is currently being investigated (Frint et al., 2011; Lefstad et al., 2012; Frint et al., 2016; Shaat, 2018). ECAP processing leads to significant grain refinement of the alloy, generally resulting in improved strength. For example, Zhang et al. (Zhang et al., 2020) found that the ultimate tensile strength of WE43 increased from 255 MPa in the as-extruded condition, to 380 MPa after three-pass ECAP. This increase in the strength of the alloy was accompanied by a decrease in the ductility, as expected: from 20.9% in the as-extruded alloy to 8.8% after three-pass ECAP (Zhang et al., 2020). Furthermore, the authors found that multi-pass ECAP led to the generation of significant dislocations and residual stresses, resulting in significant work hardening of the WE43 alloy (Zhang et al., 2020).

For HPT processing, the material, in the form of a thin disk, is compressed under high pressure, and simultaneously subjected to torsional strain (Zhilyaev and Langdon, 2008). The material is deformed by shear due to surface frictional forces that arise during the process (Zhilyaev and Langdon, 2008). Similar to ECAP, HPT leads to an increase in the ultimate tensile strength and yield strength of the alloy (Figueiredo and Langdon, 2019). Liu et al. (Liu et al., 2017) found that extruded WE43 possessed an ultimate tensile strength of 244 MPa, with 8% elongation, while processing by HPT yielded an ultimate tensile strength of 256 MPa with 0.5% elongation. Once again, the strengthening effect conferred by SPD processing of the material led to a significant decrease in alloy ductility (Liu et al., 2017).

Both ECAP and HPT are used to achieve an ultrafine grain microstructure in the processed material (Minárik et al., 2018). It has been extensively demonstrated that using ECAP (Martynenko et al., 2018; Minárik et al., 2018; Torkian et al., 2018) or HPT (Lukyanova et al., 2016; Lukyanova et al., 2017) for WE43 processing can lead to improvements in hardness and overall mechanical properties of the alloy due to significant grain refinement.

Over the last 2 decades, additive manufacturing has been considered an attractive manufacturing process for a wide range of materials (Bourell et al., 2009). Additive manufacturing has been established as a cost-efficient method to manufacture complex shapes (Zumdick et al., 2019). In recent years, additive manufacturing technology has begun to be tested for WE series magnesium alloys. To date, the most investigated additive manufacturing technique for WE43 is selective laser melting (SLM). SLM is a powder bed fusion process: thin layers of metal powder are deposited onto the working area and focused laser radiation is responsible for melting the powder into the desired shape (Frazier, 2014; Zumdick et al., 2019). Repetitive powder deposition and melting leads to the creation of three-dimensional components (Frazier, 2014). It has been shown that it is possible to manufacture WE43 with a dense and homogeneous microstructure via SLM (Zumdick et al., 2019; Gangireddy et al., 2019). However, SLM requires secondary densification processes to achieve the desired material properties (Calvert, 2015; Gangireddy et al., 2019). For example, Zumdick et al. (2019) found no significant improvement in the ultimate tensile strength of as-extruded WE43 and the same alloy subjected to SLM. In addition, high operating temperatures during SLM can lead to loss of material performance due to increased grain growth (McClelland et al., 2019). Therefore, other additive manufacturing techniques, such as additive friction stir deposition, are currently being investigated as an alternative to SLM (Calvert, 2015).

In general, direct comparison of mechanical properties of WE series alloys obtained by different processing methodologies and/or subjected to different heat and ageing treatments is not feasible, since widely different processing parameters are used throughout literature, in addition to the varying original conditions of the studied alloys.

Alloying Elements

The rare earth content specified for each magnesium alloy from the WE series is a mixture of different rare earth elements that vary from alloy to alloy. Most commonly, the rare earth elements included in the alloys are Nd and other heavier REEs such as Gd (Pan et al., 2016).

Addition of rare earth elements to magnesium and magnesium alloys brings several improvements to the properties of these materials. Rare earths are able to improve the mechanical properties of magnesium-based materials at ambient and elevated temperatures due to the precipitation of stable RE-Mg intermetallic compounds (Maruyama et al., 2002; Pai et al., 2012). These intermetallics can act as obstacles to dislocations, therefore improving the creep resistance of the material (Witte et al., 2008; Pai et al., 2012). Furthermore, it

has been shown that the presence of rare earth elements in magnesium alloys can have a positive effect on the corrosion resistance of these materials (Zhang et al., 2011). In general, rare earth elements have the ability to form intermetallic compounds with impurity elements, such as Fe for example, therefore providing a scavenger effect that mitigates the negative effect of the presence of impurity elements in magnesium alloys (Zhang et al., 2011). Furthermore, studies have shown that rare earth elements can be incorporated into the passive oxide/hydroxide surface film on magnesium alloys in aqueous media, stabilizing it and thereby increasing the protective performance of this film (Nordlien et al., 1997; Zhang et al., 2011). Despite the advantages of using rare earths as alloying elements, the addition of heavy REEs can lead to processing issues that often result in inhomogeneous composition and, therefore, performance-related problems in the final alloy (Ning et al., 2014; Pan et al., 2016). In addition, the cost of heavy rare earth elements can be very high, due to the fact that the global reserves of these elements are limited (Ning et al., 2014; Pan et al., 2016). Thus, several studies have been devoted to the modification of commercial WE series magnesium alloys, aiming for the reduction of heavy rare earth elements (Pan et al., 2016). Such modifications have mainly been focused on the substitution of heavy rare earth elements by other elements such as Y, Nd, and Zr (Pan et al., 2016).

The solid solubility of yttrium in magnesium is relatively high and yttrium enhances the strength of magnesium alloys, mainly due to solid-solution hardening (Gupta and Sharon, 2011; Ghorbanpour et al., 2019a). At 500°C, the solid solubility of Y in the α-Mg phase is ~4 at. % (Zhao et al., 2011). This solubility decreases significantly with decreasing temperature (at 450°C, solid solubility of Y decreases to 2.7 at. %), which enables effective solution and ageing strengthening effects in yttrium-containing magnesium alloys (Zhao et al., 2011; Jiang et al., 2017). It has been reported that the use of yttrium as alloying element improves the hardness and creep resistance of magnesium alloys via precipitation of intermetallic phases that impede dislocation movements (Aghion et al., 2008; Su et al., 2013). Furthermore, the increase of Y in Mg-Y-RE alloys leads to continuous increase of the yield strength of these alloys (Su et al., 2013; Luo et al., 2019). Further increase of yttrium content can, however, lead to coarse grain boundary precipitates which can lead to a decrease of the tensile strength and elongation of the alloy due to a reduction in the cohesive strength of the grain boundaries (Su et al., 2013). The precipitation of metastable Y-containing phases also contributes to the increase in the heat resistance of magnesium (Anyanwu et al., 2001). These precipitate phases remain stable at temperatures >200°C (Anyanwu et al., 2001). However, it has been reported that yttrium can be oxidized at the melting stage during alloy processing (Luo et al., 2019). If very high amounts of yttrium are used, Y_2O_3 inclusions may be formed during the casting process (Luo et al., 2019). These inclusions have a detrimental effect on the mechanical properties of the alloy (Luo et al., 2019). To overcome this issue, gadolinium can be used as a partial substitute for yttrium in magnesium alloys, due to the fact that Gd has a low tendency to form oxide inclusions during alloy processing (Luo et al., 2019). In addition, it has been shown that, due to the similar atomic radius of yttrium and gadolinium, these two rare earth elements are easily interchangeable in magnesium alloy formulations (Luo et al., 2019). Furthermore, Gd has a strengthening effect similar to the one reported for yttrium (Hort et al., 2010; Jiang et al., 2017; Luo et al., 2019). In fact, several studies have shown that an increased amount of Gd (up to 10 wt.%) can lead to a more significant improvement in the mechanical properties of WE series magnesium alloys than yttrium (Hort et al., 2010; Szakács et al., 2014; Pan et al., 2016; You et al., 2017). However, the use of high weight fractions of Gd leads to an increase in alloy density, with the added disadvantage of higher cost (Li et al., 2019). Therefore, Gd content in commercial WE series magnesium alloys is usually kept low.

Similarly to yttrium and gadolinium, neodymium, as alloying element, also has a positive effect on the mechanical properties of magnesium alloys (Jin et al., 2015). This element has been used as a substitute of heavy rare earth elements (Ning et al., 2014). Neodymium displays a decreased solid solubility in Mg compared to Y (0.63 at. % at 550°C), and forms stable precipitates with magnesium (Yan et al., 2008; Le et al., 2010; Gupta and Sharon, 2011). The $Mg_{12}Nd$ phase is thermally stable and able to pin dislocation movement, thereby improving the high temperature creep resistance of magnesium alloys (Yan et al., 2008; Gupta and Sharon, 2011). Furthermore, the presence of Nd in aluminium-containing magnesium alloys can decrease the microgalvanic corrosion rate in these alloys via formation of Al_3Nd phase (Zhang et al., 2011).

In addition to the benefits discussed above, yttrium, gadolinium, and neodymium increase the ignition temperature and flammability resistance of magnesium alloys (Tan et al., 2019). This effect has been attributed to the ability of these elements to form a rare earth-containing oxide layer on the magnesium alloy surface, preventing the access of oxygen, moisture and aggressive species to the alloy (Tan et al., 2019).

Apart from rare earth elements, zirconium and zinc are common alloying elements for WE series magnesium alloys. Zirconium is the most efficient grain refiner for magnesium alloys to date, leading to significant improvement in structural uniformity of the alloys, and to consequent improvement in alloy properties (StJohn et al., 2005; Ali et al., 2015). Zinc is usually present in WE series magnesium alloys in low quantities (<0.02 wt.%). The main effect of the use of zinc is the improvement of alloy ductility due to formation of Zn-Zr secondary phases (Jahedi et al., 2018a; Ghorbanpour et al., 2019a). In addition, it has been shown that addition of zinc to Mg-Y binary alloys leads to improved creep strength of the alloy due to a higher dislocation density in the presence of zinc (Maruyama et al., 2002; Suzuki et al., 2004). Extensive research work has been performed on the modification of commercially available WE series magnesium alloys with an increased amount of Zn. It was found that WE43-T6 modified with 0.2 wt.% of zinc leads to a tensile strength of 345 MPa, representing an improvement of 38% (Pan et al., 2016). Furthermore, it has been suggested that the use of a higher Zn-content in WE43 can lead to a decrease in the solubility of

rare earth elements, resulting in a higher volume fraction of precipitation phases that are able to reduce the mobility of dislocations (Kang et al., 2014). Zinc can also improve the stability of the passive layer formed on the surface of magnesium alloys in aqueous media (Nordlien et al., 1997).

CORROSION OF WE SERIES MAGNESIUM ALLOYS

Corrosion Mechanism

The corrosion mechanism of WE series magnesium alloys has been extensively studied over the years. In general, the corrosion resistance of metal alloys is tested during immersion of the alloy under study in an appropriate electrolyte. In the case of WE series magnesium alloys, these studies have been carried out in a wide range of different electrolytes. The most commonly used media for the study of aqueous corrosion of WE magnesium alloys are NaCl, Na_2SO_4, and electrolytes that simulate physiological conditions, such as SBF (Simulated Body Fluid).

Similarly to the general corrosion processes observed for pure magnesium and for many other magnesium alloys (as discussed in section 1.3), WE series magnesium alloys also form protective surface layers, mainly based on $Mg(OH)_2$ and MgO. However, the exact composition of these surface films is highly dependent on the conditions in which they are formed, i.e. on the composition of the electrolyte to which the alloys are exposed, and on the original alloy composition. Nonetheless, the surface films formed in Na_2SO_4, NaCl, or SBF seem to be qualitatively similar. While some authors report the formation of a uniform surface layer, mainly composed of $Mg(OH)_2$ and with low amounts of rare earth elements (Arrabal et al., 2008), others suggest a bi-layered surface film: $Mg(OH)_2$ outer layer, which has been reported to be porous, and an inner layer constituted mainly by MgO, Y_2O_3, and $Y(OH)_3$ (Ardelean et al., 2013; Chu and Marquis, 2015). Ca and P are usually present in the surface film when the alloy is exposed to SBF (Dvorský et al., 2019). WE43 has also been tested in alkaline media containing Cl^- ions, and this alloy was reported to form a passive layer composed of MgO, $Mg(OH)_2$, and RE_2O_3 phases (where REEs can be Y, Nd, or Gd) (Ninlachart et al., 2017). (Chu and Marquis, 2015)

In general, it has been found that the surface films formed on WE series magnesium alloys are thinner than for pure magnesium (Zucchi et al., 2006a; Leleu et al., 2018). This has been attributed to the fact that a steady-state condition between surface film thickening and propagation of corroded area may be achieved for WE magnesium alloys, while expansion of the corroded area prevails for pure magnesium (Zucchi et al., 2006a). While thinner, the surface films formed on WE series magnesium alloys have been reported to be more stable and more protective due to the presence of rare earth elements in their composition (Kalb et al., 2012; Dvorský et al., 2019; Leleu et al., 2019; Soltan et al., 2019).

Comparing the corrosion behaviour of WE series magnesium alloys with pure magnesium or with other magnesium alloys, there seems to be no definitive consensus as to which magnesium-material has the superior corrosion resistance. WE43 has been reported to be less susceptible to the action of aggressive Cl^- ions than pure magnesium (Leleu et al., 2018; Knapek et al., 2018), while also displaying much less severe localized damage in SBF than ZK60 (Jamesh et al., 2015). In comparison to the commonly used AZ91, it has been shown that WE43 possesses a slower hydrogen evolution reaction (**Eq. 3**) in Na_2SO_4 (Ardelean et al., 2013), and an overall higher corrosion resistance in NaCl (Arrabal et al., 2008). However, a higher corrosion rate of WE43 in Na_2SO_4 compared to AZ31 and AZ91 has also been reported (Leleu et al., 2019). The corrosion rate of WE43 has been shown to be lower than other rare earth containing magnesium alloys, such as EV31 and ZE41 (Soltan et al., 2019). WE54 was found to be slightly more resistant to *in vitro* degradation than pure magnesium, but the corrosion performance of WE54 was reported to be significantly poorer than for AZ91 for the same testing conditions (Walter and Kannan, 2011). Other authors reported that the corrosion rate of WE43 and WE54 during salt fog tests was only slightly higher than for AZ91 and for some aluminium casting alloys (e.g. A201) (Cho et al., 2008). These seemingly contradictory results can be related to the use of different combinations of parameters such as electrolyte type, electrolyte concentration, processing methodology of the studied alloys, and heat treatments to which the alloys were subjected prior to corrosion testing. As is the case for the previously stated mechanical properties of WE series magnesium alloys, the microstructure of these materials has a major influence in their corrosion behaviour.

Despite the different conclusions drawn by different researchers, the general consensus regarding the corrosion mechanism of WE series magnesium alloys lies in the fact that corrosion of these types of alloys involves the Zr-rich precipitates present in the microstructure, due to microgalvanic coupling effect (Coy et al., 2010; Ardelean et al., 2013). Zr-rich particles can be found both in WE43 and in WE54, and it has been demonstrated that these precipitates possess a Volta potential difference with respect to the magnesium matrix superior to +170 mV (Coy et al., 2010). This difference is high enough to cause significant galvanic coupling between the precipitates and the magnesium matrix, favouring the dissolution of the latter (Coy et al., 2010). This high Volta potential difference has been attributed to the presence of Fe in these precipitates (Coy et al., 2010). In this sense, the intermetallic particles act as local cathodes that promote the dissolution of the neighbouring magnesium matrix, with eventual propagation of the corrosion process (Leleu et al., 2019; Soltan et al., 2019). This phenomenon has been consistently reported for WE series magnesium alloys (Coy et al., 2010; Kalb et al., 2012; Ninlachart et al., 2017; Leleu et al., 2019; Soltan et al., 2019). In contrast, it has been reported that yttrium-containing intermetallic phases have little to no effect on the corrosion process of WE magnesium alloys. The Volta potential difference of these precipitates in relation to the magnesium matrix has been demonstrated to be negligible compared to the Zr-rich intermetallic phases, even though they demonstrate cathodic behaviour relative to the magnesium matrix (Coy et al., 2010; Kalb et al., 2012; Soltan et al., 2019; Kharitonov et al., 2021).

In general, micro-galvanic corrosion in WE series magnesium alloys may be reduced through grain refinement and a more

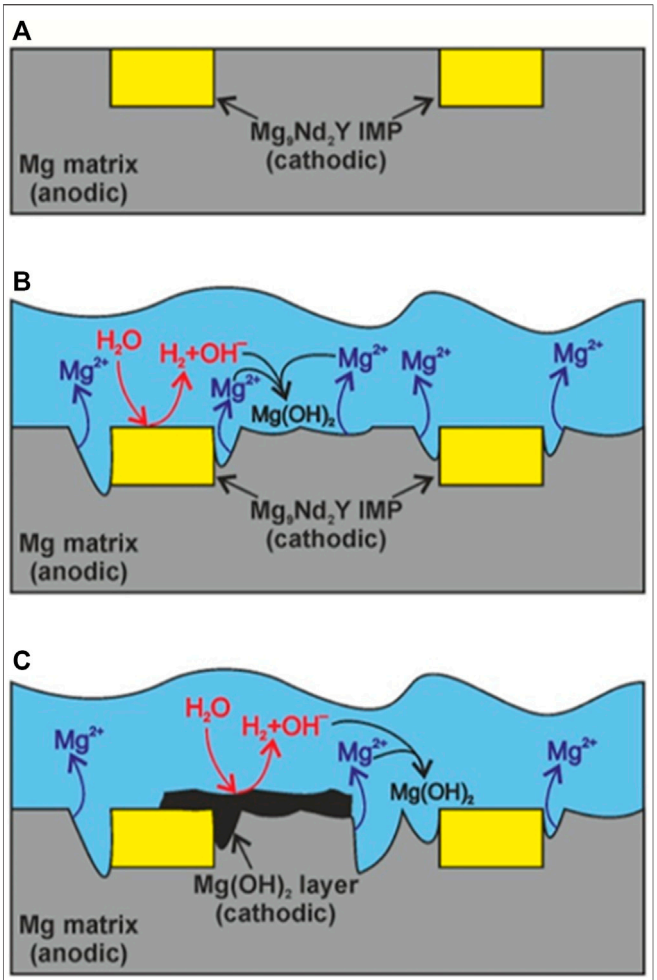

FIGURE 2 | Possible mechanism of corrosion for WE series magnesium alloys **(A)**, involving the formation of a $Mg(OH)_2$ layer on the surface of the alloy **(B)**, with localized microgalvanic corrosion at preferential sites **(C)**. Figure reproduced from (Kharitonov et al., 2021) under the terms of the Creative Commons CC-BY 4.0 License.

continuous distribution of secondary phases (Pereira et al., 2021). A high density of REE-containing secondary phases in WE series Mg alloys has been shown to attenuate the corrosion process of these alloys since these secondary phases may act as corrosion barriers (Xie et al., 2021). However, an increased density of intermetallics also increases the density of corrosion-prone grain boundaries (Eivani et al., 2021). The overall corrosion behaviour of WE series Mg alloys is, in general terms, governed by two major factors: a) the microgalvanic coupling effect between the intermetallic phases/particles and the magnesium matrix has a detrimental effect on the corrosion performance of these materials; and b) the inclusion of REEs in the alloy matrix and the incorporation of these elements in the surface film during alloy corrosion can be beneficial (Leleu et al., 2019). **Figure 2** illustrates the possible mechanism of corrosion for WE series magnesium alloys, involving the formation of a $Mg(OH)_2$ layer on the surface of the alloy and localized microgalvanic corrosion at preferential sites. However, it should be stated that, for binary Mg-Y alloys, it has been demonstrated that an increase in the Y content, which leads to an increase in the volume fraction of $Mg_{24}Y_5$ phase, may be responsible for inferior corrosion resistance due to the increase in cathodic sites (Sudholz et al., 2011). Yttrium, when present in solid solution, delays the dissolution of the magnesium matrix (Sudholz et al., 2011). It is worth to note that high purity magnesium is often reported as a material possessing higher corrosion resistance compared to magnesium alloys due to the absence of intermetallic phases that can induce microgalvanic coupling (Dvorský et al., 2019).

As previously mentioned, the corrosion behaviour of WE series magnesium alloys is dependent on the specific microstructure of the alloy. Thus, the processing conditions can play a major role in the resistance of these alloys to degradation. Comparing as-cast and aged WE54 specimens, it was reported that corrosion propagation was most uniform for the as-cast condition (Rzychoń et al., 2007). This was related to the fact that an increase in ageing time leads to an increase in the volume fraction of intermetallic phases and, therefore, of microgalvanic cells (Rzychoń et al., 2007). Similar findings were reported for both WE54 and WE43 (Smola et al., 2012; Yang et al., 2020). However, if a fine dispersion of precipitates can be achieved through ageing treatments, propagation of alloy dissolution can be delayed (Chu and Marquis, 2015).

The overall corrosion behaviour of WE series magnesium alloys seems to be governed by two major factors: on the one hand, the microgalvanic coupling effect encountered between the intermetallic phases and the magnesium matrix has a detrimental effect on the corrosion performance of these materials; on the other hand, the incorporation of rare earth elements in the surface film during alloy corrosion can be beneficial (Leleu et al., 2019).

Even though WE series magnesium alloys may possess a somewhat enhanced corrosion resistance when compared to other magnesium alloys, the anticorrosive performance of these materials has to be further improved for most applications. Several different protection strategies against corrosion of WE magnesium alloys are reported in *Corrosion Protection Strategies* .

Corrosion Protection Strategies

The application of protective coatings has been the most efficient way to protect magnesium alloys from corrosion. These coatings are designed to be effective barriers that protect the underlying metallic substrate from the aggressive environment. For years, chromate coatings were the dominant protection method for several different metals and alloys. These coatings offer a highly inhibitive effect of the corrosion processes, while displaying improved coating strength and hardness (Eppensteiner and Jenkins, 1999; Gray and Luan, 2002). However, hexavalent chromium is linked to serious health hazards and, thus, its use has been heavily regulated (European Union, 2006; Annangi et al., 2016; Junaid et al., 2016). In this sense, extensive research has been carried out regarding the search for safer coating formulations. For magnesium alloys, the most used coating alternatives to chromate are anodized coatings (Pinto

et al., 2010), Plasma Electrolytic Oxidation (PEO) coatings (Liu et al., 2016a), rare-earth conversion coatings (Montemor et al., 2007), and organic coatings (Calado et al., 2017; Calado et al., 2018). The development of protective coatings for magnesium alloys for their use in the automotive and aerospace industries, for example, is aimed at the maximum possible long-term protection of the alloy. In contrast, coatings developed for biological applications are often aimed at slowing down substrate dissolution, to allow for the use of magnesium alloys as bioresorbable temporary implants.

Given the newly-gained interest in WE series magnesium alloys for industrial applications, the vast majority of literature concerning protective strategies for WE series magnesium alloys to date is based on protective solutions which have proven efficiency for other magnesium alloy series. Coatings applied by electrolytic processes (e.g., PEO) seem to display minimal dependency on the specific composition of the alloy and/or on the type and distribution of its secondary phases. However, the microstructure and composition of each alloy is expected to play a more major role in the application of organic and hybrid organic-inorganic coatings, mainly due to different interactions between the coating and the alloy surface, influencing coating adhesion. Moreover, corrosion inhibitors may display protective mechanisms which are dependent on the interaction with specific alloying elements and/or secondary phases of the Mg alloy under study. However, presently, literature on passive corrosion protection strategies and active, self-healing coatings for WE series magnesium alloys is too scarce to evaluate these specific challenges effectively and objectively. For this reason, the protective strategies cited in this review give an overview of protective mechanisms with proven efficiency for WE43 and WE54 alloys. These examples are given below.

Anodization is an electrolytic process through which the surface of the metal is modified by formation of a stable oxide layer through the application of anodic voltage or current (Blawert et al., 2006; Gupta and Sharon, 2011). WE43 was successfully anodized in an alkaline silicate-based electrolyte (Xia et al., 2004). It was shown that the anodized coating increased the protection of the alloy during testing in 0.86 M NaCl, as no pitting of the anodized surface was detected after 140 h of immersion in the corroding medium (Xia et al., 2004). This effect was attributed to formation of MgO, and subsequent hydration of MgO to $Mg(OH)_2$, which was found to actively block the pores of the anodized film (Xia et al., 2004). Anodized WE43 was also tested in *in vivo* implants (Oshibe et al., 2019). The phosphorous-based anodized coating was able to delay the degradation of the implants while inhibiting the formation of hydrogen gas (Oshibe et al., 2019). This anodized coating also displayed good biocompatibility in bone tissue during long-term follow ups (Oshibe et al., 2019). If anodization is performed at very high voltages, the process is mostly known as Plasma Electrolytic Oxidation (PEO) (Bender et al., 2013). This process has effectively been applied to WE43. For example, subjecting WE43 to PEO in a silicate/phosphate-based electrolyte led to increased polarization resistance and decreased corrosion rate in comparison to the untreated alloy

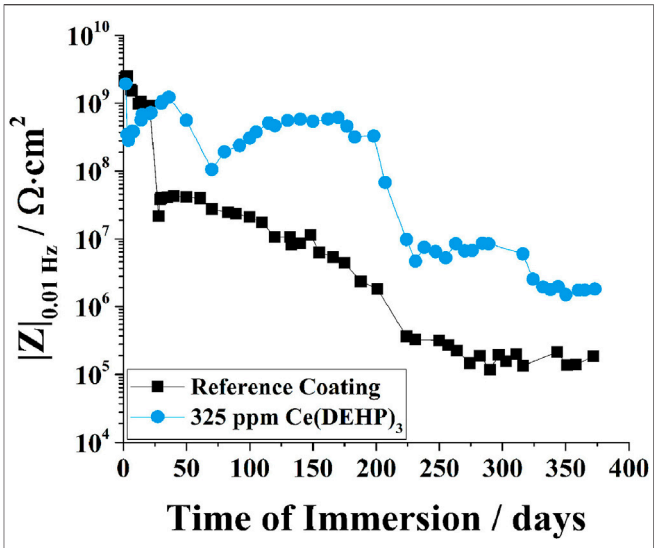

FIGURE 3 | Evolution of low frequency impedance modulus (0.01 Hz) of WE43 coated with a hybrid epoxy-silane coating (reference coating), and with a hybrid epoxy-silane coating containing 325 ppm $Ce(DEHP)_3$, during immersion in 0.5 M NaCl. Image reproduced from (Calado et al., 2021) with permission.

in 3.5 wt.% NaCl (Tekin et al., 2013). Using a commercial electrolyte formulation, it was demonstrated that implants made of WE43 subjected to PEO displayed a delayed gas release at the implant surface, while also enabling the alloy to retain its strength during an *in vivo* implantation period of 12 weeks (Imwinkelried et al., 2013). Since the coatings formed via anodization or PEO are usually porous, a top-layer can be applied to seal the pores and impart additional protection. This top-layer can, for example, be a polymeric coating.

In addition to coatings applied by electrolytic processes, organic coatings have also been successfully applied for WE series magnesium alloys. For example, long-chain silane compounds have been shown to form a crystalline-like protective structure on the surface of WE43, thereby aiding in the corrosion protection of this alloy (Zucchi et al., 2006b). In recent years, significant attention has been given to the development of anticorrosive coatings for biomedical applications of WE43. For example, efficient protection of WE43 has been achieved with bi-layered coatings consisting of hydroxyapatite/poly-L-lactic acid (Diez et al., 2016), or chitosan/bioactive glass (Witecka et al., 2021). To further improve the protective ability of coatings, corrosion inhibitors can be used. These additives have the ability to impart active protection in case the applied coating is damaged during its service-life. 8-hydroxyquinoline (Argade et al., 2019) and sodium dioctylphosphate (Chirkunov and Zheludkevich, 2018) have been found to be efficient inhibitors for WE series magnesium alloys due to their ability to form stable species with magnesium cations during substrate corrosion, thereby forming protective surface films. However, to date, very few inhibitors have been identified as effective for the protection of WE series magnesium alloys, and the protection conferred by these corrosion inhibitors

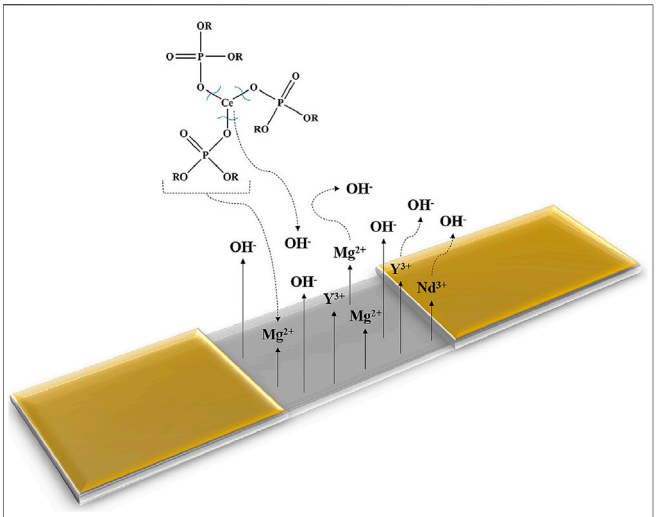

FIGURE 4 | Mechanism of corrosion protection conferred by $Ce(DEHP)_3$ to WE43 magnesium alloy. Figure reproduced from (Calado et al., 2021) with permission.

has mostly been studied in non-coated systems (Argade et al., 2019; Shi et al., 2020; Yang et al., 2015). Recently, Calado et al. (Calado et al., 2021) reported a newly-developed cerium organophosphate corrosion inhibitor for smart corrosion protection of WE43. The authors showed that addition of cerium tri(bis(2-ethylhexyl)phosphate) ($Ce(DEHP)_3$) to a thin epoxy-silane coating significantly improved coating barrier properties in comparison to the unmodified coating (Calado et al., 2021). In addition, $Ce(DEHP)_3$ displayed a cyclic protective behaviour, as illustrated in **Figure 3** (Calado et al., 2021). The corrosion protection conferred by $Ce(DEHP)_3$ was linked to its pH-dependent activation: local alkalization due to magnesium corrosion (see **Eq. 3**) leads to hydrolysis of $Ce(DEHP)_3$, resulting in the formation of cerium and organophosphate ions (Calado et al., 2021). The interaction between OH^- and cerium ions, and between OH^- and ions released from the substrate (i.e. Y^{3+}, Nd^{3+}, and Mg^{2+}) leads to the formation of $Ce(OH)_3$, $Y(OH)_3$, $Nd(OH)_3$, and $Mg(OH)_2$ (Calado et al., 2021). While $Mg(OH)_2$ is relatively soluble, the rare earth-containing hydroxides are extremely stable species, providing efficient local corrosion inhibition at cathodic sites (Calado et al., 2021). In addition, organophosphate ions can interact with Mg^{2+} ions released during magnesium dissolution, thereby forming stable magnesium-organosphosphate species, which confer corrosion inhibition at anodic sites (Calado et al., 2021). **Figure 4** shows the corrosion protection mechanism proposed by the authors. Overall, $Ce(DEHP)_3$ was shown to be one of the first truly efficient corrosion inhibitors for WE series magnesium alloys, conferring long-term, pH-sensitive, and self-healing protection. This inhibitor was also shown to be effective for AZ series magnesium alloys (Calado et al., 2020), and for mild steel (Morozov et al., 2019).

Apart from the most common coating methods that were cited above, WE series magnesium alloys have also been subjected to other alternative coating methods. Improved corrosion resistance of WE43 has been achieved, for example, by a) application of biofunctional chitosan-bioactive glass coatings via electrophoretic deposition (Heise et al., 2017; Höhlinger et al., 2017); b) surface modification using Laser Surface Melting (LSM) technique (Guo et al., 2005; Liu et al., 2016b); c) ion-implantation, e.g. hafnium (Jin et al., 2016) or Ti-O (Zhao et al., 2013); d) application of amorphous SiC film via Plasma Enhanced Chemical Vapour Deposition (Li et al., 2012); and e) application of TaN film using reactive magnetron sputtering (Jin et al., 2018).

The development of protective coatings for WE series magnesium alloys is still a growing research topic, which is in no way as explored as the development of protective solutions for other magnesium alloys, such as AZ series.

APPLICATIONS

The superior properties of WE series magnesium alloys has led to an increasing usage of these types of alloys in different industries, in addition to a growing research interest in several fields. The good high temperature behaviour of WE magnesium alloys, allied to the low density of these materials, has been of particular interest for the automotive and aerospace industries.

In the automotive sector, WE alloys are widely used in high-performance cars as engine block components, e.g., pistons and cylinders (Kierzek and Adamiec, 2011; Malayoğlu and Tekin, 2015). Furthermore, given their superior creep resistance and high temperature stability, in contrast to other magnesium alloys, WE series alloys are expected to be suitable for powertrain applications (Blawert et al., 2004).

WE43 and WE54 are both used in helicopters (Gupta and Sharon, 2011). For example, WE43 is used in the gearboxes of the *Eurocopter* EC120, *Eurocopter* NH90, and *Sikorsky* S92 (Mouritz, 2012). Due to their stability at high temperatures, WE series magnesium alloys are used in jet engines, particularly in auxiliary power units, accessory drives, constant speed drives, and engine gearboxes (Malayoğlu and Tekin, 2015; Luxfer MEL Technologies and Engines, 2019). The *Lockheed Martin* F-16 and F-35 are two examples of fighter aircraft that make use of WE alloys as engine components (Luxfer MEL Technologies and Engines, 2019).

In the past, the use of magnesium alloys for applications in commercial aircraft interiors has been restricted due to concerns about the flammability of these materials in general. However, extensive tests conducted by the FAA (U. S. Federal Aviation Administration) (Marker, 2013) have shown that WE43 meets the necessary performance and safety requirements imposed for materials to be used in aircraft interiors (Luxfer MEL Technologies and Engines, 2019). In fact, the favourable outcome of the FAA flammability tests conducted on WE43 was a major driving force in the decision to lift the long-standing ban of the use of magnesium alloys in aircraft interiors in 2015 (Society of Automotive Engineers, 2015; Luxfer MEL Technologies and Aircraft Interiors, 2019). Thus, WE43 became particularly interesting for application in cabin seat frames.

The favourable combination of properties inherent to the WE series magnesium alloys is driving further research related to these alloys, regarding their properties and potential future applications. The high damping capacity and overall good ballistic performance of WE43 and WE54 have led to several studies regarding these alloys as armour materials, such as for lightweight armoured ground vehicle applications (Cho et al., 2008) and for protective helmet shells (Mathaudhu et al., 2014).

The biodegradability of magnesium alloys in general has led to increased interest in these materials for biomedical applications (Chen et al., 2018). Furthermore, the elastic modulus of magnesium alloys (41–45 GPa) is similar to the elastic modulus of natural bone (3–20 GPa) (Chen et al., 2014). Therefore, magnesium alloys can prevent clinical issues related to biomedical incompatibility (Chen et al., 2014). In fact, the elastic modulus of common stent-material 316L stainless steel (193 GPa) is much higher than that of WE43 (44 GPa), while displaying similar yield strength (Chen et al., 2014). Given this positive biocompatibility, and the adequate corrosion resistance of WE series magnesium alloys, intensive research on the potential use of these materials for the healthcare industry has been carried out in recent years. For instance, clinical trials have been performed with WE43-based bioresorbable screws and cardiovascular stents, positively demonstrating the applicability of this alloy in the medical field (Erbel et al., 2007; Plaass et al., 2016; Chen et al., 2018). However, despite of the promising results, these alloys have to be further studied to evaluate the potentially harmful effect of certain alloying elements on human health (Chen et al., 2019).

FUTURE TRENDS

In general terms, magnesium and magnesium alloys are attractive lightweight materials for many different industries, such as the automotive and aerospace sectors. These materials are also envisaged as appropriate for biodegradable implants. In particular, the good high temperature properties and general mechanical behaviour of WE alloys make this class of magnesium-based materials especially interesting for a wide range of applications. However, as all materials, these alloys have some drawbacks associated to their use for certain applications, such as a high cost of rare earth elements and general susceptibility to corrosion. In the near future, research regarding WE series magnesium alloys will continue to focus on further enhancement of the properties of these materials and mitigation (or even elimination) of some shortcomings of these alloys. Fine-tuning alloy composition and microstructure through alloying and/or through the use of new processing methodologies will play an important role for further property improvement. To take full advantage of the favourable properties of WE series magnesium alloys, the corrosion susceptibility of these materials needs to be addressed. Advances in the development of efficient corrosion protection strategies tailored for these types of alloys are currently being made. Undoubtedly, development and application of multifunctional and self-healing coatings that are able to provide long-term protection, and that are able to prevent corrosion propagation if the coating is damaged during its lifetime, will play a major role in further improving the performance of WE magnesium alloys for an even wider range of applications. Thus, in addition to a growing interest in these materials for several industries, mainly the automotive and aerospace sectors, emergence of an increasing number of new applications is expected to lead to a continuous increase in the global demand for WE series magnesium alloys over the next years.

CONCLUDING REMARKS

WE series alloys possess superior room temperature mechanical properties when compared to other magnesium alloys. In addition, these alloys have the ability to retain their properties at high temperatures, which constitutes a clear advantage in comparison to other classes of magnesium alloys, such as AZ and ZE.

Several different thermal and solution treatments are available for WE series magnesium alloys. Properties such as strength and ductility can be precisely controlled by the use of different combinations and sequences of ageing temperature and duration. For this purpose, continued research efforts have been carried out to obtain a fundamental understanding of the precipitation sequence that occurs during ageing treatments, and of the possible changes in alloy microstructure. In addition, the role of specific alloying elements and their content in common WE series magnesium alloys has been heavily studied over the years. Direct modification of the content of specific alloying elements, or minor addition of other elements, can also be a way of controlling alloy properties.

New processing methodologies have been emerging as a means to improve the properties of magnesium alloys in general. For WE series magnesium alloys, most experimental processing techniques are based on severe plastic deformation of the alloy. These techniques have been used to obtain ultrafine grain microstructure in the processed material. Significant grain refinement has been obtained for WE alloys using ECAP and HPT, which in turn leads to improvement in hardness and overall mechanical properties of these alloys. The scalability of these processes to industrial scale is currently under study.

Despite their various advantages, WE series magnesium alloys are susceptible to corrosion. For most applications, efficient protection strategies are needed to mitigate the degradation of these materials. Anodization and PEO have been the most used techniques for the protection of WE alloys, but a wide range of coating types has been successfully tested for this class of magnesium alloys. The development of WE-specific anticorrosive coatings is a topic that has recently been receiving growing research interest, with very fast developments.

While WE43 and WE54 are already being used in the automotive and aerospace industries, there has been an

increasing interest in these alloys as lightweight biodegradable materials. Continued improvement, property tailoring for specific applications, and development of protective anticorrosive strategies for WE series magnesium alloys, will allow to take full advantage of these materials, and enable their widespread use for a wide range of applications.

AUTHOR CONTRIBUTIONS

LC wrote the manuscript. All authors contributed to the choice of the review topic, to the general outline of the manuscript, and to revision and approval of the manuscript to be submitted.

FUNDING

Funding was provided by Fundação para a Ciência e a Tecnologia (FCT) via PhD grant SFRH/BD/127341/2016, and via funding of CQE (project UIDB/00100/2020)

ACKNOWLEDGMENTS

The authors would like to acknowledge Fundação para a Ciência e a Tecnologia (FCT) for PhD grant SFRH/BD/127341/2016, CQE (funded by FCT) for project UIDB/00100/2020, and Professor Rogério Colaço for the suggestions made throughout the planning and writing of this manuscript.

REFERENCES

Adams, J. F., Allison, J. E., and Jones, J. W. (2016). The Effects of Heat Treatment on Very High Cycle Fatigue Behavior in Hot-Rolled WE43 Magnesium. *Int. J. Fatigue* 93, 372–386. doi:10.1016/j.ijfatigue.2016.05.033

Aghion, E., Gueta, Y., Moscovitch, N., and Bronfin, B. (2008). Effect of Yttrium Additions on the Properties of Grain-Refined Mg-3% Nd alloy. *J. Mater. Sci.* 43, 4870–4875. doi:10.1007/s10853-008-2708-9

Ali, Y., Qiu, D., Jiang, B., Pan, F., and Zhang, M.-X. (2015). Current Research Progress in Grain Refinement of Cast Magnesium Alloys: A Review Article. *J. Alloys Compd.* 619, 639–651. doi:10.1016/j.jallcom.2014.09.061

Annangi, B., Bonassi, S., Marcos, R., and Hernández, A. (2016). Biomonitoring of Humans Exposed to Arsenic, Chromium, Nickel, Vanadium, and Complex Mixtures of Metals by Using the Micronucleus Test in Lymphocytes. *Mutat. Research/Reviews Mutat. Res.* 770, 140–161. doi:10.1016/j.mrrev.2016.03.003

Antion, C., Donnadieu, P., Perrard, F., Deschamps, A., Tassin, C., and Pisch, A. (2003). Hardening Precipitation in a Mg-4Y-3RE alloy. *Acta Materialia* 51, 5335–5348. doi:10.1016/S1359-6454(03)00391-4

Anyanwu, I. A., Kamado, S., and Kojima, Y. (2001). Aging Characteristics and High Temperature Tensile Properties of Mg-Gd-Y-Zr Alloys. *Mater. Trans.* 42, 1206–1211. doi:10.2320/matertrans.42.1206

Ardelean, H., Seyeux, A., Zanna, S., Prima, F., Frateur, I., and Marcus, P. (2013). Corrosion Processes of Mg-Y-Nd-Zr Alloys in Na2SO4 Electrolyte. *Corrosion Sci.* 73, 196–207. doi:10.1016/j.corsci.2013.03.036

Argade, G. R., Sanders, S., Mohandass, G., Alsaleh, A., D'Souza, F., Golden, T. D., et al. (2019). Corrosion Inhibition Study of Mg-Nd-Y High Strength Magnesium Alloy Using Organic Inhibitor. *J. Materi Eng. Perform.* 28, 852–862. doi:10.1007/s11665-018-3849-x

Arrabal, R., Matykina, E., Viejo, F., Skeldon, P., and Thompson, G. E. (2008). Corrosion Resistance of WE43 and AZ91D Magnesium Alloys with Phosphate PEO Coatings. *Corrosion Sci.* 50, 1744–1752. doi:10.1016/j.corsci.2008.03.002

Arrabal, R., Pardo, A., Merino, M. C., Mohedano, M., Casajús, P., Paucar, K., et al. (2012). Effect of Nd on the Corrosion Behaviour of AM50 and AZ91D Magnesium Alloys in 3.5 wt.% NaCl Solution. *Corrosion Sci.* 55, 301–312. doi:10.1016/j.corsci.2011.10.033

Barylski, A., Kupka, M., Aniołek, K., and Rak, J. (2017). The Effect of Precipitation Hardening on the Structure and Mechanical and Tribological Properties of Magnesium alloy WE54. *Vacuum* 139, 77–86. doi:10.1016/j.vacuum.2017.02.015

Bender, S., Göllner, J., Heyn, A., Blawert, C., and Srinivasan, P. B. (2013). "Corrosion and Surface Finishing of Magnesium and its Alloys," in *Fundamentals of Magnesium Alloy Metallurgy*. Editors M. O. Pekguleryuz, K. U. Kainer, and A. A. Kaya (Cambridge, UK: Woodhead Publishing Limited). doi:10.1533/9780857097293.232

Blawert, C., Dietzel, W., Ghali, E., and Song, G. (2006). Anodizing Treatments for Magnesium Alloys and Their Effect on Corrosion Resistance in Various Environments. *Adv. Eng. Mater.* 8, 511–533. doi:10.1002/adem.200500257

Blawert, C., Hort, N., and Kainer, K. U. (2004). Automotive Applications of Magnesium and its Alloys. *Trans. Indian Inst. Met.* 57, 397–408.

Bourell D. L., Leu M. C., and Rosen D. W. (Editors) (2009). "Roadmap for Additive Manufacturing - Identifying the Future of Freeform Processing," *Roadmap for Additive Manufacturing (RAM) Workshop* (Alexandria, VA, USA: The University of Texas).

Cain, T. W., Gonzalez-Afanador, I., Birbilis, N., and Scully, J. R. (2017). The Role of Surface Films and Dissolution Products on the Negative Difference Effect for Magnesium: Comparison of Cl−versus Cl−Free Solutions. *J. Electrochem. Soc.* 164, C300–C311. doi:10.1149/2.1371706jes

Calado, L. M., and Montemor, M. F. (2017). "Handbook of Sol-Gel Science and Technology," in *Handbook of Sol-Gel Science and Technology*. Editors L. Klein, M. Aparicio, and A. Jitianu (Berlin, Germany: Springer International Publishing). doi:10.1007/978-3-319-19454-7

Calado, L. M., Taryba, M. G., Carmezim, M. J., and Montemor, M. F. (2018). Self-healing Ceria-Modified Coating for Corrosion protection of AZ31 Magnesium alloy. *Corrosion Sci.* 142, 12–21. doi:10.1016/j.corsci.2018.06.013

Calado, L. M., Taryba, M. G., Morozov, Y., Carmezim, M. J., and Montemor, M. F. (2021). Cerium Phosphate-Based Inhibitor for Smart Corrosion protection of WE43 Magnesium alloy. *Electrochimica Acta* 365, 137368. doi:10.1016/j.electacta.2020.137368

Calado, L. M., Taryba, M. G., Morozov, Y., Carmezim, M. J., and Montemor, M. F. (2020). Novel Smart and Self-Healing Cerium Phosphate-Based Corrosion Inhibitor for AZ31 Magnesium alloy. *Corrosion Sci.* 170, 108648. doi:10.1016/j.corsci.2020.108648

Callister, W. D., Jr., and Rethwisch, D. G. (2014). *Materials Science and Engineering - an Introduction*. 9th ed. Hoboken, NJ, USA: John Wiley & Sons.

Calvert, J. R. (2015). *Microstructure and Mechanical Properties of WE43 Alloy Produced via Additive Friction Stir Technology*. Blacksburg, VA, USA: Virginia Polytechnic Institute and State University.

Chen, J., Tan, L., Yu, X., Etim, I. P., Ibrahim, M., and Yang, K. (2018). Mechanical Properties of Magnesium Alloys for Medical Application: A Review. *J. Mech. Behav. Biomed. Mater.* 87, 68–79. doi:10.1016/j.jmbbm.2018.07.022

Chen, Y., Dou, J., Yu, H., and Chen, C. (2019). Degradable Magnesium-Based Alloys for Biomedical Applications: The Role of Critical Alloying Elements. *J. Biomater. Appl.* 33, 1348–1372. doi:10.1177/0885328219834656

Chen, Y., Xu, Z., Smith, C., and Sankar, J. (2014). Recent Advances on the Development of Magnesium Alloys for Biodegradable Implants. *Acta Biomater.* 10, 4561–4573. doi:10.1016/j.actbio.2014.07.005

Chirkunov, A. A., and Zheludkevich, M. L. (2018). Corrosion Inhibition of Elektron WE43 Magnesium alloy in NaCl Solution. *Int. J. Corros. Scale Inhib.* 7, 376–389. doi:10.17675/2305-6894-2018-7-3-8

Cho, K., Sano, T., Doherty, K., Yen, C., Gazonas, G., Montgomery, J., et al. (2008). "Magnesium Technology and Manufacturing for Ultra Lightweight Armored Ground Vehicles," in Army Science Conference, Orlando, FL, USA.

Choudhuri, D., Meher, S., Nag, S., Dendge, N., Hwang, J. Y., and Banerjee, R. (2013). Evolution of a Honeycomb Network of Precipitates in a Hot-Rolled

Commercial Mg-Y-Nd-Zr alloy. *Philos. Mag. Lett.* 93, 395–404. doi:10.1080/09500839.2013.791751

Chu, P.-W., and Marquis, E. A. (2015). Linking the Microstructure of a Heat-Treated WE43 Mg alloy with its Corrosion Behavior. *Corrosion Sci.* 101, 94–104. doi:10.1016/j.corsci.2015.09.005

Čížek, L., Greger, M., Pawlica, L., Dobrzański, L. A., and Tański, T. (2004). Study of Selected Properties of Magnesium alloy AZ91 after Heat Treatment and Forming. *J. Mater. Process. Technol.* 157-158, 466–471. doi:10.1016/j.jmatprotec.2004.07.149

Córdoba, L. C., Montemor, M. F., and Coradin, T. (2016). Silane/TiO2 Coating to Control the Corrosion Rate of Magnesium Alloys in Simulated Body Fluid. *Corrosion Sci.* 104, 152–161. doi:10.1016/j.corsci.2015.12.006

Coy, A. E., Viejo, F., Skeldon, P., and Thompson, G. E. (2010). Susceptibility of Rare-Earth-Magnesium Alloys to Micro-galvanic Corrosion. *Corrosion Sci.* 52, 3896–3906. doi:10.1016/j.corsci.2010.08.006

Czerwinski, F. (2014). Controlling the Ignition and Flammability of Magnesium for Aerospace Applications. *Corrosion Sci.* 86, 1–16. doi:10.1016/j.corsci.2014.04.047

Diez, M., Kang, M.-H., Kim, S.-M., Kim, H.-E., and Song, J. (2016). Hydroxyapatite (HA)/poly-l-lactic Acid (PLLA) Dual Coating on Magnesium alloy under Deformation for Biomedical Applications. *J. Mater. Sci. Mater. Med.* 27, 34. doi:10.1007/s10856-015-5643-8

Dvorský, D., Kubásek, J., Voňavková, I., and Vojtěch, D. (2019). Structure, Mechanical and Corrosion Properties of Extruded Mg-Nd-Zn, Mg-Y-Zn and Mg-Y-Nd Alloys. *Mater. Sci. Technol.* 35, 520–529. doi:10.1080/02670836.2019.1570680

Eivani, A. R., Mehdizade, M., Chabok, S., and Zhou, J. (2021). Applying Multi-Pass Friction Stir Processing to Refine the Microstructure and Enhance the Strength, Ductility and Corrosion Resistance of WE43 Magnesium alloy. *J. Mater. Res. Technol.* 12, 1946–1957. doi:10.1016/j.jmrt.2021.03.021

Eppensteiner, F. W., and Jenkins, M. R. (1999). Chromate Conversion Coatings. *Metal Finishing* 97, 497–509. doi:10.1016/S0026-0576(00)83109-8

Erbel, R., Di Mario, C., Bartunek, J., Bonnier, J., De Bruyne, B., Eberli, F. R., et al. (2007). Temporary Scaffolding of Coronary Arteries with Bioabsorbable Magnesium Stents: a Prospective, Non-randomised Multicentre Trial. *The Lancet* 369, 1869–1875. doi:10.1016/S0140-6736(07)60853-8

Esmaily, M., Blücher, D. B., Svensson, J. E., Halvarsson, M., and Johansson, L. G. (2016). New Insights into the Corrosion of Magnesium Alloys - the Role of Aluminum. *Scripta Materialia* 115, 91–95. doi:10.1016/j.scriptamat.2016.01.008

Esmaily, M., Svensson, J. E., Fajardo, S., Birbilis, N., Frankel, G. S., Virtanen, S., et al. (2017). Fundamentals and Advances in Magnesium alloy Corrosion. *Prog. Mater. Sci.* 89, 92–193. doi:10.1016/j.pmatsci.2017.04.011

European Union (2009). *Directive 2008/101/EC of the European Parliament and of the Council of 19 November 2008 Amending Directive 2003/87/EC So as to Include Aviation Activities in the Scheme for Greenhouse Gas Emission Allowance Trading within the Community*. Luxembourg: Official Journal of the European Union, 3–21.

European Union (2006). Regulation (EC) No 1907/2006 of the European Parliament and of the Council of 18 December 2006 Concerning the Registration, Evaluation, Authorisation and Restriction of Chemicals (REACH), Establishing a European Chemicals Agency. *Official J. Eur. Union* 49, 1–849.

European Union (2014). *Regulation (EU) No 333/2014 of the European Parliament and of the Council of 11 March 2014 Amending Regulation (EC) No 443/2009 to Define the Modalities for Reaching the 2020 Target to Reduce CO2 Emissions from New Passenger Cars*. Luxembourg: Official Journal of the European Union, 15–21.

Feliu, S., and Llorente, I. (2015). Corrosion Product Layers on Magnesium Alloys AZ31 and AZ61: Surface Chemistry and Protective Ability. *Appl. Surf. Sci.* 347, 736–746. doi:10.1016/j.apsusc.2015.04.189

Feliu, S., Pardo, a., Merino, M. C., Coy, a. E., Viejo, F., and Arrabal, R. (2009). Correlation between the Surface Chemistry and the Atmospheric Corrosion of AZ31, AZ80 and AZ91D Magnesium Alloys. *Appl. Surf. Sci.* 255, 4102–4108. doi:10.1016/j.apsusc.2008.10.095

Figueiredo, R. B., and Langdon, T. G. (2019). Processing Magnesium and its Alloys by High-Pressure Torsion: An Overview. *Adv. Eng. Mater.* 21, 1801039. doi:10.1002/adem.201801039

Frazier, W. E. (2014). Metal Additive Manufacturing: A Review. *J. Materi Eng. Perform.* 23, 1917–1928. doi:10.1007/s11665-014-0958-z

Frint, P., Hockauf, M., Dietrich, D., Halle, T., Wagner, M. F.-X., and Lampke, T. (2011). Influence of Strain Gradients on the Grain Refinement during Industrial Scale ECAP. *Mat.-wiss. U. Werkstofftech.* 42, 680–685. doi:10.1002/mawe.201100839

Frint, S., Hockauf, M., Frint, P., and Wagner, M. F.-X. (2016). Scaling up Segal's Principle of Equal-Channel Angular Pressing. *Mater. Des.* 97, 502–511. doi:10.1016/j.matdes.2016.02.067

Gangireddy, S., Gwalani, B., Liu, K., Faierson, E. J., and Mishra, R. S. (2019). Microstructure and Mechanical Behavior of an Additive Manufactured (AM) WE43-Mg alloy. *Additive Manufacturing* 26, 53–64. doi:10.1016/j.addma.2018.12.015

Ganguly, S., and Mondal, A. K. (2018). Influence of SiC Nanoparticles Addition on Microstructure and Creep Behavior of Squeeze-Cast AZ91-Ca-Sb Magnesium alloy. *Mater. Sci. Eng. A* 718, 377–389. doi:10.1016/j.msea.2018.01.131

Ghali, E. (2011). "Magnesium and Magnesium Alloys," in *Uhlig's Corrosion Handbook*. Editor R. W. Revie 3rd ed. (Hoboken, NJ, USA: John Wiley & Sons). doi:10.1002/9780470872864.ch58

Ghorbanpour, S., McWilliams, B. A., and Knezevic, M. (2019). Effect of Hot Working and Aging Heat Treatments on Monotonic, Cyclic, and Fatigue Behavior of WE43 Magnesium alloy. *Mater. Sci. Eng. A* 747, 27–41. doi:10.1016/j.msea.2019.01.056

Ghorbanpour, S., Mcwilliams, B. A., and Knezevic, M. (2019). "Effect of Hot Working on the High Cycle Fatigue Behavior of WE43 Rare Earth Magnesium Alloy," in *Magnesium Technology*. Editors V. Joshi, J. Jordon, D. Orlov, and N. Neelameggham (Berlin, Germany: Springer Cham), 219–225. doi:10.1007/978-3-030-05789-3_33

Ghorbanpour, S., McWilliams, B. A., and Knezevic, M. (2019). Low-cycle Fatigue Behavior of Rolled WE43-T5 Magnesium alloy. *Fatigue Fract Eng. Mater. Struct.* 42, 1357–1372. doi:10.1111/ffe.12992

Gomes, M. P., Costa, I., Pébère, N., Rossi, J. L., Tribollet, B., and Vivier, V. (2019). On the Corrosion Mechanism of Mg Investigated by Electrochemical Impedance Spectroscopy. *Electrochimica Acta* 306, 61–70. doi:10.1016/j.electacta.2019.03.080

Gray, J. E., and Luan, B. (2002). Protective Coatings on Magnesium and its Alloys - a Critical Review. *J. Alloys Compd.* 336, 88–113. doi:10.1016/S0925-8388(01)01899-0

Grote, M., Williams, I., and Preston, J. (2014). Direct Carbon Dioxide Emissions from Civil Aircraft. *Atmos. Environ.* 95, 214–224. doi:10.1016/j.atmosenv.2014.06.042

Guo, L. F., Yue, T. M., and Man, H. C. (2005). Excimer Laser Surface Treatment of Magnesium alloy WE43 for Corrosion Resistance Improvement. *J. Mater. Sci.* 40, 3531–3533. doi:10.1007/s10853-005-2888-5

Gupta, M., and Sharon, N. M. L. (2011). *Magnesium, Magnesium Alloys, and Magnesium Composites*. Hoboken, NJ, USA: John Wiley & Sons.

Gusieva, K., Davies, C. H. J., Scully, J. R., and Birbilis, N. (2015). Corrosion of Magnesium Alloys: the Role of Alloying. *Int. Mater. Rev.* 60, 169–194. doi:10.1179/1743280414Y.0000000046

Heise, S., Höhlinger, M., Hernández, Y. T., Palacio, J. J. P., Rodriquez Ortiz, J. A., Wagener, V., et al. (2017). Electrophoretic Deposition and Characterization of Chitosan/bioactive Glass Composite Coatings on Mg alloy Substrates. *Electrochimica Acta* 232, 456–464. doi:10.1016/j.electacta.2017.02.081

Höhlinger, M., Heise, S., Wagener, V., Boccaccini, A. R., and Virtanen, S. (2017). Developing Surface Pre-treatments for Electrophoretic Deposition of Biofunctional Chitosan-Bioactive Glass Coatings on a WE43 Magnesium alloy. *Appl. Surf. Sci.* 405, 441–448. doi:10.1016/j.apsusc.2017.02.049

Hort, N., Huang, Y., Fechner, D., Störmer, M., Blawert, C., Witte, F., et al. (2010). Magnesium Alloys as Implant Materials - Principles of Property Design for Mg-RE Alloys☆. *Acta Biomater.* 6, 1714–1725. doi:10.1016/j.actbio.2009.09.010

Hu, Y., Zhang, C., Zheng, T., Pan, F., and Tang, A. (2018). Strengthening Effects of Zn Addition on an Ultrahigh Ductility Mg-Gd-Zr Magnesium Alloy. *Materials* 11, 1942. doi:10.3390/ma11101942

Huang, C. (2017). *Optimisation of Heat Treatment Process for New-Developed Low Cost Creep-Resist Mg Alloy (Mg-3Nd-2Ca)*. Brisbane, Australia: University of Queensland.

Imwinkelried, T., Beck, S., Iizuka, T., and Schaller, B. (2013). Effect of a Plasmaelectrolytic Coating on the Strength Retention of *In Vivo* and *In Vitro* Degraded Magnesium Implants. *Acta Biomater.* 9, 8643–8649. doi:10.1016/j.actbio.2012.08.047

Incesu, A., and Gungor, A. (2020). Mechanical Properties and Biodegradability of Mg-Zn-Ca Alloys: Homogenization Heat Treatment and Hot Rolling. *J. Mater. Sci. Mater. Med.* 31, 123. doi:10.1007/s10856-020-06468-5

Jahedi, M., McWilliams, B. A., Kellogg, F. R., Beyerlein, I. J., and Knezevic, M. (2018). Rate and Temperature Dependent Deformation Behavior of As-Cast WE43 Magnesium-Rare Earth alloy Manufactured by Direct-Chill Casting. *Mater. Sci. Eng. A* 712, 50–64. doi:10.1016/j.msea.2017.11.092

Jahedi, M., McWilliams, B. A., and Knezevic, M. (2018). Deformation and Fracture Mechanisms in WE43 Magnesium-Rare Earth alloy Fabricated by Direct-Chill Casting and Rolling. *Mater. Sci. Eng. A* 726, 194–207. doi:10.1016/j.msea.2018.04.090

James, M., Kihiu, J. M., Rading, G. O., and Kimotho, J. K. (2011). Use of Magnesium Alloys in Optimizing the Weight of Automobile: Current Trends and Opportunities. *Sustain. Res. Innovation Conf. Proc.* 3, 4–6.

Jamesh, M. I., Wu, G., Zhao, Y., Mckenzie, D. R., Bilek, M. M. M., and Chu, P. K. (2015). Electrochemical Corrosion Behavior of Biodegradable Mg-Y-RE and Mg-Zn-Zr Alloys in Ringer's Solution and Simulated Body Fluid. *Corrosion Sci.* 91, 160–184. doi:10.1016/j.corsci.2014.11.015

Jiang, H. S., Zheng, M. Y., Qiao, X. G., Wu, K., Peng, Q. Y., Yang, S. H., et al. (2017). Microstructure and Mechanical Properties of WE43 Magnesium alloy Fabricated by Direct-Chill Casting. *Mater. Sci. Eng. A* 684, 158–164. doi:10.1016/j.msea.2016.11.009

Jin, W., Wang, G., Peng, X., Li, W., Qasim, A. M., and Chu, P. K. (2018). Tantalum Nitride Films for Corrosion protection of Biomedical Mg-Y-RE alloy. *J. Alloys Compd.* 764, 947–958. doi:10.1016/j.jallcom.2018.06.151

Jin, W., Wu, G., Feng, H., Wang, W., Zhang, X., and Chu, P. K. (2015). Improvement of Corrosion Resistance and Biocompatibility of Rare-Earth WE43 Magnesium alloy by Neodymium Self-Ion Implantation. *Corrosion Sci.* 94, 142–155. doi:10.1016/j.corsci.2015.01.049

Jin, W., Wu, G., Gao, A., Feng, H., Peng, X., and Chu, P. K. (2016). Hafnium-implanted WE43 Magnesium alloy for Enhanced Corrosion protection and Biocompatibility. *Surf. Coat. Technol.* 306, 11–15. doi:10.1016/j.surfcoat.2016.02.055

Juan, S., Feng, G., Xiaobo, G., and Haiquan, F. (2021). Study on Solid-Solution Interaction and Existing Forms of Alloying Elements in Mg-Al-Zn-Gd alloy. *J. Alloys Compd.* 854, 156209. doi:10.1016/j.jallcom.2020.156209

Junaid, M., Hashmi, M. Z., Malik, R. N., and Pei, D.-S. (2016). Toxicity and Oxidative Stress Induced by Chromium in Workers Exposed from Different Occupational Settings Around the globe: A Review. *Environ. Sci. Pollut. Res.* 23, 20151–20167. doi:10.1007/s11356-016-7463-x

Kabirian, F., and Mahmudi, R. (2009). Impression Creep Behavior of a Cast AZ91 Magnesium Alloy. *Metall. Mat Trans. A.* 40, 116–127. doi:10.1007/s11661-008-9699-7

Kalb, H., Rzany, A., and Hensel, B. (2012). Impact of Microgalvanic Corrosion on the Degradation Morphology of WE43 and Pure Magnesium under Exposure to Simulated Body Fluid. *Corrosion Sci.* 57, 122–130. doi:10.1016/j.corsci.2011.12.026

Kandalam, S., Agrawal, P., Avadhani, G. S., Kumar, S., and Suwas, S. (2015). Precipitation Response of the Magnesium alloy WE43 in Strained and Unstrained Conditions. *J. Alloys Compd.* 623, 317–323. doi:10.1016/j.jallcom.2014.09.179

Kang, Y., Huang, Z., Zhao, H., Gan, C., Zhou, N., Zheng, K., et al. (2020). Comparative Study of Hot Deformation Behavior and Microstructure Evolution of As-Cast and Extruded WE43 Magnesium Alloy. *Metals* 10, 429. doi:10.3390/met10040429

Kang, Y. H., Wang, X. X., Zhang, N., Yan, H., and Chen, R. S. (2017). Effect of Initial Temper on the Creep Behavior of Precipitation-Hardened WE43 alloy. *Mater. Sci. Eng. A* 689, 419–426. doi:10.1016/j.msea.2017.02.081

Kang, Y. H., Wu, D., Chen, R. S., and Han, E. H. (2014). Microstructures and Mechanical Properties of the Age Hardened Mg-4.2Y-2.5Nd-1Gd-0.6Zr (WE43) Microalloyed with Zn. *J. Magnesium Alloys* 2, 109–115. doi:10.1016/j.jma.2014.01.010

Kharitonov, D. S., Zimowska, M., Ryl, J., Zieliński, A., Osipenko, M. A., Adamiec, J., et al. (2021). Aqueous Molybdate Provides Effective Corrosion Inhibition of WE43 Magnesium alloy in Sodium Chloride Solutions. *Corrosion Sci.* 190, 109664. doi:10.1016/j.corsci.2021.109664

Kiani, M., Gandikota, I., Rais-Rohani, M., and Motoyama, K. (2014). Design of Lightweight Magnesium Car Body Structure under Crash and Vibration Constraints. *J. Magnesium Alloys* 2, 99–108. doi:10.1016/j.jma.2014.05.005

Kiełbus, A. (2018). "Microstructure and Properties of Casting Magnesium Alloys Designed to Work in Elevated Temperature," in *Magnesium Alloys*. Editors T. Tański, W. Borek, and M. Król (London, UK: IntechOpen).

Kierzek, A., and Adamiec, J. (2011). Design Factors Influencing Weldability of the Mg-4Y-3RE Cast Magnesium alloy. *IOP Conf. Ser. Mater. Sci. Eng.* 22, 012002. doi:10.1088/1757-899X/22/1/012002

Knapek, M., Minárik, P., Čapek, J., Král, R., Kubásek, J., and Chmelík, F. (2018). Corrosion of Pure Magnesium and a WE43 Magnesium alloy Studied by Advanced Acoustic Emission Analysis. *Corrosion Sci.* 145, 10–15. doi:10.1016/j.corsci.2018.09.006

Kondori, B., and Mahmudi, R. (2017). Effect of Ca Additions on the Microstructure and Creep Properties of a Cast Mg-Al-Mn Magnesium alloy. *Mater. Sci. Eng. A* 700, 438–447. doi:10.1016/j.msea.2017.06.007

Kujur, M. S., Manakari, V., Parande, G., Tun, K. S., Mallick, A., and Gupta, M. (2018). Enhancement of thermal, Mechanical, Ignition and Damping Response of Magnesium Using Nano-Ceria Particles. *Ceramics Int.* 44, 15035–15043. doi:10.1016/j.ceramint.2018.05.133

Kulekci, M. K. (2008). Magnesium and its Alloys Applications in Automotive Industry. *Int. J. Adv. Manuf Technol.* 39, 851–865. doi:10.1007/s00170-007-1279-2

Le, Q.-C., Zhang, Z.-Q., Shao, Z.-W., Cui, J.-Z., and Xie, Y. (2010). Microstructures and Mechanical Properties of Mg-2%Zn-0.4%RE Alloys. *Trans. Nonferrous Met. Soc. China* 20, s352–s356. doi:10.1016/S1003-6326(10)60496-7

Lefstad, M., Pedersen, K., and Dumoulin, S. (2012). Up-scaled Equal Channel Angular Pressing of AA6060 and Subsequent Mechanical Properties. *Mater. Sci. Eng. A* 535, 235–240. doi:10.1016/j.msea.2011.12.073

Leleu, S., Rives, B., Bour, J., Causse, N., and Pébère, N. (2018). On the Stability of the Oxides Film Formed on a Magnesium alloy Containing Rare-Earth Elements. *Electrochimica Acta* 290, 586–594. doi:10.1016/j.electacta.2018.08.093

Leleu, S., Rives, B., Causse, N., and Pébère, N. (2019). Corrosion Rate Determination of Rare-Earth Mg Alloys in a Na2SO4 Solution by Electrochemical Measurements and Inductive Coupled Plasma-Optical Emission Spectroscopy. *J. Magnesium Alloys* 7, 47–57. doi:10.1016/j.jma.2018.12.002

Li, F., Peh, W. Y., Nagarajan, V., Ho, M. K., Danno, A., Chua, B. W., et al. (2016). Development of Non-flammable High Strength AZ91 + Ca Alloys via Liquid Forging and Extrusion. *Mater. Des.* 99, 37–43. doi:10.1016/j.matdes.2016.03.014

Li, G., Zhang, J., Wu, R., Liu, S., Song, B., Jiao, Y., et al. (2019). Improving Age Hardening Response and Mechanical Properties of a New Mg-RE alloy via Simple Pre-cold Rolling. *J. Alloys Compd.* 777, 1375–1385. doi:10.1016/j.jallcom.2018.11.082

Li, M., Cheng, Y., Zheng, Y. F., Zhang, X., Xi, T. F., and Wei, S. C. (2012). Surface Characteristics and Corrosion Behaviour of WE43 Magnesium alloy Coated by SiC Film. *Appl. Surf. Sci.* 258, 3074–3081. doi:10.1016/j.apsusc.2011.11.040

Li, Q., Wang, Q., Wang, Y., Zeng, X., and Ding, W. (2007). Effect of Nd and Y Addition on Microstructure and Mechanical Properties of As-Cast Mg-Zn-Zr alloy. *J. Alloys Compd.* 427, 115–123. doi:10.1016/j.jallcom.2006.02.054

Liu, C., Li, Q., Liang, J., Zhou, J., and Wang, L. (2016). Microstructure and Corrosion Behaviour of Laser Surface Melting Treated WE43 Magnesium alloy. *RSC Adv.* 6, 30642–30651. doi:10.1039/C5RA27010C

Liu, C., Liang, J., Zhou, J., Li, Q., Peng, Z., and Wang, L. (2016). Characterization and Corrosion Behavior of Plasma Electrolytic Oxidation Coated AZ91-T6 Magnesium alloy. *Surf. Coat. Technol.* 304, 179–187. doi:10.1016/j.surfcoat.2016.07.021

Liu, D. X., Pang, X., Li, D. L., Guo, C. G., Wongsa-Ngam, J., Langdon, T. G., et al. (2017). Microstructural Evolution and Properties of a Hot Extruded and HPT-

Processed Resorbable Magnesium WE43 Alloy. *Adv. Eng. Mater.* 19, 1600698. doi:10.1002/adem.201600698

Liu, K., Rokhlin, L. L., Elkin, F. M., Tang, D., and Meng, J. (2010). Effect of Ageing Treatment on the Microstructures and Mechanical Properties of the Extruded Mg-7Y-4Gd-1.5Zn-0.4Zr alloy. *Mater. Sci. Eng. A* 527, 828–834. doi:10.1016/j.msea.2009.10.031

Liu, M., Zanna, S., Ardelean, H., Frateur, I., Schmutz, P., Song, G., et al. (2009). A First Quantitative XPS Study of the Surface Films Formed, by Exposure to Water, on Mg and on the Mg-Al Intermetallics: Al3Mg2 and Mg17Al12. *Corrosion Sci.* 51, 1115–1127. doi:10.1016/j.corsci.2009.02.017

Liu, Z., Wu, G., Liu, W., Pang, S., and Ding, W. (2013). Microstructure, Mechanical Properties and Fracture Behavior of Peak-Aged Mg34Y32Nd31Gd Alloys under Different Aging Conditions. *Mater. Sci. Eng. A* 561, 303–311. doi:10.1016/j.msea.2012.09.060

Lukyanova, E. A., Martynenko, N. S., Serebryany, V. N., Belyakov, A. N., Rokhlin, L. L., Dobatkin, S. V., et al. (2017). Structure and Mechanical and Corrosion Properties of a Magnesium Mg-Y-Nd-Zr Alloy after High Pressure Torsion. *Russ. Metall.* 2017, 912–921. doi:10.1134/S0036029517110088

Lukyanova, E. A., Martynenko, N. S., Shakhova, I., Belyakov, A. N., Rokhlin, L. L., Dobatkin, S. V., et al. (2016). Strengthening of Age-Hardenable WE43 Magnesium alloy Processed by High Pressure Torsion. *Mater. Lett.* 170, 5–9. doi:10.1016/j.matlet.2016.01.106

Luo, A. A. (2013). Magnesium Casting Technology for Structural Applications. *J. Magnesium Alloys* 1, 2–22. doi:10.1016/j.jma.2013.02.002

Luo, A. A. (2004). Recent Magnesium alloy Development for Elevated Temperature Applications. *Int. Mater. Rev.* 49, 13–30. doi:10.1179/095066004225010497

Luo, K., Zhang, L., Wu, G., Liu, W., and Ding, W. (2019). Effect of Y and Gd Content on the Microstructure and Mechanical Properties of Mg-Y-RE Alloys. *J. Magnesium Alloys* 7, 345–354. doi:10.1016/j.jma.2019.03.002

Luxfer MEL Technologies, Aircraft Interiors (2019). Luxfer MEL Technologies, Aircraft Interiors. Available at: https://www.luxfermeltechnologies.com/markets/aerospace/aircraft-interiors-magnesium-extrusion/(Accessed July 16, 2019).

Luxfer MEL Technologies, Engines (2019). Luxfer MEL Technologies, Engines. Available at: https://www.luxfermeltechnologies.com/markets/aerospace/engines/(Accessed July 16, 2019).

Lyon, P., King, J. F., and Fowler, G. A. (1991). "Developments in Magnesium Based Materials and Processes," in International Gas Turbine and Aeroengine Congress and Exposition, Orlando, FL, USA. doi:10.1115/91-GT-015

Magnesium Alloy Fatigue Data (1995). "Magnesium Alloy Fatigue Data," in *Fatigue Data Book: Light Structural Alloys* (Ohio, EUA: ASM International).

Makar, G. L., and Kruger, J. (1993). Corrosion of Magnesium. *Int. Mater. Rev.* 38, 138–153. doi:10.1179/imr.1993.38.3.138

Malayoğlu, U., and Tekin, K. C. (2015). Wear Behaviour of Plasma Electrolytic Oxide Coatings on E21 and WE43 Mg Alloys. *Surf. Eng.* 31, 526–533. doi:10.1179/1743294414Y.0000000409

Manakari, V., Parande, G., and Gupta, M. (2017). Selective Laser Melting of Magnesium and Magnesium Alloy Powders: A Review. *Metals* 7, 2. doi:10.3390/met7010002

Marker, T. R. (2013). *Evaluating the Flammability of Various Magnesium Alloys during Laboratory- and Full-Scale Aircraft Fire Tests, Atlantic City, USA*.

Martynenko, N. S., Lukyanova, E. A., Serebryany, V. N., Gorshenkov, M. V., Shchetinin, I. V., Raab, G. I., et al. (2018). Increasing Strength and Ductility of Magnesium alloy WE43 by Equal-Channel Angular Pressing. *Mater. Sci. Eng. A* 712, 625–629. doi:10.1016/j.msea.2017.12.026

Maruyama, K., Suzuki, M., and Sato, H. (2002). Creep Strength of Magnesium-Based Alloys. *Metall. Mat Trans. A.* 33, 875–882. doi:10.1007/s11661-002-1020-610.1007/s11661-002-0157-7

Mathaudhu, S. N., and Nyberg, E. A. (2014). "Magnesium Alloys in U.S. Military Applications: Past, Current and Future Solutions," in *Essential Readings in Magnesium Technology*. Editors S. N. Mathaudhu, A. A. Luo, N. R. Neelameggham, E. A. Nyberg, and W. H. Sillekens (Hoboken, NJ, USA: John Wiley & Sons), 71–76. doi:10.1002/9781118859803.ch10

McClelland, Z., Avery, D. Z., Williams, M. B., Mason, C. J. T., Rivera, O. G., Leah, C., et al. (2019). "Microstructure and Mechanical Properties of High Shear Material Deposition of Rare Earth Magnesium Alloys WE43," in *The Minerals, Metals & Materials Series*. Editors V. Joshi, J. Jordon, D. Orlov, and N. Neelameggham (Cham: Springer). doi:10.1007/978-3-030-05789-3_41

Mengucci, P., Barucca, G., Riontino, G., Lussana, D., Massazza, M., Ferragut, R., et al. (2008). Structure Evolution of a WE43 Mg alloy Submitted to Different thermal Treatments. *Mater. Sci. Eng. A* 479, 37–44. doi:10.1016/j.msea.2007.06.016

Minárik, P., Veselý, J., Čížek, J., Zemková, M., Vlasák, T., Krajňák, T., et al. (2018). Effect of Secondary Phase Particles on thermal Stability of Ultra-fine Grained Mg-4Y-3RE alloy Prepared by Equal Channel Angular Pressing. *Mater. Characterization* 140, 207–216. doi:10.1016/j.matchar.2018.04.006

Mirza, F. A., and Chen, D. L. (2013). "Fatigue of Magnesium Alloys," in *Aerospace Materials Handbook*. Editors S. Zhang and D. Zhao (Boca Raton, Florida, USA: CRC Press).

Mokhtarishirazabad, M., Azadi, M., Hossein Farrahi, G., Winter, G., and Eichlseder, W. (2013). Improvement of High Temperature Fatigue Lifetime in AZ91 Magnesium alloy by Heat Treatment. *Mater. Sci. Eng. A* 588, 357–365. doi:10.1016/j.msea.2013.09.067

Montemor, M. F. (2014). Functional and Smart Coatings for Corrosion protection: A Review of Recent Advances. *Surf. Coat. Technol.* 258, 17–37. doi:10.1016/j.surfcoat.2014.06.031

Montemor, M. F., Simões, A. M., and Carmezim, M. J. (2007). Characterization of Rare-Earth Conversion Films Formed on the AZ31 Magnesium alloy and its Relation with Corrosion protection. *Appl. Surf. Sci.* 253, 6922–6931. doi:10.1016/j.apsusc.2007.02.019

Morozov, Y., Calado, L. M., Shakoor, R. A., Raj, R., Kahraman, R., Taryba, M. G., et al. (2019). Epoxy Coatings Modified with a New Cerium Phosphate Inhibitor for Smart Corrosion protection of Steel. *Corrosion Sci.* 159, 108128. doi:10.1016/j.corsci.2019.108128

Moosbrugger C., (Editor) (2017). "Introduction to Magnesium Alloys," *Engineering Properties of Magnesium Alloys* (Russell, OH, USA: ASM International).

Mouritz, A. P. (2012). *Introduction to Aerospace Materials*. Sawston, USA: Woodhead Publishing Limited.

Natta, M. G. L.-B. (2001). Evidence of Two Anodic Processes in the Polarization Curves of Magnesium in Aqueous media. *Corrosion* 57, 712–720. doi:10.5006/1.3290399

Nie, J.-F. (2012). Precipitation and Hardening in Magnesium Alloys. *Metall. Mat Trans. A.* 43, 3891–3939. doi:10.1007/s11661-012-1217-2

Nie, J. F., and Muddle, B. C. (2000). Characterisation of Strengthening Precipitate Phases in a Mg-Y-Nd alloy. *Acta Materialia* 48, 1691–1703. doi:10.1016/S1359-6454(00)00013-6

Nie, J. F., Xiao, X. L., Luo, C. P., and Muddle, B. C. (2001). Characterisation of Precipitate Phases in Magnesium Alloys Using Electron Microdiffraction. *Micron* 32, 857–863. doi:10.1016/S0968-4328(00)00094-9

Ning, Z. L., Yi, J. Y., Qian, M., Sun, H. C., Cao, F. Y., Liu, H. H., et al. (2014). Microstructure and Elevated Temperature Mechanical and Creep Properties of Mg-4Y-3Nd-0.5Zr alloy in the Product Form of a Large Structural Casting. *Mater. Des.* 60, 218–225. doi:10.1016/j.matdes.2014.03.062

Ninlachart, J., Karmiol, Z., Chidambaram, D., and Raja, K. S. (2017). Effect of Heat Treatment Conditions on the Passivation Behavior of WE43C Mg-Y-Nd alloy in Chloride Containing Alkaline Environments. *J. Magnesium Alloys* 5, 147–165. doi:10.1016/j.jma.2017.03.003

Nordlien, J. H., Nisancioglu, K., Ono, S., and Masuko, N. (1997). Morphology and Structure of Water-Formed Oxides on Ternary MgAl Alloys. *J. Electrochem. Soc.* 144, 461–466. doi:10.1149/1.1837432

Oshibe, N., Marukawa, E., Yoda, T., and Harada, H. (2019). Degradation and Interaction with Bone of Magnesium alloy WE43 Implants: A Long-Term Follow-Up *In Vivo* Rat Tibia Study. *J. Biomater. Appl.* 33, 1157–1167. doi:10.1177/0885328218822050

Pachla, W., Mazur, A., Skiba, J., Kulczyk, M., and Przybysz, S. (2012). Wrought Magnesium Alloys ZM21, ZW3 and WE43 Processed by Hydrostatic Extrusion with Back Pressure. *Arch. Metall. Mater.* 57, 485–493. doi:10.2478/v10172-012-0050-3

Pai, B. C., Pillai, U. T. S., Manikandan, P., and Srinivasan, A. (2012). Modification of AZ91 Mg Alloys for High Temperature Applications. *Trans. Indian Inst. Met.* 65, 601–606. doi:10.1007/s12666-012-0166-1

Pan, F., Yang, M., and Chen, X. (2016). A Review on Casting Magnesium Alloys: Modification of Commercial Alloys and Development of New Alloys. *J. Mater. Sci. Technol.* 32, 1211–1221. doi:10.1016/j.jmst.2016.07.001

Penghuai, F., Liming, P., Haiyan, J., Wenjiang, D., and Chunquan, Z. (2014). Tensile Properties of High Strength Cast Mg Alloys at Room Temperature: A Review. *China Foundry* 11, 277–286.

Pereira, G. S., Koga, G. Y., Avila, J. A., Bittencourt, I. M., Fernandez, F., Miyazaki, M. H., et al. (2021). Corrosion Resistance of WE43 Mg alloy in Sodium Chloride Solution. *Mater. Chem. Phys.* 272, 124930. doi:10.1016/j.matchemphys.2021.124930

Pereira, P. H. R., Huang, Y., Kawasaki, M., and Langdon, T. G. (2017). An Examination of the Superplastic Characteristics of Al-Mg-Sc Alloys after Processing. *J. Mater. Res.* 32, 4541–4553. doi:10.1557/jmr.2017.286

Pinto, R., Carmezim, M. J., Ferreira, M. G. S., and Montemor, M. F. (2010). A Two-step Surface Treatment, Combining Anodisation and Silanisation, for Improved Corrosion protection of the Mg alloy WE54. *Prog. Org. Coat.* 69, 143–149. doi:10.1016/j.porgcoat.2010.04.014

Plaass, C., Ettinger, S., Sonnow, L., Koenneker, S., Noll, Y., Weizbauer, A., et al. (2016). Early Results Using a Biodegradable Magnesium Screw for Modified Chevron Osteotomies. *J. Orthop. Res.* 34, 2207–2214. doi:10.1002/jor.23241

Polmear, I. J. (1994). Magnesium Alloys and Applications. *Mater. Sci. Technol.* 10, 1–16. doi:10.1179/mst.1994.10.1.1

Prabhu, T. R., Vedantam, S., and Singh, V. (2017). "Magnesium Alloys," in *Aerospace Materials and Material Technologies*. Editors N. E. Prasad and R. J. H. Wanhill (Basingstoke, USA: Springer Nature). doi:10.1007/978-981-10-2134-3_1

Riontino, G., Massazza, M., Lussana, D., Mengucci, P., Barucca, G., and Ferragut, R. (2008). A Novel thermal Treatment on a Mg-4.2Y-2.3Nd-0.6Zr (WE43) alloy. *Mater. Sci. Eng. A* 494, 445–448. doi:10.1016/j.msea.2008.04.043

Rzychoń, T., and Kiełbus, A. (2007). Microstructure of WE43 Casting Magnesium alloy. *J. Achievements Mater. Manufacturing Eng.* 21, 31–34.

Rzychoń, T., Michalska, J., and Kiełbus, A. (2007). Effect of Heat Treatment on Corrosion Resistance of WE54 alloy. *J. Achievements Mater. Manufacturing Eng.* 20, 191–194.

Salandari-Rabori, A., Zarei-Hanzaki, A., Abedi, H. R., Lecomte, J. S., and Khatami-Hamedani, H. (2018). Micro and Macro Texture Evolution during Multiaxial Forging of a WE43 Magnesium alloy. *J. Alloys Compd.* 739, 249–259. doi:10.1016/j.jallcom.2017.12.181

Santamaria, M., Di Quarto, F., Zanna, S., and Marcus, P. (2007). Initial Surface Film on Magnesium Metal: A Characterization by X-ray Photoelectron Spectroscopy (XPS) and Photocurrent Spectroscopy (PCS). *Electrochimica Acta* 53, 1314–1324. doi:10.1016/j.electacta.2007.03.019

Shaat, M. (2018). Effects of Processing Conditions on Microstructure and Mechanical Properties of Equal-Channel-Angular-Pressed Titanium. *Mater. Sci. Technol.* 34, 1149–1167. doi:10.1080/02670836.2018.1478481

Shi, X., Zhu, Y., Zhang, S., Zhao, R., Zhang, R., Chen, L., et al. (2020). Characteristics of Selenium-Containing Coatings on WE43 Magnesium alloy by Micro-arc Oxidation. *Mater. Lett.* 261, 126944. doi:10.1016/j.matlet.2019.126944

Smola, B., Joska, L., Březina, V., Stulíková, I., and Hnilica, F. (2012). Microstructure, Corrosion Resistance and Cytocompatibility of Mg-5Y-4Rare Earth-0.5Zr (WE54) alloy. *Mater. Sci. Eng. C* 32, 659–664. doi:10.1016/j.msec.2012.01.003

Society of Automotive Engineers (2015). *Performance Standard for Seats in Civil Rotorcraft, Transport Aircraft, and General Aviation Aircraft - AS8049C*.

Soltan, A., Dargusch, M. S., Shi, Z., Gerrard, D., and Atrens, A. (2019). Understanding the Corrosion Behaviour of the Magnesium Alloys EV31A, WE43B, and ZE41A. *Mater. Corrosion* 70, 1527–1552. doi:10.1002/maco.201910845

Song, G., Atrens, A., and Dargusch, M. (1999). Influence of Microstructure on the Corrosion of Diecast AZ91D. *Corrosion Sci.* 41, 249–273. doi:10.1016/S0010-938X(98)00121-8

Song, G. L., and Atrens, A. (1999). Corrosion Mechanisms of Magnesium Alloys. *Adv. Eng. Mater.* 1, 11–33. doi:10.1002/(sici)1527-2648(199909)1:1<11:aid-adem11>3.0.co;2-n

StJohn, D. H., Qian, M., Easton, M. A., Cao, P., and Hildebrand, Z. (2005). Grain Refinement of Magnesium Alloys. *Metall. Mat Trans. A.* 36, 1669–1679. doi:10.1007/s11661-005-0030-6

Su, Z. J., Liu, C. M., Wang, Y. C., and Shu, X. (2013). Effect of Y Content on Microstructure and Mechanical Properties of Mg-2·4Nd-0·2Zn-0·4Zr Alloys. *Mater. Sci. Technol.* 29, 148–155. doi:10.1179/1743284712Y.0000000149

Sudholz, A. D., Gusieva, K., Chen, X. B., Muddle, B. C., Gibson, M. A., and Birbilis, N. (2011). Electrochemical Behaviour and Corrosion of Mg-Y Alloys. *Corrosion Sci.* 53, 2277–2282. doi:10.1016/j.corsci.2011.03.010

Suzuki, M., Kimura, T., Koike, J., and Maruyama, K. (2004). Effects of Zinc on Creep Strength and Deformation Substructures in Mg-Y alloy. *Mater. Sci. Eng. A* 387-389, 706–709. doi:10.1016/j.msea.2003.12.071

Szakács, G., Wiese, B., Mendis, C. L., Tolnai, D., Stark, A., Schell, N., et al. (2014). "*In Situ* Synchrotron Radiation Diffraction during Solidification of Mg4Y and Mg4YxGd Alloys (X=1,4 wt.%)," in *Magnesium Technology*. Editors M. Alderman, M. V. Manuel, N. Hort, and N. R. Neelameggham (San Diego, California, USA: Springer International Publishers), 213–218. doi:10.1007/978-3-319-48231-6

Tan, Q., Yin, Y., Mo, N., Zhang, M., and Atrens, A. (2019). Recent Understanding of the Oxidation and Burning of Magnesium Alloys. *Surf. Innov.* 7, 71–92. doi:10.1680/jsuin.18.00062

Tekin, K. C., Malayoğlu, U., and Shrestha, S. (2013). Electrochemical Behavior of Plasma Electrolytic Oxide Coatings on Rare Earth Element Containing Mg Alloys. *Surf. Coat. Technol.* 236, 540–549. doi:10.1016/j.surfcoat.2013.10.051

Toda-Caraballo, I., Galindo-Nava, E. I., and Rivera-Díaz-del-Castillo, P. E. J. (2014). Understanding the Factors Influencing Yield Strength on Mg Alloys. *Acta Materialia* 75, 287–296. doi:10.1016/j.actamat.2014.04.064

Torkian, A., Faraji, G., and Karimpour, M. (2018). Mechanical Properties and Microstructure of WE43 Mg Alloy Processed by Warm ECAP Followed by Extrusion. *Arch. Metall. Mater.* 63, 1093–1100. doi:10.24425/123781

Tun, K. S., Jayaramanavar, P., Nguyen, Q. B., Chan, J., Kwok, R., and Gupta, M. (2012). Investigation into Tensile and Compressive Responses of Mg-ZnO Composites. *Mater. Sci. Technol.* 28, 582–588. doi:10.1179/1743284711Y.0000000108

Walter, R., and Kannan, M. B. (2011). *In-vitro* Degradation Behaviour of WE54 Magnesium alloy in Simulated Body Fluid. *Mater. Lett.* 65, 748–750. doi:10.1016/j.matlet.2010.11.051

Wang, B. J., Xu, D. K., Wang, S. D., and Han, E. H. (2019). Fatigue Crack Initiation of Magnesium Alloys under Elastic Stress Amplitudes: A Review. *Front. Mech. Eng.* 14, 113–127. doi:10.1007/s11465-018-0482-1

Wang, L., Jiang, J., Ma, A., Li, Y., and Song, D. (2017). A Critical Review of Mg-Based Hydrogen Storage Materials Processed by Equal Channel Angular Pressing. *Metals* 7, 324. doi:10.3390/met7090324

Wang, Z., Wang, J.-G., Chen, Z.-Y., Zha, M., Wang, C., Liu, S., et al. (2019). Effect of Ce Addition on Modifying the Microstructure and Achieving a High Elongation with a Relatively High Strength of As-Extruded AZ80 Magnesium Alloy. *Materials* 12, 76. doi:10.3390/ma12010076

Westengen, H., and Aune, T. K. (2006). "Magnesium Casting Alloys," in *Magnesium Technology - Metallurgy, Design Data, Applications*. Editors H. E. Friedrich and B. L. Mordike (Berlin, Germany: Springer-Verlag Berlin Heidelberg).

Witecka, A., Valet, S., Basista, M., and Boccaccini, A. R. (2021). Electrophoretically Deposited High Molecular Weight Chitosan/bioactive Glass Composite Coatings on WE43 Magnesium alloy. *Surf. Coat. Technol.* 418, 127232. doi:10.1016/j.surfcoat.2021.127232

Witte, F., Hort, N., Vogt, C., Cohen, S., Kainer, K. U., Willumeit, R., et al. (2008). Degradable Biomaterials Based on Magnesium Corrosion. *Curr. Opin. Solid State. Mater. Sci.* 12, 63–72. doi:10.1016/j.cossms.2009.04.001

Xia, S. J., Yue, R., Rateick, R. G., Jr., and Birss, V. I. (2004). Electrochemical Studies of AC/DC Anodized Mg Alloy in NaCl Solution. *J. Electrochem. Soc.* 151, B179–B187. doi:10.1149/1.1646139

Xiang, C., Gupta, N., Coelho, P., and Cho, K. (2018). Effect of Microstructure on Tensile and Compressive Behavior of WE43 alloy in as Cast and Heat Treated Conditions. *Mater. Sci. Eng. A* 710, 74–85. doi:10.1016/j.msea.2017.10.084

Xie, J., Zhang, J., You, Z., Liu, S., Guan, K., Wu, R., et al. (2021). Towards Developing Mg Alloys with Simultaneously Improved Strength and Corrosion Resistance via RE Alloying. *J. Magnesium Alloys* 9, 41–56. doi:10.1016/j.jma.2020.08.016

Xu, D., Zhao, K., Yang, C., Li, H., and Zhang, J. (2018). Effect of Heat Treatment on Microstructure and Mechanical Properties of the AZ31/WE43 Bimetal Composites. *Metals* 8, 971. doi:10.3390/met8110971

Yan, J., Sun, Y., Xue, F., Xue, S., and Tao, W. (2008). Microstructure and Mechanical Properties in Cast Magnesium-Neodymium Binary Alloys. *Mater. Sci. Eng. A* 476, 366–371. doi:10.1016/j.msea.2007.05.058

Yang, C., Gupta, N., Ding, H., and Xiang, C. (2020). Effect of Microstructure on Corrosion Behavior of We43 Magnesium alloy in as Cast and Heat-Treated Conditions. *Metals* 10, 1552. doi:10.3390/met10111552

Yang, L., Li, Y., Qian, B., and Hou, B. (2015). Polyaspartic Acid as a Corrosion Inhibitor for WE43 Magnesium alloy. *J. Magnesium Alloys* 3, 47–51. doi:10.1016/j.jma.2014.12.009

You, S., Huang, Y., Kainer, K. U., and Hort, N. (2017). Recent Research and Developments on Wrought Magnesium Alloys. *J. Magnesium Alloys* 5, 239–253. doi:10.1016/j.jma.2017.09.001

Yu, K., Li, W., Wang, R., Wang, B., and Li, C. (2008). Effect of T5 and T6 Tempers on a Hot-Rolled WE43 Magnesium Alloy. *Mater. Trans.* 49, 1818–1821. doi:10.2320/matertrans.MRA2008602

Yuwono, J. A., Birbilis, N., Taylor, C. D., Williams, K. S., Samin, A. J., and Medhekar, N. V. (2019). Aqueous Electrochemistry of the Magnesium Surface: Thermodynamic and Kinetic Profiles. *Corrosion Sci.* 147, 53–68. doi:10.1016/j.corsci.2018.10.014

Zeng, Z., Stanford, N., Davies, C. H. J., Nie, J.-F., and Birbilis, N. (2019). Magnesium Extrusion Alloys: a Review of Developments and Prospects. *Int. Mater. Rev.* 64, 27–62. doi:10.1080/09506608.2017.1421439

Zhang, J., Niu, X., Qiu, X., Liu, K., Nan, C., Tang, D., et al. (2009). Effect of yttrium-rich misch metal on the microstructures, mechanical properties and corrosion behavior of die cast AZ91 alloy. *J. Alloys Compd.* 471, 322–330. doi:10.1016/j.jallcom.2008.03.089

Zhang, T., Meng, G., Shao, Y., Cui, Z., and Wang, F. (2011). Corrosion of Hot Extrusion AZ91 Magnesium alloy. Part II: Effect of Rare Earth Element Neodymium (Nd) on the Corrosion Behavior of Extruded alloy. *Corrosion Sci.* 53, 2934–2942. doi:10.1016/j.corsci.2011.05.035

Zhang, X., Wu, G., Peng, X., Li, L., Feng, H., Gao, B., et al. (2015). Mitigation of Corrosion on Magnesium Alloy by Predesigned Surface Corrosion. *Sci. Rep.* 5, 17399. doi:10.1038/srep17399

Zhang, Y., Gao, M., Etim, I. P., Tan, L., and Yang, K. (2020). Optimising the Torsional Properties and Corrosion Resistance of Biodegradable WE43 Mg alloy by ECAP and Subsequent Ageing. *Mater. Technol.* 35, 402–410. doi:10.1080/10667857.2019.1688539

Zhao, H. D., Qin, G. W., Ren, Y. P., Pei, W. L., Chen, D., and Guo, Y. (2011). The Maximum Solubility of Y in α-Mg and Composition Ranges of Mg24Y5−x and Mg2Y1−x Intermetallic Phases in Mg-Y Binary System. *J. Alloys Compd.* 509, 627–631. doi:10.1016/j.jallcom.2010.09.120

Zhao, Y., Wu, G., Lu, Q., Wu, J., Xu, R., Yeung, K. W. K., et al. (2013). Improved Surface Corrosion Resistance of WE43 Magnesium alloy by Dual Titanium and Oxygen Ion Implantation. *Thin Solid Films* 529, 407–411. doi:10.1016/j.tsf.2012.05.046

Zhilyaev, A., and Langdon, T. (2008). Using High-Pressure Torsion for Metal Processing: Fundamentals and Applications. *Prog. Mater. Sci.* 53, 893–979. doi:10.1016/j.pmatsci.2008.03.002

Zomorodian, A., Garcia, M. P., Moura E Silva, T., Fernandes, J. C. S., Fernandes, M. H., and Montemor, M. F. (2013). Corrosion Resistance of a Composite Polymeric Coating Applied on Biodegradable AZ31 Magnesium alloy. *Acta Biomater.* 9, 8660–8670. doi:10.1016/j.actbio.2013.02.036

Zomorodian, A., Santos, C., Carmezim, M. J., Silva, T. M. e., Fernandes, J. C. S., and Montemor, M. F. (2015). "*In-vitro*" Corrosion Behaviour of the Magnesium alloy with Al and Zn (AZ31) Protected with a Biodegradable Polycaprolactone Coating Loaded with Hydroxyapatite and Cephalexin. *Electrochimica Acta* 179, 431–440. doi:10.1016/j.electacta.2015.04.013

Zucchi, F., Grassi, V., Frignani, A., Monticelli, C., and Trabanelli, G. (2006). Electrochemical Behaviour of a Magnesium alloy Containing Rare Earth Elements. *J. Appl. Electrochem.* 36, 195–204. doi:10.1007/s10800-005-9053-3

Zucchi, F., Grassi, V., Frignani, A., Monticelli, C., and Trabanelli, G. (2006). Influence of a Silane Treatment on the Corrosion Resistance of a WE43 Magnesium alloy. *Surf. Coat. Technol.* 200, 4136–4143. doi:10.1016/j.surfcoat.2005.02.073

Zumdick, N. A., Jauer, L., Kersting, L. C., Kutz, T. N., Schleifenbaum, J. H., and Zander, D. (2019). Additive Manufactured WE43 Magnesium: A Comparative Study of the Microstructure and Mechanical Properties with Those of Powder Extruded and As-Cast WE43. *Mater. Characterization* 147, 384–397. doi:10.1016/j.matchar.2018.11.011

Conflict of Interest: The authors declare that the research was conducted in the absence of any commercial or financial relationships that could be construed as a potential conflict of interest.

Publisher's Note: All claims expressed in this article are solely those of the authors and do not necessarily represent those of their affiliated organizations, or those of the publisher, the editors and the reviewers. Any product that may be evaluated in this article, or claim that may be made by its manufacturer, is not guaranteed or endorsed by the publisher.

frontiers in Materials

CORRECTION
published: 02 March 2022
doi: 10.3389/fmats.2022.858921

Corrigendum: Rare Earth Based Magnesium Alloys—A Review on WE Series

Lénia M. Calado[1]*, *Maria J. Carmezim*[1,2] and *M. Fátima Montemor*[1]

[1]Centro de Química Estrutural-CQE, DEQ, Instituto Superior Técnico, Universidade de Lisboa, Lisbon, Portugal, [2]ESTSetúbal, CDP2T, Instituto Politécnico de Setúbal, Setúbal, Portugal

Keywords: magnesium alloys, rare earth elements, corrosion, corrosion protection, coatings

OPEN ACCESS

Edited and reviewed by:
Yingwei Song,
Institute of Metal Research (CAS), China

***Correspondence:**
Lénia M. Calado
leniacalado@tecnico.ulisboa.pt

Specialty section:
This article was submitted to Structural Materials, a section of the journal Frontiers in Materials

Received: *20 January 2022*
Accepted: *31 January 2022*
Published: *02 March 2022*

Citation:
Calado LM, Carmezim MJ and Montemor MF (2022) Corrigendum: Rare Earth Based Magnesium Alloys—A Review on WE Series. Front. Mater. 9:858921. doi: 10.3389/fmats.2022.858921

A Corrigendum on

Rare Earth Based Magnesium Alloys—A Review on WE Series
by Calado, L. M., Carmezim, M. J., and Montemor, M. F. (2022). Front. Mater. 8:804906. doi: 10.3389/fmats.2021.804906

In the original article, there was a mistake in the legend for **Figure 2** as published. The reference cited in the figure legend is not correct. The correct legend appears below.

The authors apologize for this error and state that this does not change the scientific conclusions of the article in any way. The original article has been updated.

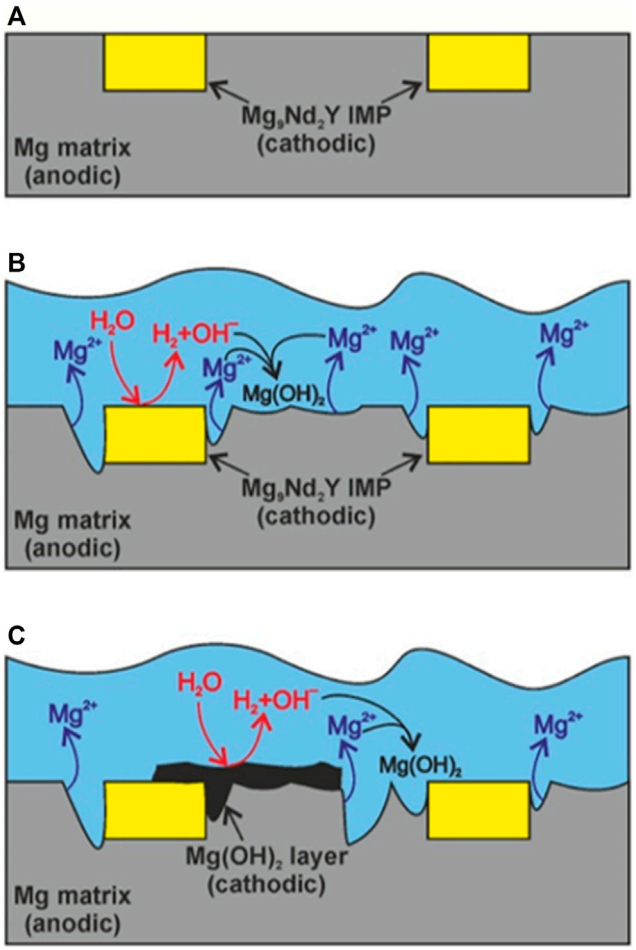

FIGURE 2 | Possible mechanism of corrosion for WE series magnesium alloys **(A)**, involving the formation of a $Mg(OH)_2$ layer on the surface of the alloy **(B)**, with localized microgalvanic corrosion at preferential sites **(C)**. Figure reproduced from (Kharitonov et al., 2021) under the terms of the Creative Commons CC-BY 4.0 License.

frontiers in Materials

ORIGINAL RESEARCH
published: 27 January 2022
doi: 10.3389/fmats.2021.799780

Effect of $ZrSiO_4$ Concentration on the Microstructure and Corrosion Resistance of MAO Coatings Formed on AZ91 Magnesium Alloy

Tianlu Li[1†], Guorui Chen[1†], Mingzhe Xiang[1], Yun Zhao[1,2,3] and Minfang Chen[1,2,3]**

[1]School of Materials Science and Engineering, Tianjin University of Technology, Tianjin, China, [2]Key Laboratory of Display Materials and Photoelectric Device (Ministry of Education), Tianjin University of Technology, Tianjin, China, [3]National Demonstration Center for Experimental Function Materials Education, Tianjin University of Technology, Tianjin, China

As a metallic material with lightweight and high specific strength, magnesium alloy has excellent application prospects. However, the rapid corrosion rate and localized corrosion behavior of magnesium alloys limit the practical application in the automobile industry. In this study, to improve the corrosion resistance of AZ91 alloy, the film of different concentrations containing zirconium (AZR0, AZR5, AZR10, AZR15) was prepared on the surface of AZ91 alloy by micro-arc oxidation technology in the Na_2SiO_3-Na_3PO_4 system. Furthermore, the influence of electrolyte composition on the corrosion resistance of the MAO film was systematically investigated. The experimental results revealed that the $ZrSiO_4$ particles added in the electrolyte could enter into the MAO film and $ZrSiO_4$ particles were also decomposed into ZrO_2 and $Mg_2Zr_5O_{11}$ in the process of micro-arc oxidation. More importantly, the formation of micro-cracks and other defects in the film could be reduced after this process. The addition of 15 g l^{-1} $ZrSiO_4$ in the electrolyte was contributed to the best comprehensive properties of MAO-processed AZ91 specimens, including improved Vickers hardness of 167.16 Hv, Young's modulus of 652 MPa, and enhanced corrosion resistance (R_P = 9.82 × 10^5 Ω cm^2). This approach could provide the approach for developing Mg-based materials with high anticorrosion in industrial fields.

Keywords: magnesium alloy, micro-arc oxidation (MAO), $ZrSiO_4$, anti-corrosion, microstructure

OPEN ACCESS

Edited by:
Liang Wu,
Chongqing University, China

Reviewed by:
You Zhang,
Beijing Institute of Petrochemical Technology, China
Zhihui Xie,
China West Normal University, China

***Correspondence:**
Yun Zhao
yun_zhaotju@163.com
Minfang Chen
mfchentj@126.com

†These authors have contributed equally to this work

Specialty section:
This article was submitted to Structural Materials, a section of the journal Frontiers in Materials

Received: *22 October 2021*
Accepted: *25 November 2021*
Published: *27 January 2022*

Citation:
Li T, Chen G, Xiang M, Zhao Y and Chen M (2022) Effect of $ZrSiO_4$ Concentration on the Microstructure and Corrosion Resistance of MAO Coatings Formed on AZ91 Magnesium Alloy. Front. Mater. 8:799780. doi: 10.3389/fmats.2021.799780

INTRODUCTION

Magnesium-based (Mg-based) material has been recognized as a promising alternative to conventional Al-based load-bearing materials due to its high strength-to-weight ratio and low density (Zhang et al., 2019). The considerable drawback of magnesium and its alloys is that they are impressionable to corrosion in a high-humidity atmosphere, which seriously restricts their industrial applications (Li et al., 2020a).

Defense of Mg in anti-corrosion can usually be acquired by three strategies: alloying, composite formation, and protective coatings. Generally, surface modification can observably improve the corrosion resistance of substrate without influencing its initial properties (Li et al., 2020b). Surface treatment techniques, including anodic oxidation (Zarei et al., 2021), plasma spraying (Cao et al., 2021), vapor deposition (Li et al., 2021), sol–gel film (Zhang et al., 2021), and micro-arc oxidation

(Zhang et al., 2020a), were widely used for this purpose. Among the techniques as mentioned above, micro-arc oxidation (MAO) technology can contribute to a protective oxide layer on the surface of metallic materials in instantaneous high temperature and high pressure by generating spark discharges. Because of the feature of MAO, the oxide layer is formed on the substrate, resulting in strong interfacial bonding between the metallic substrate and MAO coating (Lu et al., 2016). Thus, the MAO process is extensively used to improve the corrosion resistance of Mg-based materials. Several previous studies have revealed that the electrolyte composition is essential and crucial to improving the comprehensive performance of MAO coating, like corrosion resistance and adhesion strength, and control the corrosion behavior of Mg-relevant materials (Fattah-alhosseini et al., 2020).

Researchers have added miscellaneous micro/nano irresolvable particles into the electrolytes, which can participate in the MAO process and form into parts of the coatings. Generally, this *in-situ* technology for preparing composite coating deposits ceramic particles, such as SiC (Wang et al., 2015) and CeO_2 (Lim et al., 2012). For example, MAO coating incorporated with CeO_2 was obtained on AZ91D Mg alloy. The EIS and potentiodynamic tests in 3.5 wt% NaCl solution indicated that the anticorrosion behavior of MAO-processed AZ31 Mg alloy was markedly improved (Lim et al., 2012).

Zirconium is a potential biomaterial for dental and orthopedic implants owing to its high mechanical strength, high corrosion resistance, and excellent biocompatibility. ZrO_2 has the strengths of high mechanical strength, strong toughness, and good corrosion resistance. In addition, ZrO_2 influences stress-induced transformation toughening (Zhou et al., 2021).

Therefore, in some studies, K_2ZrF_6- and ZrO_2-doped composite MAO coatings were prepared. For example, Arrable et al. (Arrabal et al., 2008) showed the allocation of ZrO_2 nanoparticles across the surface and cross section of the coating. Li et al. (Li et al., 2015) reported enrichment in the anticorrosion of the ZrO_2-containing MAO coatings on TC4 alloy. Zhang et al. (Zhang et al., 2010) used K_2ZrF_6-based electrolyte and acquired MAO coatings consisting of the ZrO_2 phase. Koo et al. (Rehman et al., 2017) studied the MAO coatings manufactured on AZ31B Mg alloy in K_2ZrF_6-Na_2SiO_3-based electrolyte. It was observed that the hardness and anticorrosion properties of the coatings were highly improved after MAO processing.

Zircon ($ZrSiO_4$), as a common and cheap particle for industrial use, has excellent physical and chemical capabilities, such as good mechanical properties, reducing friction coefficient, and enhancing corrosion resistance (Yang et al., 2021). However, the participant investigation in the literature has been rarely recorded, showing that ZrO_2 ceramic coating can be provided with MAO technology. Therefore, in this work, MAO of AZ91 Mg alloy was conducted in $ZrSiO_4$-containing Na_2SiO_3-Na_3PO_4-based electrolyte, and electrochemical corrosion properties of $ZrSiO_4$ particle-containing MAO coatings on AZ91 Mg alloy were evaluated by the potentiodynamic test.

TABLE 1 | Composition of electrolyte.

Samples	Concertation of electrolytes			
	NaOH	$Na_3PO_4·9H_2O$	$Na_2SiO_3·12H_2O$	$ZrSiO_4$
AZR0	6 g/l	9.3 g/l	2.3 g/l	0 g/l
AZR5	6 g/l	9.3 g/l	2.3 g/l	5 g/l
AZR10	6 g/l	9.3 g/l	2.3 g/l	10 g/l
AZR15	6 g/l	9.3 g/l	2.3 g/l	15 g/l

MATERIALS AND METHODS

Materials

The substrate used in this work was a commercial material, AZ91 Mg alloy (wt%:0.35 Zn, 0.15 Mn, 8.3 Al, Mg Bal.). For the MAO process, the extruded bar samples of AZ91 Mg alloy were cut into

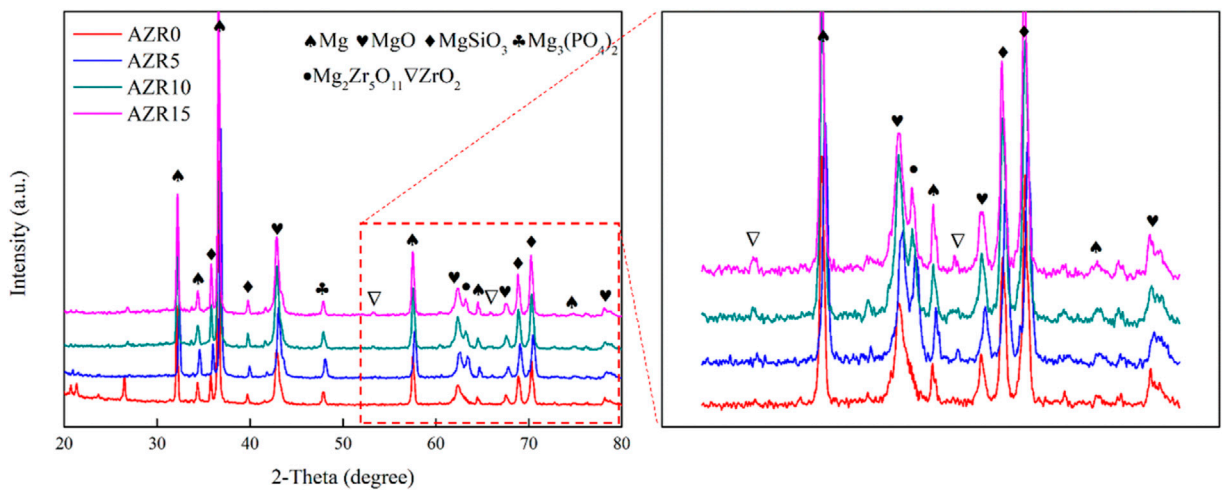

FIGURE 1 | The XRD patterns of the samples.

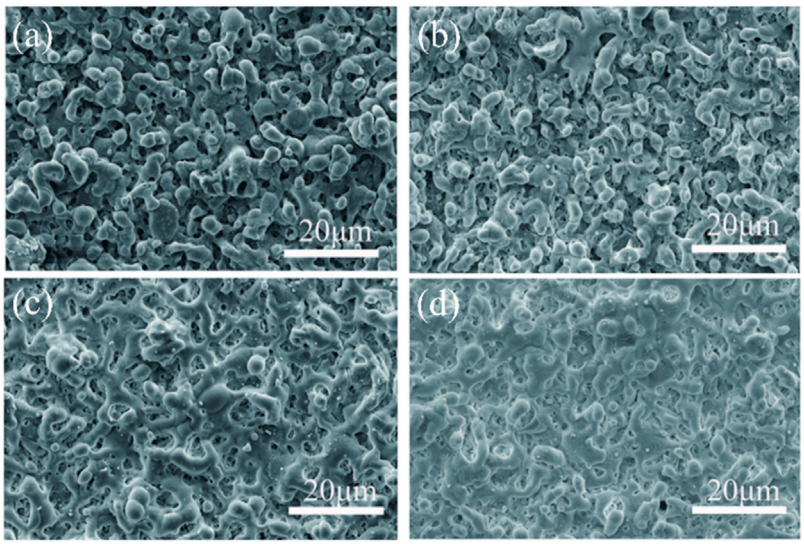

FIGURE 2 | SEM morphologies of the different samples **(A)** AZR0, **(B)** AZR5, **(C)** AZR10, and **(D)** AZR15.

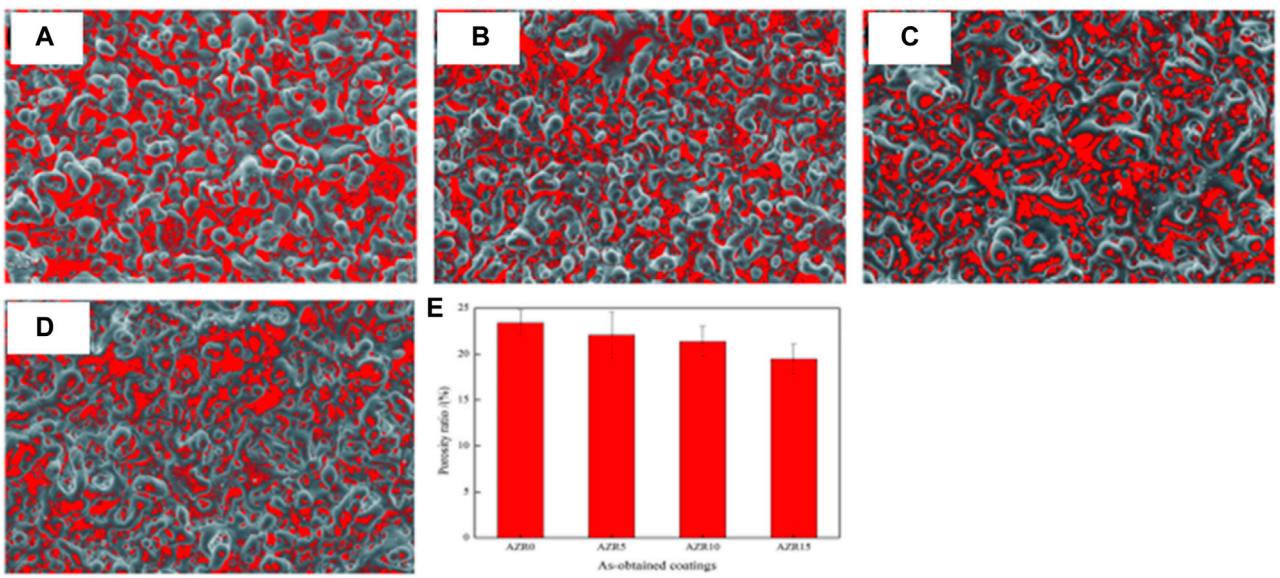

FIGURE 3 | Porosity ratio of the different samples **(A)** AZR0, **(B)** AZR5, **(C)** AZR10, and **(D)** AZR15.

TABLE 2 | Elemental compositions of different samples analyzed by EDS.

Samples	Element (Weight %)				
	O	Mg	Si	P	Zr
AZR0	42.71	49.80	3.11	4.38	--
AZR5	39.78	47.64	3.96	1.49	7.11
AZR10	38.45	42.62	4.90	0.76	13.27
AZR15	38.72	36.12	5.72	1.44	18.00

a shape Φ 8 mm × 3 mm. The samples were then ground by SiC sandpaper up to 2000#, washed with ethanol in ultrasound for 10 min, and dried in air.

Preparation of MAO Coating

The MAO coatings were accomplished utilizing an installation consisting of an MAO-50D power supply. Mg alloy AZ91 was regarded as the anode, and stainless steel was used as the cathode. The mode of MAO was constant pressure. The termination

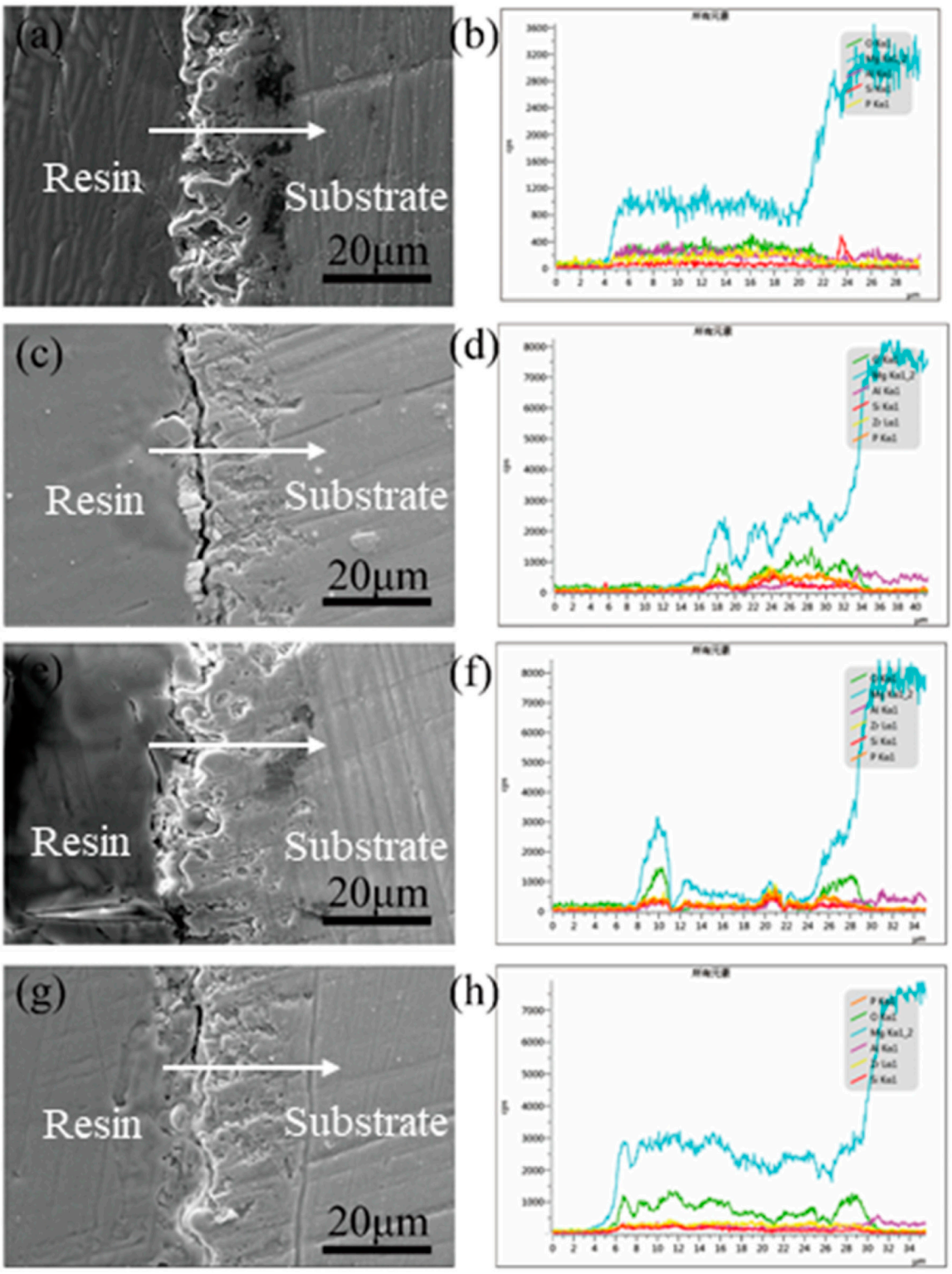

FIGURE 4 | SEM morphologies and EDS results of the cross-sectional views of the different samples **(A)** AZR0, **(B)** AZR5, **(C)** AZR10, and **(D)** AZR15.

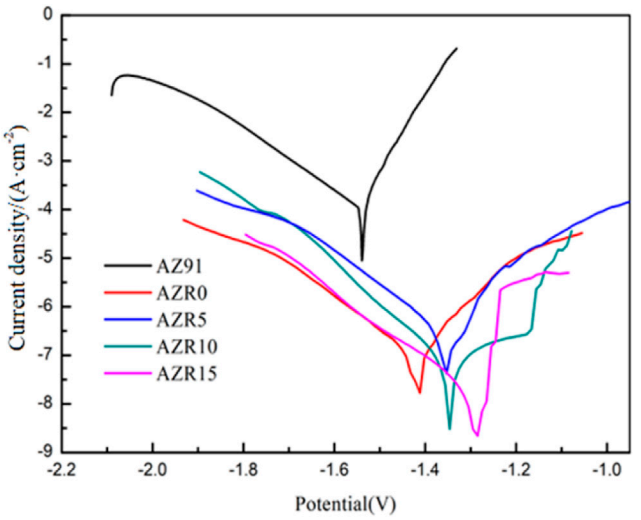

FIGURE 5 | Potentiometric polarization curves of the different samples.

voltage, frequency, duty cycle, and oxidation time were fixed at 400 V, 600 Hz, 30%, and 10 min, respectively. The electrolytes used in the MAO process are shown in **Table 1**. The average size of $ZrSiO_4$ powder particles in the electrolyte was approximately 737.5 nm, and sodium dodecylbenzene sulfonate was added as an anionic surfactant to ensure the particles evenly dispersed in the solution.

Characterization

The phase constituents of obtained samples were analyzed using an X-ray diffractometer (XRD, D/max-2500). The surface and cross-section morphology were investigated using a field emission scanning electron microscope (SEM, Quanta FEG-250). Moreover, elemental compositions of surface and cross section were observed using a SEM-attached energy dispersive X-ray spectrometry (EDS) device. Sample wettability was characterized *via* a static contact angle goniometer (DSA1000, Kruss, Germany) using deionized water droplets (volume of one drop = 3 μl). Three different positions were chosen to be measured for each sample. The porosity ratio in the coating surface was analyzed using ImageJ software.

The corrosion behavior was gauged using a Zennium electrochemical workstation after the open circuit potential (OCP) for 30 min to be stabilized in a 3.5% NaCl solution. A representative three-electrode mechanism was composed of graphite electrode as an auxiliary electrode, saturated calomel electrode (SCE) as a reference electrode, and specimen (1 cm^2 exposed area) as a working electrode. The corrosion resistance was employed to study the Tafel curve to give the corrosion potential (E_{corr}), the corrosion current density (I_{corr}), the slope of cathodic polarization (β_c), and the slope of the anodic polarization branch (β_a). In addition, the polarization resistance, R_p, and inverse ratio to corrosion rate can be computed using the simplified Stern–Geary **Equation 1** (Li et al., 2020c). **Eq. 2** was converted to the protection efficiency (Rahman et al., 2020).

$$Rp = \frac{\beta a \times \beta c}{2.303 \times I_{corr}\left(\beta a + \beta c\right)} \tag{1}$$

$$E_{protection} = 1 - \frac{I_{(corr)c}}{I_{(corr)uc}} \tag{2}$$

$I(_{corr})_{uc}$ is the corrosion current density of substrate AZ91 Mg alloy, and $I(_{corr})_c$ is the corrosion current density after the MAO process on AZ91 Mg alloy.

A binding force tester (WS-2005) was utilized for testing the adhesion strength of samples. The adhesion strength of the film was calculated using the formula shown by **Equation 3**. The dynamic load was 40 N, the loading time was 1 min, and the scratch length was 3 mm.

$$P = \frac{F}{\pi R^2} \tag{3}$$

P represents the strength of adhesion strength, and F is the load value. R is the radius of the diamond indenter.

A dimensional hardness tester (HMV-2T) was used to analyze the hardness of the sample. The loading load was 10 N, and the loading time was 20 s. An atomic force microscope (AFM Dimension Icon), analyzed by NanoScope Analysis software, can be utilized to analyze Young's modulus of the MAO coatings.

RESULTS AND DISCUSSIONS

Microstructure and Phase Analysis

Figure 1 shows the XRD pattern of the MAO coatings on AZ91 Mg alloy prepared at different concentrations of $ZrSiO_4$. Besides the Mg phase from the substrate, the diffraction peaks of ZrO_2, $Mg_2Zr_5O_{11}$, $Mg_3(PO_4)_2$, $MgSiO_3$, and MgO could be observed, indicating the active involvement of electrolytes in the solution for the MAO process. Specifically, the existence of ZrO_2 and $Mg_2Zr_5O_{11}$ in the coatings also showed the participation of $ZrSiO_4$ decomposed into ZrO_2 and SiO_2 in the MAO process (Ur Rehman and Choi, 2019). The SiO_2 reacted with MgO to form $MgSiO_3$. Additionally, with the increase in $ZrSiO_4$

TABLE 3 | The parameters obtained from potentiodynamic polarization tests in 3.5wt% NaCl.

Sample	I_{corr}/(A/cm^2)	E_{corr}/(V)	βa/(mV)	-βc/(mV)	R_p/(Ω·cm2)	Ep/%
AZ91	2.51×10^{-5}	−1.54	12.9	14.8	1.19×10^{2}	——
AZR0	6.10×10^{-7}	−1.43	119	148	4.70×10^{4}	97.57
AZR5	4.16×10^{-8}	−1.38	126	122	6.47×10^{4}	99.83
AZR10	$2.67 \times {}^{-}10^{-8}$	−1.35	126	93.5	8.73×10^{5}	99.89
AZR15	1.49×10^{-8}	−1.29	75.8	52.8	9.82×10^{5}	99.94

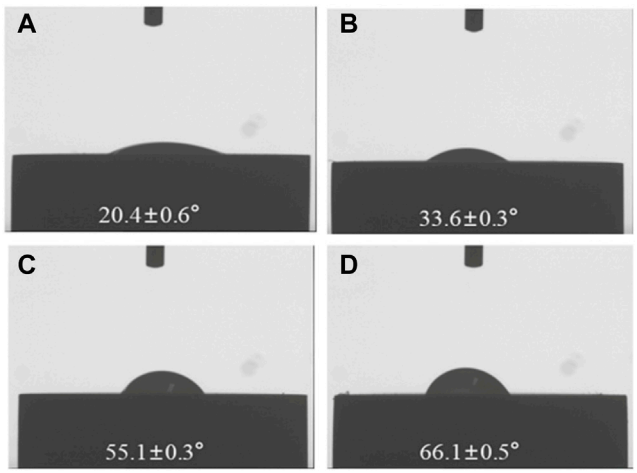

FIGURE 6 | Contact angles of the different samples.

concentration, the peak strength of ZrO_2 was also raised gradually (Kovaleva et al., 2021).

Figure 2 represents the surface morphologies of the MAO coatings prepared under preset conditions. All the coatings performed a porous configuration with many crateriform micro-pores unevenly distributed due to the mutual effect of fusional oxides and the gas bubbles in the processes (Xia et al., 2013). As the $ZrSiO_4$ concentrations varied, the surface of samples exhibited a distinct difference. The surfaces of AZR10 and ZAR15 seemed relatively smoother in comparison to AZR0 and ZAR5. The results of the porosity ratio in **Figure 3E** also illustrated that an increasing $ZrSiO_4$ concentration was simultaneously beneficial to reducing the micro-pores on the surface. These were possibly contributed to the decrease in crateriform pore size and the formation of many blocked pores, combined with more significant amounts of ZrO_2 and SiO_2 from $ZrSiO_4$ decomposition (Zhang et al., 2020b).

Table 2 shows the contents of each element on the MAO coating surface corresponding to those in **Figure 2**. It was found that the elements of O, Si, P, Mg, and Zr were primary in the final MAO coatings. In addition, the contents of Zr and Si in AZR15 were higher than those of others, indicating that the content of $ZrSiO_4$ added could directly influence the Zr and Si contents in the coating, thereby possibly affecting the property of MAO coating.

Figure 4 displays the cross-sectional morphologies and the elemental distribution of different MAO coatings. It shows that all coatings adhered to the Mg alloy substrate tightly, and there was a relatively dense structure without micropores and large cracks appearing (Gao et al., 2018). Their thickness was also increased clearly with increasing $ZrSiO_4$ content in the electrolyte. In **Figures 4B,D,F,H**, it could be seen that the elements distributed in the cross section were identical to those on the coating surface. Zr of the cross-sectional distribution indicated that $ZrSiO_4$ particles were involved in the MAO process.

The variation of film thickness and defects present in coating had a significant impact on the corrosion resistance of the coating to the substrate. Thus, the analysis of corrosion resistance for the coatings was conducted.

Corrosion Resistance

Figure 5 presents the potentiodynamic polarization curves for the MAO coatings in 3.5 wt% NaCl solution. Tafel fitting was also carried out, and the results are listed in **Table 3**. β_c represents cathodic hydrogen evolution, and β_a represents the dissolution of Mg. E_{corr} and I_{corr} were the self-etching potential and current density, respectively (Xiong et al., 2018). R_p represents polarization resistance. Generally, higher E_{corr}, lower I_{corr}, and

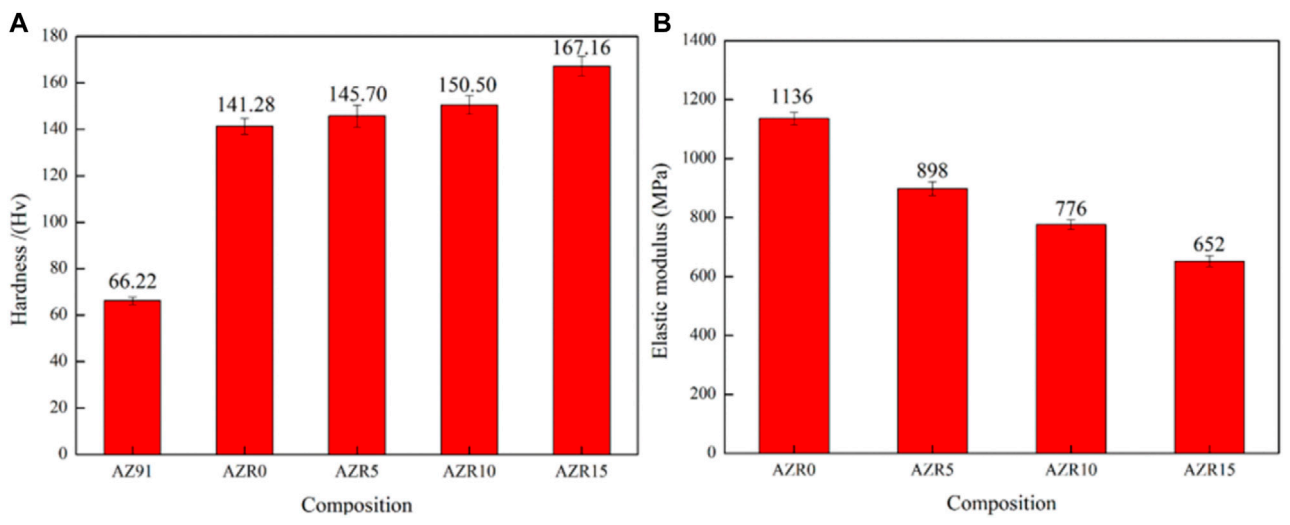

FIGURE 7 | Hardness. **(A)** Young's modulus and **(B)** of MAO coating of the different samples.

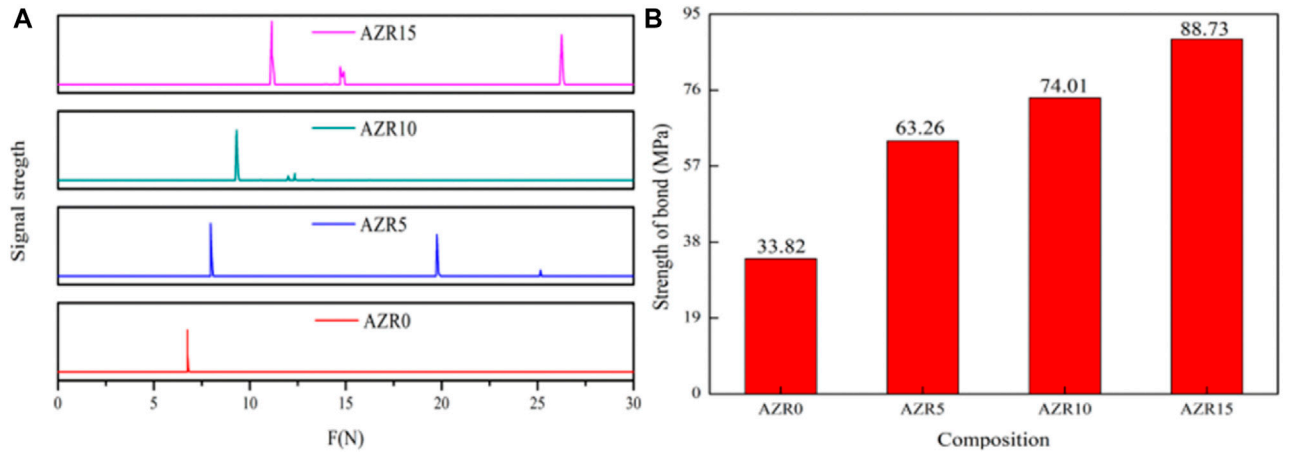

FIGURE 8 | The binding force of the different samples.

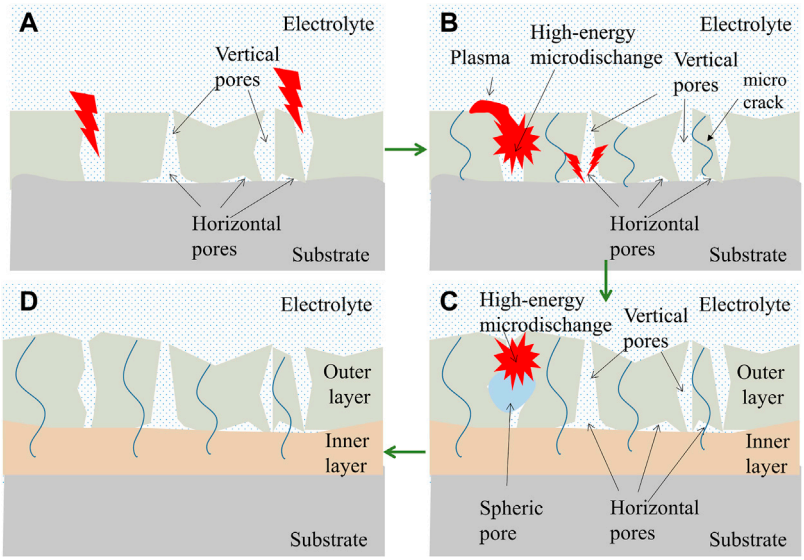

FIGURE 9 | Formation mechanism of the MAO film.

higher R_p values implied better anti-corrosion of materials (Wang et al., 2018). It is revealed that adding $ZrSiO_4$ was favorable to increase the E_{corr} and R_p of the coating, and the higher the $ZrSiO_4$ content was, the more significant the improvement of coating anti-corrosion.

Furthermore, the AZR15 specimen, whose I_{corr} decreased from 2.51×10^{-5} for the substrate to 1.49×10^{-8} A cm^{-2}, had the best corrosion resistance performance among all samples.

Wettability

The wettability of the surface also had a significant effect on the corrosion resistance of the coating.

Because of the porous structure of the surface, the MAO coating was susceptible to be hydrophilic (Bordbar-Khiabani et al., 2019). After adding $ZrSiO_4$ to the electrolyte, the contact angle of the coated samples was remarkably and gradually increased. The AZR15 had the highest value of $66.1 \pm 0.5^{\circ}$ in **Figure 6**. It is revealed that the increase in the $ZrSiO_4$ concentration could significantly enhance the hydrophobicity of the coating surface, thereby preventing the direct contact between corrosive medium and specimen and improving the corrosion resistance of MAO coating. This was consistent with the results of electrochemical tests.

The circulation reaction of corrosive ions (Cl^-) into the film with the substrate was the pre-condition for the corrosion of the Mg alloy substrate. The inner layer of MAO coating mainly improved the corrosion resistance of the film. According to the above results, there were two main aspects of the improvement of corrosion resistance. Firstly, with the increase in the $ZrSiO_4$ concentration, the hydrophobic surface restrained the entrance

of corrosive ions (Cl^-) from the surface (Kirkland et al., 2012). Moreover, as seen in **Figure 3**, the coatings with $ZrSiO_4$ had a low pore density. This behavior could also limit the breakthrough of Cl^- to the coating/substrate boundary. Moreover, the thickness rise of the coating further enhanced the paths for the corrosive ions through the coating, thus increasing the anticorrosion of MAO coating.

Mechanical Properties

Figure 7 exhibits the change of the hardness 1) and Young's modulus 2) at the different samples. Owing to the increasing concentration of $ZrSiO_4$ in the coatings, the samples' hardness was also increased. AZR15 had the highest value of 167.16 Hv (Zuo et al., 2019). Meanwhile, Young's modulus of the samples was lower than that of pure AZ91 alloy (1136 MPa), and this value of AZR15 was decreased to 652 MPa. Its mechanical strength depended on porosity, which depended on its manufacturing process (Es-saddik et al., 2021). During the MAO process, $ZrSiO_4$ particles could separate into ZrO_2, thereby reducing the micro-cracks and other defects in the film and affecting the mechanical properties of the samples.

Adhesion Strength

Figure 8 shows the binding strength of the coatings for the specimens. It can be seen that the binding strength of AZR0 and AZR15 films were 33.82 and 88.73 MPa, respectively, indicating the significant effect of $ZrSiO_4$ on enhancing the binding strength between coating and substrate. The $ZrSiO_4$ dispersed in the electrolyte could enter the discharge channel of forming coating during the MAO process. Its decomposition ZrO_2 could be as particles present in the cooling and solidifying coating process, which may be improved compactness and restrain the crack propagation of formed MAO coating, resulting in higher binding force and lower Young's modulus (Yao et al., 2019).

Formation Mechanism of the Coating

Figure 9 shows formation mechanism of MAO film. The forming process of the composite coating was presented as follows: during the MAO process, the high voltage generated an electric domain between the cathode and anode attended by the constitution of micro discharge exiting on the Mg alloy substrate. The micro discharges burning under the loose coating layer caused the oxidation of the Mg alloy substrate, but the oxides were not carried to the surface of the loosened coating. During this stage, two micro discharges (blunt little micro-discharges and transparently burning ones) occurred on the coating surface. Then in the next stage, there was a higher possibility of blocking the pores above the dense coating layer or these pores moving from the substrate to the interface of inner/outer layers. This is the result in regional sealing of the pores when inner micro discharges were ignited. Micro discharges with weak stress could be observed (high-energy micro discharges blank) on the surfaces. At this stage, sealing of the pores in the coating of AZ91 was dominated (Rakoch et al., 2020).

The phase composition was formed by the different reactions during the MAO process (Baghdadabad et al., 2020; Kovaleva et al., 2021).

$$Mg = Mg^{2+} + 2e^- \quad (4)$$

$$Mg^{2+} + O^{2-} = MgO \quad (5)$$

$$3Mg^{2+} + 2PO_4^{3-} = Mg_3(PO_4)_2 \quad (6)$$

$$ZrSiO_4 = ZrO_2 + SiO_2 \quad (7)$$

$$2Mg^{2+} + SiO_3^{2-} + 2OH^- = Mg_2SiO_4 + H_2O \quad (8)$$

$$Mg_2SiO_4 + SiO_2 = MgSiO_3\ (Heat) \quad (9)$$

$$Mg^{2+} + SiO_3^{2-} = MgSiO_3 \quad (10)$$

$$MgO + SiO_2 = MgSiO_3 \quad (11)$$

$$2MgO + 5ZrO_2 = Mg_2Zr_5O_{11} \quad (12)$$

CONCLUSION

In this work, MAO coatings were successfully prepared on the AZ91 Mg alloy in Na_2SiO_3-Na_3PO_4 based solution with various $ZrSiO_4$ concentrations. The results of the present investigation were as the following:

1. ZrO_2 and SiO_2 are produced by $ZrSiO_4$ particles and participate in the process into the MAO layer. With $ZrSiO_4$ particles concentration increasing, the MAO coatings became denser, and the holes in the coating significantly decreased. The micro-cracks and defects were also reduced on the surface of the coating.
2. The corrosion resistance and mechanical properties were significantly improved when $ZrSiO_4$ was added to the electrolyte. Meanwhile, the best performance in aspects of self-corrosion potential (−1.289 V), self-corrosion current (1.49×10^{-8} A cm^2), polarization resistance (9.82×10^5 Ω·cm2), and protection efficiency (99.94%) were found in the $ZrSiO_4$ concentration of 15 g/l. In addition, the $ZrSiO_4$ concentration also enhanced the hardness and decreased Young's modulus of the coatings.

DATA AVAILABILITY STATEMENT

The raw data supporting the conclusion of this article will be made available by the authors, without undue reservation.

AUTHOR CONTRIBUTIONS

TL: writing–original draft, formal analysis. GC: methodology, visualization. MX: formal analysis. YZ: writing–review and editing, supervision. MC: writing–review and editing, supervision, project administration.

ACKNOWLEDGMENTS

The authors acknowledge the financial support for this work from the Key projects of the Joint Foundation of the National Natural Science Foundation of China (U1764254), and National Nature Science Foundation of China (51871166 and 51801137).

REFERENCES

Arrabal, R., Matykina, E., Skeldon, P., and Thompson, G. E. (2008). Incorporation of Zirconia Particles into Coatings Formed on Magnesium by Plasma Electrolytic Oxidation. *J. Mater. Sci.* 43, 1532–1538. doi:10.1007/s10853-007-2360-9

Baghdadabad, D. M., Baghdadabad, A. R. M., and Khoei, S. M. M. (2020). Characterization of Bioactive Ceramic Coatings Synthesized by Plasma Electrolyte Oxidation on AZ31 Magnesium alloy Having Different Na2SiO3 Center Dot 9H(2)O Concentrations. *Mater. Today Commun.* 25, 101642. doi:10.1016/j.mtcomm.2020.101642

Bordbar-Khiabani, A., Yarmand, B., and Mozafari, M. (2019). Enhanced Corrosion Resistance and *In-Vitro* Biodegradation of Plasma Electrolytic Oxidation Coatings Prepared on AZ91 Mg alloy Using ZnO Nanoparticles-Incorporated Electrolyte [J]. *Surf. Coat. Technol.* 360, 153–171. doi:10.1016/j.surfcoat.2019.01.002

Cao, Y., Ning, X., and Wang, Q. (2021). Compositional Control and High-Temperature Phase Stability of Plasma-Sprayed Ba(Mgu(1/3)Ta(2/3))O-3 Coatings. *Surf. Coat. Technol.* 425, 127714. doi:10.1016/j.surfcoat.2021.127714

Es-saddik, M., Laasri, S., Taha, M., Laghzizil, A., Guidara, A., Chaari, K., et al. (2021). Effect of the Surface Chemistry on the Stability and Mechanical Properties of the Zirconia-Hydroxyapatite Bioceramic. *Surf. Inter.* 23, 100980. doi:10.1016/j.surfin.2021.100980

Fattah-alhosseini, A., Chaharmahali, R., and Babaei, K. (2020). Effect of Particles Addition to Solution of Plasma Electrolytic Oxidation (PEO) on the Properties of PEO Coatings Formed on Magnesium and its Alloys: A Review. *J. Magnesium Alloys* 8, 799–818. doi:10.1016/j.jma.2020.05.001

Gao, G., Li, Y., Hu, D., and Xi, Z. (2018). Structure and Infrared Emissivity Properties of the MAO Coatings Formed on TC4 Alloys in K2ZrF6-Based Solution. *Materials* 11, 254. doi:10.3390/ma11020254

Kirkland, N. T., Schiller, T., and Medhekar, N. (2012). Exploring Graphene as a Corrosion protection Barrier. *Corrosion Sci.* 56, 1–4. doi:10.1016/j.corsci.2011.12.003

Kovaleva, E., Kusiak, M. A., Kenny, G. G., Whitehouse, M. J., Habler, G., Schreiber, A., et al. (2021). Nano-Scale Investigation of Granular Neoblastic Zircon, Vredefort Impact Structure, South Africa: Evidence for Complete Shock Melting. *Earth Planet. Sci. Lett.* 565, 116948. doi:10.1016/j.epsl.2021.116948

Li, C.-Y., Fan, X.-L., Cui, L.-Y., and Zeng, R.-C. (2020). Corrosion Resistance and Electrical Conductivity of a Nano ATO-Doped MAO/Methyltrimethoxysilane Composite Coating on Magnesium alloy AZ31. *Corrosion Sci.* 168, 108570. doi:10.1016/j.corsci.2020.108570

Li, C.-Y., Yu, C., Zeng, R.-C., Zhang, B.-C., Cui, L.-Y., Wan, J., et al. (2020). *In Vitro* corrosion Resistance of a Ta2O5 Nanofilm on MAO Coated Magnesium alloy AZ31 by Atomic Layer Deposition. *Bioactive Mater.* 5, 34–43. doi:10.1016/j.bioactmat.2019.12.001

Li, H., Sun, Y., and Zhang, J. (2015). Effect of ZrO2 Particle on the Performance of Micro-arc Oxidation Coatings on Ti6Al4V. *Appl. Surf. Sci.* 342, 183–190. doi:10.1016/j.apsusc.2015.03.051

Li, T., Li, L., Qi, J., and Chen, F. (2020). Corrosion protection of Ti6Al4V by a Composite Coating with a Plasma Electrolytic Oxidation Layer and Sol-Gel Layer Filled with Graphene Oxide. *Prog. Org. Coat.* 144, 105632. doi:10.1016/j.porgcoat.2020.105632

Li, Z., He, Z., Lai, H., He, Y., Zhu, Z., Chen, Y., et al. (2021). One-Step Synthesis of Oxygen-Defects Modified Ta2O5 Nanosheets with High Photocatalytic Performance by Chemical Vapor Deposition Method. *Appl. Surf. Sci.* 567, 150776. doi:10.1016/j.apsusc.2021.150776

Lim, T. S., Ryu, H. S., and Hong, S.-H. (2012). Electrochemical Corrosion Properties of CeO2-Containing Coatings on AZ31 Magnesium Alloys Prepared by Plasma Electrolytic Oxidation. *Corrosion Sci.* 62, 104–111. doi:10.1016/j.corsci.2012.04.043

Lu, X., Mohedano, M., Blawert, C., Matykina, E., Arrabal, R., Kainer, K. U., et al. (2016). Plasma Electrolytic Oxidation Coatings with Particle Additions - A Review. *Surf. Coat. Technol.* 307, 1165–1182. doi:10.1016/j.surfcoat.2016.08.055

Rahman, M., Li, Y., and Wen, C. (2020). Realization and Characterization of Double-Layer Ca-P Coating on WE43 Mg alloy for Biomedical Applications. *Surf. Coat. Technol.* 398, 126091. doi:10.1016/j.surfcoat.2020.126091

Rakoch, A. G., Monakhova, E. P., Khabibullina, Z. V., Serdechnova, M., Blawert, C., Zheludkevich, M. L., et al. (2020). Plasma Electrolytic Oxidation of AZ31 and AZ91 Magnesium Alloys: Comparison of Coatings Formation Mechanism. *J. Magnesium Alloys* 8, 587–600. doi:10.1016/j.jma.2020.06.002

Rehman, Z. U., Shin, S. H., Hussain, I., and Koo, B. H. (2017). Investigation of Hybrid PEO Coatings on AZ31B Magnesium alloy in Alkaline K2ZrF6-Na2SiO3 Electrolyte Solution. *Prot. Met. Phys. Chem. Surf.* 53, 495–502. doi:10.1134/s2070205117030194

Ur Rehman, Z., and Choi, D. (2019). Investigation of ZrO2 Nanoparticles Concentration and Processing Time Effect on the Localized PEO Coatings Formed on AZ91 alloy. *J. Magnesium Alloys* 7, 555–565. doi:10.1016/j.jma.2019.10.001

Wang, S.-Y., Si, N.-C., Xia, Y.-P., and Liu, L. (2015). Influence of Nano-SiC on Microstructure and Property of MAO Coating Formed on AZ91D Magnesium alloy. *Trans. Nonferrous Met. Soc. China* 25, 1926–1934. doi:10.1016/s1003-6326(15)63800-6

Wang, Y., Zhang, S., Lu, Z., Wang, L., and Li, W. (2018). Preparation and Performances of Electrically Conductive Nb-Doped TiO2 Coatings for 316 Stainless Steel Bipolar Plates of Proton-Exchange Membrane Fuel Cells. *Corrosion Sci.* 142, 249–257. doi:10.1016/j.corsci.2018.07.034

Xia, Y. H., Zhang, B. P., Lu, C. X., and Geng, L. (2013). Improving the Corrosion Resistance of Mg-4.0Zn-0.2Ca alloy by Micro-arc Oxidation. *Mater. Sci. Eng. C* 33, 5044–5050. doi:10.1016/j.msec.2013.08.033

Xiong, C., Li, W., Jin, Z., Gao, X., Wang, W., Tian, H., et al. (2018). Preparation of Phytic Acid Conversion Coating and Corrosion protection Performances for Steel in Chlorinated Simulated concrete Pore Solution. *Corrosion Sci.* 139, 275–288. doi:10.1016/j.corsci.2018.05.018

Yang, Q., Li, P., and Zhang, S. (2021). Low Temperature Synthesis of green Submicro Cr-ZrSiO 4 Ceramic Pigments by Solid-State Method. *Int. J. Appl. Ceram. Technol.* 18, 345–352. doi:10.1111/ijac.13648

Yao, J., Wang, Y., Wu, G., Sun, M., Wang, M., and Zhang, Q. (2019). Growth Characteristics and Properties of Micro-arc Oxidation Coating on SLM-Produced TC4 alloy for Biomedical Applications. *Appl. Surf. Sci.* 479, 727–737. doi:10.1016/j.apsusc.2019.02.142

Zarei, M., Nourouzi, S., Jamaati, R., Cano, I. G., Dosta, S., and Sarret, M. (2021). Water-Assisted Crystallization of Nanoporous Tin Oxide Formed by Anodic Oxidation on Cold Sprayed Tin Coating. *J. Alloys. Compd.* 876, 160207. doi:10.1016/j.jallcom.2021.160207

Zhang, X.-M., Chen, D.-F., Gong, C.-Z., Yang, S.-Q., and Tian, X.-B. (2010). Modulation Effects of K2ZrF6 Additive on Microstructure and Heat Resistance of Micro-arc Oxide Coatings Fabricated on LY12 Alumi-Num Alloy. *J. Inorg. Mater.* 25, 865–870. doi:10.3724/sp.j.1077.2010.00865

Zhang, Y., Chen, F., Zhang, Y., and Du, C. (2020). Influence of Graphene Oxide Additive on the Tribological and Electrochemical Corrosion Properties of a PEO Coating Prepared on AZ31 Magnesium alloy. *Tribology Int.* 146, 106135. doi:10.1016/j.triboint.2019.106135

Zhang, Y., Chen, F., Zhang, Y., Liu, Z., Wang, X., and Du, C. (2019). Influence of Graphene Oxide on the Antiwear and Antifriction Performance of MAO Coating Fabricated on Mg Li alloy. *Surf. Coat. Technol.* 364, 144–156. doi:10.1016/j.surfcoat.2019.01.103

Zhang, Y., Sil, M. C., and Chen, C. (2021). Organosiloxane Nanolayer as Diffusion Barrier for Cu Metallization on Si. *Appl. Surf. Sci.* 567, 150800. doi:10.1016/j.apsusc.2021.150800

Zhang, Z.-Q., Wang, L., Zeng, M.-Q., Zeng, R.-C., Kannan, M. B., Lin, C.-G., et al. (2020). Biodegradation Behavior of Micro-arc Oxidation Coating on Magnesium alloy-from a Protein Perspective. *Bioactive Mater.* 5, 398–409. doi:10.1016/j.bioactmat.2020.03.005

Zhou, K., Xie, F., Wu, X., and Wang, S. (2021). Fretting Wear Behavior of Nano ZrO2 Doped Plasma Electrolytic Oxidation Composite Coatings on TC21 Titanium alloy. *Surf. Coat. Technol.* 421, 127429. doi:10.1016/j.surfcoat.2021.127429

Zuo, Y., Li, T., Yu, P., Zhao, Z., Chen, X., Zhang, Y., et al. (2019). Effect of Graphene Oxide Additive on Tribocorrosion Behavior of MAO Coatings Prepared on Ti6Al4V alloy. *Appl. Surf. Sci.* 480, 26–34. doi:10.1016/j.apsusc.2019.02.065

Conflict of Interest: The authors declare that the research was conducted in the absence of any commercial or financial relationships that could be construed as a potential conflict of interest.

Publisher's Note: All claims expressed in this article are solely those of the authors and do not necessarily represent those of their affiliated organizations, or those of the publisher, the editors, and the reviewers. Any product that may be evaluated in this article, or claim that may be made by its manufacturer, is not guaranteed or endorsed by the publisher.

frontiers in Materials

ORIGINAL RESEARCH
published: 08 March 2022
doi: 10.3389/fmats.2022.857671

Electrochemical Properties of Diluted Al-Mg Alloys With Columnar-To-Equiaxed Transition

*Alejandra Silvina Román[1†], Edgar Rolando Ibañez[1†], Claudia Marcela Méndez[1], Marianela Pedrozo[1], Gustavo Raúl Kramer[1], Natalia Silvina Zadorozne[1], Paula Regina Alonso[2] and Alicia Esther Ares[1]**

[1]Materials Institute of Misiones, Instituto de Materiales de Misiones, IMAM—CONICET-UNaM, Posadas, Argentina, [2]Comisión Nacional de Energía Atómica—Universidad Nacional de San Martín, Buenos Aires, Argentina

The objective of the present research is to study the corrosion susceptibility of two Al-Mg diluted alloys (Al-0.5wt.%Mg and Al-2wt.%Mg) with different grains structures obtained by directional solidification (columnar, equiaxed and columnar-to-equiaxed transition, CET) in 0.5% NaCl solution, at room temperature. The corrosion resistance is analyzed by potentiodynamic polarization and electrochemical impedance spectroscopy (EIS) techniques in both longitudinal and transversal sections of the samples. The columnar grain zone presents higher corrosion resistance than the equiaxed grain zone. In addition, the transversal section shows higher corrosion resistance than the longitudinal section of the samples. Then, the Al-0.5wt.% Mg alloy displays higher corrosion resistance than the Al-2wt.% Mg alloy. The values of the polarization resistance are used as a basic criterion for the evaluation of the corrosion resistance of both alloys. In this way, when the polarization resistance decreases with the increasing in the distance from the base, the grain size, secondary dendritic arm spacings and hardness increases. In addition, when the polarization resistance increases, the critical temperature gradient decreases.

Keywords: Al-Mg diluted alloys, corrosion resistance, directional solidification, thermal parameters, structures, microhardness

OPEN ACCESS

Edited by:
Liang Wu,
Chongqing University, China

Reviewed by:
Sheng Lu,
Jiangsu University of Science and Technology, China
Pavlo Maruschak,
Ternopil Ivan Pului National Technical University, Ukraine

****Correspondence:***
Alicia Esther Ares
aares@fceqyn.unam.edu.ar

†These authors have contributed equally to this work and share first authorship

Specialty section:
This article was submitted to Environmental Degradation of Materials, a section of the journal Frontiers in Materials

Received: *18 January 2022*
Accepted: *17 February 2022*
Published: *08 March 2022*

Citation:
Román AS, Ibañez ER, Méndez CM, Pedrozo M, Kramer GR, Zadorozne NS, Alonso PR and Ares AE (2022) Electrochemical Properties of Diluted Al-Mg Alloys With Columnar-To-Equiaxed Transition. Front. Mater. 9:857671. doi: 10.3389/fmats.2022.857671

1 INTRODUCTION

Aluminum and its alloys stand out for two main properties: low density and excellent mechanical strength. These characteristics have led to its use in applications where weight is a determining factor, as it is the case in the transportation, automotive and naval industries (Davis, 1993; Canales et al., 2012; Jayalakshmi et al., 2013). The use of aluminum in these industries dates back to 1899, when Karl Benz presented the first sports car with an aluminum chassis. At the same time, Zeppelin was working on the construction of the first rigid airship using the same material in the frame of the structure. However, the mechanical properties of pure aluminum did not meet the demands required in structural applications, and for that reason, its industrialization did not take place until 1930 with the design of aluminum-based alloys. The incorporation of alloying elements enables a considerable increase in mechanical properties, which in turn, widens its range of applicability (Shu-qing and Xing-fu, 2014; Kaygisiz and Marasli, 2015).

Magnesium is the lightest structural metal. In the automotive industry, it reduces the total weight of the car by 10 percent and saves between 20 and 30 percent on fuel. Other advantages include not

only excellent stiffness, specific strength, high electrical and thermal conductivity, but also great protection against electromagnetic interference. It is characterized by an excellent tolerance in the final dimensions of the parts as well as good endings; it also allows parts of small thickness (up to Ø wall = 2 mm), is fully recyclable and is easy to machine; besides, its costs are lower in relation to polymers (Jayalakshmi et al., 2013; Shu-qing and Xing-fu, 2014).

However, application of aluminum casting alloys for structural components requires high strength and suitable high elongations (Totten et al., 2004). In addition, the use of indentation at several scale levels was proposed in order to estimate strengthening kinetics of heat-resistant steel 15Kh2MFA (II) after high-temperature deformation (Maruschak et al., 2012). Recently, the effect of electron beam energy densities on the surface morphology and tensile property of additively manufactured Al-Mg alloy was analyze and it was determined that the crystallization and tensile strength of Al-Mg alloy are optimum at the condition EBED = 10 J/cm^2 (Geng et al., 2021a). In another research, the authors demonstrate the tensile properties and fracture mechanism with the analysis of microstructure and phase composition of Al-5.0 Mg alloys. The results achieved from experiments can enrich the information of studies about Al-5.0 Mg alloys produced by WAAM-CMT (Geng et al., 2021b).

Grain size, their morphology, interdendritic distance and distribution of secondary phases are crucial factors affecting mechanical properties of cast parts (Canales et al., 2012; Luna et al., 2013; Shokuhfar and Nejadseyfi, 2014; Krupin´ski et al., 2016). The quality of the microstructure of aluminum alloys mainly depends on the chemical composition, melting process, cooling rates and temperature gradients (Xia et al., 2014; Kro´l et al., 2015; Krupin´ski et al., 2016). Due to those facts, it is important to understand how to control structure forming of aluminum alloys through casting.

Generally, a columnar structure has large grain boundaries, which are sensitive locations for crack initiation. However, it can be used to produce the strong texture and the anisotropic properties for special applications (Liu and To, 2017). In contrast, homogeneous equiaxed grains are commonly desirable for the sake of enhancing resistance to crack propagation (Liu et al., 2018; Zhang et al., 2019; Liu et al., 2020). In addition, columnar-to-equiaxed transition (CET) behavior is determined by the temperature gradient and the solidification rate during the directional solidification process (Ares and Schvezov, 2000; Spittle, 2006; Ares and Schvezov, 2007; Ares et al., 2010; Gueijman et al., 2010; Ares and Schvezov, 2011; Song et al., 2018; Xiang et al., 2019; Zhang et al., 2019; Oliveira et al., 2020). Either an equiaxed or a columnar microstructure can be achieved by selecting appropriate processing parameters, which further determine the mechanical properties of the alloy.

Several researches about the corrosion behavior and the characteristics of films formed (Song et al., 2019; Xu et al., 2021; Chen et al., 2021). Other previous studies evaluated corrosion susceptibility of Al alloys (Smialowska, 1999; Amin et al., 2008; Boag et al., 2010; Osório et al., 2013; Zhou et al., 2015; Yasakau et al., 2018). The influence of the concentration of aggressive ions in the electrolyte on the pitting potential of Al alloys has always been a matter of great interest; therefore, it was extensively studied (Smialowska, 1999; Hui Zhao et al., 2006; Amin et al., 2008; Arrabal et al., 2013; Wang et al., 2014; Yasakau et al., 2018). However, there are previous investigations evaluating the susceptibility to corrosion of directionally solidified aluminum alloys (Ares et al., 2008; Ares and Gassa, 2012; Osório et al., 2013; Ares et al., 2018; Satizabal et al., 2019). It is evident that the results are governed by a complex set of interacting phenomena, and even more when we consider the thermal parameters for obtaining the alloys with the mechanical and electrochemical parameters.

Electrochemical techniques are fast and can be used to obtain instantaneous information on a corrosion process, which cannot be provided by weight loss measurements. Also, impedance techniques, along with the linear polarization technique, are the most commonly used methods for determining corrosion rates. The electrochemical impedance spectroscopy (EIS) technique is a particularly useful method to study electrode kinetics at the corrosion potential. The nature of the corrosion process can be often revealed by an impedance spectrum (Barsoukov and Ross McDonald, 2005).

In previous works, we correlated the effect of several parameters, like thermal, mechanical and electrochemical ones, on the CET macrostructure of different alloys systems (Ares et al., 2008; Ares et al., 2011; Román et al., 2014; Román et al., 2015; Kociubczyk et al., 2015; Ares and Schvezov, 2015; Ares et al., 2016; Rozicki et al., 2018; Kociubzyk et al., 2018; Ares et al., 2018; Ares et al., 2018; Kramer et al., 2016; Méndez et al., 2018; Román et al., 2021). Earlier, we had analyzed the thermal and structural parameters of Al-Mg alloys during the columnar-to equiaxed transition (Al-2wt.%Mg and Al-4wt.% Mg) (Ares et al., 2003a; Ares et al., 2003b; Ares et al., 2004) and the corrosion of Al-Mg alloys exposed to ethanol solutions and bioethanol fuel (Kramer et al., 2017; Gauto et al., 2018; Kramer et al., 2018).

In this investigation, we examined the susceptibility to corrosion of directionally solidified aluminum-magnesium diluted alloys (Al-0.5wt.%Mg and Al-2wt.%Mg) with different grain structures (columnar (C), equiaxed (E) and columnar-to-equiaxed transition, CET), obtained by a directional solidification process, in 0.5 M NaCl solution, at room temperature, using potentiodynamic polarization and electrochemical impedance spectroscopy (EIS) as principal electrochemical techniques.

2 EXPERIMENTAL SECTION

2.1 Directional Solidification

The Al-0.5wt.%Mg and Al-2wt.%Mg alloys were prepared by using commercially pure metals (Chemical composition of Al: 99.93 Al, 0.038 Fe, < 0.001 Pb, 0.033 Si and <0.001 others. Chemical composition of Mg: 99.97 Mg, 0.015 Fe, 0.012 Pb, 0.003 Si and <0.001 others). Then, they were solidified by

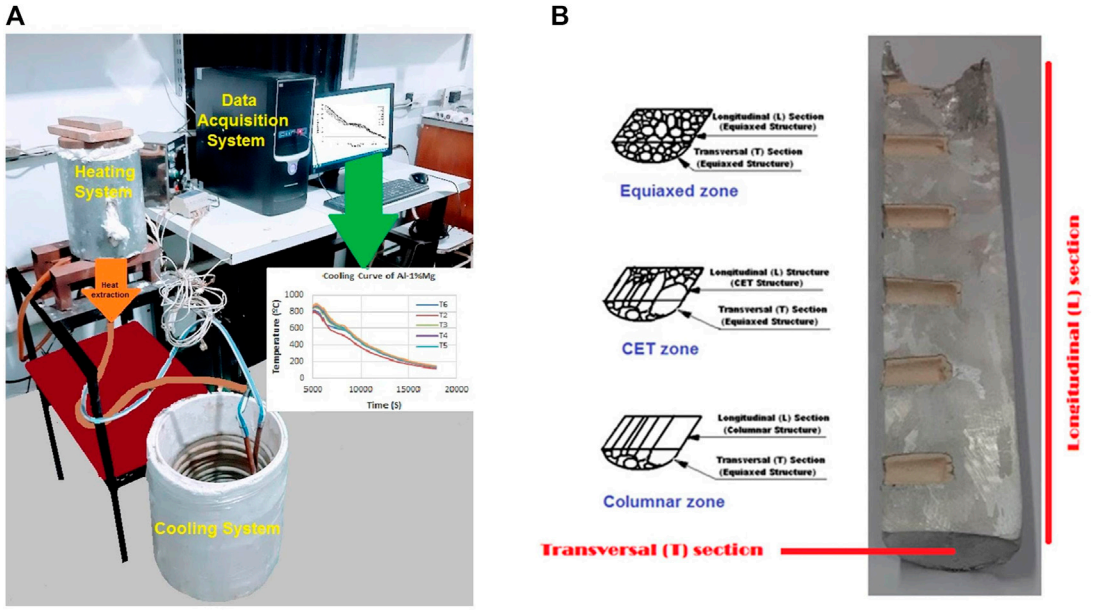

FIGURE 1 | (A) Experimental setup used in directional solidification experiments. **(B)** The longitudinal (L) and transversal (T) sections of the cylindrical sample.

TABLE 1 | Cooling velocity in the liquid ($V.E._{LIQ.}$) and cooling velocity in the solid ($V.E._{SOL.}$), minimum CET position ($CET_{MIN.}$) and maximum CET position ($CET_{MAX.}$), critical gradients (G_C) and recalescence values (REC.) obtained from the temperature versus time curves.

#	Alloy	$V.E._{LIQ.}$ (°C/s)	$V.E._{SOL.}$ (°C/s)	$CET_{MIN.}$ (cm)	$CET_{MAX.}$ (cm)	G_C (°C/cm)	REC. (°C)
1	Al-0.5wt.%Mg	2.4	1.3	3.7	5.4	−1.52	1.98
2	Al-0.5wt.%Mg	2.2	1.2	3.3	4.9	0.01	0.99
3	Al-0.5wt.%Mg	1.9	1.1	2.6	3.8	−0.95	0.96
4	Al-0.5wt.%Mg	1.8	1.05	2.1	3.2	−0.62	1.71
5	Al-0.5wt.%Mg	1.7	1.0	1.7	2.9	0.48	1.63
6	Al-2wt.%Mg	2.4	1.3	3.9	5.4	−0.86	1.15
7	Al-2wt.%Mg	2.2	1.2	3.6	5.1	−1.33	1.35
8	Al-2wt.%Mg	1.9	1.1	3.1	4.7	0.09	1.42
9	Al-2wt.%Mg	1.8	1.05	2.8	5.6	−0.23	0.96
10	Al-2wt.%Mg	1.7	1.0	0.6	6.2	−0.72	1.23

using a directional solidification device, which consists of a heating unit, and a control system with data acquisition. Data acquisition was carried out by means of six thermocouples connected to a data acquirer, which were placed in the holes of the molds of the specimens with a depth of 0.7 cm and a distance between each one of 2 cm, coinciding with the center of the diameter of the specimen. Thus, allowing the determination of the time-dependent temperature profiles (Ares and Schvezov, 2000; Spittle, 2006; Ares and Schvezov, 2007; Ares et al., 2010; Gueijman et al., 2010; Ares and Schvezov, 2011). **Figure 1A** shows the experimental setup with a vertical heat extraction system at the bottom of the furnace.

Prior to solidification, the crucibles and cylindrical molds were prepared with commercial clay. An adapted manual extruder was used to obtain the molds, with an approximate length of 13 cm and an internal diameter of 2.5 cm. Its firings were carried out in a muffle at 300°C for 1 h, then at 600°C for another 1 h and finally at 900°C for 1 h again.

The pure elements were also melted in the muffle, in the crucibles, each one at its respective melting temperature, using 159.44 g of aluminum and 1.61 g of magnesium for the first Al-2wt.%Mg cylindrical sample, and 160.66 g of aluminum and 0.85 g of magnesium for the second Al-0.5wt.%Mg sample, occupying a volume of 40 cm^3, respectively. Once melted, they were mixed using a graphite rod, and then, placed in the solidification furnace to obtain the alloy samples. Five alloy samples of each concentration were tested, as it can be seen in **Table 1**.

When the specimens were cooled, they were cut in longitudinal direction, devastated with SiC paper up to granulometry #1500, and chemically attacked with Keller reagent (distilled water, 32% hydrochloric acid, 65% nitric

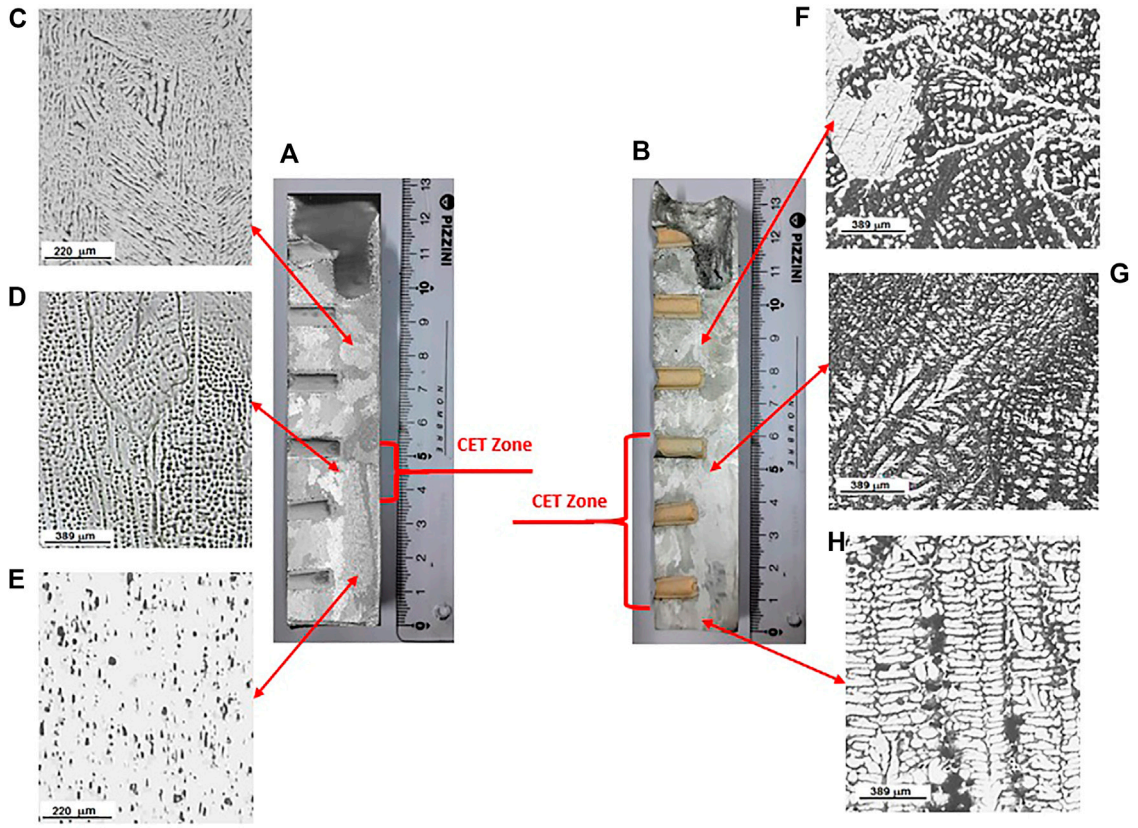

FIGURE 2 | Macrostructures: **(A)** Al-0.5wt.%Mg. **(B)** Al-2wt.%Mg. Microstructures: **(C–E)** Al 0.5wt.%Mg. **(F–H)** to (h) Al-2wt.%Mg.

acid, 40% hydrofluoric acid) for approximately 3 min at room temperature to reveal the macro and microstructures (Vander Voort, 2004). This made it possible to locate the three defined zones of grain structures by visual observation and optical microscopy, as it can be seen in **Figure 2**.

The position of the CET was located by visual observation and an optical microscopy, and the distance from the chill zone of the sample was measured with a ruler. Also, the grain structure was inspected by visual observation with an Arcano® optical microscopy. The dimensions of the grain sizes obtained from the macrostructures were determined on the basis of ASTM E-112 (Boyer and Gall, 1990) standards with the help of TSView® free image processing software. The equiaxed grain size was measured at equally spaced intervals. The columnar region was divided in a similar way and the width and length of the grains were directly measured.

2.2 Electrochemical Tests

Electrochemical tests were performed on Al-Mg alloys with two compositions: Al-0.5wt.% Mg and Al-2wt.% Mg. Working electrodes were obtained from the longitudinal (L) and transversal (T) sections of the three grain structures zones of the specimens tested: columnar, CET and equiaxed, as can be seen in **Figure 1B**.

The electrochemical tests were carried out in a three-electrode Pyrex glass cell, using a saturated calomel reference electrode and a platinum wire as a counter electrode. A 0.5 M NaCl solution at room temperature was used as electrolyte. Prior to the tests, nitrogen was bubbled into the solution for at least 10 min to remove dissolved oxygen.

Potentiodynamic polarization curves were performed at a rate of 0.16 mV/s. They started at 300 mV below the corrosion potential. The curves ended when a current value of 1 mA/cm^2 was reached. Electrochemical Impedance Spectroscopy tests were performed after a 10 min stabilization period, with a potential amplitude of 10 mVrms, around the open circuit potential. The frequency range of the test was from 105 Hz to 5.10^{-2} Hz. The linear least squares method was used to analyze the results.

2.3 Microstructures

Before and after the corrosion tests, the samples were analyzed with a FEI Quanta200 SEM together with an EDS detector of the Electron Microscopy and Microanalysis Service (SeMFi-LIMF) (Microscopía Electrónica y Microanálisis (SeMFi-LIMF)—Facultad de Ingeniería, UNLP, Argentina). Secondary dendritic spacings were determined by using an Arcano® metallurgical microscope, employing the linear intercept method with a TSView® free image processing software.

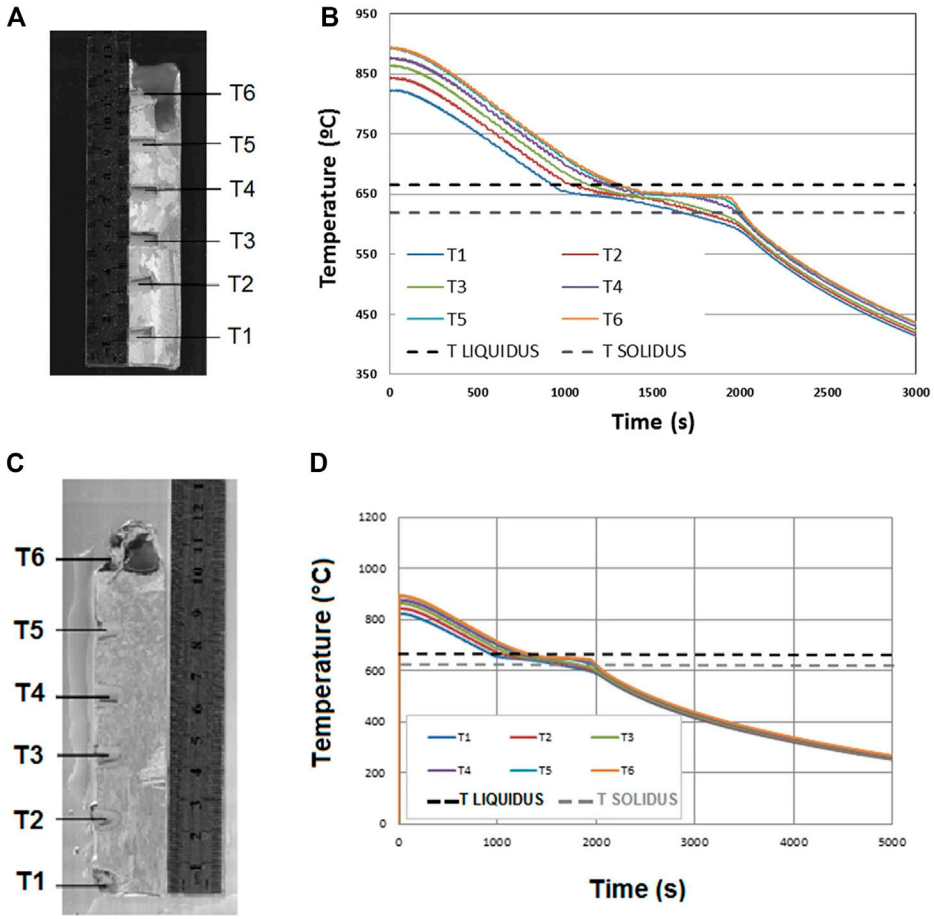

FIGURE 3 | (A) Macrostructure of Al-0.5wt.%Mg alloy indicating the position of the thermocouples during the experiment. **(B)** Cooling curves of Al-0.5wt.%Mg alloy in each position of the thermocouples. **(C)** Macrostructure of Al-2wt.%Mg alloy indicating the position of the thermocouples during the experiment. **(D)** Cooling curves of Al-2. wt.%Mg alloy in each position of the thermocouples.

2.4 Microhardness and Hardness Tests

The microhardness measurements of these alloys were done at room temperature, using a Future Tech® microhardness tester (Instituto de Materiales de Misiones (IMAM), Posadas, Misiones, Argentina). The measurements were performed under ASTM E 384-89 standard, using a pressing time of 10 s with a load of 50 g_f.

The harness measurements of the same alloys were carried out using a BRIN200C Brinell calibration hardness machine (Comisión Nacional de Energía Atómica (CNEA), Buenos Aires, Argentina) to ISO 6506-3:1999 using a load rating (P/D^2) = 5, an application time of 60 s and a sphere diameter of 2.5 mm.

3 RESULTS

3.1 Macrostructures and Microstructures

A number of 10 successful experiments were performed where the transition from columnar-to-equiaxed grain structure was produced. It is noted in **Figure 2** that the CET is not sharp, showing a zone where some equiaxed grains co-exist with columnar grains. The size of the transition zone is in the order of up to 1 cm. The CET occurred between 0.6 and 6.2 cm from the bottom of the sample. Typical columnar—to—equiaxed transitions can be observed in **Figure 2** for the two alloys tested, Al-0.5wt.%Mg and Al-2wt.%Mg.

Also, **Figure 2** shows the microstructure for hypoeutectic composition, in which the presence of two phases is observed: α-Al phase in the case of Al-0.5wt.%Mg (**Figures 2C–E**) and α-Al plus eutectic phase (α-Al + Mg) for Al-2wt.%Mg (**Figures 2F–H**). Both phases are well distributed throughout the system. The α-Al, is the light gray (free Mg) zone phase while the eutectic phase is observed as fine needles of Mg (black color) dispersed in a matrix of α-Al.

3.2 Thermal Parameters

3.2.1 Liquidus and Solidus Temperatures

Figures 3A,C indicate the position of each thermocouple in the sample during the experiment. The liquidus, T_L, and solidus,

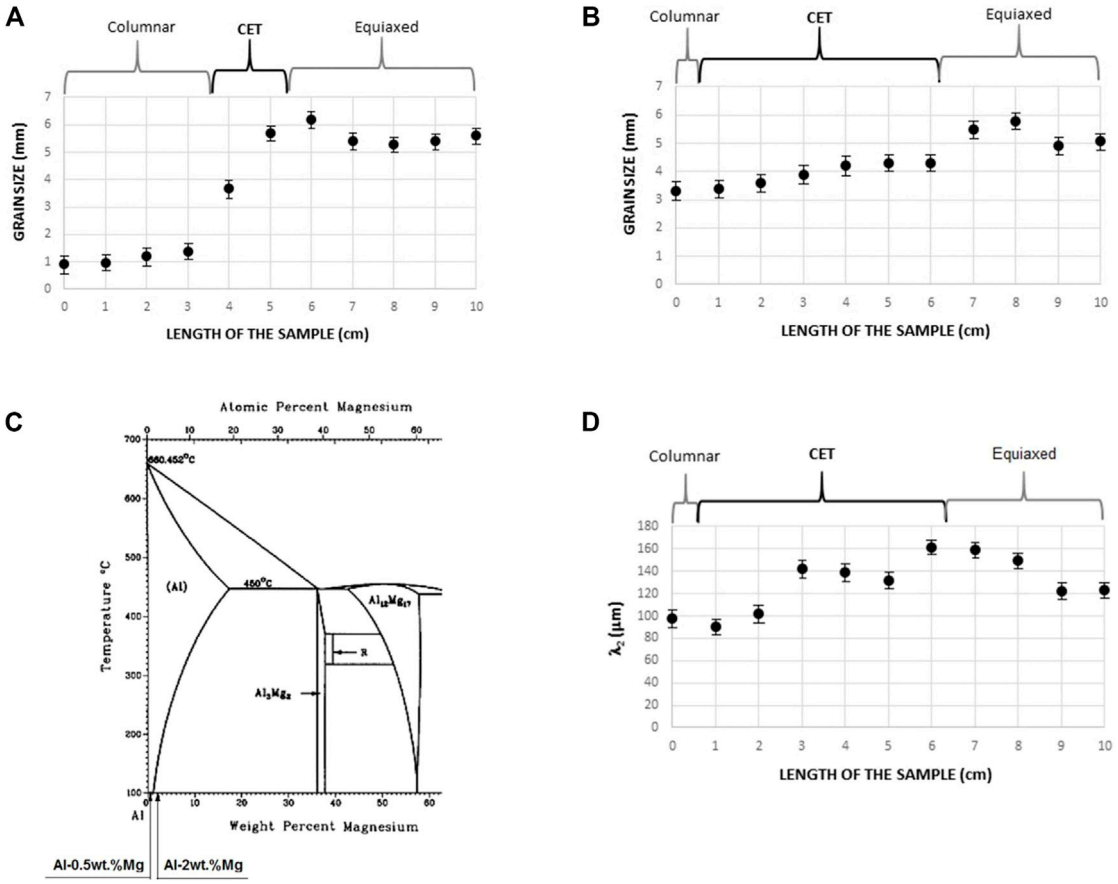

FIGURE 4 | Grain size as a function of the length of the sample. **(A)** Al-0.5wt.%Mg. **(B)** Al-2wt.%Mg. **(C)** Al-Mg phase diagram (on the Al side) showing the positions of the Al-0.5wt.%Mg and Al-2wt.%Mg alloys (adapted from Boyer and Gall, 1990). **(D)** Secondary dendritic arm spacing, λ_2, as a function of the length of the sample for Al-2wt.%Mg alloy.

T_S, temperatures were taken from the heating and cooling curves as usual (Ares and Schvezov, 2000; Ares and Schvezov, 2011; Ares and Schvezov, 2007; Ares et al., 2010; Gueijman et al., 2010). The results, which are shown in **Figures 3B,D**, are within the predicted values given by the phase diagram for the two alloys tested [52]: $T_{Liquidus\ (Al\text{-}0.5wt.\%Mg)} = 658^{\circ}C$, $T_{Solidus\ (Al\text{-}0.5wt.\%Mg)} = 645^{\circ}C$, $T_{Liquidus\ (Al\text{-}2wt.\%Mg)} = 655^{\circ}C$, $T_{Solidus\ (Al\text{-}2wt.\%Mg)} = 623^{\circ}C$.

3.2.2 Cooling Curves

The cooling velocity of the liquid alloy was determined from the temperature versus the time curves at each thermocouple position and by taking the average slope. The temperature versus the time curves for Al-0.5wt%Mg and Al-2wt.%Mg alloys are presented in **Figures 3B,D**. The cooling velocity in the liquid was calculated from these types of curves and are listed in **Table 1** for all the experiments as $V.E._{LIQ.}$; velocities of 1.7–2.4°C/s were obtained. The values of cooling velocity in the solid, $V.E._{SOL.}$, were ranging between 1 and 1.3°C/s. **Table 1** also lists the location of the CET zone from the bottom of the sample, which is in the range of $CET_{MIN.}$ to CET_{MAX}. The values of the $CET_{MIN(Al\text{-}0.5wt.\%Mg)}$ were between 1.7 and 3.7 cm. The values of the $CET_{MAX(Al\text{-}0.5wt.\%Mg)}$ were between 2.9 and 5.4 cm. Likewise, the values for the $CET_{MIN(Al\text{-}2wt.\%Mg)}$ were between 0.6 and 3.9 cm and the $CET_{MAX(Al\text{-}0.5wt.\%Mg)}$ were between 4.7 and 6.2 cm. Comparing the cooling velocities with the distances, which correspond to the length of the columnar zone for all alloys, it is observed that increasing the velocity, increases the length of the columnar grains.

The temperature versus time curves also show that the temperature evolution depends on the structure being formed. During columnar solidification, the temperature decreases steadily and monotonically; on the contrary, in the equiaxed region, and during the transition, there is a recalescence which increases the temperature from a minimum.; the level of recalescence for each experiment is listed in **Table 1** as REC (°C).

3.2.3 Temperature Gradients

The temperature gradients, G, were calculated for each pair of neighbour thermocouples as the temperature difference between the thermocouple readings divided by the separation distance between thermocouples. As it is shown in **Table 1**, the gradients

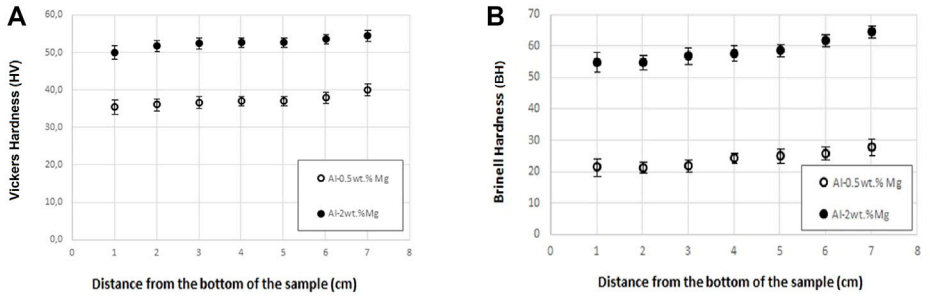

FIGURE 5 | (A) Vickers microhardness (HV) and **(B)** Brinell hardness values versus length of the samples. Al-0.5wt%Mg and Al-2wt.%Mg alloys.

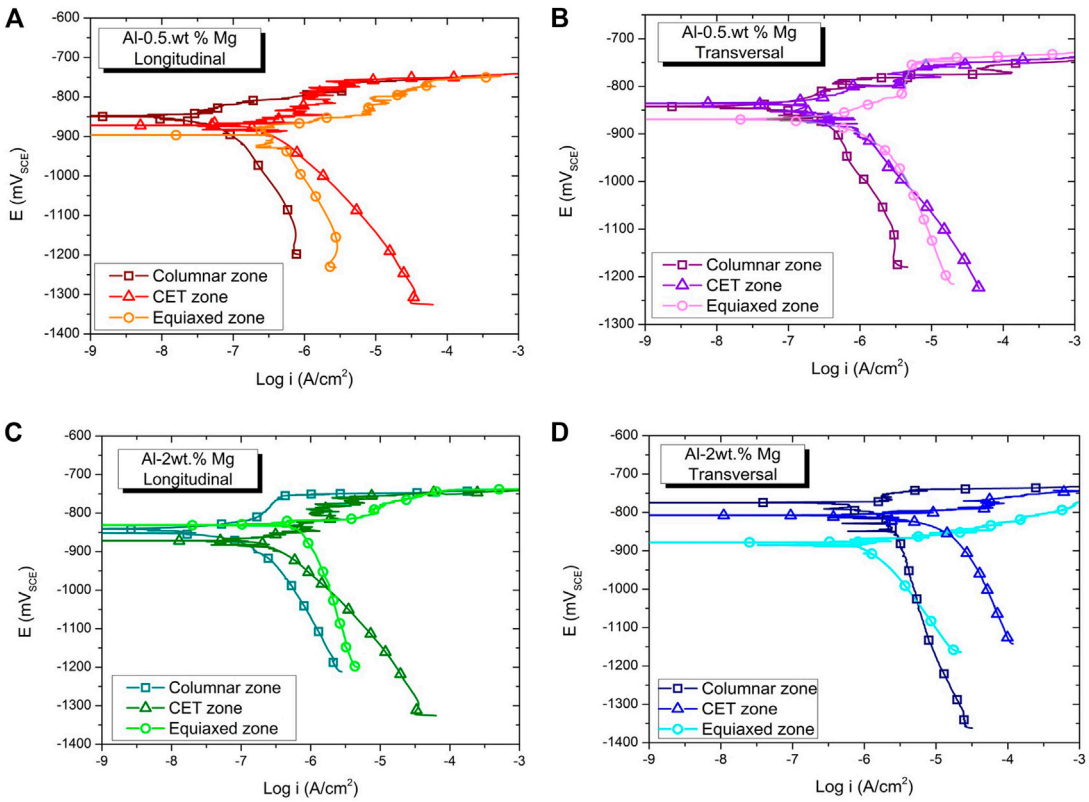

FIGURE 6 | Potentiodynamic curves of Al-Mg alloys. **(A)** Al-0.5wt.% Mg (Longitudinal section). **(B)** Al-0.5wt.% Mg (Transversal section). **(C)** Al-2wt.% Mg (Longitudinal section). **(D)** Al-2wt.% Mg (Transversal section).

determined at the moment of the CET (which is called the critical temperature gradient, G_c) are negative in most experiments. This negative value is an indication of a reversal in the temperature profiles ahead of the interface, which could be associated to the recalescence due to massive nucleation of equiaxed grains, and previously reported and discussed by the authors for others alloy systems (Ares and Schvezov, 2000; Ares and Schvezov, 2007; Ares et al., 2010; Gueijman et al., 2010; Ares and Schvezov, 2011; Kociubczyk et al., 2015; Ares and Schvezov, 2015; Ares et al., 2016; Kociubzyk et al., 2018; Rozicki et al., 2018). The fact that in some cases the position of the thermocouples is not located at the precise position where the transition occurs, it may prevent the detection of the negative gradients which is believed to occur in all the cases.

3.3 Grain Size and Secondary Dendritic Arm Spacings

The grain size along the samples is affected by the degree of heat extraction, which is higher at the base than at the

TABLE 2 | Fitting corrosion potentials, E_{corr}, and corrosion current density, I_{corr}, of Al-Mg alloys in 0.5 M NaCl.

	Al-0.5wt.% Mg				Al-2wt.% Mg			
	Longitudinal section		Transversal section		Longitudinal section		Transversal section	
	E_{corr} (mV)	I_{corr} (μA/cm^2)	E_{corr} (mV)	I_{corr} (μA/cm^2)	E_{corr} (mV)	I_{corr} (μA/cm^2)	E_{corr} (mV)	I_{corr} (μA/cm^2)
Columnar zone	−845	1.09	−841	1.18	−840	3.96	−774	6.21
CET zone	−871	1.27	−835	2.63	−871	4.14	−806	8.65
Equiaxed zone	−896	1.33	−869	4.52	−835	5.43	−877	6.04

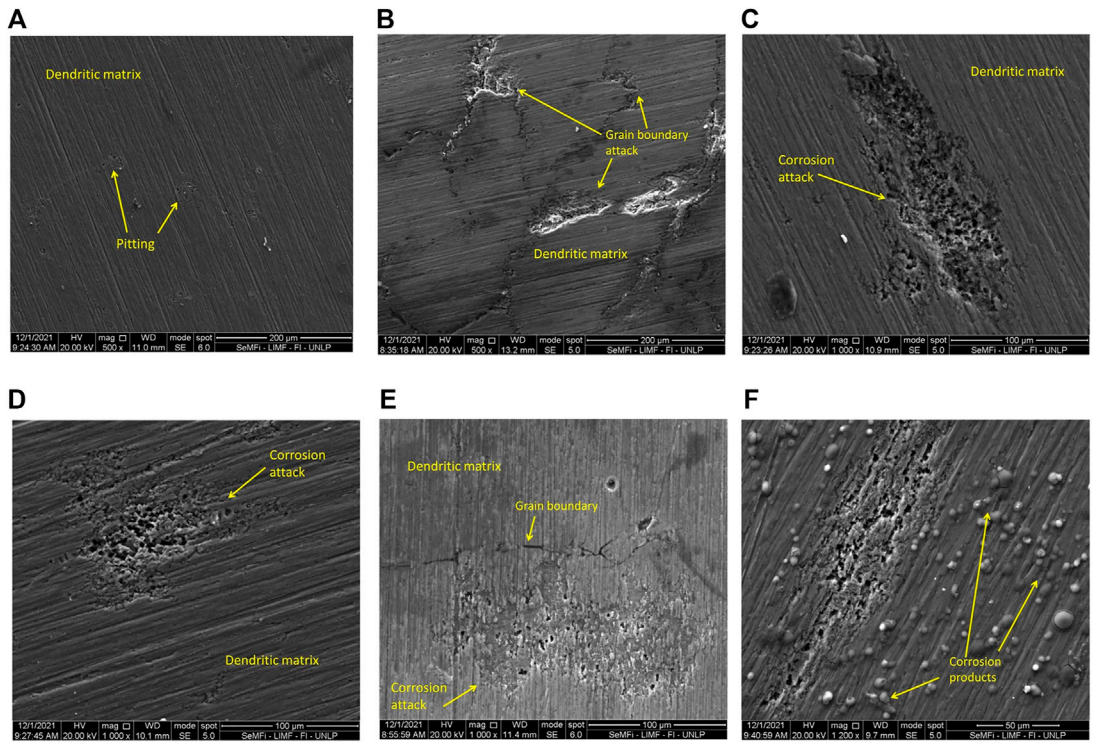

FIGURE 7 | SEM micrographs of Al-Mg alloys after corrosion tests: **(A)** Al-0.5wt.%Mg columnar zone (longitudinal). **(B)** Al-0.5wt.%Mg equiaxed zone (longitudinal section). **(C)** Al-0.5wt.%Mg columnar zone (transversal section). **(D)** Al-0.5wt.%Mg equiaxed zone (transversal section). **(E)** Al-2wt.%Mg columnar zone (longitudinal section). **(F)** Al-2wt.%Mg equiaxed zone (longitudinal section).

top of the samples, as it can be seen in **Figures 4A,B** for both alloys.

The secondary dendritic arm spacing, λ_2, was only possible to measure in Al-2wt.%Mg alloy (**Figure 4C** adapted from Boyer and Gall, 1990) due to the Al-0.5wt.%Mg, is a solid solution of α-Al.

The behavior of the secondary dendritic arm spacing, λ_2, in Al-2wt.%Mg alloys, is also linked to the degree of heat extraction. The values of λ_2 are smaller at the base of the samples, as it can be seen in **Figure 4D**. Otherwise, the dendritic structure is finer at the base of the samples (columnar zone).

3.4 Microhardness and Hardness Tests

First, we analyze microhardness (HV) variations as a function of sample length for both alloys, using load of 50 g_f. **Figure 5A** show the experimental results. It can be seen that Vickers microhardness have greater values in the equiaxed zone than in the columnar and the columnar to equiaxed transition (CET) zones.

The same behavior is observed with the variation of Brinell hardness (HB) versus sample length (**Figure 5B**).

Comparing the Vickers microhardness and Brinell hardness values with the literature, we observe that the measured values are within the established for Al-Mg alloys (Totten et al., 2004).

3.5 Electrochemical Tests

3.5.1 Potentiodynamic Polarization Curves

Figures 6A,B shows the curves obtained for the Al-0.5wt.%Mg alloy. **Figure 6A** corresponds to the longitudinal section and **Figure 6B** to the transversal section of the samples. For both

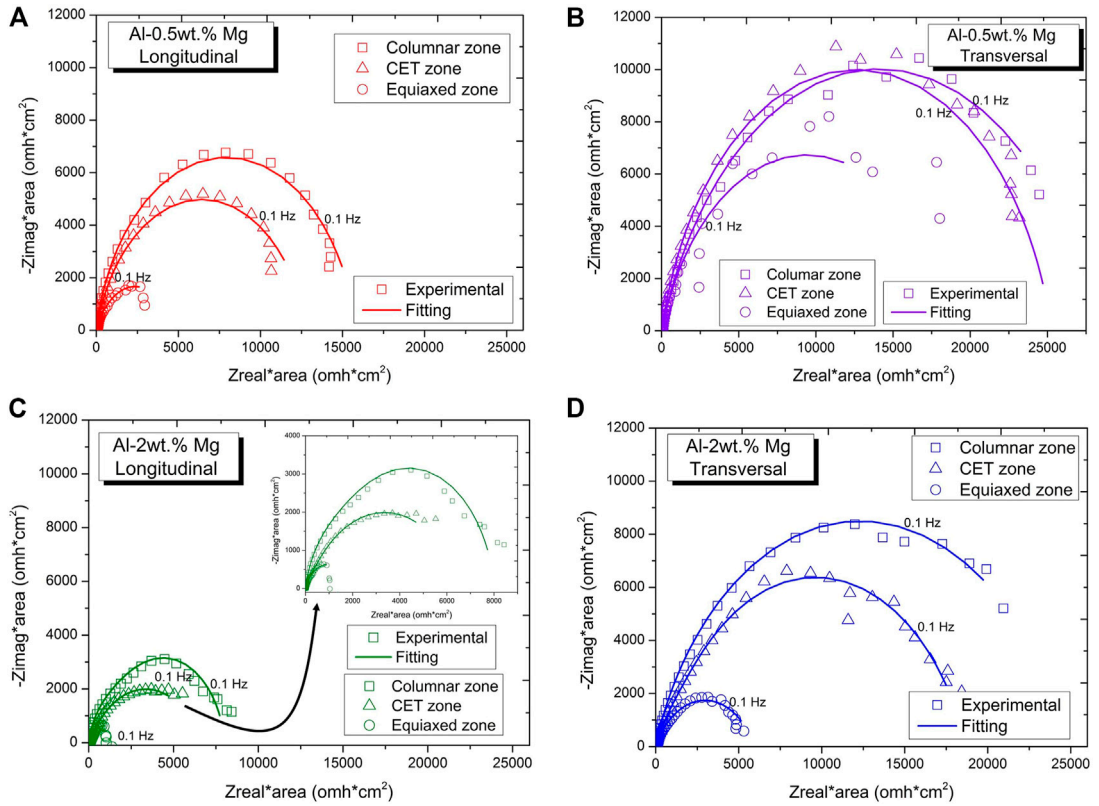

FIGURE 8 | Nyquist diagrams of Al-Mg alloys. **(A)** Al-0.5wt.% Mg alloy (longitudinal). **(B)** Al-0.5wt.% Mg alloy (transversal). **(C)** Al-2wt.%Mg alloy (longitudinal). **(D)** Al-2wt.%Mg (transversal) alloy.

sections, it is observed that the columnar grain zone presents the noblest corrosion potential value, E_{corr}. For the longitudinal section, after reaching E_{corr}, a region where the current increases gradually, until reaching the pitting potential, E_p, is observed. The current values reached in this anodic region move towards higher values from the columnar zone to the equiaxed zone of grains. The E_p is equal to −750 mV coincident for the three-grain zones.

The curves obtained for the cross section show a behavior similar to that described above. However, the E_p of the equiaxed grain zone is equal to −734 mV, slightly nobler than that reached by the other samples described.

Figures 6C,D shows the potentiodynamic curves obtained for the alloy Al-2wt.%Mg. As observed in **Figure 6A**, the longitudinal section also presents a region of gradual increase of the current after E_{corr} is reached. This region is well defined for the columnar grain zone and can be considered a region of passivity. The noblest E_{corr} corresponds to the CET zone. The difference in E_{corr} between the columnar and equiaxed grain zones is not considered significant. Again, the three zones show an E_p around −750 mV.

Figure 6B presents the curves obtained for the transversal section of the Al-2wt.%Mg alloy. The columnar grain zone shows, again, the noblest E_{corr}. However, after reaching this potential, a rapid increase in current is observed, associated with the direct dissolution of the material. The corrosion potentials, E_{corr}, as well as the corrosion current density, I_{corr}, of the Al-Mg alloys are listed in **Table 2**.

In general, it is observed that, for the same composition, the transversal section presents nobler values of E_{corr}. In addition, it was observed that with increasing Mg content, E_{corr} increases. This was evident for the transversal section, while in the longitudinal section, this effect was observed only for the equiaxed grain zone.

The micrographs obtained by scanning electron microscopy (SEM) after the polarization tests are shown in **Figure 7**. From the comparison of **Figures 7A,B**, corresponding to the longitudinal section of the Al-0.5wt.%Mg alloy, it can be seen that the columnar zone is less affected. In the equiaxed grain zone (**Figure 7B**) the damage is clearly located in the grain border region. In the transversal section of the Al-0.5wt.%Mg alloy (**Figures 7C,D**), the corrosion is localized in the α-Al matrix. **Figures 7E,F** correspond to the Al-2wt.% Mg alloy. **Figure 7E** shows that the corrosion is located in the dendritic matrix close to the interdendritic boundary. **Figure 7F** denotes the presence of particles that may correspond to the oxide deposited in the region close to the corrosion affected zone.

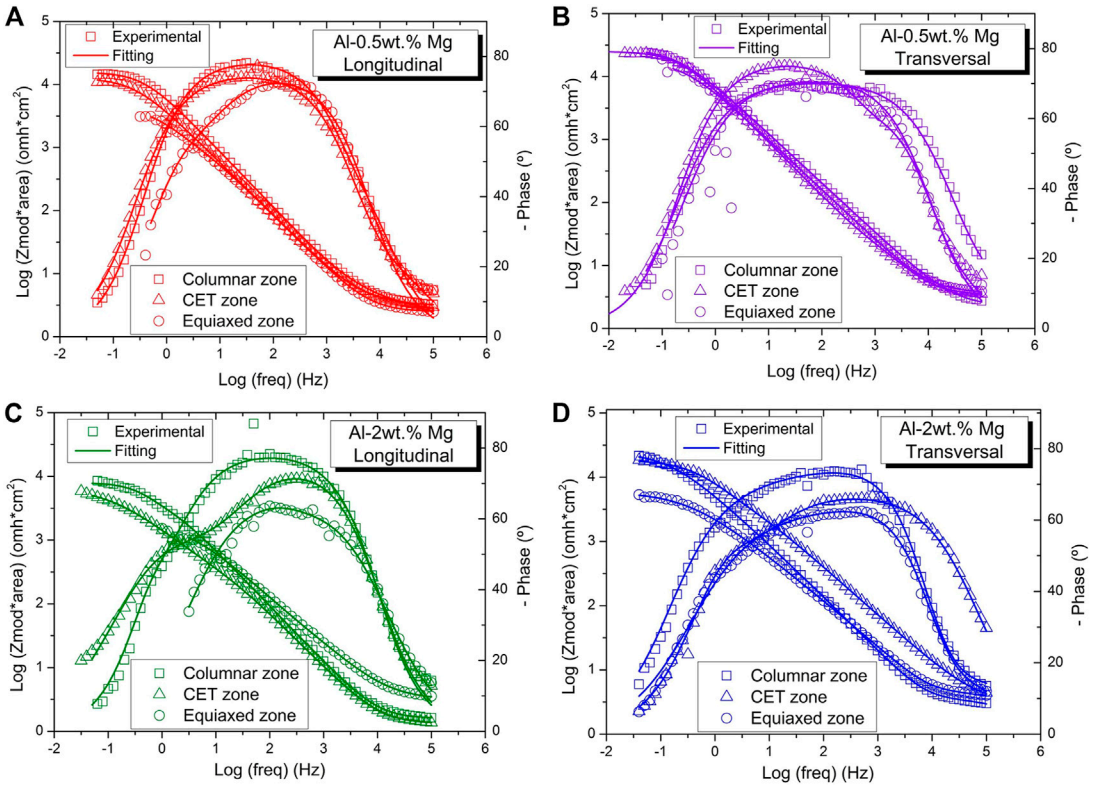

FIGURE 9 | Bode diagrams of Al-Mg alloys. **(A)** Al-0.5wt.% Mg alloy (longitudinal). **(B)** Al-0.5wt.% Mg alloy (transversal). **(C)** Al-2wt.% Mg alloy (longitudinal). **(D)** Al-2wt.% Mg alloy (transversal).

3.5.2 Electrochemical Impedance Spectroscopy (EIS)

Figure 8 shows the Nyquist diagrams obtained from the EIS measurements of the Al-Mg alloys. As it has been reported in other works on aluminum base alloys in chloride-containing solutions, the analysis of impedance data at frequencies lower than 0.1 Hz is difficult, probably due to the non-stationary nature of the pitting phenomenon (Frankel, 2008; Román et al., 2021). Consequently, we have decided not to consider points at frequencies below 0.05 Hz. The scattering of the data was even more evident for the samples from the equiaxed grain zone, because in those cases we chose to ignore data below 0.1 Hz.

For all the samples studied, the Nyquist diagram showed a capacitive semicircle at high and medium frequencies. For the same alloy composition, it can be seen that the diameter of such semicircle increases for the cross section of the samples. Ares et al. (Ares et al., 2011) pointed out that the diameter of such semicircle is related to the corrosion resistance. Therefore, it can be deduced that the transversal section of the Al-Mg samples presented higher corrosion resistance than the longitudinal section. The size of the capacitive arcs obtained for the longitudinal section of the Al-2wt.%Mg were notably smaller than the rest of the alloys studied.

Figure 9 displays the Bode diagrams of the alloys studied. The impedance responses were simulated using the equivalent circuit of two nested time constants shown in **Figure 10**. The use of such a circuit has been reported to explain the behavior of aluminum base alloys as well as Mg base alloys with aluminum coatings (Frankel, 2008; Román et al., 2021; Wei et al., 2021; Ma et al., 2022). R_Ω represents the solution resistance. R_1 and CPE_1 correspond to the pore resistance and the capacitance of the outer porous layer respectively. R_2 and CPE_2, represent the resistance and the capacitance of the barrier layer (Orazem and Tribollet, 2008; Sekularac and Milosev, 2018; Wei et al.,

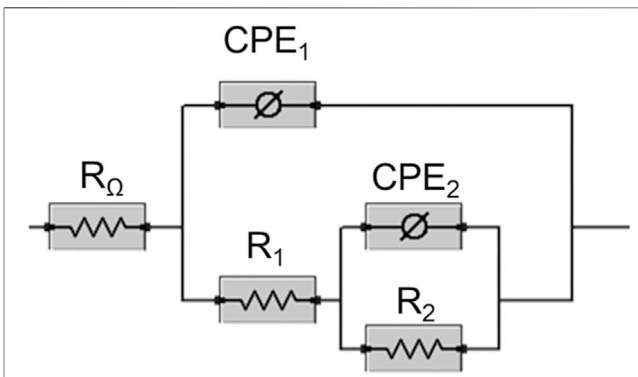

FIGURE 10 | Equivalent circuit used to fit the experimental data.

TABLE 3 | Electrochemical impedance spectroscopy fitting parameters.

		Zone	RΩ	CPE_1	n_1	R_1	R_2	CPE_2	n_2
			Ω^*cm^2	$\Omega^{-1}s^{-n}*cm^{-2}$		Ω^*cm^2	Ω^*cm^2	$\Omega^{-1}s^{-n}*cm^{-2}$	
Al-0.5wt.%Mg	Longitudinal section	Columnar	3.12	1.84E-05	0.89	1.20E+01	1.58E+04	1.14E-05	0.87
		CET	2.59	1.96E-05	0.85	2.86E+00	1.28E+04	3.33E-05	0.83
		Equiaxed	2.40	5.25E-05	0.85	1.96E+03	2.57E+03	6.09E-05	0.81
Al-0.5wt.%Mg	Transversal section	Columnar	1.85	1.11E-05	0.79	9.27E-01	2.82E+04	1.96E-05	0.79
		CET	3.38	2.54E-05	0.84	8.16E+01	2.52E+04	6.58E-06	0.89
		Equiaxed	3.46	3.72E-05	0.79	7.69E+00	1.80E+04	6.22E-07	1.00
Al-2wt.%Mg	Longitudinal section	Columnar	1.58	3.75E-05	0.88	5.21E+03	2.82E+03	8.42E-05	1.00
		CET	1.31	5.83E-05	0.85	5.40E+02	6.00E+03	1.48E-04	0.64
		Equiaxed	3.12	6.04E-05	0.75	6.71E+02	1.20E+03	1.01E-06	1.00
Al-2wt.%Mg	Transversal section	Columnar	2.00	3.76E-05	0.72	2.00E+00	2.50E+04	8.00E-06	0.94
		CET	2.90	1.88E-05	0.75	7.68E+03	1.10E+04	1.20E-05	0.88
		Equiaxed	3.10	1.01E-04	0.67	3.91E+00	5.95E+03	2.04E-06	1.00

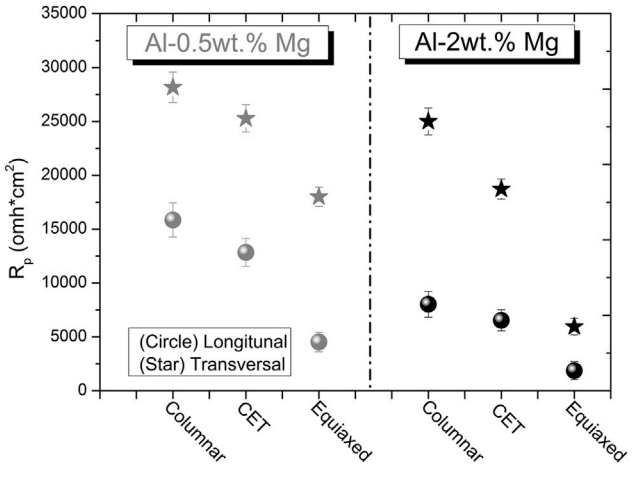

FIGURE 11 | Polarization resistance, Rp, of Al-Mg alloys in 0.5 M NaCl solution.

2021). The deviation from the ideal capacitive behavior due to the inhomogeneous interface, is represented by using CPE with coefficients n_1 and n_2 (Román et al., 2021; Ma et al., 2022).

The parameters of the impedance settings of the samples studied are presented in **Table 3**. From the summation of the resistances R_1 and R_2, the values of the polarization resistance R_p were obtained, which can be seen in **Figure 11**. Higher values of R_p indicate higher corrosion resistance (Ares and Gassa, 2012).

4 DISCUSSION

Figure 11 shows that the corrosion resistance, for the same alloy, decreases from the base to the upper zone of the samples; that is, from the columnar grain zone to the equiaxed grain zone. This behavior coincides with that observed in the polarization curves. Moreover, for the same alloy composition, the transversal section shows better polarization resistance than the longitudinal section. However, the polarization curves seem to show a better corrosion behavior for the longitudinal section. This could be explained by considering the values of the impedance matching parameters shown in **Table 3**. Comparing the values of n_1, corresponding to the CPE_1 of the two sections for the same sample, it is observed that the longitudinal section presents values closer to 1 with respect to the transverse zone. This would indicate that the porosity of the oxide formed in the longitudinal section is lower. This behavior could be due to the adhesion of the detached oxide product of the corrosive attack, which can be observed in **Figure 7F**. In addition, it is evident that the values of the resistance associated to the pores, R_1 are higher for the longitudinal section than for the transversal section. This could explain the behavior observed in the potentiodynamic curves. These curves would be reflecting the "performance" of this resistance R_1, associated to the pores, but that is not significant in relation to the corrosion resistance of the samples. According to **Table 3**, the R_2 values are higher than the R_1 values for all the samples, so that the barrier layer evidently provided the corrosion resistance (Osório et al., 2013). On the other hand, it is clear that as the Mg content increases, for the same grain zone and the same transversal-section, the polarization resistance decreases.

In the case of the correlation of the polarization resistance, R_p, with the secondary dendritic arm spacing for Al-2wt.%Mg alloy; so, when λ_2 increases, the polarization resistance, R_p, decreases (**Figure 12A**).

The values of the polarization resistance, R_p, were correlated with the values of temperature gradient in the liquid at the moment of the CET (critical values), G_C, for each concentration, where it is observed that, when G_C becomes more negative (**Figure 12B**), the R_p increases.

Since the microhardness is a very localized parameter, and the hardness allows a deeper understanding of the relationship between the structure and properties of a material (Maruschak et al., 2012), the polarization resistance, Rp, is correlated to the Brinell hardness, HB, in **Figure 12C** it is possible to observe that

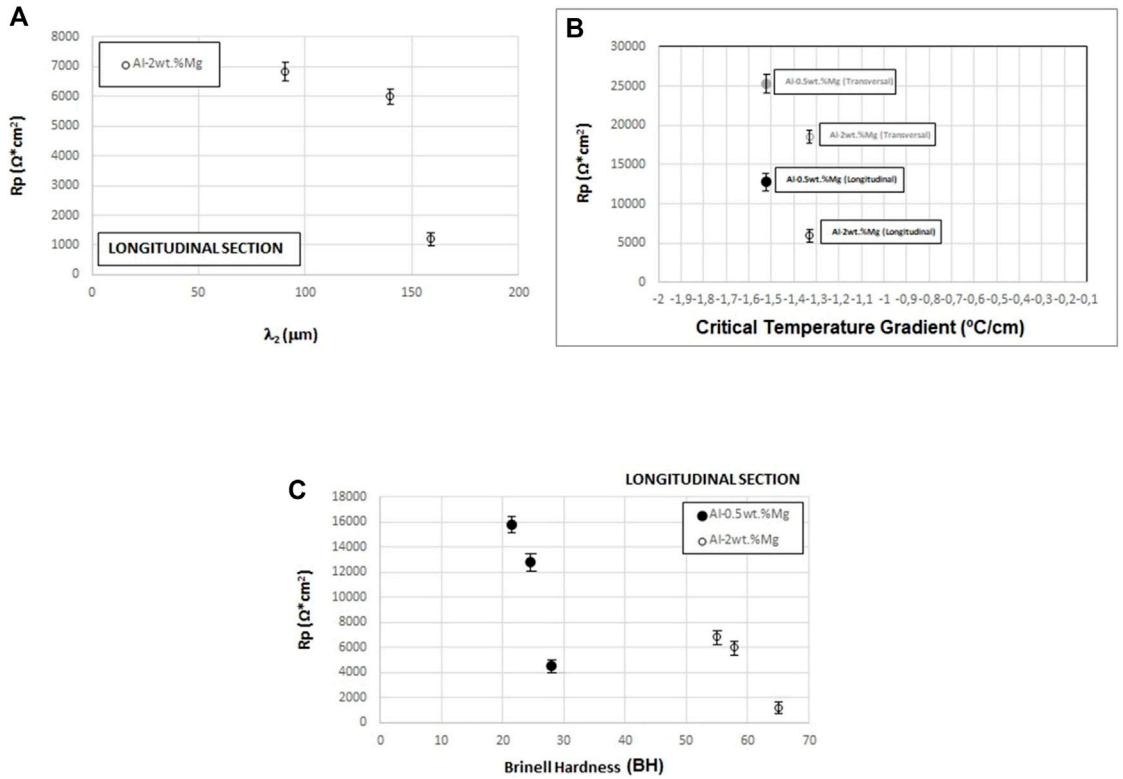

FIGURE 12 | Polarization resistance, R_p, versus **(A)** secondary dendritic arm spacing, λ_2, for Al-2wt.%Mg alloy, **(B)** critical temperature gradient, G_C, and **(C)** Brinell hardness, BH, for Al-0.5wt.%Mg and Al-2wt.%Mg alloys.

when the Brinell hardness, HB, increases the polarization resistance decreases for both alloys.

The polarization resistance increases when the critical temperature gradient decreases.

5 CONCLUSION

Using potentiodynamic polarization and electrochemical impedance spectroscopy (EIS) techniques, allowed us to evaluate the corrosion behavior of Al-0.5wt.% Mg and Al-2wt.% Mg alloys in a 0.5% NaCl solution.

The values of the polarization resistance were used as a basic criterion for the evaluation of the corrosion resistance of both alloys, but do not indicate the protective properties of the films formed on the directionally solidified Al-Mg alloys.

For both compositions of Al-Mg alloys and sections of the samples, the columnar grain zone presents a higher corrosion resistance than that of the equiaxed grain zone.

Considering the polarization resistance values obtained for the EIS tests, it is concluded that the transversal section presents a higher corrosion resistance than the longitudinal section of the samples. In the same sense, the Al-0.5wt.% Mg alloy presents higher corrosion resistance than the Al-2wt.% Mg alloy.

The polarization resistance decreases with 1) the increasing in the distance from the base of the sample, 2) the increasing in grain size and secondary dendritic arm spacing, and 3) the increasing in Brinell hardness and Vickers microhardness.

DATA AVAILABILITY STATEMENT

The original contributions presented in the study are included in the article/Supplementary Material, further inquiries can be directed to the corresponding author.

AUTHOR CONTRIBUTIONS

All authors listed have made a substantial, direct, and intellectual contribution to the work and approved it for publication.

FUNDING

National Agency of Scientific and Technological Promotion of Argentina (ANPCyT) under PICT-2017-0079 grant. National Scientific and Technical Research Council (Consejo Nacional de Investigaciones Científicas y Técnicas—CONICET) under PUE-CONICET- Announcement 2018 of the Materials Institute of Misiones (Instituto de Materiales de Misiones-IMAM) grant.

ACKNOWLEDGMENTS

The authors appreciate the financial support provided by the National Scientific and Technical Research Council (Consejo Nacional de Investigaciones Científicas y Técnicas—CONICET), the National Council for Scientific and Technological Outreach (Agencia Nacional de Promoción Científica y Tecnológica de Argentina (ANPCyT) for their funding through the grant PICT-2017-0079 and the Research Project of the executing entity—PUE-CONICET: PUE 22920180100025CO—Announcement 2018 of the Materials Institute of Misiones (Instituto de Materiales de Misiones-IMAM).

REFERENCES

Aguilera Luna, I., Mancha Molinar, H., Castro Román, M. J., Escobedo Bocardo, J. C., and Herrera Trejo, M. (2013). Improvement of the Tensile Properties of an Al-Si-Cu-Mg Aluminum Industrial alloy by Using Multi Stage Solution Heat Treatments. *Mater. Sci. Eng. A* 561, 1–6. doi:10.1016/j.msea.2012.10.064

Amin, M. A., Abd El Rehim, S. S., Moussa, S. O., and Ellithy, A. S. (2008). Pitting Corrosion of Al and Al-Cu Alloys by ClO4– Ions in Neutral Sulphate solutionsPitting Corrosion of Al and Al-Cu Alloys by ClO4 Ions in Neutral Sulphate Solutions. Electrochim. *Electrochimica Acta* 53, 5644–5652. doi:10.1016/j.electacta.2008.03.010

Ares, A. E., Caram, R., and Schvezov, C. E. (2003a). "Analysis of Grain Size Obtained during Directional Solidification of Aluminum Based Alloys," in The Light Metals 2003: Proceedings of the technical sessions presented by the TMS Aluminium Committee at the 132nd TMS Annual Meetings, Warrendale, PA (The Minerals, Metals and Materials Society), 1055–1061. 087339531X.978-087339531-1.

Ares, A. E., Caram, R., and Schvezov, C. E. (2003b). "Columnar to Equiaxed Transition Studies in Aluminum-Magnesium and Aluminum-Zinc Alloys," in The Light Metals 2003: Proceedings of the technical sessions presented by the TMS Aluminium Committee at the 132nd TMS Annual Meetings, Warrendale, PA (The Minerals, Metals and Materials Society), 1047–1054. 087339531X.978-087339531-1.

Ares, A. E., Caram, R., and Schvezov, C. E. (2004). "The Effect of Solidification Parameters on Dendrite Spacing in Unidirectional Solidification," in The 2004 TMS Annual Meeting, Warrendale, PA (The Minerals, Metals and Materials Society), 751–765.

Ares, A. E., and Gassa, L. M. (2012). Corrosion Susceptibility of Zn-Al Alloys with Different Grains and Dendritic Microstructures in Nacl Solutions. *Corrosion Sci.* 59, 290–306. doi:10.1016/j.corsci.2012.03.015

Ares, A. E., Gassa, L. M., Gueijman, S. F., and Schvezov, C. E. (2008). Correlation between Thermal Parameters, Structures, Dendritic Spacing and Corrosion Behavior of Zn-Al Alloys with Columnar to Equiaxed Transition. *J. Cryst. Growth* 310, 1355–1361. doi:10.1016/j.jcrysgro.2007.11.169

Ares, A. E., Gassa, L. M., Schvezov, C. E., and Gueijman, S. F. (2011). "Relationship between Structure and Properties of Al-Cu Alloys," in The Shape Cast. 4th International Symposium, Warrendale, PA (The Minerals, Metals and Materials Society), 207–214. doi:10.1002/9781118062050.ch25

Ares, A. E., Gueijman, S. F., and Schvezov, C. E. (2010). An Experimental Investigation of the Columnar-To-Equiaxed Grain Transition in Aluminum-Copper Hypoeutectic and Eutectic Alloys. *J. Cryst. Growth* 312, 2154–2170. doi:10.1016/j.jcrysgro.2010.04.040

Ares, A. E., Ramos, S. G., and Méndez, C. M. (2018). "Electrochemical Characterization of Al–Li–Cu–Mg Alloys," in The Minerals, Metals and Materials Series, Part F4, Warrendale, PA (The Minerals, Metals and Materials Society), 983–989. doi:10.1007/978-3-319-72284-9_128

Ares, A. E., and Schvezov, C. E. (2015). "Columnar-to-equiaxed Transition in Zn-27wt.%Al Alloys: A Comparation between Vertical and Horizontal Directional Solidifications," in The TMS Annual Meeting, Warrendale, PA (The Minerals, Metals and Materials Society), 93–100. doi:10.1002/9781119093367.ch12

Ares, A. E., and Schvezov, C. E. (2007). Influence of Solidification Thermal Parameters on the Columnar-To-Equiaxed Transition of Aluminum-Zinc and Zinc-Aluminum Alloys. *Metall. Mat Trans. A.* 38, 1485–1499. doi:10.1007/s11661-007-9111-z

Ares, A. E., and Schvezov, C. E. (2000). Solidification Parameters during the Columnar-To-Equiaxed Transition in Lead-Tin Alloys. *Metall. Mat Trans. A.* 31, 1611–1625. doi:10.1007/s11661-000-0171-6

Ares, A. E., and Schvezov, C. E. (2011). The Effect of Structure on Tensile Properties of Directionally Solidified Zn-Based Alloys. *J. Cryst. Growth* 318, 59–65. doi:10.1016/j.jcrysgro.2010.11.112

Ares, A., Rodriguez, C. M., Méndez, C. M., Schvezov, C. E., and Rosenberger, M. R. (2016). "Microhardness, Corrosion Behaviour and Microstructures of Directionally Solidified Al-Cu Alloys," in The Minerals, Metals and Materials Series, Warrendale, PA (The Minerals, Metals and Materials Society), 469–473. doi:10.1007/978-3-319-65136-1_81

Arrabal, R., Mingo, B., Pardo, A., Mohedano, M., Matykina, E., and Rodríguez, I. (2013). Pitting Corrosion of Rheocast A356 Aluminium Alloy in 3.5wt.% NaCl Solution. *Corros. Sci.* 73, 342–355. doi:10.1016/j.corsci.2013.04.023

Barsoukov, E., and Ross McDonald, J. (2005). *Impedance Spectroscopy. Theory, Experiment and Applications, John, Wiley & Sons, Inc., Hoboken*. New Jersey and Canada.

Boag, A., Taylor, R. J., Muster, T. H., Goodman, N., McCulloch, D., Ryan, C., et al. (2010). Stable Pit Formation on AA2024-T3 in a NaCl Environment. *Corrosion Sci.* 52, 90–103. doi:10.1016/j.corsci.2009.08.043

Boyer, H. E., and Gall, T. L. (1990). *Metals Handbook, Desk Edition*. American Society for Metals, 35–18.

Canales, A. A., Carrera, E., Silva, J. T., Valtierra, S., and Colás, R. (2012). Mechanical Properties in As-Cast and Heat Treated Al-Si-Cu Alloys. *Ijmmp* 7 (4), 281–300. doi:10.1504/ijmmp.2012.048518

Chen, L.-Y., Zhang, H.-Y., Zheng, C., Yang, H.-Y., Qin, P., Zhao, C., et al. (2021). Corrosion Behavior and Characteristics of Passive Films of Laser Powder Bed Fusion Produced Ti-6Al-4V in Dynamic Hank's Solutionfilms of Laser Powder Bed Fusion Produced Ti–6Al–4V in Dynamic Hank's Solution. *Mater. Des.* 208, 109907. doi:10.1016/j.matdes.2021.109907

Davis, J. R. (1993). *2017 Aluminum and Aluminum Alloys*. Materials Park, Ohio: ASM International.

Frankel, G. (2008). Electrochemical Techniques in Corrosion: Status, Limitations and Needs. *J. ASTM Int.* 5, 1–27. doi:10.1520/jai101241

Gauto, E., Kramer, G. R., Méndez, C. M., and Ares, A. E. (2018). Effects of the Use of Support Electrolytes in Electrochemical Tests of Al-4wt.% Mg alloy Exposed to Bioethanol Fuel. *Revista Materia* 23 (22018), e-12050. doi:10.1590/S1517-707620180002.0386

Geng, Y., Panchenko, I., Chen, X., Ivanov, Y., and Konovalov, S. (2021b). Investigation of Microstructure and Fracture Mechanism of Al-5.0Mg Alloys Fabricated by Wire Arc Additive Manufacturing. *J. Materi Eng. Perform.* 30 (10), 7406–7416. doi:10.1007/s11665-021-05973-0

Geng, Y., Panchenko, I., Konovalov, S., Chen, X., and Ivanov, Y. (2021a). Effect of Electron Beam Energy Densities on the Surface Morphology and Tensile Property of Additively Manufactured Al-Mg alloy. *Nucl. Instr. Methods Phys. Res. Section B: Beam Interactions Mater. Atoms* 498, 15–22. doi:10.1016/j.nimb.2021.04.008

Gueijman, S. F., Schvezov, C. E., and Ares, A. E. (2010). Vertical and Horizontal Directional Solidification of Zn-Al and Zn-Ag Diluted Alloys. *Mater. Trans.* 51, 1861–1870. doi:10.2320/matertrans.M2010036

Jayalakshmi, S., Dezhi, Q., Sankaranarayanan, S., and Gupta, M. (2013). Microstructure and Mechanical Properties of Mg-Al Alloys with *In Situ* Al4C3 Phase Synthesised by CO2 Incorporation during Liquid State Processing. *Ijmmp* 8 (4/5), 283–298. doi:10.1504/ijmmp.2013.057066

Kaygisiz, Y., and Marasli, N. (2015). Microstructural, Mechanical and Electrical Characterization of Directionally Solidified Al–Si–Mg Eutectic alloy. *J. Alloys Compd.* 618, 197–203. doi:10.1016/j.jallcom.2014.08.056

Kociubczyk, A. I., Desrosin, W., Boycho, L. M., Schvezov, C. E., and Ares, A. E. (2015). "Interphase Evolution and Defect Formation during Horizontally Directional Solidification Process of Sn-Zn Alloys," in The EPD Congress

2015Warrendale, PA (The Minerals, Metals and Materials Society), 57–64. doi:10.1007/978-3-319-48214-9_7

Kociubzyk, A. I., Rozicki, R. S., and Ares, A. E. (2018). Movement of the Interphases during the Horizontal Solidification of Tin-Zinc Alloys. *Revista Materia* 23 (2), e-11993. doi:10.1590/s1517-707620180002.0330

Kramer, G. R., Gauto, E., Rozicki, R. S., Méndez, C. M., and Ares, A. E. (2017). "Corrosion of Al–Mg Alloys in Ethanol," in The Minerals, Metals and Materials Series, Warrendale, PA (The Minerals, Metals and Materials Society), 455–461. doi:10.1007/978-3-319-51541-0_57

Kramer, G. R., Méndez, C. M., and Ares, A. E. (2016). "Corrosion Resistance of Different Aluminum Alloys in Ethanol," in The Light Metals 2016, Warrendale, PA (The Minerals, Metals and Materials Society), 265–270. doi:10.1002/9781119274780.ch44

Kramer, G. R., Méndez, C. M., and Ares, A. E. (2018). Evaluation of Corrosion Resistance of Commercial Aluminum Alloys in Ethanol Solutions. *Mater. Res.* 21 ((62018)), e20170272. doi:10.1590/1980-5373-MR-2017-0272

Kro´l, M., Tan´ski, T., Matula, G., Snopin´ski, P., and Tomiczek, A. E. (2015). Analysis of Crystallisation Process of Cast Magnesium Alloys Based on thermal Derivative Analysis. Arch Metall Mater. *2015* 60 (4), 2993–3000. doi:10.1515/amm-2015-0478

Krupin´ski, M., Labisz, K., Tan´ski, T., Krupin´ska, B., Kro´l, M., and Polok Rubiniec, M. (2016). Influence of Mg Addition on Crystallisation Kinetics and Structure of the Zn–Al–Cu alloy. *Arch. Metall. Mater.* 61 (2), 785–790. doi:10.1515/amm-2016-0132

Liu, D.-R., Wang, S., and Yan, W. (2020). Grain Structure Evolution in Transition-Mode Melting in Direct Energy Deposition. *Mater. Des.* 194, 108919. doi:10.1016/j.matdes.2020.108919

Liu, J., and To, A. C. (2017). Quantitative Texture Prediction of Epitaxial Columnar Grains in Additive Manufacturing Using Selective Laser Melting. *Additive Manufacturing* 16, 58–64. doi:10.1016/j.addma.2017.05.005

Liu, S., Zhu, H., Peng, G., Yin, J., and Zeng, X. (2018). Microstructure Prediction of Selective Laser Melting AlSi10Mg Using Finite Element Analysis. *Mater. Des.* 142, 319–328. doi:10.1016/j.matdes.2018.01.022

Ma, Y., Liu, Y., and Wang, M. (2022). Microstructures and Corrosion Resistances of Hypoeutectic Al-6.5Si-0.45 Mg Casting alloy with Addition of Sc and Zr. *Mater. Chem. Phys.* 276, 125321. doi:10.1016/j.matchemphys.2021.125321

Maruschak, P. O., Okipnyi, I. B., PoberezhnyiYa, L., and Maruschak, E. V. (2012). Study of Heat-Resistant Steel Strain Hardening by Indentation. *Metallurgist* 56 (11–12), 946–951.

Méndez, C. M., Scheiber, V. L., Rozicki, R. S., Kociubczyk, A. I., and Ares, A. E. (2018). Electrochemical Behavior of Sn-Zn Alloys with Different Grain Structures in Chloride-Containing Solutions. *Arabian J. Chem.* 11 (7), 1084–1096. doi:10.1016/j.arabjc.2016.12.019

Oliveira, J. P., LaLonde, A. D., and Ma, J. (2020). Processing Parameters in Laser Powder Bed Fusion Metal Additive Manufacturing. *Mater. Des.* 193, 108762. doi:10.1016/j.matdes.2020.108762

Orazem, M., and Tribollet, B. (2008). *Hoboken*. Wiley, 157–159. doi:10.1002/9780470381588 Electrochemical Impedance Spectroscopy

Osório, W. R., Freitas, E. S., and Garcia, A. (2013). EIS and Potentiodynamic Polarization Studies on Immiscible Monotectic Al-In Alloys. *Electrochimica Acta* 102, 436–445. doi:10.1016/j.electacta.2013.04.047

Román, A. S., Méndez, C. M., and Ares, A. E. (2014). Corrosion Resistance of Al-Cu Alloys in Function of the Microstructure. *Msf* 783-786, 100–107. doi:10.4028/www.scientific.net/msf.783-786.100

Román, A. S., Méndez, C. M., Gervasi, C. A., Rebak, R. B., and Ares, A. E. (2021). Corrosion Resistance of Aluminum-Copper Alloys with Different Grain Structures. *J. Materi Eng. Perform.* 30 (1), 131–144. doi:10.1007/s11665-020-05344-1

Román, A. S., Méndez, C. M., Schvezov, C. E., and Ares, A. E. (2015). "Electrochemical Properties of Al-Cu Alloys in NaCl Solutions," in The TMS 2015, Characterization of Minerals, Metals, and Materials 2015, Warrendale, PA (The Minerals, Metals and Materials Society), 727–734. doi:10.1007/978-3-319-48191-3_92

Rozicki, R. S., Kociubczyk, A. I., Kramer, G. R., and Ares, A. E. (2018). "Observations of Microhardness and Evolution of Constituents in Al–Zn and Zn–Al Specimens with Columnar-To-Equiaxed Grain Transition," in The Minerals, Metals and Materials Series, Part F4, Warrendale, PA (The Minerals, Metals and Materials Society), 1081–1088. doi:10.1007/978-3-319-72284-9_141

Satizabal, L. M., Costa, D., Moraes, P. B., Bortolozo, A. D., and Osório, W. R. (2019). Microstructural Array and Solute Content Affecting Electrochemical Behavior of Sn Ag and Sn Bi Alloys Compared with a Traditional Sn Pb alloyMicrostructural Array and Solute Content Affecting Electrochemical Behavior of SnAg and SnBi Alloys Compared with a Traditional SnPb alloy. *Mater. Chem. Phys.* 223, 410–425. doi:10.1016/j.matchemphys.2018.11.003

Sekularac, G., and Milosev, I. (2018). Corrosion of Aluminium Alloy AlSi7Mg0.3 in Artificial Sea Water with Added Sodium Sulphide. *Corros. Sci.* 144, 54–73. doi:10.1016/j.corsci.2018.08.038

Shokuhfar, A., and Nejadseyfi, O. (2014). A Comparison of the Effects of Severe Plastic Deformation and Heat Treatment on the Tensile Properties and Impact Toughness of Aluminum alloy 6061. *Mater. Sci. Eng. A* 594, 140–148. doi:10.1016/j.msea.2013.11.067

Shu-qing, Y., and Xing-fu, L. (2014). The Effect of Si Morphology on the Microstructure and Wear Property of ZA48 alloy. *Int. J. Microstruct Mater. Prop* 9 (1), 88–96.

Song, D., Sang, P., Chen, L., Zhao, C., Wang, Z., Wang, H., et al. (2019). Particle Size-dependent Microstructure, Hardness and Electrochemical Corrosion Behavior of Atmospheric Plasma Sprayed NiCrBSi Coatings. *Metals* 9, 1342. doi:10.3390/met9121342

Song, J., Chew, Y., Bi, G., Yao, X., Zhang, B., Bai, J., et al. (2018). Numerical and Experimental Study of Laser Aided Additive Manufacturing for Melt-Pool Profile and Grain Orientation Analysis. *Mater. Des.* 137, 286–297. doi:10.1016/j.matdes.2018.11.01410.1016/j.matdes.2017.10.033

Spittle, J. A. (2006). Columnar to Equiaxed Grain Transition in as Solidified Alloys. *Int. Mater. Rev.* 51, 247–269. doi:10.1179/174328006X102493

Szklarska-Smialowska, Z. (1999). Pitting Corrosion of Aluminum. *Corrosion Sci.* 41, 1743–1767. doi:10.1016/j.corsci.2011.11.01010.1016/s0010-938x(99)00012-8

Totten, G. E., Xie, L., and Funatani, K. (2004). *Handbook of Mechanical Alloy Design*. 6000 Broken Sound Parkway NW, USA: Taylor & Francis.

Vander Voort, G. (2004). Metallography and Microstructures, in ASM Handbook (ASM International).

Wang, X.-h., Wang, J.-h., and Fu, C.-w. (2014). Characterization of Pitting Corrosion of 7A60 Aluminum Alloy by EN and EIS Techniques. *Trans. Nonferrous Met. Soc. China* 24, 3907–3916. doi:10.1016/s1003-6326(14)63550-0

Wei, B., Cheng, Y., Liu, Y., Zhu, Z., and Cheng, Y. (2021). Corrosion and Wear Resistance of AZ31 Mg alloy Treated by Duplex Process of Magnetron Sputtering and Plasma Electrolytic Oxidation. Trans Nonferrous Met Soc China. *Trans. Nonferrous Met. Soc. China* 31, 2287–2306. doi:10.1016/S1003-6326(21)65655–65658

Xia, S. L., Ma, M., Zhang, J. X., Wang, W. X., and Liu, W. C. (2014). Effect of Heating Rate on the Microstructure, Texture and Tensile Properties of Continuous Cast AA 5083 Aluminum alloy. *Mater. Sci. Eng. A* 609, 168–176. doi:10.1016/j.msea.2014.05.002

Xiang, S., Li, J., Luan, H., Amar, A., Lu, S., Li, K., et al. (2019). Effects of Process Parameters on Microstructures and Tensile Properties of Laser Melting Deposited CrMnFeCoNi High Entropy Alloys. *Mater. Sci. Eng. A* 743, 412–417. doi:10.1016/j.matdes.2020.10926210.1016/j.msea.2018.11.110

Xu, C., Chen, L.-Y., Zheng, C.-B., Zhang, H.-Y., Zhao, C.-H., Wang, Z.-X., et al. (2021). Improved Wear and Corrosion Resistance of Microarc Oxidation Coatings on Ti-6Al-4V Alloy with Ultrasonic Assistance for Potential Biomedical Applications. *Adv. Eng. Mater.* 23, 2001433. doi:10.1002/adem.202001433

Yasakau, K. A., Zheludkevich, M. L., and Ferreira, M. G. S. (2018). "Role of Intermetallics in Corrosion of Aluminum Alloys," in *Smart Corrosion Protection* (Amsterdam: Elsevier). doi:10.1016/b978-0-85709-346-2.00015-7

Zhang, X., Chen, H., Xu, L., Xu, J., Ren, X., and Chen, X. (2019). Cracking Mechanism and Susceptibility of Laser Melting Deposited Inconel 738 Superalloy. *Mater. Des.* 183, 108105. doi:10.1016/j.matdes.2019.108105

Zhao, X.-h., Zuo, Y., Zhao, J.-m., Xiong, J.-p., and Tang, Y.-m. (2006). A Study on the Self-Sealing Process of Anodic Films on Aluminum by EIS. *Surf. Coat. Tech.* 200, 6846–6853. doi:10.1016/j.surfcoat.2005.10.031

Zhou, K., Wang, B., Zhao, Y., and Liu, J. (2015). Corrosion and Electrochemical Behaviors of 7A09 Al-Zn-Mg-Cu alloy in Chloride Aqueous Solution. *Trans. Nonferrous Met. Soc. China* 25, 2509–2515. doi:10.1016/S1003-6326(15)63869-9

Conflict of Interest: The authors declare that the research was conducted in the absence of any commercial or financial relationships that could be construed as a potential conflict of interest.

Publisher's Note: All claims expressed in this article are solely those of the authors and do not necessarily represent those of their affiliated organizations, or those of the publisher, the editors and the reviewers. Any product that may be evaluated in this article, or claim that may be made by its manufacturer, is not guaranteed or endorsed by the publisher.

frontiers | Frontiers in Materials

ORIGINAL RESEARCH
published: 24 May 2022
doi: 10.3389/fmats.2022.825120

Effect of Y Concentration on the *In Situ* Growth Behavior and Corrosion Protection of the MgAlY-LDH Sealing Film on the Anodized Surface of Mg–2Zn–4Y Alloy

Yuqi Hong[1,2], Liang Wu[1,2], Xinyi Zhang[1,2], Guoxiang Zhan[1,2], Yanning Chen[1,2], Wenhui Yao[1,2], Xu Dai[1,2], Tao Wu[1,2], Xiaowei Dai[1,2], Jianpeng Xiang[1,2], Yan Zhou[1,2] and Fusheng Pan[1,2]*

[1]State Key Laboratory of Mechanical Transmission, College of Materials Science and Engineering, Chongqing University, Chongqing, China, [2]National Engineering Research Center for Magnesium Alloys, Chongqing University, Chongqing, China

OPEN ACCESS

Edited by:
Daokui Xu,
Chinese Academy of Sciences (CAS), China

Reviewed by:
Xiaopeng Lu,
Northeastern University, China
You Zhang,
Beijing Institute of Petrochemical Technology, China

***Correspondence:**
Liang Wu
wuliang@cqu.edu.cn

Specialty section:
This article was submitted to Environmental Degradation of Materials, a section of the journal Frontiers in Materials

Received: 30 November 2021
Accepted: 20 April 2022
Published: 24 May 2022

Citation:
Hong Y, Wu L, Zhang X, Zhan G, Chen Y, Yao W, Dai X, Wu T, Dai X, Xiang J, Zhou Y and Pan F (2022) Effect of Y Concentration on the In Situ Growth Behavior and Corrosion Protection of the MgAlY-LDH Sealing Film on the Anodized Surface of Mg–2Zn–4Y Alloy. Front. Mater. 9:825120. doi: 10.3389/fmats.2022.825120

The successful doping of Yttrium (Y) in the Mg-Al layered double hydroxide film (MgAlY-LDHs) is obtained by hydrothermal way on the anodic oxide film of Mg-2Zn-4Y alloys. The composition, morphology and structure of MgAlY-LDHs were characterized by the Fourier transform infrared spectroscopy (FT-IR), X-ray diffractometer (XRD), field-emission scanning electronic microscope (FE-SEM) and energy dispersive spectrometry (EDS) respectively. The electrochemical behavior was observed by polarization curves and electrochemical impedance spectroscopy (EIS). Y ions can be incorporated into the MgAl-LDHs film in a completely isomorphic replacement manner and have the ability to improve the corrosion resistance of the film. Moreover, the ternary LDHs film grown in situ on the Mg-2Zn-4Y alloy provides a high possibility for the corrosion resistance of industrial metals. The schematic representation of electrochemical behavior and the growth mechanism of MgAlY-LDHs nanosheet are as following eventually.

Keywords: ion concentration, anode oxide film, yttrium, ternary-layered double hydroxides, corrosion resistance

1 INTRODUCTION

Magnesium alloys are considered to have a bright prospect because of their low density and environmentally friendly properties (Mordike and Ebert, 2001; Prado and Cepeda-Jiménez, 2015; Polmear, 2017). However, the high chemical activity of magnesium leads to its susceptibility to corrosion, limiting its industrial application (Srinivas et al., 2022). Therefore, the corrosion and protection of magnesium alloys have been listed as an important research topic in the material field in recent years. At present, the main method to effectively improve the corrosion resistance is the technology of surface coating, which is to prevent the corrosion of metal materials by a special treatment process and physical barrier method to limit the contact between the external corrosion medium and internal matrix (Stoltenhoff et al., 2002). Among the rest, anodic oxidation is the most effective method. Because of its simple and mature process, this method is widely used (Hornberger et al., 2012; Atrens, 2015). However, the magnesium alloy matrix is unprotected when the film is in the corrosive environment because of the porous and loose structure of the anodic oxide surface (Blawert et al., 2006). This is why magnesium anodization is rarely used commercially to improve

corrosion resistance (Blawert et al., 2006). Therefore, it is necessary to research an effective way to seal the anodic oxide film (Huang et al., 2014).

The layered double hydroxides (LDHs) have the possible ability to possess an active corrosion system. LDHs are a typical two-dimensional layered nanomaterial that has broad prospects (Scarpellini et al., 2014; Zhang et al., 2014), the chemical formula of which is $[M_{1-x}^{2+}M^{3+}(OH)_2]^{x+}(An^-)_{x/n}mH_2O$, in which the anion An^- is in the hydrated interlayer galleries (such as OH^-, NO_3^-, and PO_4^{3-}), and the metal cations M^{3+} and M^{2+} (such as Al^{3+}, Y^{3+}, and Mg^{2+}) occupy the octahedral holes in the brucite-like layer (Dong et al., 2014). This inorganic nanocontainer is widely applied in the research on corrosion protection because of high loadings, easy modification, and small size. Corrosion occurs when the corrosion environment destroys the main physical barrier of metals, causing the corrosive medium (such as Cl^-) to contact the bare metal substrate. Thus, the obvious feature of ion exchange is that it can release the interlayer anion and adsorb Cl^- when it confronts corrosive ions (Lu, 2018). As a result, the LDH film grown on the surface of anodized magnesium can not only seal the porous anodic oxide layer but also improve the thickness of the protective film successfully. Thus, this structure has a synergistic impact of promotion on improving the corrosion resistance of magnesium alloy.

As a unique two-dimensional-layered structure, the structure characteristics are maximized to the modification of LDHs to enhance the resistance of corrosion property. Nowadays, a great number of researchers (Zhang, 2017a; Zhang, 2017b; Zahedi Asl, 2019) paid more attention to change rare earth ions (La and Ce) in LDHs, and research studies started with being published in the study of corrosion. Zhou et al. (2019) found that the fabrication of ZnAlLa-LDHs can improve the anti-corrosion of 6,061 aluminum alloys. The phenomenon that MgAl-LDHs doping with Ce can enhance the corrosion protection property of magnesium alloys was found in one of our previous research studies (Zhang, 2018; Zahedi Asl, 2019; Zhang, 2019). However, compared to light rare earth elements (La, Ce), heavy rare earth elements (particularly Y) with low content on earth have no awareness. In addition, although Y has good corrosion inhibition performance, Y-doped ternary LDH films are rarely researched (He et al., 2010; Liu et al., 2010). In fact, ternary LDH has been widely studied in the field of catalysts. Y, La, and Ce addition in MgAl-LDHs can effectively enhance the performance of catalysis (Angelescu et al., 2004; Das et al., 2006; Mrózek, 2019) and luminescence activity (Smalenskaite et al., 2017). Particularly, compared with Ce and La, Y has the lowest electronegativity (1.22) and the smallest ionic radius (0.90 Å) in the same IIIB group (Wang et al., 2014), which makes it theoretically possible to carry Y in MgAl-LDH structure. Meanwhile, the adulteration of Y can improve the specific surface region (Świrk, 2019) and increase the dispersion of active sites (Pavel, 2011) as well as get finer LDH crystallites (Świrk, 2018), which can be used to make contributions to the synthesis of MgAlY-LDH film.

Moreover, the preparation of ternary LDHs usually uses the co-precipitation way. Recently, the study hotpot is that the *in situ* growth method is often used in preparing LDH film, which can contain less impurity phase concentration, possess the binding force between the substrate and film, and get a wide application prospect. Furthermore, the protective Y_2O_3 coating can be grown voluntarily on the surface of Mg substrates (Guo et al., 2010; Ardelean et al., 2013; Lyu et al., 2020). Furthermore, component cations can be provided by the anodic oxide film of Mg–2Zn–4Y alloys for *in situ* ternary LDHs, and the film can serve as a physical barrier to prevent the invasion of corrosive media. MgAlY-LDHs can possess the property of self-healing and anti-corrosion ability by the way of sealing the anodic oxide films (Bîrjega, 2005).

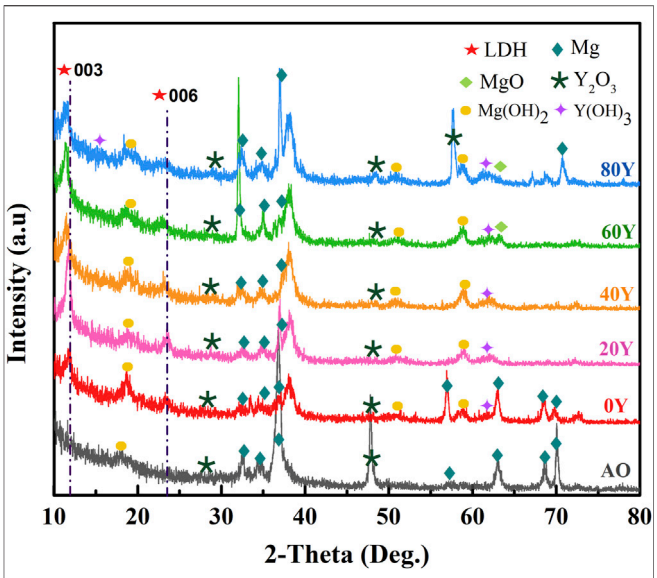

FIGURE 1 | XRD image of specimens with different Y% fabricated on anodized oxide films on Mg–2Zn–4Y alloys.

In this work, we investigated the possibility of ternary MgAlY-LDHs growing on the anodic oxide film of Mg–2Zn–4Y alloy *in situ* and investigated the isomorphous substitution mechanism of MgAlY-LDHs by adding different concentrations of Y. Furthermore, the morphology, structure characteristics, and composition of MgAlY-LDHs were studied. The corrosion resistance of MgAlY-LDHs was initially evaluated by electrochemical activity.

2 EXPERIMENTAL

2.1 Materials

Mg–2Zn–4Y alloy was manufactured in an anti-electric furnace under an environment of protective gas admixture (1% SF6 and 99% CO_2). The raw materials were commercially pure Mg (Ni % < 0.007%, Al % < 0.006%, Si % < 0.005%, Fe % < 0.004%, Cu % < 0.003%, and Mg ≥ 99.95%), pure Al (Al % ≥99.5%, impurity <0.15%), pure Zn (Ni % < 0.01%, Si % < 0.03%, Cu % < 0.01%, Al % < 0.03%, Fe % < 0.05%, and Zn % ≥ 99.9%), and Mg-Y master alloys (purity ≥99.5%, Ni% < 0.01%, Al % < 0.03%, Si % < 0.03%, Cu % < 0.01%, Fe % < 0.05%, and Y % = 30%). The alloys were melted at 750°C for 20 min, and then the film was placed in a mild steel mold (size φ200 mm × 85 mm) preheated at 300°C to

TABLE 1 | Structure data of specimens with different Y% fabricated on anodized oxide films on Mg–2Zn–4Y alloys.

Specimen	0Y	20Y	40Y	60Y	80Y	AO
Lattice constant a	3.0378	3.0466	3.0598	3.0456	3.0306	—
Lattice constant c	22.6353	22.6092	23.21295	23.1513	22.93815	—

(a) Lattice parameter a = 2 × d110, (b) c = 3/2(d003 + 2d006).

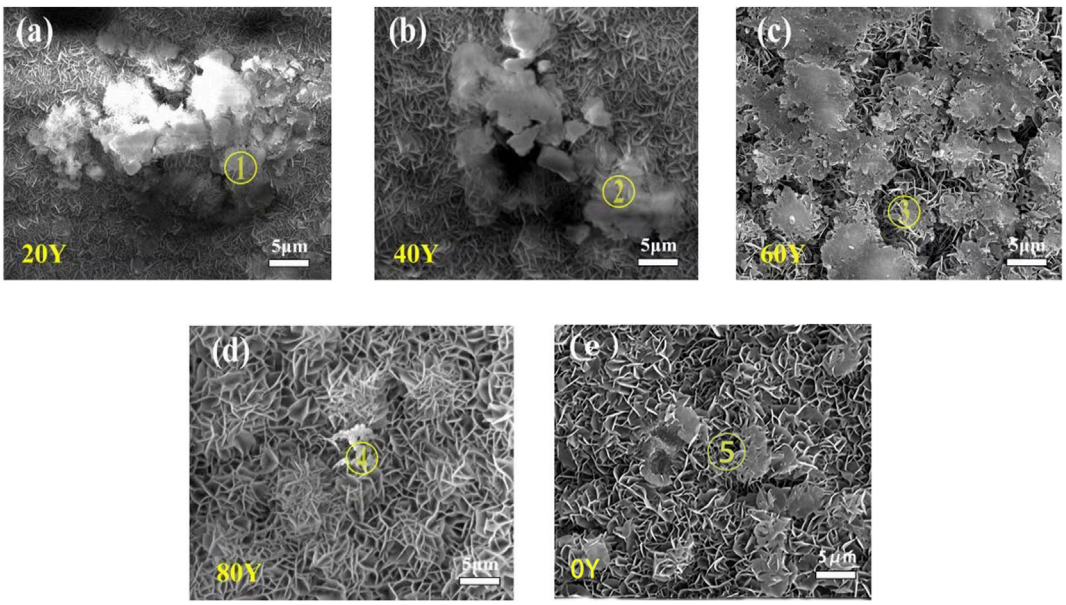

FIGURE 2 | SEM image of LDH specimens with different Y% fabricated on anodized oxide films on Mg–2Zn–4Y alloys: 20Y **(A)**; 40Y **(B)**; 60Y **(C)**; 80Y **(D)**; and 0Y **(E)**.

prepare Mg–2Zn–4Y ingots and finally cooled in an air solution for 6 h. The Mg–2Zn–4Y alloy was cut into slices of 10 mm × 10 mm × 2 mm and 20 mm × 20 mm × 2 mm. The samples were grounded from # 150 to # 3,000 using particle size silicon carbide sandpaper, washed with ethanol and deionized water, and finally dried.

2.2 Preparation of the Anodic Oxide Film

The samples were anodized in the successively stirred electrolyte of 0.6 mol/L NaF, 0.21 mol/L Na_3PO_4, and 3 mol/L NaOH, and the stable voltage is 20 V for 30 min by DC-regulated power. The prepared samples are anodic oxide films of the phosphoric acid system. All anodized samples are named AO. The cathode is made of 1Cr18Ni9Ti stainless steel, and the anode is made of magnesium alloy. The sample with the micro-arc oxidation film is cleaned with ethanol and dried.

2.3 Preparation of MgAlY-LDHs

The MgAlY-LDH films were produced by immersing the anodized samples in 0.3 M $NaNO_3$ and 0.05 M $M(NO_3)_3$ (M = Al and Y) mixture solution with a pH value in the alkaline range by putting the diluted ammonia on. The mixture solutions are put into the Teflon-lined autoclave, and the synthesis was performed at 125°C for 12 h. Then, the filmed samples were rinsed with deionized water, ultrasonically cleaned with ethanol, and finally dried under environmental conditions. Meanwhile, the *in situ* growth of MgAlY-LDH films on different anodic oxide films is researched by changing the ratio of Y^{3+} to Al^{3+} (including Al and Y ions): 0, 20, 40, 60, and 80%. The final samples prepared with different Y^{3+} concentrations are named as 0Y, 20Y, 40Y, 60Y, and 80Y.

2.3.1 Permission to Reuse and Copyright

Figures, tables, and images will be published under a Creative Commons CC-BY licence and permission must be obtained for use of copyrighted material from other sources (including re-published/adapted/modified/partial figures and images from the internet). It is the responsibility of the authors to acquire the licenses, to follow any citation instructions requested by third-party rights holders, and cover any supplementary charges.

2.4 Characterization and Performance Test

The morphology components of each sample are tested by VEGA3 field-emission scanning electron microscopy (FE-SEM, Vega3 TESCAN SRO Czech) and EDS. The crystal structure of ternary LDHs of each sample is examined using an X-ray

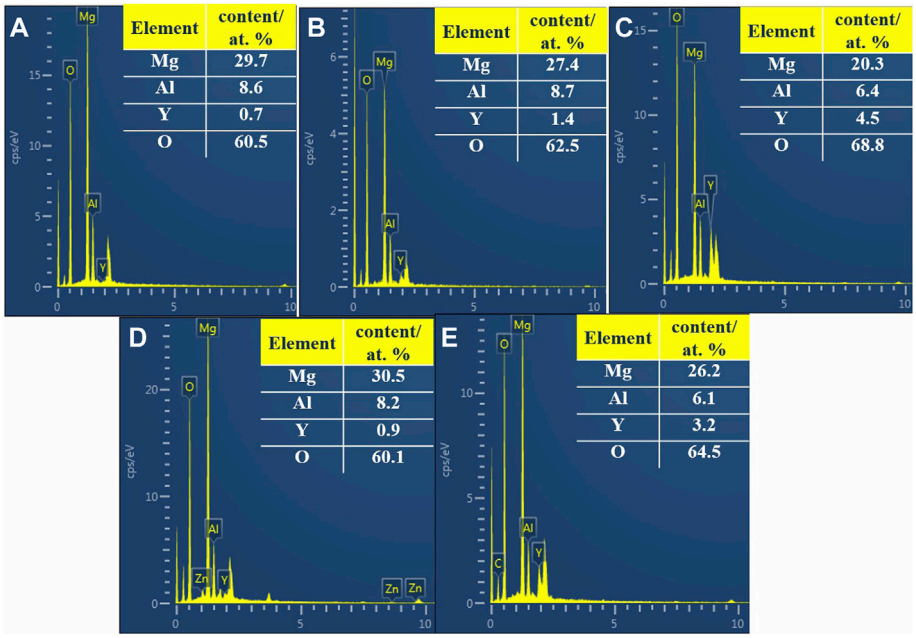

FIGURE 3 | EDS spectra of the corresponding points in **Figure 2**: 20Y [**(A)**, 1]; 40Y [**(B)**, 2]; 60Y [**(C)**, 3]; 80Y [**(D)**, 4]; and 0Y [**(E)**, 5].

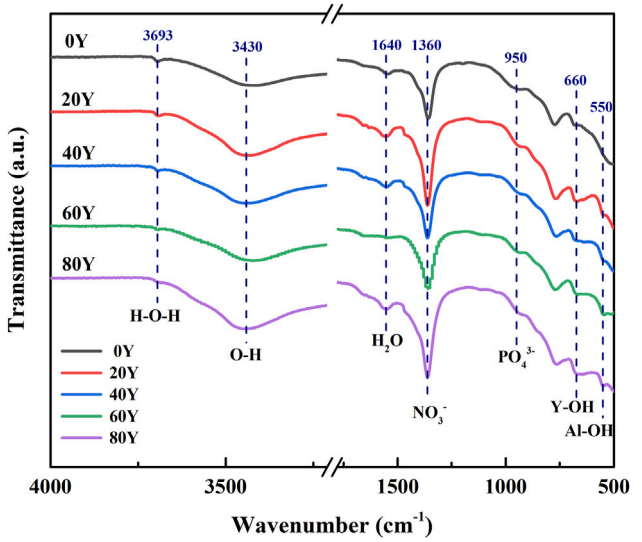

FIGURE 4 | FT-IR pattern of different specimens.

diffractometer (XRD, D/Max 2,500 × Rigaku Japan) and a Nicolet IS5 model Fourier infrared spectrometer (FT-IR, Nicolet IS5 Thermo Scientific, United States). The corrosion behavior of the sample in 3.5 wt% NaCl solution is tested using an electrochemical workstation (Parstat 4000A PAR, United States). A three-electrode battery system with the saturated calomel electrode as the reference electrode, the platinum mesh as the counter electrode, and the sample with an exposed area of 1 cm^2 as the working electrode is established in a Faraday electromagnetic shielding box. Among them, when the scan rate is set to 2 mV s^{-1}, the Tafel polarization curve with reference open circuit potential (OCP) from −0.8 to 0.8 V is obtained.

3 RESULTS AND DISCUSSION

3.1 Characterization of Film Composition, Structure, and Morphology

Figure 1 shows the XRD patterns of different specimens. Among all, the characteristic peaks of MgO and Y_2O_3 are found in all samples, which indicates the compound composition of the phosphate anodized film on Mg–2Zn–4Y alloy. Significantly, the characteristic peaks of Y_2O_3 and Mg substrate in samples 60Y and 80Y are more obvious than others. This may indicate that the moderate concentration of Y^{3+} is conducive to the dissolution of the anodized film. Furthermore, the characteristic peaks (003 and 006) are found in the each LDH sample. In particular, the peaks of 003 and 006 in 60Y shift most obviously to the left, that is to say, adulteration Y leads to the increase of the lattice parameter, interlayer distance, and crystallite dimension. This may indicate that the most obvious changes have taken place in the main structure of LDHs when Y^{3+}/Al^{3+} equals 1.5, which means *in situ* substitution is the strongest. In addition, the characteristic peaks of $Y(OH)_3$ are found in all samples. This may indicate that part of rare earth Y ions can turn to $Y(OH)_3$ on LDHs.

Table 1 illustrates the lattice parameters of specimens with different Y%, which can be calculated by the formula a, b inferred by XRD data. With the increasing proportion of Y, the lattice constants a and c are seen to increase in most specimens.

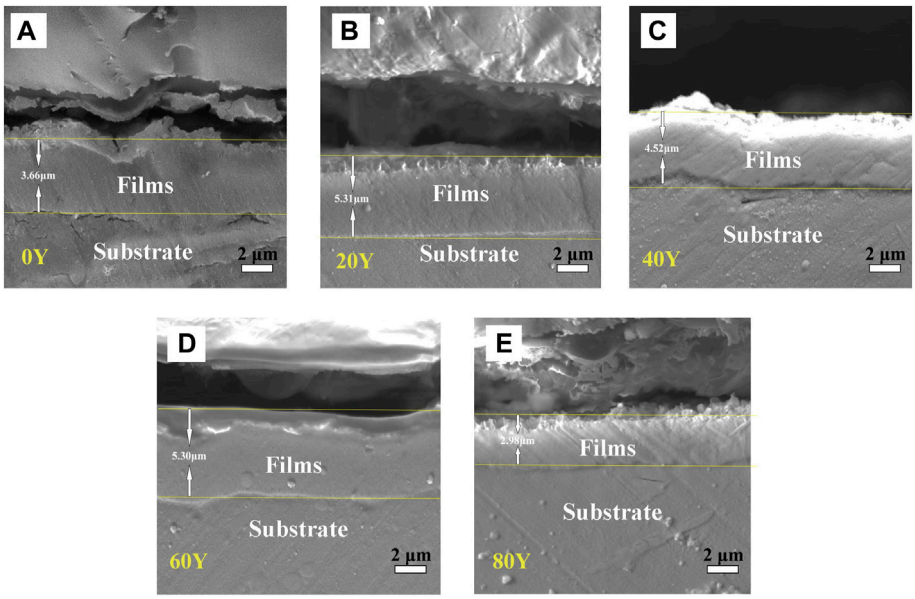

FIGURE 5 | Cross-sectional images of different specimens: 0Y **(A)**; 20Y **(B)**; 40Y **(C)**; 60Y **(D)**; and 80Y **(E)**.

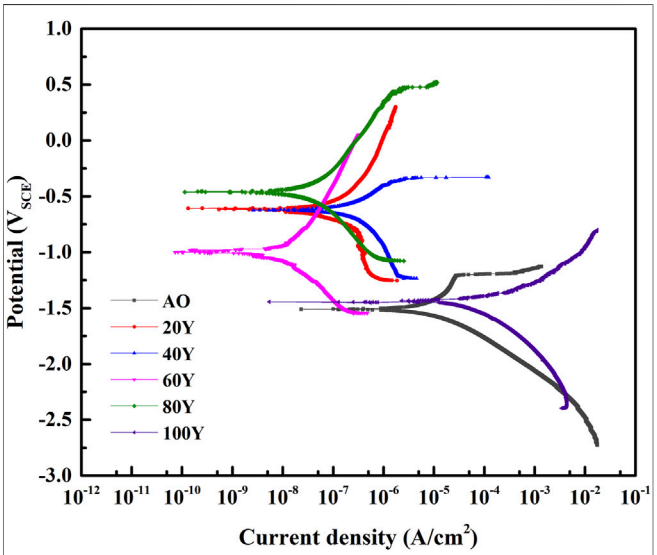

FIGURE 6 | Polarization curves of LDH specimens with different Y% fabricated on phosphoric acid anodized oxide films on Mg–2Zn–4Y alloys of specimens immersed in 3.5 wt% NaCl solution.

TABLE 2 | EDS profile recorded for the corresponding points on different specimens in **Figure 2**: 0Y (a, 1); 20Y (b, 2); 40Y (c, 3); 60Y (d, 4); and 80Y (e, 5).

Sample	0Y (at.%)	20Y (at.%)	40Y (at.%)	60Y (at.%)	80Y (at.%)
Mg	29.7	27.4	20.3	30.5	26.2
Al	8.6	8.7	6.4	8.2	6.1
Y	0.7	1.4	4.5	0.9	3.2
O	60.5	62.5	68.8	60.1	64.5

Generally, the lattice parameter-a is considered the interplanar distance, which equals the average distance of cations in LDH (Wang et al., 2019a). The slight increase of constant-a indicates that the large cations enter LDH, causing the planar distance enlarges, or even the fragmentation, and refinement resulting from the isovalent substitution. The big size of Y cations leads to the increase of planar distance abnormally. The prominent increase of parameter-c reveals the expansion of the interlayer passage (Wang et al., 2019a). The hydrated anion species significantly are relied on parameter-c, and the degree of trivalent cation substitution has an influence on electrostatic forces from anions (Smalenskaite et al., 2017; Wang et al., 2019b). Meanwhile, Y element has relatively low electronegativity, resulting in parameter-c increases by improving the electrostatic forces from anions. In addition, the parameter-a for 80 Y and parameter-c for 20Y show slight decline, which means Y species did not infiltrate LDH very well related to cracks between coatings and the substrate in **Figure 5**. The cracks cause volume expansion and irregular deformation, leading to constant a and c drops. Overall, the addition of Y species leads to obvious changes in structure data as shown in **Table 1**; **Figure 1**.

Figure 2 shows the SEM micrographs of samples. All the samples show typical undulating LDH nanosheet morphology, and some areas are covered with some substances (**Figures 2A–D**). **Figure 2** e shows that a great number of coarse lamellar structures are found. Moreover, EDS analysis of the protrusion area of the samples is shown in **Figure 3**; **Table 1**. The element contents of areas 1 and 2 in **Figure 2** show that the

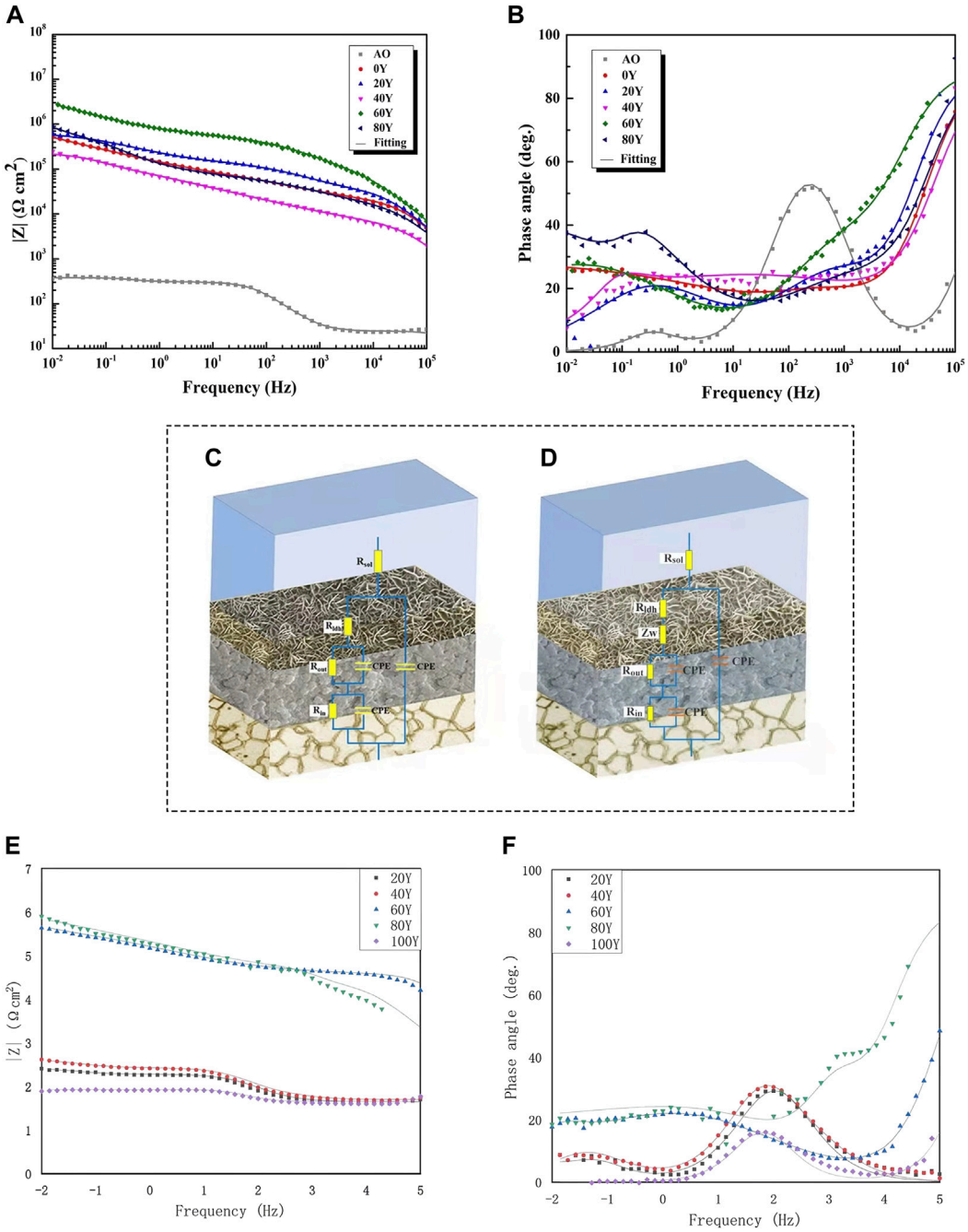

FIGURE 7 | EIS spectra of specimens immersed in 3.5 wt% NaCl solution. **(A,B)**; equivalent circuits and physical models of coatings **(C,D)**; EIS data and fitting curves (straight line) of different coatings in 3.5 wt% NaCl solution after immersion for **(E,F)** 4 days.

accumulated material may be $Y(OH)_3$. Area 3 shows a large number of clusters of LDHs distributed uniformly on the surface. The composition of ternary LDHs can be determined by EDS analysis. EDS analysis of some agglomerates in area 4 shows the morphology of incompletely crystallized ternary LDHs. The energy spectrum analysis of area 5 shows that the flake material may be Mg $(OH)_2$. Combining SEM and EDS analysis of different Y contents, the morphology of MgAlY-LDH nanosheets may be a convex cluster, and some rare earth Y ions in cluster-like material are covered on the LDH sheet. Some of the isomorphic substitutions of Al ions on Y ions existed, and ternary LDHs nanosheets were successfully obtained. In addition, rare earth ions (Y^{3+}), which are larger than aluminum ions, enter the LDH matrix layer to form a matrix crystal lattice, resulting in the morphology of ternary LDHs as convex clusters (Dai et al., 2021).

TABLE 3 | Fitted parameters of different specimens for the EIS spectrum.

Sample	R_s ($\Omega \cdot cm^2$)	CPE (S s^n cm^{-2})	N	R_{film} ($\Omega \cdot cm^2$)	W	CPE (S s^n cm^{-2})	n	R_{out} ($\Omega \cdot cm^2$)	CPE (S sn cm^{-2})	n	R_{in} ($k\Omega \cdot cm^2$	χ^2
AO	0.01	7.3×10^{-3}	1	7.1×10^4	—	1.5×10^{-5}	0.9	2.8×10^2	3.0×10^{-8}	1.0	2.4×10^0	5.3×10^{-3}
0Y	0.01	3.0×10^{-10}	1	1.6×10^4	—	4.7×10^{-6}	0.6	1.0×10^1	0.5×10^{-6}	0.8	1.9×10^1	1.6×10^{-3}
20Y	0.01	3.0×10^{-10}	1	3.0×10^4	—	1.4×10^{-7}	0.6	1.0×10^5	2.6×10^{-6}	0.6	5.2×10^5	1.2×10^{-3}
40Y	0.01	7.2×10^{-10}	1	1.9×10^4	—	7.5×10^{-7}	0.5	4.9×10^4	4.6×10^{-6}	0.5	4.9×10^4	6.6×10^{-3}
60Y	0.01	2.2×10^{-8}	1	7.9×10^4	—	3.3×10^{-8}	0.6	4.0×10^5	1.2×10^{-6}	0.4	1.2×10^7	1.9×10^{-3}
80Y	0.01	3.9×10^{-10}	1	1.3×10^4	5.5×10^{-6}	4.3×10^{-7}	0.5	5.3×10^4	1.3×10^{-5}	1.0	1.0×10^5	6.3×10^{-3}

TABLE 4 | Electrochemical parameters of different specimens.

Specimen	Ecorr (V SCE^{-1})	icorr (A cm^{-2})
AO20Y	–1.511–0.615	7.693 × 10–69.160 × 10–8
40Y	–0.761	1.080 × 10–7
60Y	–0.997	9.052 × 10–9
80Y	–0.459	2.933 × 10–8
0Y	–1.454	4.219 × 10–5

The FT-IR spectrum of each sample is shown in **Figure 4**. In the chemical formula of LDH, anions An^- contain OH^-, NO_3^- and PO_4^{3-}, and metal cations M^{3+} are composed of Al^{3+} and Y^{3+}. Meanwhile, the mental ion Y^{3+} is considered to relate to $Y(OH)_3$ in the XRD image (**Figure 1**.). Thus, the result of the FT-IR spectrum is in accordance with the XRD image. The vibration wavelengths of all samples at 3,693, 3,430, and 1,640 cm^{-1} correspond to the hydroxyl bands of water or LDHs, respectively (Luo, 2019). Each sample showed characteristic peaks at 1,360 and 950 cm^{-1}, which was attributed to the vibration absorption of NO_3^- and PO_4^{3-}, indicating the presence of NO_3^- and PO_4^{3-} in the interlayer of LDHs (Zăvoianu, 2018). In addition, the vibrational stretching of Y-OH appears in the band around 660cm^{-1}. In addition, the bands around 660 and 550 cm^{-1} are attributed to the vibrational stretching of Y-OH and Al-OH, respectively (Zhang, 2016; Zhang, 2019; Jiang et al., 2021). With the gradually increasing Y content, we can find that the strength of Y-OH increases gradually, indicating that more $Y(OH)_3$ is attached to the surface of the film.

The SEM image of the cross section of each sample is shown in **Figure 5**. The thickness of the samples of 0Y, 20Y, 40Y, 60Y, and 80Y correspond to 3.66, 5.31, 4.52, 5.30, and 2.98 μm, respectively. The reason why the thickness of the samples is different is that the growth condition of films is controlled by the concentration of Y. It can be seen from the cross-sectional image that the samples of 20Y, 40Y, and 60Y have grown a relatively thick film, which may indicate that 20Y, 40Y, and 60Y samples have appropriate conditions for film growth. However, there are cracks between the 0Y, 20Y, 40Y, and 80Y coatings and the substrate, indicating that the bonding force between the coating and the substrate is relatively poor. In addition, the cross section of the 60Y sample is relatively dense and thick, and there is no gap between the sample and the substrate, indicating that the coating has a better growth condition when the concentration is 60Y.

3.2 Corrosion Resistance Test of the Film

We make the corrosion resistance tests aiming at LDH specimens with different Y% fabricated on phosphoric acid anodized oxide films on Mg–2Zn–4Y alloys of specimens. **Figure 6** shows the polarization curves of different samples immersed in 3.5 wt% NaCl solutions. The electrochemical parameters corresponding to each polarization curve are listed in **Table 2**. Here, the corrosion potential (Ecorr) cannot measure the corrosion resistance of the coating because Ecorr will be significantly affected by thermodynamic properties of the material (Adsul et al., 2021; Cui et al., 2021). Usually, a lower corrosion density (icorr) is regarded as an excellent corrosion prevention property (Ramezanzadeh et al., 2016; Chen et al., 2022). It can be seen in **Table 2** that the current density of 20Y, 40Y, 60Y, and 80Y is close; among these, 20Y, 40Y, and 60Y have relatively thick coating making their current density rather low. However, it may indicate that because there are cracks between coating and substrate and the bonding force is poor in 20Y and 40Y, their current density is higher than 60Y, while 80Y has relatively thin coating leading to climbing of current density. Meanwhile, the 0Y and 100Y samples have more cracks and thin-film leading to corrosion current much higher than other samples. The 60Y sample has the lowest corrosion current, reaching 2.933×10^{-8} A cm^{-2}, indicating that the ternary MgAlY-LDH film prepared on the phosphoric acid anodic oxide film has the best corrosion resistance. Also, other samples with a concentration close to 60Y (20Y, 40Y, and 80Y) all have good corrosion resistance. Therefore, the LDH film grown *in situ* on the phosphoric acid anodic oxidation system has better corrosion resistance.

In order to study the corrosion resistance mechanism of different samples in a corrosive environment, electrochemical impedance spectroscopy was studied. The Bode impedance and phase angle spectra of different samples in 3.5 wt% NaCl solution are shown in **Figures 7A,B**. The impedance of matrix and coating is illustrated by the $|Z|_{0.01\ Hz}$ impedance. The high-frequency range reflects the properties of the coating (10^2–10^5 Hz), the middle frequency range reflects the inner layer (1–10^2 Hz), and the characteristics of the substrate and coating intersection are reflected in the low frequency (less than 1 Hz). The greater the value of the impedance modulus (*0.01 Hz*) in the low-frequency region, the better the corrosion resistance of the sample in a corrosive environment (Chen et al., 2020; Zhang et al., 2018; Chen et al., 2021). Among them, the 60Y sample has the highest impedance modulus of all samples, exceeding 10^6 Ω cm^2, which is an order of magnitude higher than the impedance value of the

anodized sample (**Figure 7A**). In the Bode-phase angle spectrum, three relaxation phenomena corresponding to the time constant can be found in all samples (**Figure 7B**). The time constant is used to characterize the structural characteristics and corrosion performance of the composite coating. **Table 3** has listed the fitted electrochemical impedance spectroscopy parameters. R_s is considered the electrolyte resistance. R_{film} corresponds to the sample surface film (LDHs) resistance. R_{out} *and* R_{in} represent the external porous layer resistance of the anodic oxide film and the internal dense layer resistance of the anodic oxide film, respectively. A larger R-value represents a better corrosion resistance of the coating. The constant phase element (CPE) is the response capacitance connected in parallel with the corresponding resistance. n indicates the angular frequency, and it can be considered that CPE is an ideal capacitor when n is close to 1. The lower the chi-squared error (χ^2) indicates that the circuit fits well (Cui et al., 2018; Chen, 2019). At low frequency, diffusion of the corrosion medium affects the control corrosion process (Ye, 2018). Therefore, a Warburg impedance part (Z_W) is included in the circuit of the 80Y specimen. SEM and EDS show that (**Figure 2** and **Figure 3**) a passivation film of Y $(OH)_3$ is formed on the coating surface when the content of Y is relatively high, and it has a certain protective effect on the sample (Ye, 2018). Compared with other coatings, the values of R_{film}, $R_{out,}$ and R_{in} of the 60Y sample are the largest among all the tests, and the corrosion resistance is the highest, indicating that the ternary MgAlY-LDHs formed by the 60Y sample has the best corrosion performance (**Table 4**).

Figure 7 (e.f.) illustrates the Bode impedance plots of the different coatings during the 4 days. After 4 days of immersion, 60Y still has the largest |Z| 0.01 Hz value, which indicates that 60Y has the best corrosion resistance. At intermediate frequency, the phase angles of 0Y, 20Y, 40Y, and 80Y decrease quickly, indicating that the electrolyte penetrates these samples' coating system. However, 60Y has an increasing phase angle, indicating that the electrochemical reaction does not occur under the coating. In conclusion, the coating of 60Y has the best performance in corrosion resistance.

4 CONCLUSION

The MgAlY-LDH film was fabricated successfully on the anodized film of Mg–2Zn–4Y alloys. The introduction of Y ions with larger ionic radius into the LDH laminates affects the crystal lattice changes of LDHs and ultimately leads to the formation of MgAlY-LDH nanosheets in the shape of convex clusters of flowers. MgAlY-LDHs can adsorb the corrosive medium (Cl^-) into the intermediate layer in a corrosive environment, thereby triggering the stable appearance of the Y element and improving the corrosion performance of LDHs.

DATA AVAILABILITY STATEMENT

The original contributions presented in the study are included in the article/Supplementary Material; further inquiries can be directed to the corresponding author.

AUTHOR CONTRIBUTIONS

YH: conceptualization, investigation, methodology, data curation, and writing—original draft. LW: conceptualization, methodology, supervision, writing—review and editing, and funding acquisition. XZ: writing—review and editing and investigation. GZ: methodology. YC: investigation. TW: formal analysis. XD: methodology. JX: investigation. YZ: formal analysis. FP: writing—review and editing.

FUNDING

This work was supported by the National Natural Science Foundation of China (51971040, 52171101), the Natural Science Foundation of Chongqing (cstc2021jcyj-msxmX0613), National College Students' Innovation and Entrepreneurship Training Program(202110611045), and the National Natural Science Foundation of China (52001036, 51971044).

ACKNOWLEDGMENTS

We thank the Analytical and Testing Center of Chongqing University for performing the SEM test and National Engineering Research Center for magnesium Alloys for XRD, FT-IR, and electrochemical experiments.

REFERENCES

Adsul, S. H., Bagale, U. D., Sonawane, S. H., and Subasri, R. (2021). Release Rate Kinetics of Corrosion Inhibitor Loaded Halloysite Nanotube-Based Anticorrosion Coatings on Magnesium Alloy AZ91D. *J. Magnesium Alloys* 9 (1), 202–215. doi:10.1016/j.jma.2020.06.010

Angelescu, E., Pavel, O. D., Che, M., Bîrjega, R., and Constentin, G. (2004). Cyanoethylation of Ethanol on Mg-Al Hydrotalcites Promoted by Y^{3+} and La^{3+}. *Catal. Commun.* 5 (10), 647–651. doi:10.1016/j.catcom.2004.07.016

Ardelean, H., Seyeux, A., Zanna, S., Prima, F., Frateur, I., and Marcus, P. (2013). Corrosion Processes of Mg-Y-Nd-Zr Alloys in Na_2SO_4 Electrolyte. *Corros. Sci.* 73, 196–207. doi:10.1016/j.corsci.2013.03.036

Atrens, A. (2015). Review of Recent Developments in the Field of Magnesium Corrosion: Recent Developments in Mg Corrosion. *Adv. Eng. Mater.* 17, 2–3. doi:10.1002/adem.201400434

Bîrjega, R. (2005). Rare-earth Elements Modified Hydrotalcites and Corresponding Mesoporous Mixed Oxides as Basic Solid Catalysts. *Appl. Catal. A General* 288 (1), 185–193. doi:10.1016/j.apcata.2005.04.030

Blawert, C., Dietzel, W., Ghali, E., and Song, G. (2006). Anodizing Treatments for Magnesium Alloys and Their Effect on Corrosion Resistance in Various Environments. *Adv. Eng. Mater.* 8, 511–533. doi:10.1002/adem.200500257

Chen, Y. (2019). Enhanced Corrosion Protective Performance of Graphene Oxide-Based Composite Films on AZ31 Magnesium Alloys in 3.5 Wt% NaCl Solution. *Appl. Surf. Sci.* 493, 1224–1235.

Chen, Y., Ren, B., Gao, S., and Cao, R. (2020). The Sandwich-like Structures of Polydopamine and 8-Hydroxyquinoline Coated Graphene Oxide for Excellent Corrosion Resistance of Epoxy Coatings. *J. Colloid Interface Sci.* 565, 436–448. doi:10.1016/j.jcis.2020.01.051

Chen, Y., Wu, L., Yao, W., Chen, Y., Zhong, Z., Ci, W., et al. (2022). A Self-Healing Corrosion Protection Coating with Graphene Oxide Carrying 8-Hydroxyquinoline Doped in Layered Double Hydroxide on a Micro-arc Oxidation Coating. *Corros. Sci.* 194, 109941. doi:10.1016/j.corsci.2021.109941

Chen, Y., Wu, L., Yao, W., Zhong, Z., Chen, Y., Wu, J., et al. (2021). One-step *In Situ* Synthesis of Graphene Oxide/MgAl-Layered Double Hydroxide Coating on a Micro-arc Oxidation Coating for Enhanced Corrosion Protection of Magnesium Alloys. *Surf. Coatings Technol.* 413, 127083. doi:10.1016/j.surfcoat.2021.127083

Cui, L.-Y., Gao, L., Zhang, J.-C., Tang, Z., Fan, X.-L., Liu, J.-C., et al. (2021). *In Vitro* corrosion Resistance, Antibacterial Activity and Cytocompatibility of a Layer-By-Layer Assembled DNA Coating on Magnesium Alloy. *J. Magnesium Alloys* 9 (1), 266–280. doi:10.1016/j.jma.2020.03.009

Cui, M., Ren, S., Zhao, H., Xue, Q., and Wang, L. (2018). Polydopamine Coated Graphene Oxide for Anticorrosive Reinforcement of Water-Borne Epoxy Coating. *Chem. Eng. J.* 335, 255–266. doi:10.1016/j.cej.2017.10.172

Dai, X., Wu, L., Xia, Y., Chen, Y., Zhang, Y., Jiang, B., et al. (2021). Intercalation of Y in Mg-Al Layered Double Hydroxide Films on Anodized AZ31 and Mg-Y Alloys to Influence Corrosion Protective Performance. *Appl. Surf. Sci.* 551, 149432. doi:10.1016/j.apsusc.2021.149432

Das, J., Das, D., and Parida, K. M. (2006). Preparation and Characterization of Mg-Al Hydrotalcite-Like Compounds Containing Cerium. *J. Colloid Interface Sci.* 301 (2), 569–574. doi:10.1016/j.jcis.2006.05.014

Dong, Y., Wang, F., and Zhou, Q. (2014). Protective Behaviors of 2-Mercaptobenzothiazole Intercalated Zn-Al-Layered Double Hydroxide Coating. *J. Coat. Technol. Res.* 11 (5), 793–803. doi:10.1007/s11998-014-9568-9

Guo, X., Zhang, F., Evans, D. G., and Duan, X. (2010). Layered Double Hydroxide Films: Synthesis, Properties and Applications. *Chem. Commun. Camb. Engl.* 46, 5197–5210. doi:10.1039/c0cc00313a

He, W., Zhang, E., and Yang, K. (2010). Effect of Y on the Bio-Corrosion Behavior of Extruded Mg-Zn-Mn Alloy in Hank's Solution. *Mater. Sci. Eng. C* 30, 167–174. doi:10.1016/j.msec.2009.09.014

Hornberger, H., Virtanen, S., and Boccaccini, A. R. (2012). Biomedical Coatings on Magnesium Alloys - A Review. *Acta biomater.* 8, 2442–2455. doi:10.1016/j.actbio.2012.04.012

Huang, Y., Jin, F.-M., Chen, F.-J., and Chen, L. (2014). Improved Cycle Stability and High-Rate Capability of Li_3VO_4-Coated $Li[Ni_{0.5}Co_{0.2}Mn_{0.3}]O_2$ Cathode Material Under Different Voltages. *J. Power Sources* 256, 1–7. doi:10.1016/j.jpowsour.2014.01.003

Jiang, Q., Lu, D., Wang, N., Wang, X., Zhang, J., Duan, J., et al. (2021). The Corrosion Behavior of Mg-Nd Binary Alloys in the Harsh Marine Environment. *J. Magnesium Alloys* 9 (1), 292–304. doi:10.1016/j.jma.2019.12.010

Liu, M., Schmutz, P., Uggowitzer, P. J., Song, G., and Atrens, A. (2010). The Influence of Yttrium (Y) on the Corrosion of Mg-Y Binary Alloys. *Corros. Sci.* 52 (11), 3687–3701. doi:10.1016/j.corsci.2010.07.019

Lu, H. (2018). Comparative Study on Synchronous Adsorption of Arsenate and Fluoride in Aqueous Solution onto MgAlFe-LDHs with Different Intercalating Anions. *RSC Adv.* 8, 33301–33313.

Luo, S. (2019). Synthesis of Calcined La-Doped Layered Double Hydroxides and Application on Simultaneously Removal of Arsenate and Fluoride. *J. Solid State Chem.* 275, 275. doi:10.1016/j.jssc.2019.04.017

Lyu, J., Kim, J., Liao, H., She, J., Song, J., Peng, J., et al. (2020). Effect of Substitution of Zn with Ni on Microstructure Evolution and Mechanical Properties of LPSO Dominant Mg-Y-Zn Alloys. *Mater. Sci. Eng. A* 773, 138735. doi:10.1016/j.msea.2019.138735

Mordike, B. L., and Ebert, T. (2001). Magnesium. *Mater. Sci. Eng. A* 302 (1), 37–45. doi:10.1016/s0921-5093(00)01351-4

Mrózek, O. (2019). Mg-Al-La LDH-$MnFe_2O_4$ Hybrid Material for Facile Removal of Anionic Dyes from Aqueous Solutions. *Appl. Clay Sci.* 169, 1–9.

Pavel, O. D. (2011). The Activity of Yttrium-Modified Mg,Al Hydrotalcites in the Epoxidation of Styrene with Hydrogen Peroxide. *Appl. Catal. A General* 403 (1), 83–90. doi:10.1016/j.apcata.2011.06.017

Polmear, I. (2017). *Light Alloys : Metallurgy of the Light Metals*. Butterwort: Elsevier.

Prado, M. T. P., and Cepeda-Jiménez, C. M. (2015). Strength Ceiling Smashed for Light Metals. *Nature* 528, 486–487. doi:10.1038/528486a

Ramezanzadeh, B., Ahmadi, A., and Mahdavian, M. (2016). Enhancement of the Corrosion Protection Performance and Cathodic Delamination Resistance of Epoxy Coating through Treatment of Steel Substrate by a Novel Nanometric Sol-Gel Based Silane Composite Film Filled with Functionalized Graphene Oxide Nanosheets. *Corros. Sci.* 109, 182–205. doi:10.1016/j.corsci.2016.04.004

Scarpellini, D., Falconi, C., Gaudio, P., Mattoccia, A., Medaglia, P. G., Orsini, A., et al. (2014). Morphology of Zn/Al Layered Double Hydroxide Nanosheets Grown onto Aluminum Thin Films. *Microelectron. Eng.* 126, 129–133. doi:10.1016/j.mee.2014.07.007

Smalenskaite, A., Vieira, D. E. L., Salak, A. N., Ferreira, M. G. S., Katelnikovas, A., and Kareiva, A. (2017). A Comparative Study of Co-precipitation and Sol-Gel Synthetic Approaches to Fabricate Cerium-Substituted Mg Al Layered Double Hydroxides with Luminescence Properties. *Appl. Clay Sci.* 143, 175–183. doi:10.1016/j.clay.2017.03.036

Srinivas, A., Pavan, D., Venkatesha, B. K., Rao, R. R., and Mohith, L. (2022). Study on Mechanical Properties of AZ91 Magnesium Alloy. *Mater. Today Proc.* 54, 291–294. doi:10.1016/j.matpr.2021.09.171

Stoltenhoff, T., Kreye, H., and Richter, H. J. (2002). An Analysis of the Cold Spray Process and its Coatings. *J. Therm. Spray Technol.* 11, 542–550. doi:10.1361/105996302770348682

Świrk, K. (2018). Yttrium Promoted Ni-Based Double-Layered Hydroxides for Dry Methane Reforming. *J. CO2 Util.* 27, 247–258.

Świrk, K. (2019). Ce- and Y-Modified Double-Layered Hydroxides as Catalysts for Dry Reforming of Methane: On the Effect of Yttrium Promotion. *Catalysts* 9, 56.

Wang, J., Wei, F., Shi, B., Ding, Y., and Jin, P. (2019a). The Effect of Y Content on Microstructure and Tensile Properties of the As-Extruded Mg-1Al-xY Alloy. *Mater. Sci. Eng. A* 765, 138288. doi:10.1016/j.msea.2019.138288

Wang, Y., Zhang, Y., Zhou, B., Li, C., Gao, F., Wang, X., et al. (2019b). *In-situ* Observation of the Growth Behavior of ZnAl Layered Double Hydroxide Film Using EQCM. *Mater. Des.* 180, 107952. doi:10.1016/j.matdes.2019.107952

Wang, Z., Fongarland, P., Lu, G., and Essayem, N. (2014). Reconstructed La-, Y-, Ce-Modified MgAl-Hydrotalcite as a Solid Base Catalyst for Aldol Condensation: Investigation of Water Tolerance. *J. Catal.* 318, 108–118. doi:10.1016/j.jcat.2014.07.006

Ye, Y. (2018). One-step Synthesis of Superhydrophobic Polyhedral Oligomeric Silsesquioxane-Graphene Oxide and its Application in Anti-corrosion and Anti-Wear Fields. *Corros. Sci.* 147, 9. doi:10.1016/j.corsci.2018.10.034

Zahedi Asl, V. (2019). The Effect of Cerium Cation on the Microstructure and Anti-Corrosion Performance of LDH Conversion Coatings on AZ31 Magnesium Alloy. *J. Alloys Compd.* 821, 153248.

Zăvoianu, R. (2018). Effect of Hydration Temperature on the Structure Reconstruction of MgAlY Layered Materials. *Comptes Rendus Chim.* 21 (3), 318–326.

Zhang, F. (2016). Corrosion Resistance of the Superhydrophobic Mg(OH)2/Mg-Al Layered Double Hydroxide Coatings on Magnesium Alloys. *Metals* 6 (4), 85. doi:10.3390/met6040085

Zhang, F., Liu, Z.-G., Zeng, R.-C., Li, S.-Q., Cui, H.-Z., Song, L., et al. (2014). Corrosion Resistance of Mg-Al-LDH Coating on Magnesium Alloy AZ31. *Surf. Coatings Technol.* 258, 1152–1158. doi:10.1016/j.surfcoat.2014.07.017

Zhang, G. (2018). Active Corrosion Protection by a Smart Coating Based on a MgAl-Layered Double Hydroxide on a Cerium-Modified Plasma Electrolytic Oxidation Coating on Mg Alloy AZ31. *Corros. Sci.* 139, 370. doi:10.1016/j.corsci.2018.05.010

Zhang, G. (2019). *In-situ* Grown Super- or Hydrophobic Mg-Al Layered Double Hydroxides Films on the Anodized Magnesium Alloy to Improve Corrosion Properties. *Surf. Coatings Technol.*, 366. doi:10.1016/j.surfcoat.2019.03.016

Zhang, G., Wu, L., Tang, A., Pan, H., Ma, Y., Zhan, Q., et al. (2018). Effect of Micro-arc Oxidation Coatings Formed at Different Voltages on the *In Situ* Growth of Layered Double Hydroxides and Their Corrosion Protection. *J. Electrochem. Soc.* 165 (7), C317–C327. doi:10.1149/2.0531807jes

Zhang, Y. (2017a). Double-doped LDH Films on Aluminum Alloys for Active Protection. *Mater. Lett.*, 192. doi:10.1016/j.matlet.2017.01.038

Zhang, Y. (2017b). Enhancement of Anticorrosion Protection via Inhibitor-Loaded ZnAlCe-LDH Nanocontainers Embedded in Sol–Gel Coatings. *J. Coatings Technol. Res.* 15, 1–11. doi:10.1007/s11998-017-9978-6

Zhou, B., Wei, X., Wang, Y., Huang, Q., Hong, B., and Wei, Y. (2019). Effect of Lanthanum Addition on Microstructures and Corrosion Behavior of ZnAl-LDHs Film of 6061 Aluminum Alloys. *Surf. Coatings Technol.* 379, 125056. doi:10.1016/j.surfcoat.2019.125056

Conflict of Interest: The authors declare that the research was conducted in the absence of any commercial or financial relationships that could be construed as a potential conflict of interest.

Publisher's Note: All claims expressed in this article are solely those of the authors and do not necessarily represent those of their affiliated organizations, or those of the publisher, the editors and the reviewers. Any product that may be evaluated in this article, or claim that may be made by its manufacturer, is not guaranteed or endorsed by the publisher.

Advantages of publishing in Frontiers

OPEN ACCESS
Articles are free to read for greatest visibility and readership

FAST PUBLICATION
Around 90 days from submission to decision

HIGH QUALITY PEER-REVIEW
Rigorous, collaborative, and constructive peer-review

TRANSPARENT PEER-REVIEW
Editors and reviewers acknowledged by name on published articles

Frontiers
Avenue du Tribunal-Fédéral 34
1005 Lausanne | Switzerland

Visit us: www.frontiersin.org
Contact us: frontiersin.org/about/contact

REPRODUCIBILITY OF RESEARCH
Support open data and methods to enhance research reproducibility

DIGITAL PUBLISHING
Articles designed for optimal readership across devices

FOLLOW US
@frontiersin

IMPACT METRICS
Advanced article metrics track visibility across digital media

EXTENSIVE PROMOTION
Marketing and promotion of impactful research

LOOP RESEARCH NETWORK
Our network increases your article's readership